VILNIUS UNIVERSITY
CENTER FOR PHYSICAL SCIENCES AND TECHNOLOGY

Ramūnas
LEVINAS

Electrodeposition and characterization of photo-/electrocatalytic MoS$_2$ and WO$_3$ films for water splitting catalysis

DOCTORAL DISSERTATION

Natural sciences,
Chemistry (N 003)

VILNIUS 2021

Academic supervisor:
Prof. Dr. Henrikas Cesiulis (Vilnius University, Natural Sciences, Chemistry – N 003).
Academic consultant:
Assoc. Prof. Dr. Natalia Tsyntsaru (Vilnius University, Natural Sciences, Chemistry – N 003).

This doctoral dissertation will be defended in a public/closed meeting of the Dissertation Defence Panel:
Chairman – **Prof. Habil. Dr. Aivaras Kareiva** (Vilnius University, Natural Sciences, Chemistry – N 003).

Members:
Dr. Pavel Chulkin (The Silesian University of Technology, Natural Sciences, Chemistry – N 003).
Dr. Inga Morkvėnaitė-Vilkončienė (Vilnius Gediminas Technical university, Natural Sciences, chemistry – N 003).
Doc. Dr. Deivis Plaušinaitis (Vilnius University, Natural Sciences, Chemistry – N 003).
Doc. Dr. Ieva Plikusienė (Vilnius University, Natural Sciences, chemistry – N 003).

The dissertation shall be defended at a public meeting of the Dissertation Defence Panel at 14:00 on 6 September 2021 in Room KDA of the Faculty of Chemistry and Geosciences. Address: Naugarduko st., 24., KDA., Vilnius, Lithuania
Tel. (8 5) 219 3108; e-mail: info@chgf.vu.lt

The text of this dissertation can be accessed at the library of Vilnius University and at the library of FTMC, as well as on the website of Vilnius University:
www.vu.lt/lt/naujienos/ivykiu-kalendorius

https://orcid.org/0000-0003-3324-6472

VILNIAUS UNIVERSITETAS
FIZINIŲ IR TECHNOLOGIJOS MOKSLŲ CENTRAS

Ramūnas
LEVINAS

Foto-/elektrokatalizinių MoS$_2$ ir WO$_3$ plonų sluoksnių elektrocheminis nusodinimas ir pritaikymas vandens skaidymo katalizei

DAKTARO DISERTACIJA

Gamtos mokslai,
Chemija (N 003)

VILNIUS 2021

Mokslinis vadovas:
Prof. Dr. Henrikas Cesiulis (Vilniaus universitetas, gamtos mokslai, chemija, N 003).
Mokslinis konsultantas:
Assoc. Prof. Dr. Natalia Tsyntsaru (Vilniaus universitetas, IFA Taikomosios fizikos institutas, gamtos mokslai, chemija, N 003).

Gynimo taryba:
Pirmininkas – **Prof. habil. Dr. Aivaras Kareiva** (Vilniaus universitetas, gamtos mokslai, chemija, N 003).

Nariai:
Dr. Pavel Chulkin (Silezijos Technologijų Universitetas, gamtos mokslai, chemija, N 003).
Dr. Inga Morkvėnaitė-Vilkončienė (Vilniaus Gedimino technikos universitetas, gamtos mokslai, chemija, N 003).
Doc. dr. Deivis Plaušinaitis (Vilniaus universitetas, gamtos mokslai, chemija, N 003).
Doc. dr. Ieva Plikusienė (Vilniaus universitetas, gamtos mokslai, chemija, N 003).

Disertacija ginama viešame Gynimo tarybos posėdyje 2021 m. rugsėjo mėn. 6 d. 14:00 val. Chemijos ir Geomokslų fakulteto KDA auditorijoje. Adresas: [Naugarduko g. 24, KDA, Vilnius, Lietuva], tel. (8 5) 219 3108; el. paštas info@chgf.vu.lt.

Disertaciją galima peržiūrėti Vilniaus universiteto, FTMC Chemijos instituto bibliotekose ir VU interneto svetainėje adresu: https://www.vu.lt/naujienos/ivykiu-kalendorius

ABSTRACT

The renewable energy field faces challenges in every step from energy production, storage, to consumption. It is thought that in lieu of fossil fuels, green hydrogen could fill the role of a liquid energy storage medium. However, in order to compete with batteries, the entire hydrogen economy must still be extensively researched and worked on.

Green hydrogen (i.e., hydrogen produced without emission of polluting by-products) can be produced by water electrolysis – electrochemical water splitting. However, in order to make this process more viable, heterogenous catalysts must be used to catalyze the hydrogen evolution reaction (HER) and oxygen evolution reaction (OER). The best-performing catalysts are, unfortunately, expensive precious metals or their compouds. As such, much research is devoted to finding and, perhaps more importantly, applying alternatives to these precious metals.

In this study MoS_2 was considered for heterogenous HER catalysis in acidic media. The material was obtained by electrochemical deposition under varying conditions and deposition parameters. Moreover, the possibility for scaled-up application was investigated by considering 2D (wire) and 3D (metallic foam) electrodes. It was found that, while catalyst loading had the defining effect on total electrode activity, the intrinsic per-site activity could be optimized by tuning either electrodeposition parameters or by considering additives that influence the synthesis of the film. Electrochemical impedance spectroscopy was used to characterize the catalyst/solution interface.

WO_3 films, obtained by anodization, were investigated as photoanodes for OER. It was found that a tunable film thickness could be achieved by modifying anodization voltage (if potentiostatic), current density (if galvanostatic), and time. Moreover, the obtained film morphologies ranged from compact to highly porous. The possibility to form a composite WO_3-MoS_x film by one-step anodization was also elaborated. The electrochromic nature of WO_3 was exploited in order to electrochemically induce H^+ intercalation, thus modifying the material's structure and its photocatalytic properties. All of the manufactured photoanodes were extensively tested for their OER photocatalytic activity and compared with each other in order to select the most photocatalytically active film.

Overall, the materials and methods presented in this dissertation were aimed not only towards producing highly catalytically active materials, but also towards discussing photo-/electrochemical characterization methods that could be used to overcome certain inconsistencies in the field of published heterogenous catalysis research.

PUBLICATION LIST

Paper 1:   **R. Levinas**, N. Tsyntsaru, M. Lelis, H. Cesiulis

Synthesis, electrochemical impedance spectroscopy study and photoelectrochemical behaviour of as-deposited and annealed WO_3 films.

Electrochimica Acta 225 (2017), p. 29 – 38.

Paper 2:   **R. Levinas**, N. Tsyntsaru, H. Cesiulis

Insights into electrodeposition and catalytic activity of MoS_2 for hydrogen evolution reaction electrocatalyis

Electrochimica Acta 317 (2019), p. 427 – 436.

Paper 3:   **R. Levinas**, N. Tsyntsaru, H. Cesiulis

The characterization of electrodeposited MoS_2 thin films on a foam-based electrode for hydrogen evolution

Catalysts 10 (2020), 1182.

LIST OF SYMBOLS AND ABBREVIATIONS

C_a – adsorption capacitance C_{sc} – space charge layer capacitance C_{dl} – double layer capacitance **CV** – cyclic voltammetry **CVD** – chemical vapor deposition	η_{10mA} – overpotential to reach 10 mA of HER current
DFT - density functional theory	**PEIS** – photo electrochemical impedance spectroscopy
EDX – energy-dispersive x-ray spectroscopy **EEC** – equivalent electric circuit **EIS** – electrochemical impedance spectroscopy **EQE** – external quantum efficiency	**OCP** – open circuit potential **OER** – oxygen evolution reaction
h^+ - photogenerated hole **HER** – hydrogen evolution reaction η - overpotential	$Q_{deposition}$ - charge passed during electrodeposition
IPCE – incident photon conversion efficiency **IMPS** – intensity modulated photocurrent spectroscopy I_0 – light intensity i_0 – exchange current	R_s – solution resistance R_{ct} – charge transfer resistance R_a – adsorption resistance R_{sc} – space charge layer capacitance
j_0 – exchange current density j_{ph} – photocurrent j_{ss} – steady-state photocurrent	**SEM** – scanning electron microscopy **SHE** – standard hydrogen electrode
k_{tr} – hole transfer constant k_{rec} – surface recombination constant	**TOF** – turnover frequency **TTM** - tetrathiomolybdate τ_s – cell time constant τ_{LF} – low-frequency time constant τ_{LF} – high-frequency time constant
LSV – linear sweep voltammetry	**UV** - ultraviolet
N_A – Avogadro's number η – overpotential	**XPS** – X-ray photoelectron spectroscopy

TABLE OF CONTENTS

INTRODUCTION

In 2004, during the European Conference for Renewable energy in Berlin, the EU defined a goal that by the year 2020 20% of its total energy consumption would be provided by renewable energy sources. At the end of 2019 the target had almost been reached and stood at 19.7%, with most countries meeting or exceeding their ambitions. This prompted a new goal to be set for 2030 – that nearly a third (27%) of the EU's energy consumption would come from renewable sources.

Typically, any potential source of power that could be restored within a reasonable timeframe and with minimal impact on the environment is considered renewable. Electric energy obtained from solar or wind power would be a classic example. Wood-burning furnaces, used in northern countries to heat homes, are also considered to use a renewable resource – trees that could grow back in several decades. In contrast, fossil fuels such as coal or oil would take an unsustainable amount of time to replenish, and as such are considered at best a transient resource to satisfy humanity's future energy needs.

Although it is a simple term and concept, full utilization of renewable energy will require will require vast infrastructure to be built or adapted in order to make full use of these resources. Electric power can be fed into already existing grids, but, for example, internal combustion engines cannot be easily modified to accept non-fossil-fuel based liquids. Moreover, energy production as an applied technology is well more advanced than energy storage. Solar and wind power are, by their nature, intermittent and unreliable. While global grids are perpetually supplied by more stable fossil-fuel burning plants, renewable energy sources act as supplementary. Ideally, at some point a switch would happen when these sources would become the main supplier of power.

Therefore, a significant part of renewable energy systems is storage: some process should be made to occur when surplus power exists, that could then be reversed to produce power when the source is inactive. The simplest form of electrical energy storage is a battery, and a lot of research has been and will continue to be carried out on this subject. However, a typical energy density of a Li-ion battery, which is considered to be the most promising due to its weight, is 152 Wh kg^{-1} and could be brought up to 690 Wh kg^{-1} by nanostructurization [1,2]. Conventionally used fossil fuels such as diesel and petrol have energy densities of ~ 13 000 Wh kg^{-1}, and hydrogen gas exceeds 30 000 Wh kg^{-1} [3]. Although batteries have been successfully integrated into

various industries – automotive in particular – their low gravimetric energy density makes large-scale use prohibitive.

It is natural to assume that liquid fossil fuels have found a specific niche in human civilization, and so they should be replaced by liquid renewable fuels. As hinted to earlier, hydrogen seems like the most likely candidate. In 2020 the EU had reaffirmed its intention to reach total carbon neutrality by 2050, and the use of green hydrogen is strongly counted on to meet this goal. However, green or clean hydrogen is not currently standard. It was reported that as of 2019 only 4% of the EU's produced hydrogen was clean – most H_2 was obtained by steam reforming natural gas, resulting in large CO_2 emissions. Clean hydrogen, meanwhile, is produced without any byproducts. This can be achieved through electrolysis of water, whereby application of a sufficient potential in an aqueous solution will result in the splitting of an H_2O molecule into H_2 at the cathode and O_2 at the anode.

The adoption of any new technology is ultimately a matter of economic feasibility, and this is what currently hinders the production, storage, and consumption of clean hydrogen – its price. A Bloomberg report on the future outlook on the hydrogen economy published in 2020 calculated that electrolyzed hydrogen costs from $2.5 per kg to $4.5 per kg, in comparison to as low as $1.1 per kg for hydrogen that was obtained from coal or natural gas. This difference is expected to disappear by 2030, and if current trends hold then electrolyzed hydrogen could range from $0.7 - $1.6 per kg in 2050. Admittedly, the production (electrolysis) would require immense amounts of renewable power; storage, transport, and shipping would likely face as of yet unforeseeable issues. The economy of hydrogen is only in its initial stages.

If hydrogen finds its place in technology as a fuel, then electrocatalysis is sure to play a major part in its production. The price of electrolyzed H_2 would be a function of the costs of electrical energy, material used (water), and the electrolyzer/cell. The cell and its power consumption would be closely interlinked. Simple materials such as stainless steel are cheap, but ineffective. Catalysts may be costly, but are more energy-efficient. It is important to find a balance between cost and efficiency, and this search has resulted in a massive drive to find cheap, effective catalytic materials over recent decades.

In its simplest form, an electrolyzer for water splitting would consist of two electrodes in an aqueous electrolyte – an anode and a cathode – connected to a power source. That means that two possibilities exist to make the cell more effective: a photo-/electrocatalytic cathode (for the hydrogen evolution reaction - **HER**) and a photo-/electrocatalytic anode (to catalyze oxygen evolution - **OER**). Precious metals, such as Pt or Pd, are excellent HER catalysts, but their price makes their use prohibitively expensive on an

industrial scale. For this reason, research on HER catalysis has focused on elucidating the catalytic pathways of these materials and replicating them through other means. Similarly, OER is best catalyzed by precious metal oxides, such as ruthenium and iridium, and potential replacements are being sought-after.

This search will doubtlessly continue for years to come, as more materials are being (re)discovered, as was the case with molybdenum sulfide (MoS_2) and tungsten oxide (WO_3). Both of which had been synthesized, characterized, and set aside in the late 20th century, and had resurged when it became clear that they possess the exact properties that photo-/ electrocatalysts for water splitting require.

Objectives of the study:

This research focuses on electrochemical synthesis of photo-/electrocatalytic MoS_2, WO_3 and new WO_3+MoS_x films by tuning deposition parameters and electrolytic bath, including tailored scaling of electrodes in order to increase catalytic performance of fabricated materials in the view to elaborate advanced electrodes for HER and OER.

The main research objectives, therefore, are:

1. To synthesize MoS_2, WO_3 and new WO_3+MoS_x films by cathodic deposition and anodic oxidation, correspondingly. Also, to optimize them by adjusting catalyst loading, composition of electrolyte, and modification of active sites.

2. To elucidate the interdependencies between deposition conditions, structural & morphological characteristics, and photo-/electrocatalytic activity of the obtained films.

3. To achieve reliable evaluation of the synthesized materials by steady-state measurements and their complex interrelation to non-stationary methods (EIS, PEIS, IMPS); and to assess the performance vs. applicability of fabricated advanced catalysts.

Scientific novelty:

Heterogenous electrocatalysis is a method used to increase the rate and lower the activation energy of an electrochemical reaction, thus reducing the amount of energy consumed overall. This process is critical to develop efficient electrochemical water splitting cells for H_2 and O_2 production. Many photo- /electrocatalytic materials have been synthesized, but each of them suits a certain purpose. Refractory metal materials in particular exhibit various catalytic properties due to their semiconductor nature. MoS_2 catalyzes HER in acidic media by readily adsorbing H^+ on its active sites. However, the per-site

activity is not thermodynamically ideal, and can be improved through manipulating the formation of Mo – S bonds. Furthermore, more technical issues, like distribution of the material on a large surface area electrode, can overcome mechanical stability issues that electrodeposited MoS_2 is known to have. On the other hand, WO_3 is a viable candidate for OER photocatalysis because its band gap allows for the utilization of a portion of the visible light spectrum. WO_3 photoanodes can be improved by smart ratio between the penetration depth of incident light and film thickness, optimizing the amount of defect sites in their structure, or even further lowering the bandgap through co-deposition with other materials.

Therefore, evaluation of heterogenous catalysts lacks standardization and technical feasibility for future application. Inconsistencies in approximation of surface area, failure to distinguish between the electrochemically and electrocatalytically active surface, as well as uncertainty on what parameters to report on skew the results from study to study. In contrast, a fundamental-based approach (e.g., DFT simulations, solving for kinetic constants) may be beyond the scope of most studies that focus on creating efficient new catalytic materials.

The research core of this study is based on steady-state measurements and their complex interrelation to non-stationary methods (EIS, PEIS, IMPS). Owing to this investigation, evaluation of a HER electrocatalyst's activity was quantified by calculating the H^+ adsorption resistance independently on surface area. Also, adsorption capacitance data of MoS_2 films were used to approximate the number of active sites.

Moreover, the photoconductivity of WO_3 catalysts was evaluated to objectively quantify the material's charge carrier photogeneration. Thus, the gathered results are a step towards bridging the fundamental and the practical aspects of heterogenous photo-/electrocatalysis.

Statements for defense:

1. Scaling-up from flat to foam (3D) electrodes and matching the deposition conditions & electrolyte leads to the improvement of HER catalytic feedback of cathodically deposited MoS_2 films.

2. Inducing transformations in electrochemically synthesized WO_3 photoelectrodes by H^+ intercalation or co-deposition with MoS_2 result in rational activity of elaborated materials for photocatalytic OER applications.

3. Integrating and combining non-stationary methods (EIS, PEIS, IMPS) with steady-state photo-/electrocatalytic response can be used to overcome inconsistencies in experimental results evaluation on MoS_2 cathodes and WO_3 photoanodes for water splitting applications.

1. LITERATURE OVERVIEW

This chapter will consist of two distinct parts: one will focus on describing the cathodic hydrogen evolution reaction (**HER**) and the role of MoS_2 in catalyzing it, and the other will elucidate the application of WO_3 as photoanodes for oxygen evolution catalysis. This overview does not represent the entirety of scientific research on these materials and their uses, but instead focuses on the methods that are more directly comparable to those used in this dissertation.

1.1 Application of MoS₂ for HER catalysis

One of the first studies on MoS_2 as a catalytic material was published in 1977, wherein naturally occurring MoS_2 crystals were tested for their activity as oxygen evolution reaction (**OER**) photoanodes; it was, unfortunately, found that the dominant reaction is oxidation of the sulfur in MoS_2 to SO_4^{2-} [4]. Regardless, this started a wave of interest in the material that lasts to this day, with the number of publications rising sharply [5]. The true breakthrough for MoS_2 as a viable HER catalyst came when, in an attempt to mimic biological enzymes, *B. Hinneman et al.* used MoS_2 edge sites to successfully reproduce a nitrogenase-like active site [6]. This led to the spread of the logic that a good HER catalyst should have a free hydrogen adsorption energy $\Delta G_H^0 \approx 0$, and various methods were developed to obtain catalytic MoS_2 films that satisfy this condition [7].

1.1.1 MoS₂ electrodeposition

An often-used precursor to obtain MoS_2 through various methods is ammonium tetrathiomolybdate (**TTM**) – $(NH_4)_2MoS_4$, and electrochemical deposition is no exception.

Cathodic reduction of TTM occurs through the following reaction [8]:

$$MoS_4^{2-} + 2e^- + 2H_2O \rightarrow MoS_2 + 2SH^- + 2OH^- \qquad (1)$$
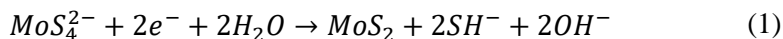
Whereas anodic deposition is also possible by oxidation of MoS_4^{2-}, and yields MoS_3 [9,10] as per **eq. 2** [11].

$$MoS_4^{2-} \rightarrow MoS_3 + \frac{1}{8}S_8 + 2e^- \qquad (2)$$
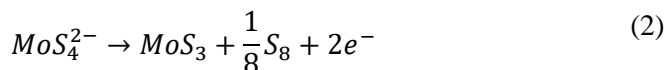
The MoS_3 films deposited in such a way were found to be amorphous, and have a stoichiometry of $MoS_{3.8}$ – experimentally confirming the deposition of

elemental sulfur [12].Furthermore, by comparing the XPS binding energies of Mo of the electrodeposited film with a thermally prepared MoS_3 material, it was found that they were identical, thus confirming the MoS_3 stoichiometry [13].

Cathodic electrodeposition, carried out on a conducting glass (SnO_2) electrode, showed that deposition starts at rather high potentials (-0.9 V vs. SCE), and reaches a maximum efficiency in the region of -1.2 V to -1.4 V, then decreases at more negative potentials due to simultaneous hydrogen evolution [8]. The thickness of these films was found to increase with charge passed through the cell during deposition, and a linear trend was observed until 500 nm at 1 C cm^{-2}, after which the drop in current efficiency would cause a diversion from linearity. The films were X-ray amorphous, and had a featureless surface morphology as observed by SEM. A substantial amount of oxygen was present in the films, and this was attributed to either Mo-O or mixed Mo-O-S species, or water that had been adsorbed in the growing film.

The versatility of the MoS_4^{2-} precursor, and its ability to participate in both cathodic and anodic deposition, led to different methods of electrodeposition. For example *D. Merki et al.* deposited mixed MoS_x films by carrying out cyclic voltammetry (**CV**) scans in varying potential ranges [14]:

♦ Potential was cycled from 0.3 V to -0.8 V *vs. SHE* at a rate of 50 mV s^{-1} in a 2.0 mM $(NH_4)_2[MoS_4]$ solution for 25 scans. Quantification by XPS gave a Mo : S ratio of 1 : 2.9. The material was assigned as **MoS_3-CV**.

♦ An oxidatively deposited film was produced by anodic electrolysis of a TTM solution at 0.55 V *vs. SHE*; the deposition occurs as per **eq. 2**. The obtained film had a S to Mo ratio of 3.2, and its XPS spectra were similar to those of MoS_3-CV. This material was designated as **MoS_3-AE**.

♦ Cathodic deposition was carried out to produce a film with an S to Mo ratio of 1.9. The XPS spectrum of this film was compared and found to be similar to commercial MoS_2 particles. This film was called **MoS_3-CE**.

♦ The last material was deposited by cycling the potential as for MoS_3-CV, but the final scan was set to end at the cathodic potential -0.8 V. XPS spectra revealed that this material was more similar to MoS_2 than MoS_3, with an S to Mo ratio of 2. This material was called **MoS_2-CV**.

The hydrogen evolution catalytic properties of these films were found to vary greatly as did their electrochemical behavior. Upon application of a cathodic potential the MoS_3 materials would undergo „activation ", and the study concluded that regardless of its initial state the best HER catalyst is amorphous MoS_{2-x}. But the materials produced and the differences in their

structure testify to the possibilities of electrochemically forming mixed MoSx materials from a simple solution for various applications.

1.1.2 Characterization of HER catalytic activity

Mechanistically the hydrogen evolution reaction is a simple process, especially in acidic media. Three stages are typically distinguished [15]:

$$Volmer: H^+ + e^- \rightarrow H_{ads} \qquad (3)$$
$$Heyrovsky: H_{ads} + H^+ + e^- \rightarrow H_2 \uparrow \qquad (4)$$
$$Tafel: H_{ads} + H_{ads} \rightarrow H_2 \uparrow \qquad (5)$$
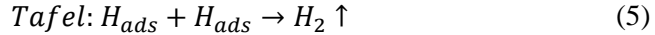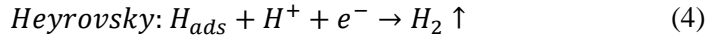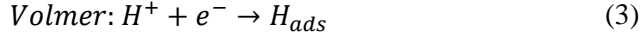
The first stage is the *Volmer* hydrogen adsorption step in which an electron is transferred from the electrode and used to reduce a proton on an empty active site, yielding an adsorbed hydrogen atom. Although **eq. 3** is simplified, the source of protons in acidic electrolytes is the hydronium cation (H_3O^+).

Although the Volmer step is unavoidable, typically only one of the following two pathways dominates. The *Heyrovsky* electrochemical reaction (**eq. 4**) occurs through a transfer of a second electron to the adsorbed hydrogen atom, followed by a coupling with another proton from the solution, to evolve hydrogen gas. Alternatively, if HER proceeds through the *Tafel* chemical desorption step (**eq. 5**) then two adsorbed hydrogen atoms recombine to produce H_2.

All three steps can occur simultaneously, but one pathway will dominate kinetically – Volmer-Heyrovsky or Volmer-Tafel. The rate determining step can be distinguished from Tafel slope analysis[16]. For a simple, symmetric, one-electron transfer reaction, the Tafel equation can be simplified to:

$$\eta = b \cdot \log \frac{j}{j_0} \qquad (6)$$

where η is the applied overpotential, b is the Tafel slope, j is the measured current density and j_0 is the exchange current density. Here the exchange current density is correlated to the rate of electron transfer at zero overpotential.

Theoretical considerations of the Butler-Volmer equation under limiting cases [17] at 25°C revealed that:

(1) If HER occurs through a Volmer-Tafel mechanism, and the rate limiting step is the Tafel recombination reaction, then a Tafel slope of 29 mV dec^{-1} will be observed.

(2) If the Heyrovsky electrochemical recombination step is rate limiting, then a slope of 38 mV dec^{-1} should be seen. This is the mechanism through which HER occurs on a MoS_2 catalyst, as shown in **Fig. 1**.

(3) If the Volmer hydrogen adsorption step is slow and rate limiting, then regardless of whether recombination occurs through the Heyrovsky or Tafel steps, the Tafel slope will equal 116 mV dec^{-1}.

So, the two parameters that are most often extracted from electrocatalytic characterization experiments in order to describe the efficiency of a catalyst are Tafel slope and exchange current density.
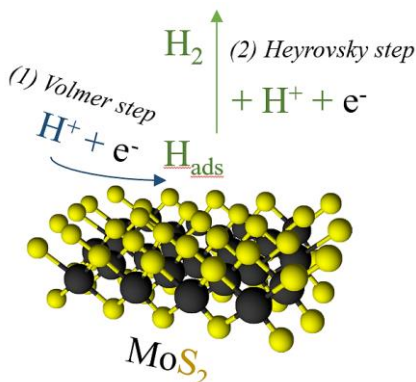
Fig. 1. *Schematic representation of the HER pathway on a MoS$_2$ electrocatalyst.*

It is typical in HER electrocatalysis that the Volmer hydrogen adsorption step is rate-limiting, so research is focused on finding or modifying materials to facilitate easy hydrogen adsorption/desorption. As mentioned earlier, a good HER catalyst is one that has a free hydrogen adsorption energy ΔG_H^0 near to zero. This characteristic has been proposed to be a good indication of intrinsic HER activity. So-called „volcano plots" that relate the experimentally measured catalytic activity of a material with its density functional theory calculated Gibbs free energy of adsorbed hydrogen are often used to illustrate the different catalytic activities of materials [18]. In these plots precious metals like Pt, Pd, and Ir have a ΔG_H^0 close to 0 and, consequently, the highest catalytic activity, while other metals bind hydrogen much more strongly – even Ni, which is a good HER catalyst in acidic media, has a ΔG_H^0 of ~ -0.28 eV [19].

The volcano plot and free hydrogen adsorption energy logic has since been extended to all catalytic materials: the ideal HER catalyst should be at the peak of the volcano plot. Materials to the left of it ($\Delta G_H^0 < 0$) bind hydrogen too strongly and hinder desorption. Materials, for which $\Delta G_H^0 > 0$ bind hydrogen too weakly, fail to stabilize intermediates, and prevent the reaction from completing [20]. In other words, HER catalysts should obey the Sabatier principle – the chemical interaction between the catalyst and the substrate should be „just right "; that is to say neither too strong, nor too weak.

The binding of hydrogen occurs on active sites – atomic-scale points within the material's crystal lattice that are exposed to the electrolyte and are energetically different to the bulk structure. A sufficient understanding of the various active sites is important when working with any heterogenous catalysis, and this was also the case with MoS_2. Early research had shown that bulk MoS_2 (the basal plane) is a poor catalyst [21]. Later, it was discovered that on nanoparticulate MoS_2 edges acted as the active sites for HER catalysis [22], and that with a $\Delta G_H^0 \approx 0.08$ eV an edge-site based MoS_2 catalyst would be near the center of the volcano plot. However, when comparing edge-site-rich MoS_2 flakes with a monolayer film, it was found that the film exhibited much better HER activity, which led to proof of other important active sites – sulfur vacancies. Currently, the active sites of a MoS_2 material for HER catalysis are thought to be [23]:

♦ Sulfur vacancies ($\Delta G_H^0 \approx$ -0.095 eV);
♦ Mo edge sites ($\Delta G_H^0 \approx 0.115$ eV);
♦ Grain boundaries ($\Delta G_H^0 \approx 0.181$ eV to 0.566 eV);
♦ The basal plane is effectively inert ($\Delta G_H^0 \approx 1.218$ eV);

According to these values, sulfur vacancies should be the most efficient active sites for HER catalysis, and defect engineering has been the subject of much research [24]. It is now thought that an optimal amount of vacancies should result in the best HER activity [25]. Electrodeposition, as described earlier, typically yields amorphous, sulfur-deficient films (MoS_{2-x}) that are particularly active towards HER due to their rough, nanostructured surface morphology and consequently higher density of defect (active) sites [14,26,27].

The methods described here, along with some other more specific characterizations, are typically sufficient to test the viability of a HER catalyst. Alongside the Tafel analysis, electrochemical impedance spectroscopy can be used to delve into charge transfer kinetics and interfacial capacitances occurring from adsorbed hydrogen coverage. EIS can be used to determine rate constants of the three HER steps [28], charge transfer kinetics [29], and the capacitance of the double electric layer, which is proportional to the electrochemically active surface area [30,31]. A broad overview is shown in **Fig. 2**.
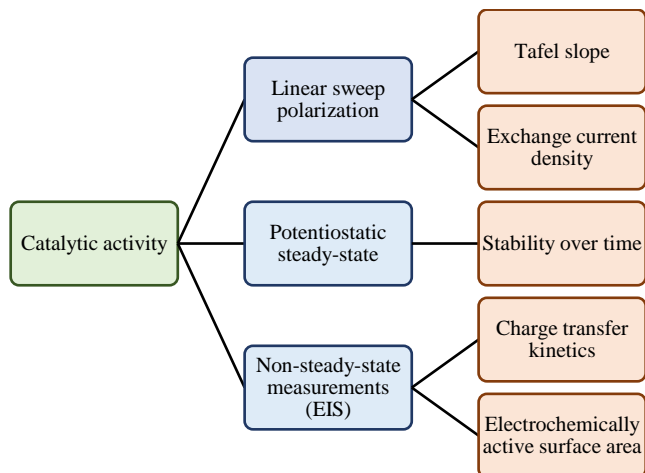
Fig. 2. *Electrochemical measurements and parameters extracted from them that can be used to comprehensively characterize an electrocatalytic material.*

1.1.3 Methods to improve the activity of MoS₂ catalysts

By its nature, MoS_2 is an excellent HER catalyst in acidic media. Its active sites have a small free hydrogen adsorption energy and thus catalyze the Volmer step of HER. However, various forms of MoS_2 do have their drawbacks. For instance, their electrochemical stability is an often-omitted issue. Some authors report that thicker films (> 1 μm) tended to peel off the substrate, and that after removing the electrodeposited film from its aqueous solution and drying it a network of cracks had appeared in films thicker than 0.5 μm [8,32]. This is fundamentally related to the structure of MoS_2, which consists of S – Mo – S layers (where S and Mo are bound by covalent bonds), and only weak Van der Waals forces connect the layers to each other, and to the substrate. Furthermore, it had been shown that after aging a CVD-grown MoS_2 monolayer for 1 year the S to Mo ratio decreased from 2 to 1.05 due to oxidation of sulfide sites [33]. DFT calculations showed that on a sulfur-deficient MoS_2 surface the kinetic oxygen dissociative adsorption barrier is relatively low, and that the oxidation/passivation of sulfur vacancy active sites is thermodynamically favorable [34]. The other active sites – edges and grain boundaries – were also found to be susceptible to oxidation, and it was theorized that the misfit between the MoS_2 and MoO_3 lattices may be the cause of mechanical stress that results in cracks appearing throughout the film [35].

Therefore, various means have been tried and developed to address these issues, and ultimately increase the activity and applicability of MoS_2-based HER catalysts.

Intercalation with Li^+, for example, is a novel method that was shown to greatly enhance the HER catalytic properties and stability of MoS_2 [36]. Of all the variations considered, it was found that the stoichiometry of $Li_{0.29}MoS_2$ exhibited the best catalytic activity and long-term stability. In addition, $Li_{0.25}MoS_2$ and $Li_{0.31}MoS_2$ had ΔG_H^0 of 0.11 eV and 0.12 eV respectively, attesting to their excellent catalytic activity. Doping with transition metals has also been widely reported on: with Fe, Co, and Mo [37], Ti [38], V, Nb, Cr, Mn and more [39]. Incorporation of 0.5 at % of Fe into MoS_2 was shown to enhance its semiconducting behavior by increasing free carrier concentration [40]. Fewer studies exist on the effect of doping on the HER catalytic properties. Doping with Pt (Pt-MoS_2) resulted in significantly enhanced catalytic activity over a plain MoS_2 material; as Pt is expensive, Co and Ni have also been proposed as potential dopants that demonstrably increase the HER activity of MoS_2 nanosheets [41]. In fact, doping with Ni has been shown to enhance the catalytic activity of MoS_2 not just in acidic, but also in alkaline media [42], which is a prospective new frontier of hydrogen evolution catalysts that have, until now, mostly focused on operation in acidic media. Finally, anion engineering (incorporation of anionic N) was also reported to have a positive effect on MoS_2 activity [43].

Among the simplest and most popular ways to enhance the electrocatalytic activity of MoS_2 materials is nanostructurization. Due to their molecular structure, MoS_2 films tend to be flat and layered. This may be useful for optoelectronics or where this material could otherwise be used for its semiconducting properties, but in electrochemical catalysis a large surface area in contact with the electrolyte is desirable. Thus, nanostructuring of the surface in order to obtain a micro- or even nanoroughness is an excellent way to modify MoS_2-based HER catalysts.

For example, and edge-rich hierarchically nanostructured MoS_2 catalyst that had been developed via solvothermal synthesis was show to have a low HER onset overpotential and a Tafel slope of 41 mV dec^{-1} [44]. Interesting nanostructures whose structure depended on deposition time were also observed for electrodeposited films, although these had been applied for dye-sensitized solar cells and not HER catalysis [45]. A large surface area can be achieved not just by nanostructuring MoS_2 itself, but by dispersing MoS_2 on already nanostructured materials. *Teng et al.* had manufactured a photoanode for oxygen evolution by decorating n-type TiO_2 vertical nanotube arrays with n-type MoS_2 by a photo-assisted deposition method, resulting in a device with increased photocatalytic activity [46]. MoS_2-covered ZnO nanotube arrays made by a solvothermal synthesis method were shown to act as both HER

catalysts and OER photoanodes with a HER onset overpotential of just under 0.2 V and a Tafel slope of 45 mV dec^{-1} [47,48].

From the studies briefly described in this chapter it should become apparent that research on the ideal application of MoS$_2$ is still intense. Because HER catalysts are varied, and their characterization is not yet standardized in scientific literature, the best overview would be provided by a table (**Table 1**) comparing the reported parameters of differently prepared catalysts.

Table 1. *Comparison of HER current density at overpotential η$_j$, and Tafel slope of various MoS$_2$-based catalysts as obtained in 0.5 M H$_2$SO$_4$ electrolytes.*

Catalyst	j mA cm^{-2}	η$_j$ mV	Tafel slope mV dec^{-1}	Synthesis method	Reference
Ni-MoS$_2$		310	47	Hydrothermal	[49]
VG/CC/MoS$_2$	10	78	53		[50]
CC/CoMoS$_x$		100	70	Electrodeposition	[51]
GC/MoS$_2$ film		202	48		[52]
CC/MoS$_2$	86	250	50	Solvothermal	[53]
Ti/MoS$_2$	30	250	-	Hydrothermal	[54]
CC/Mo-W-S		198	54	Electrodeposition	[55]
MoO$_3$-MoS$_2$		254	-	CVD/sulfidation	[56]
Amorphous MoS$_3$		242	-	Electrodeposition	[14]
MoS$_2$/RGO	10	160	41	Solvothermal	[57]
Hollow MoS$_2$ spheres		214	74		[58]
MoS$_2$ nanodots		248	61	Liquid exfoliation	[59]
Exfoliated MoS$_2$		207	-		[60]

Broadly speaking, good catalytic activity is evidenced by a lower Tafel slope and a high HER current density at a low overpotential. Although current density calculations are questionable for electrodes with intricate 3D structures, it is becoming customary to report the overpotential at which a current density of – 10 mA cm^{-2} is reached in near-steady-state LSV measurements.

1.2 Use of WO$_3$ for OER photocatalysis

Oxides, and especially transition metal oxide materials, are thought to be promising photoanodes due to their abundance, thermodynamic stability, and favorable semiconductor properties. With band gaps within the range of 2.3 to 3.7 eV [61], they may still be photoexcited by a portion of the visible light spectrum. TiO$_2$ and WO$_3$ are particularly stable in an acidic environment, and for this reason much research has been focused on the application of these materials as photoanodes for OER. WO$_3$ has received much attention as it has

a smaller band gap than TiO_2 (~ 3 eV), typically reported within the range of 2.5 – 2.8 eV, although up to 3.38 eV for certain films [62,63]. However, the band gap and other electrical parameters like conductivity of WO_3 films can vary greatly with their microstructure, grain size, and crystallinity [63,64]. Therefore, the catalytic properties of WO_3 films will depend on their synthesis technique.

1.2.1 Forming WO₃ films by anodization

Anodization is a convenient and fast way to electrochemically form a WO_3 film: upon application of a sufficient anodic potential in corrosive media, the metal dissolves into a WO_2^{2+} complex, and through an unstable intermediate W_2O_5 becomes WO_3 as per eqs. 7 – 9 [65].

$$W + 2H_2O \rightarrow WO_2^{2+} + 4H^+ \tag{7}$$

$$2WO_2^{2+} + 2H_2O \rightarrow W_2O_5 + 2H^+ \tag{8}$$

$$W_2O_5 + H_2O \rightarrow 2WO_3 + 2H^+ \tag{9}$$
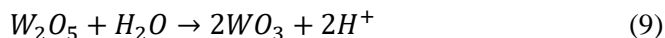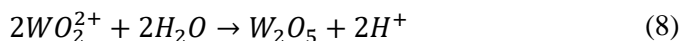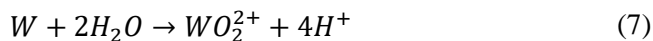
Although these reactions are not strictly reversible, and WO_3 is thermodynamically stable in acidic media according to its Pourbaix diagram, a partial chemical dissolution step can occur (**eq. 10**) [66]:

$$WO_3 + 2H^+ \rightarrow WO_2^{2+} + H_2O \tag{10}$$

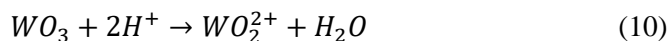Furthermore, it has become typical to use certain additives during anodization in order to promote the kinetics of the chemical dissolution step, thus forming intricate nanostructures. These additives are those that have strong corrosive properties; F^- is the most commonly used one. As discovered on TiO_2, fluorine anions participate in the formation of metal oxide films by efficiently complexing the metal from its oxide (**eq. 11**) [67], or by permeating through the oxide and facilitating the dissolution of the base metal itself (**eq. 12**) [68].

$$WO_3 + 6H^+ + nF^- \rightarrow [WF_n]^{(n-6)} + 3H_2O \tag{11}$$

$$W + nF^- \rightarrow [WF_n]^{(n-6)} + 6e^- \tag{12}$$
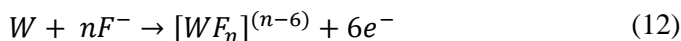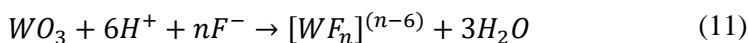
Eqs. 10 and **11** describe the same step – dissolution of the formed WO_3 film, or so-called etching. However, owing to the thermodynamic stability of WO_3 in acidic media, acid etching is a slow process [69]. In contrast, F^- ions etch the film much faster, and are often added to anodization electrolytes in order to etch a nanostructured surface into the film. The mechanism of oxide film growth – the point defect model – had been elucidated by *Macdonald et al.*, and it describes a balance between lattice conservative processes (those

that do not result in the movement of the oxide layer's boundaries relative to a fixed reference frame), and nonconservative [70]. This mechanism is an interesting insight into the formation of oxide films, but the most important observation for the purpose of this overview is that film thickness is expected to increase linearly with the strength of the applied electric field (i.e. potential).

To summarize, the formation of a porous WO_3 film occurs through an equilibrium between electrochemical film formation and chemical dissolution. As the oxide dissolves, pores that had nucleated on its surface propagate toward the bulk of the material and merge into porous macrostructures [71,72]. The entire process can be schematically represented through four stages of film formation, pore nucleation, and pore propagation, as shown in **Fig. 3**:

(1) Immediately after applying an anodic potential on the W substrate a WO_3 film starts to grow. During the first stages (seconds to a minute) of anodization a relatively compact oxide film forms.

(2) Through chemical etching fine pathways/cracks/pits form on the oxide's surface. This can also be considered as nucleation of future pores.

(3) The individual pathways that had nucleated earlier begin propagating deeper into the film. It is worth noting that dissolution of the substrate still occurs.

(4) A steady-state is reached, where a fairly stable porous structure is now etched into the oxide film.
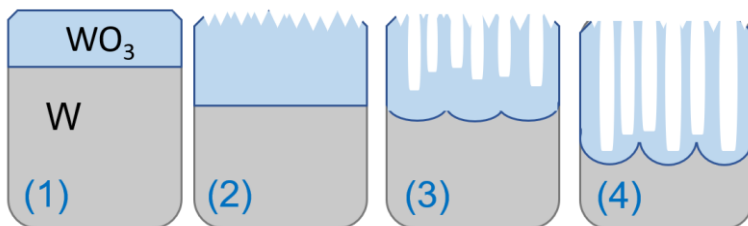
Fig. 3. *Schematic representation of the stages of porous oxide growth during anodization.*

The geometrical parameters of these pores will depend on anodization conditions (electrolyte, potentiostatic, galvanostatic, or even pulsed regime, additives, etc.).

Anodization can be performed potentiostatically or galvanostatically. Under potentiostatic conditions, as mentioned before, the film's thickness is easier to predict as it will depend linearly on the applied potential [73]. The WO_3 film's morphology will also be different based on the potential applied. For example, it was found that anodization at 20 V for 15 minutes (in a 1 M

Na$_2$SO$_4$ containing 0.7g of NH$_4$F) yielded just a compact oxide layer, and increasing the potential to 40 V and 50 V facilitated the formation of a nanoporous morphology [74]. It was also found that in a 0.3 M oxalic acid electrolyte WO$_3$ films of varying nanoporosity could be obtained at even 110 V, although the most ordered pore structure would be obtained when anodizing at 60 V to 80 V, and that porosity would also depend on anodization time [75,76].

Galvanostatic anodization is less often considered, but it is a particularly interesting method to obtain highly porous films because the strength of the applied electric field is not being held constant, and thus etching of WO$_3$ occurs more readily. It is then found that the voltage typically peaks, which corresponds to the maximum thickness of the oxide film, and the following voltage drop indicates pore formation by field-induced oxide dissolution [77].

Moreover, the morphological, structural, and even photocatalytic properties of anodized WO$_3$ films can be improved with the use of certain additives/complexing agents during anodization. Fluoride had already been discussed – it is known to increase the rate of dissolution of W and WO$_3$, which typically has an effect on the morphology of the pores [68,78]. A small concentration of H$_2$O$_2$ (0.05 M) has also been shown to result in a 244% increase in photocurrent over the respective control film [79]; like F$^-$, the peroxo group (O$_2^{2-}$) performs as a ligand as it reacts with tungstates to form peroxotungstates, thus altering WO$_3$ dissolution kinetics and forming different surface morphologies.

Finally, although this is not yet widespread, sodium hypophosphite (NaH$_2$PO$_2$) seems to have a positive effect on the formation of porous films with vigorous oxygen bubbling, as it prevents excess oxygen from accumulating on the pore walls of the anodized film[80,81]. This, in turn, facilitates the formation of a more even, homogenous, nanoporous structure.

1.2.2 Characterization of photocatalytic activity

Heterogenous photoelectrochemical catalysis is, in essence, similar to heterogenous electrochemical catalysis in that half of the process occurs at the catalyst/electrolyte interface. On WO$_3$ photoanodes during OER certain species adsorb on the material's active sites, forming metastable intermediates, which further react with charge carriers from the catalyst and evolve O$_2$. However, the other half of the process is charge carrier photogeneration occurring after illumination by light of sufficient energy to photoexcite its electrons. It is therefore important to consider at least the basics of photocurrent generation.

WO$_3$ is an *n*-type semiconductor whose majority charge carriers are electrons (*e$^-$*), and minor charge carriers are holes (*h$^+$*). Once illuminated, the photoanode will generate photoexcited e$^-$ and *h$^+$* pairs. Electrons will move to the back contact, and holes will transport towards the semiconductor/electrolyte interface. The movement of *h$^+$* should be thought of as a spatial flux of holes per cm^2 per second. This flux will be proportional to the incident photon flux multiplied by a certain conversion coefficient. The photocurrent for such a system is described by the simplified Gärtner equation [82]:

$$j_{ph} = -q\varphi A \left[1 - \frac{e^{-\alpha W}}{1 + \alpha L_p} \right] = I_0 A K \qquad (13)$$

where *q* is the elementary charge, φ is the incident photon flux, and *A* is the illuminated area.

If the three were multiplied, they would yield the amount of charge transferred by the photon flux (i.e., current density). Assuming perfect conversion, the photocurrent would equal the current of the photon flux. The parameter in the brackets is effectively what determines how many photons are converted into charge carriers, and is typically referred to as Incident photon conversion efficiency (**ICPE**), or External quantum efficiency (**EQE**). Its three parameters determine the conversion efficiency: α is the absorption coefficient, *W* is the width of the space-charge layer (also known as the depletion zone), and L_p is the hole diffusion length.

From the Gärtner equation it is apparent that electrochemical photocurrent can be controlled in two ways: by varying the incident photon flux and width of the space charge layer. The incident photon flux can be varied by increasing the intensity of the light source (*I$_0$*). As predicted by **eq. 13**, which has the form of *y = kx*, a linear correlation of *j$_{ph}$ – I$_0$* should exist provided *k* remains constant.

In turn, increasing the width of the space charge layer is also expected to result in higher photocurrents. Although the incident flux remains constant, more charge carriers that are susceptible to photogeneration become available as the layer grows. In the Gärtner equation this is represented by *W* – a base e exponential function. W itself is a function of the bias potential by the following law [82]:

$$W = W_0 \sqrt{V} \qquad (14)$$

where *W$_0$* is the "width constant" of the depletion layer, and V is the voltage across it.

Therefore, variations in applied potential will result in variations of the space-charge layer's width, and $j_{ph} - E$ should manifest as some form of power law.

A more practical way to calculate the incident photon conversion efficiencies is by simply dividing the flux of photogenerated h^+ by the incident photon flux. A convenient expression of the formula by using the steady state photocurrent and light intensity is:

$$IPCE(\%) = \frac{j_{ss}(mA\ cm^{-2})\cdot 1240\ (V\ nm)}{I_0(mW\ cm^{-2})\cdot \lambda\ (nm)}\cdot 100 \tag{15}$$

As had been mentioned before, the total photocatalytic effect of a photoanode is the sum of charge carrier photogeneration, and transfer of photogenerated charge carriers into the electrolyte to carry out a Faradaic reaction (water splitting in this case). Both photo- and electrochemical effects must be considered. **Fig. 4** shows the areas of interest and points that must be addressed when characterizing a photocatalyst.
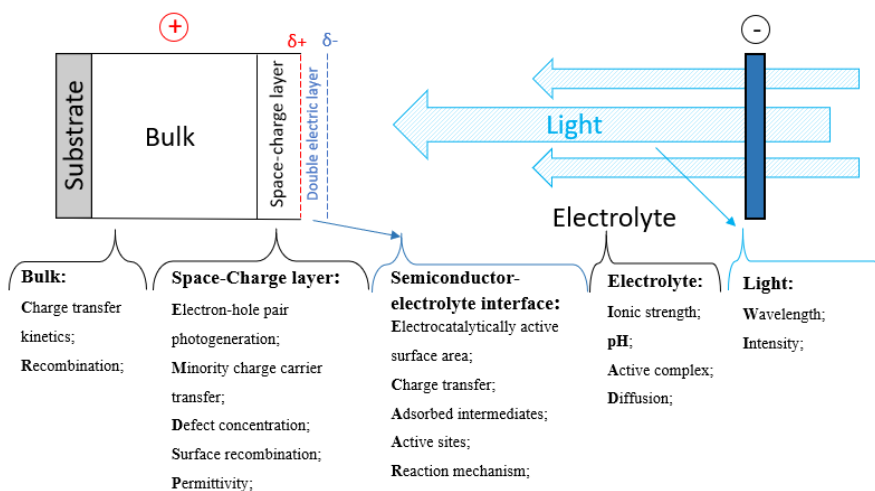
Fig. 4. A schematical representation of the operating areas of a photoelectrochemical cell.

The material's bulk is not usually taken into account when characterizing photocatalytic reactions, but depending on certain parameters (such as conductivity or defect amount) it may have a large impact on the photocatalyst's performance. For example, for electrodeposited WO_3 it had been found that while to an extent thicker films generated stronger photocurrents, a thick film but with a defective and stressed nanostructure would yield lower catalytic performance, owing to an increased number of defect/recombination sites [83]. Further growth of film thickness (> 600 nm)

had led to a decrease in photocurrent conversion efficiency, and it was proposed that for thinner films the surface band gap components dominates, whereas for thicker films the bulk band gap component determines the photocurrent [84]. Increasing film thickness can result in excessive electron diffusion distance, increased film resistivity, a longer charge carrier equilibration time, and an increased amount of electron-hole recombination sites [85–87].

The space charge layer (sometimes referred to as depletion zone in semiconductor physics) is where the photogeneration, separation, and transfer of e^- - h^+ pairs is considered to occur, though in reality there is no strict border between the space charge layer and the bulk. However, a detectable capacitive layer does exist, and it forms in the following way: after photogeneration, e^- - h^+ pairs are separated by an applied electric field, and electrons move toward the positive contact, while holes move toward the negative contact (i.e. toward the semiconductor/electrolyte interface) [88]. The fluxes of electrons and holes reach saturation at a certain spatial point – holes most likely at the interface, and electrons toward the bulk of the material. Thus, a capacitance is formed. For photocatalytic reactions another important consideration is the ratio between photogenerated holes and holes that had been transferred into the electrolyte, which will be discussed later.

The semiconductor-electrolyte interface is where the photoelectrochemical reaction would take place. The considerations to keep in mind here would be the same as for HER – the electrochemically active surface area, kinetics of charge (h^+) transfer across the interface, and mechanistic implications (active sites, adsorbed intermediates, etc.). The precise mechanism of photocatalytic OER is difficult to elucidate, but the process can be summarized as:

$$2OH^- + h^+ \rightarrow O_2 \uparrow + 2H^+ \tag{16}$$
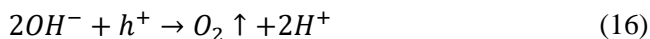
Lastly, both the electrolyte and illumination parameters (wavelength, intensity) should be selected carefully. As was mentioned earlier, WO_3 is most stable in acidic environments and has a band gap of 2.5 eV to 2.8 eV, so acidic media and a 365 nm near-UV light source are often used.

Photo-electrochemical impedance spectroscopy (PEIS)

Electrochemical experiments that apply a non-stationary perturbation on a system can be utilized to freeze the occurrence of certain physical or electrochemical processes and isolate the signal of others. At its simplest, EIS is based on the perturbation of a system with a potential that is being modulated at a specified amplitude for varying frequencies. At high

frequencies, the slower processes cannot occur, and the measured signal belongs entirely to the charge and discharge of the electrical double layer. Conversely, at lower frequencies the signal belongs to slower, often Faradaic processes.

In PEIS the sample is being illuminated by a constant photon flux while the potential is modulated. As per **eqs. 13 and 14**, this will result in a modulation of the width of the space charge layer, which causes variations in the amount of minority charge carriers. As the layer expands, more charge carriers can be photoexcited, as it contracts – the opposite. Such modulation of the amount of charge carriers gives the PEIS signal. Both charge carrier flux and density are worth considering, as the signal is obtained from the entire space charge layer.

For photoanodes, the simplest expression of impedance is a combination of the series resistance (R_s), the double layer capacitance coupled with charge transfer resistance (C_{dl} and R_{ct}), and the space-charge capacitance coupled with the space charge resistance (C_{sc} and R_{sc}). As will be shown later in this study, R_{sc} and C_{sc} can be correlated to the observed steady state photocurrent.

Intensity modulated photocurrent spectroscopy (IMPS)

Like EIS, IMPS is also a non-stationary electrochemical analysis method, except the parameter being modulated in this case is the illumination intensity I_0. In photoactive materials, this causes a photocurrent response with the same frequency but at a different magnitude and phase. The integrated j_{ph} response and the phase shift are therefore the variables that determine the IMPS spectra. In IMPS the real and imaginary axes may be considered in terms of the Q-plane plot (if from the perspective of photon conversion efficiencies), or H-plane plot (from the perspective of the mathematical transfer function). Because in this study the signal is presented as obtained from the potentiostat, the complex plots will be designated as H-plots, with H' and H'' real and imaginary axes.

The interpretation of modulated photocurrent spectra is not necessarily complicated, but currently only scattered information exists on the application of IMPS on various complex electrochemical systems. Moreover, in recent years reasonable doubts have been cast on many of the traditionally accepted IMPS interpretation methods. For example, it was often assumed that the intermediate-frequency intercept of the real axis equals the photogenerated hole current, but it has been demonstrated that this intercept is no more than the mathematical consequence of a ratio of Helmholtz and space-charge capacitances [89]. Therefore, in this study a combination of empirical and theoretical considerations is employed in order to characterize photoanodes

by means of IMPS. The classic theory has been elucidated by *Ponomarev* and *Peter* in their seminal work [90]. Textbook applications have been excellently explained in multiple publications [91–96] and will not be discussed here. However, several important nuances must be discussed in order to interpret experimental spectra. Firstly, an IMPS spectrum is described by two time constants:

$$\tau_s = R_s \cdot C_{tot} \tag{17}$$

$$\tau_{tr} = \frac{1}{k_{tr} + k_{rec}} \tag{18}$$

where τ_s is the time constant that belongs to the electrochemical cell, and it is expressed by multiplying the series resistance and the total capacitance. In turn, the total capacitance is the sum of the Helmholtz and space charge capacitances:

$$C_{tot} = \frac{C_{SC} \cdot C_H}{C_{SC} + C_H} \tag{19}$$

where τ_{tr} is the transfer time constant (not to be confused with the charge transfer time constant from PEIS), and it is a product of the inverse sum of the rate of minority charge carrier transfer to the electrolyte k_{tr} and the rate of electron-hole recombination $k_{rec.}$

Much like EIS, the IMPS response can be distinguished into two domains: the high frequency and the low frequency responses. Typically, the high frequency response yields a semicircle in the fourth quadrant of a Nyquist plot. The lowest point of this semicircle has a specific angular frequency that relates directly to τ_s in the following manner:

$$\omega_{min} = (R_s \cdot C_{tot})^{-1} \tag{20}$$

That is to say, the high frequency response is determined by the cell time constant.

In a textbook scenario, the low frequency response would be a small semicircle at positive H'' values in the first quadrant. The highest point of this semicircle would be a characteristic angular frequency that is related to the transfer and recombination constants:

$$\omega_{max} = (\tau_{tr})^{-1} = k_{tr} + k_{rec} \tag{21}$$

And finally, at low frequencies when the perturbation and response are in phase, and $\omega \rightarrow 0$, the spectrum should end in an intercept with the H' axis, and this value corresponds to the transfer efficiency:

$$Q_{tr} = \frac{k_{tr}}{k_{tr} + k_{rec}} \tag{22}$$

Here it must be again pointed out that the IMPS interpretation will not be universal for all systems. In a case where $k_{tr} \gg k_{rec}$ it is apparent from **eqs. 21 and 21** that the values of ω_{max} and Q_{tr} will change significantly. The transfer efficiency will equal 1, and ω_{max} will directly equal k_{tr}. Additionally, if the condition that no surface recombination occurs is met, the IMPS spectrum will have a different profile – there will be no recombination response in the first quadrant of the complex coordinate plane. ω_{max} then gains a different meaning (**eq. 23**).

$$\omega_{LF} = (\tau_{tr})^{-1} = k_{tr} \tag{23}$$

That is to say, it becomes the characteristic angular frequency of the low frequency response/semicircle. The expression of ω_{min} does not change, as it is independent of transfer and recombination rate constants, but for the sake of consistency, it may be called the characteristic angular frequency of the high frequency response – ω_{HF}.

If this interpretation holds true, then the IMPS spectra with different transfer rate constants should have a near-identical high frequency response, and a different low frequency response.

1.2.3 Modifications to improve photocatalytic activity

As may have been inferred from the previous chapter, due to the immense number of variables in photoelectrochemical experiments reports on the activity of WO_3 photoanodes present very scattered data. One normalized characteristic – incident photon conversion efficiency (IPCE) – may be more universally compared, and yet even then different light sources or their configurations are used. Regardless, WO_3 photoanodes exhibit some known issues that are easily identifiable, though not that easily quantifiable.

For instance WO_3 films have been found to suffer from loss of photoactivity (up to 74% of initial activity in 30 minutes of operation), and there seems to be a relation to the way in which they had been deposited [97–99]. This may have been related to some photo corrosion, but more likely the loss in activity occurs due to non-reversible charge carrier recombination with defects/traps (oxygen vacancies) in the WO_3 lattice. A common way to repair these defects is thermal annealing in an oxygen atmosphere, which typically results in much larger photocurrents and stability [100–102].

Apart from annealing and the modifications during film formation/anodization that had already been discussed, several methodologies exist to enhance the photocatalytic properties of WO_3 materials and devices. WO_3 is a classic electrochromic material; that is to say it is able to reversibly

intercalate small ions (H^+, Li^+) into its structure upon application of a certain electrical potential [103,104]:

$$WO_3 + xe^- + xH^+ \leftrightarrows H_xWO_3 \qquad (24)$$
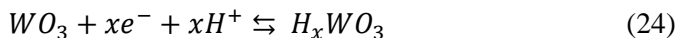
The immediately apparent result is a change in color – optical coloration. After intercalation (at a cathodic potential) the otherwise colorless films turn blue. Electrochromism by itself is a huge discipline of electrochemistry. However, it is being discovered that this process can also be taken advantage of in catalysis.

It is thought that the reduced films gain a blue appearance due to the formation of a tungsten bronze material – H_xWO_3 [105,106]. This process is reversible, and at anodic potentials the film will become bleached again after the protons de-intercalate. In fact, it had been reported that a larger number of color-bleach cycles can even change the microstructure and porosity of the WO_3 as the penetration of water into the film causes expansion of the lattice [107]. One study on the effect of protonation on the photocatalytic water splitting properties of a CVD-formed WO_3 film found that the result was negative [108] – protonated films performed marginally worse photoelectrochemically than comparable non-reduced films. However, a highly beneficial result of cathodic reduction was observed on differently-prepared WO_3 nanoflakes; a five-fold increase in photocurrent was observed after reduction, and this effect was ascribed to a similar increase in donor density as measured by the Mott-Schottky method [109].

It has been hypothesized that due to the interaction of conduction and valence bands of semiconducting WO_3 and metallic H_xWO_3 the photogenerated electron-hole recombination is suppressed and the life-time of photogenerated holes consequently increases – all of which results in higher charge separation efficiency [110]. Photoelectrochemical analysis suggests that electrochemical doping of WO_3 with H^+ passivates surface trap states, thus reducing recombination and improving the charge separation efficiency [111]. Moreover, modification by substitutional cation doping, thermal oxygen vacancy engineering, and chemical reduction have been shown to have similarly beneficial effects on the properties of modified WO_3 photoanodes [112–114].

Finally, it is also common to combine WO_3 with other materials in order to create intricate nanostructures and composites with combined properties. As an example, WO_3 nanoparticles had been synthesized on graphene sheets sonochemically, and the obtained composite was found to more effectively evolve O_2 than a comparable WO_3 film [115]. A nitrogen-doped WO_3/TiO_2 catalyst, prepared through a sol-gel route, was demonstrated to have increased

performance in photodegradation of diclofenac, and this was due to WO_3 narrowing the band gap of the composite material, as well as reducing the recombination of charge carriers [116]. WO_3 has been used in combination with polypyrrole as a catalyst in microbial fuel cells [117], in combination with carbide for electrochemical capacitors [118], composited with carbon nanotubes for low-temperature ammonia sensing [119], and many more uses.

1.3 Composite films based on WO_3 and MoS_2

Both MoS_2 and WO_3 are excellent catalytic materials by themselves. However, their combinable properties gave rise to much research on WO_3-MoS_2 composites, as presented in **Table 2**.

Table 2. Reported WO_3 and MoS_2 composites and their applications.

Material	Application	Publication year	Reference
Sb-Mo(O,S)$_2$/WO$_3$	Degradation of methylene blue	2020	[120]
MoS$_2$/WO$_3$ hybrid	H$_2$S sensing	2020	[121]
MoS$_2$/WO$_3$-based ECD	Electrochromic devices	2020	[122]
WO$_3$/MoS$_2$-rGO	Photodegradation of Rhodamine B.	2020	[123]
MoS$_2$-CdS/WO$_3$-MnO$_2$ composite	Photocatalytic water splitting	2020	[124]
g-C$_3$N$_4$/WO$_3$/MoS$_2$ ternary composite	Photocatalytic organic pollutant removal from water	2020	[125]
WO$_3$/WS$_2$-MoS$_2$	Photocatalytic water splitting	2020	[126]
WO$_3$@MoS$_2$/Ag hollow tubes	Degradation of bisphenol	2019	[127]
MoS$_2$-WO$_3$ nanoflake array heterojunction	Supercapacitance	2018	[128]

It is evident, that even now research into the various possible applications of such composite materials is active, and that combinations WO_3 and MoS_2 do often exhibit enhanced, possibly even synergistic properties. It may therefore be interesting not just to examine WO_3 and MoS_2 for their respective photocatalytic OER and electrocatalytic HER properties, but also to look into ways to combine both materials.

1.4 Summary

To conclude, photo- and electrocatalytic materials evidently play a very important role in future technological development. Whether used for water splitting to produce hydrogen and oxygen, wastewater treatment by decomposing pollutants, as sensors, or many other applications – they fundamentally decrease a reaction's thermodynamic barrier and often accelerate its kinetics. When total reproducibility and stability are achieved, industrial applications are bound to begin.

The literature considered in this overview represents only a small part of research into heterogenous catalysis, focused on the application of MoS_2 and WO_3 for water splitting. Electrochemical methods to form catalytically active MoS_2 and WO_3 films on conducting substrates had been discussed, as well as common ways to improve these materials. Perhaps most importantly – a brief but comprehensive overview of experimental techniques used to fully characterize the electrocatalytic activity of heterogenous photo- and electrocatalysts has been offered. The application of these techniques and their interpretation will be discussed in more detail in the experimental and results sections.

It may be questioned why these materials, despite decades of research and seemingly infallible demonstration of their applicability, have not yet found widespread use. Adoption of novel technologies is always in competition with economics, and it seems that, at least for the time being, less efficient methods are in fact more profitable. However, this is bound to change in the years to come.

2. EXPERIMENTAL

In the experimental part materials and methods used to form catalytic MoS_2 and WO_3 films will be elaborated on, as well as the experimental procedures used to characterize their structural and electrochemical properties.

2.1 Cathodic electrodeposition of MoS$_2$ thin films

In these studies, MoS_2 thin films had been cathodically electrodeposited on plain copper wire electrodes, but also large surface area metallic 3D-structured copper foams. Regardless of the substrate used, the methods were largely identical.

2.1.1 MoS$_4^{2-}$ precursor electrolyte synthesis

Molybdenum disulfide films on copper wire substrates were electrodeposited from a solution containing a common precursor of Mo^{6+} and S^{2-} ions – tetrathiomolybdate (TTM / MoS_4^{2-}). In order to prepare the electrolyte, ammonium heptamolybdate tetrahydrate $(NH_4)_6Mo_7O_{24}*4H_2O$ ($\geq$ 99 %, *Carl Roth*) and sodium sulfide hydrate Na_2S*xH_2O (60 %, *Carl Roth*) were mixed in a ratio of $Mo/S = 1/4$. The sulfidation of molybdate ions (MoO_4^{2-}) to tetrathiomolybdate is a four-step reaction, where each step is reversible, and the total reaction can be represented as follows:

$$MoO_4^{2-} + 4HS^- + 4H^+ \leftrightarrow MoS_4^{2-} + 4H_2O \qquad (25)$$
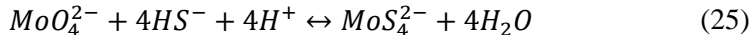
The pH of the mixture as-prepared was ~ 12, and it was acidified up to pH of 7 with sulfuric acid to push the reaction equilibrium towards the product side and to favor the formation of MoS_4^{2-} over the intermediates. The reference indicator of MoS_4^{2-} formation was the solution color changing to a deep red. 25 ml of 2-propanol ($\geq$ 99.5 %, *Carl Roth*) was added to the electrolyte in order to decrease surface tension and increase wettability of the working electrode. The final electrolyte composition contained: $C_{MoS_4^{2-}} = 0.025$ M + 10% of 2-propanol. The pH was kept weakly alkaline (pH ~ 8) to prevent precipitation of insoluble MoS_3.

The electrolyte for electrodeposition of MoS_2 films on Cu foam substrates was slightly modified: 0.1 M Na_2SO_4 ($\geq$ 99 %, *Carl Roth*) was added to ensure more stable ionic strength, and in order to study the effect of a chemical reducing agent 0.1 M of sodium hypophosphite NaH_2PO_2 ($\geq$ 99 %, *Carl Roth*) was added to it. Here 2-propanol was not added. The pH was again adjusted to pH 8 prior to electrodeposition.

2.1.2 Electrodeposition of MoS$_2$ films

All electrochemical measurements were carried out using a standard three-electrode cell set-up (potentiostat/galvanostat Metrohm µAutolab Type III and Metrohm Autolab 302N). Unless specified otherwise, all potentials were referenced to Ag/AgCl.

The copper wire substrates were prepared from ⌀2 mm commercial copper wire, and were isolated to expose a 1 cm^2 working surface area to the electrolyte. Before electrodeposition they were polished with a commercial detergent, then immersed in 2 M H$_2$SO$_4$ (prepared from 95-98 % sulfuric acid, *Carl Roth*; 97 % Sulfuric acid, *Honeywell*) to dissolve surface oxides, rinsed with distilled water, and finally degreased with 2-propanol. Initially, linear sweep voltammetry measurements were carried out to determine the electrodeposition potential range in the investigated electrolyte. MoS$_{2-x}$ films were deposited under potentiostatic mode, at various cathodic potentials (-0.8 V to - 1.2 V); or at constant potential (-1.0 V), but for different deposition times (200 s - 7200 s).

For 3D electrodes, open-cell commercial copper foam was used as the deposition substrate. The foam had a density of 1.02 g cm^{-3}, a porosity of 87.6%, and an approximate ligament diameter of 150 to 200 µm. Electrodes for deposition were prepared from a 2 x 2 x 0.13 cm cut-out of the copper foam sheet, shaped into a cylinder to promote equal current density distribution across the entire geometrical surface area. The substrates were degreased in acetone ultrasonic bath for 5 minutes. Before an electrodeposition they were immersed into a 2 M H$_2$SO$_4$ solution to remove surface oxides, and then rinsed well with distilled water. Cyclic voltammetry (CV) measurements were used to assess the working potential range for MoS$_2$ electrodeposition in both solutions. The electrodeposition was carried out for four values of passed charge: 10 C, 20 C, 30 C and 40 C (at a galvanostatic current of -10 mA) in order to evaluate the effect of catalyst loading on HER activity. The electrodes were weighed before electrodeposition and after characterization. Current efficiencies were calculated from the obtained data, assuming that MoS$_2$ electrodeposition is a two-electron reaction (**eq. 1**).

2.2 Formation of WO$_3$ films by anodization

Different modes of anodization were investigated: potentiostatic anodization in a collection of acidic and fluoride-containing electrolytes was used to form compact films, investigate thin film growth kinetics, and to prepare thicker films for photoanode applications.

Meanwhile, galvanostatic anodization was used to form thick, porous WO_3 and WO_3 + MoS_x films meant for the construction of efficient OER photocatalysts.

2.2.1 Potentiostatic anodization

All electrodes were prepared from pure W (plates - 0.1 mm and 0.25 mm thick, wire – 1 mm diameter, 99.95% metal basis, *Alfa Aesar*):

(a) Plates of 1 cm x 1 cm dimensions were used for structural analysis and photocurrent measurements.

(b) A wire of 1 cm^2 surface area was used for voltammetry and electrochemical impedance spectroscopy.

Prior to experiments, the electrodes were polished, degreased in acetone ($\geq$ 99.5 %, *Carl Roth*) in an ultrasonic EMAG Emmi-20HC bath, and rinsed with distilled water. Based on previous research [66,77,129–134], several electrolytes have been selected for investigation (1 M HCl, 1 M H_2SO_4, 14 M H_3PO_4, 14 M H_3PO_4 + 1 M NH_4F, 0.3 M oxalic acid). All measurements were carried out using a programmable potentiostat Autolab 302N and NOVA software. For high-voltage anodization, a Consort EV 245 galvanostat/potentiostat was used.

These anodizations were distinguished into relatively low potentials and high potentials. Low potentials were used to investigate film growth kinetics, and will be discussed in a seperate chapter. High potentials were used to grow thick WO_3 films for use as photoanodes. These WO_3 films were obtained by anodization in a two-electrode cell (where the anode was the W foil, and the cathode was a stainless-steel coil) for 30 minutes at voltages ranging from 10 to 60 V just in 0.3 M oxalic acid (prepared from oxalic acid dihydrate, $\geq$ 99.5 %, *Carl Roth*). The thickness of obtained oxide films was measured based on cross-section images.

2.2.2 Galvanostatic anodization

The films investigated in this part were prepared by anodizing metallic tungsten (99.5% *Alfa Aesar*, 0.1 mm thick) substrates. The foils were shaped to have 1x1 cm working areas (2 cm^2 surface area). Before anodization, the substrates were degreased in 2-propanol, cleaned in a NaOH ($\geq$ 99 %, *Carl Roth*) solution to remove residual oxides, and rinsed well with distilled water. The anodization was carried out in a two-electrode cell, where the anode was the W foil, and the cathode was a stainless-steel coil. A high-voltage power supply unit (Consort EV245) was used, and galvanostatic conditions were chosen in order to obtain more porous surfaces. The electrolyte was slightly basic (pH ~ 8) and fluoride-based with the following composition: 1M Na_2SO_4

($\geq$ 99 %, *Carl Roth*), 75mM NaF ($\geq$ 99 %, *Carl Roth*), 0.1M NaH_2PO_2 ($\geq$ 99 %, *Carl Roth*). Sodium hypophosphite was added as it has a proven effect on preventing excess oxygen from accumulating on the pore walls of the growing film, which is especially important during anodization when oxygen evolution is vigorous as in this study [80,81]. Also, the photocatalytic activity of films obtained without hypophosphite was inferior. A galvanostatic current density of 25 mA cm^{-2} was used, and anodization was carried out for 1 to 30 minutes. The films were not annealed, but they were dried with a heat gun that could produce temperatures up to 250° C, and this may have imparted the films with some thermally-induced crystallinity. Still, they were considered as-anodized. To synthesize composite WO_3 + MoS_x films, the exact same conditions were applied, but the electrolyte also contained 25 mM of MoS_4^{2-}.

2.3 Electrochemical characterization

2.3.1 HER electrocatalytic activity measurements of MoS₂ films

For MoS_2 films on copper wire substrates, the as-deposited films were rinsed with distilled water and immediately transferred to a 0.5 M H_2SO_4 solution (prepared from 95-98 % Sulfuric acid, *Carl Roth*; 97 % Sulfuric acid, *Honeywell*). A three-electrode cell was used, with an Ag/AgCl reference electrode and a stainless-steel counter electrode. A multi-faceted characterization of the obtained MoS_2 films towards HER consisted of the following measurements:

(1) Open circuit potential (OCP) determination;

(2) Electrochemical impedance spectroscopy (EIS) at -0.32 V vs. Ag/AgCl (-0.1 V vs. RHE);

(3) 10 linear sweep voltammetry (LSV) curves at 10 mV s^{-1} from OCP to - 40 mA cm^{-2} cut-off condition;

(4) Stability measurement for 20 minutes at -40 mA cm^{-2}.

It is imperative to mention that for the steady-state electrochemical characterization (LSV and stability measurements) of MoS_2 films that had been deposited on copper wire substrates, the current densities have been normalized to the geometrical surface area of the electrode (1 cm^2).

Registering an EIS spectrum before electrocatalytic measurements served two purposes: it allowed analysis of the catalyst in a non-destructive way, and supplied an accurate value of electrolyte resistance (for *iR* correction). Accordingly, all polarization curves were corrected for the *iR* drop.

In addition, EIS was used to estimate the H^+ adsorption and double layer capacitances (C_a and C_{dl}) of the electrodeposited MoS_{2-x} films. The cathodic overpotential for EIS recording was chosen to be not far from Nernst potential (-0.1 V). HER polarization experiments showed that at this overpotential range the reaction of hydrogen evolution occurs slowly. EIS spectra were measured in the range 10 kHz - 0.1 Hz. An amplitude of 20 mV was used based on the data of performed Kronig-Kramers analysis.

For MoS_2 films on copper foam substrates, the same after-deposition procedure was carried out, and the measurements were conducted in an identical cell setup. These films were characterized in the following manner:

(1) OCP for 120 s;

(2) LSV at a rate of 2 mV s^{-1} from 0 V vs RHE to a cut off condition of -100 mA, for 3 scans;

(3) EIS measurements at increasingly cathodic overpotentials (0 V, -0.1 V, -0.15 V, -0.175 V, -0.2 V, -0.25 V, -0.3 V).

It must be mentioned that for MoS_2 films, deposited on copper foam substrates, the geometrical surface area was not evaluated, and the steady-state experiments were not normalized. Instead, the electrochemically active surface area was investigated by AC methods.

The EIS spectra were measured in the frequency range 10 kHz to 10 mHz, with an amplitude of 20 mV. The system had satisfactory linearity, causality, and stability, and therefore this amplitude provided excellent electrochemical impedance spectra.

The EIS data were interpreted in the frame of equivalent electric circuits (EEC). It was taken care that the discrete elements of the chosen circuit had a physical meaning in the corresponding system, and that, as much as possible, the mathematical fitting errors should not exceed 10 %. Furthermore, the quality of fitting was controlled by ensuring that χ^2 and the sum of squares are as low as possible. The values of the pseudocapacitance, attributed to the adsorption time constant process, were used for an approximation of the number of active sites.

2.3.2 Investigation of WO₃ growth kinetics by EIS

Investigation of WO_3 growth kinetics was carried out in a two-electrode cell in order to operate in conditions as similar to high-voltage anodizing as possible. A stainless-steel wire coil of significantly larger surface area (~30 cm^2) as the counter electrode. It was considered that the possible potential shift during the measurement would be negligible compared to the applied voltage.

Polarization curves were obtained by linear sweep voltammetry in the 0–5 V potential range at scan rate of 10 mV s^{-1}. EIS spectra were registered in as follows: an automated program has been set up to increase the potential in steps of 0.1 V (see **Table 3**). During each of these steps, the electrode was kept at corresponding anodization potential for 10 minutes (a steady-state current has been settled within this period), then an EIS spectrum was registered in the 10 kHz – 0.01 Hz frequency range at perturbation amplitude of ±5 mV. In such way, a continuous growth of the oxide film could be examined in situ. Due to the bigger electrode area and large capacitance of the counter electrode, the measured impedance belonged entirely to the working electrode. The obtained EIS data quality and causality was confirmed by applying Kramers-Kronig procedure integrated into the NOVA software. The determined residuals were very small for the real part of the impedance (up to 0.8%), and their distribution appears to be random. Larger residuals occur on the imaginary part; their appearance coincides with the frequency range that exhibits inductance in the spectrum. Even so, only a few points are particular outliers, and generally the residuals are also within the vicinity of 1%. The sum of squares of the relative residuals reflects the compliance to Kramers-Kronig transforms, because the overall sums of residuals, $\chi 2$ were ranged from 10^{-6} to 10^{-4} dependently of solution.

Table 3. *Electrolytes and conditions of the EIS study.*

Electrolyte	Anodization potential range	No. of steps	Duration of each step
1 M HCl			
1 M H$_2$SO$_4$			
14 M H$_3$PO$_4$	0.1 V – 5.0 V	50	10 min.
14 M H$_3$PO$_4$ + 1 M NH$_4$F			
0.3 M oxalic acid			

2.3.3 OER photocatalytic activity measurements of WO$_3$ films

Linear sweep voltammetry, chronoamperometric, photo-electrochemical impedance spectroscopy, and intensity modulated photocurrent spectroscopy responses were measured in a three-electrode photoelectrochemical quartz cell: the working electrode (photoanode) was the WO$_3$ film, a stainless-steel counter electrode, and a saturated Ag/AgCl reference electrode. The photoanodes were illuminated from the front, with the back side insulated. Reflection losses from the cell and possible light absorption by the electrolyte were not accounted for. Measurements were carried out by means of Autolab

Optical Bench system (with a calibrated 365 nm UV LED and light intensities up to 80 mW cm^{-2}) connected to Autolab N302 potentiostat.

For the *potentiostatically* synthesized films in *0.3 M oxalic acid,* a 0.5 M Na$_2$SO$_4$ electrolyte was selected. Chronoamperometric and LSV chopped-UV measurements were carried out.

For the *galvanostatically synthesized* films in *1 M Na$_2$SO$_4$ + 75 mM NaF + 0.1 M NaH$_2$PO$_2$* (and + 25 mM MoS$_4^{2-}$ for WO$_3$ + MoS$_x$ composites), the same setup was used, with minor adjustments. The measurements were all carried out in 0.1 M Na$_2$SO$_4$, adjusted with sulfuric acid to a pH of 2, to ensure better electrochemical stability of tungsten oxide.

In PEIS the spectra were obtained in the 10 kHz – 0.1 Hz frequency range, with an amplitude of 10%, at applied potentials of from 0.4 V to 2.0 V. Care was taken to ensure that the conditions of causality, linearity, and stability are met, and the spectra were verified with the Kramers-Kronig transform procedure to ensure adequate validity. The spectra were fitted with equivalent electric circuits using the Zview software.

In IMPS the spectra were also obtained in the 10 kHz – 0.1 Hz range, using an amplitude of 10% for the LED's set output of 50 mW cm^{-2}. The spectra were measured at the same applied potentials. Semicircle fitting-simulation was carried out with the Zview software.

A typical characterization procedure for a film was:

(1) OCP determination for 60 seconds;

(2) LSV from OCP to 2.0 V (vs. Ag/AgCl) at 2 mV s^{-1} with chopped UV ON/OFF light;

(3) IMPS measurements at potentials from 0.4 V to 2.0 V;

(4) 3 potentiostatic 80 second UV ON/OFF pulses at 1.2 V;

(5) electrochemical impedance spectroscopy measurements with UV OFF and ON at potentials from 0.4 V to 2.0 V;

In order to improve the photoelectrochemical properties of the WO$_3$ films, a cathodic reduction step was performed *in-situ* before photocatalysis measurements. The reduction was carried out by applying a potential of -0.5 V (vs. Ag/AgCl) for 300 s, as it had been determined that these conditions result in a considerable improvement of the photoanode's OER catalytic properties. Before characterization, the reduced-WO$_3$ (r-WO$_3$ from here on in) were "activated" by applying constant illumination of 50 mW cm^{-2} under potentiostatic conditions (1.2 V) for 3000 seconds. This activation step allowed for the background re-oxidation current to subside and ensured that

the measured photocurrent can be confidently attributed to just photocatalytic oxygen evolution. An overview of the films considered and their lab-codes that will be used throughout the text is presented in **Table 4**.

Table 4. *The overview of investigated samples and their lab-codes.*

Anodization time min	Lab-code		
	WO_3	Reduced WO_3	WO_3+MoS_x composite
2	2min-WO_3	2min-r-WO_3	2min-WO_3+MoS_x
5	5min-WO_3	5min-r-WO_3	5min-WO_3+MoS_x
30	30min-WO_3	30min-r-WO_3	30min-WO_3+MoS_x

2.4 Morphology, structure, and composition

The surface morphology and chemical composition of the prepared catalysts were evaluated by scanning electron microscopy (SEM, Hitachi TM 3000, Tokyo, Japan, Hitachi S-3400N) with an integrated energy-dispersive X-ray module (EDS, Oxford Instruments, Buckinghamshire, UK).

A dual beam system Helios Nanolab 650 with an energy dispersive X-ray (EDX) spectrometer INCA Energy 350 and X-Max 20 mm^2 detector was also used for the study of surface morphology. A Ga$^+$ ion beam was used to create precise channels for cross sections on a sample surface.

The XPS analyses were carried out with a Kratos Axis Supra spectrometer using a monochromatic Al K(alpha) source (25mA, 15kV). The Kratos charge neutralizer system was used on all specimens. Survey scan analyses were carried out with an analysis area of 300 x 700 microns and a pass energy of 160 eV. High resolution analyses were carried out with an analysis area of 300 x 700 microns and a pass energy of 20 eV. The XPS signal due to adventitious carbon located at 284.8 eV was used as a binding energy (BE) reference.

3. RESULTS AND DISCUSSIONS

3.1 Electrodeposition and HER catalytic activity of MoS_2 films

3.1.1 MoS_2 film electrodeposition on copper wire and foam electrodes

To develop a necessary understanding of the chosen system, linear sweep voltammetry (LSV) measurements at increasing potential scan rates were performed on copper wire substrates. OCP was chosen as the starting point, and the potential was scanned toward -1.2 V (**Fig. 5a**). At a low scan rate (5 mV s-1) no clear reduction peaks can be distinguished – MoS_2 electrodeposition occurs alongside hydrogen evolution. When the potential scan rate is increased to 20 mV s^{-1} and more, a small peak in the reduction region (-1.0 V to -1.15 V) becomes apparent, after which further cathodic current increase results in hydrogen evolution. The peak shift towards more cathodic values with increased potential scan rate suggests slow reaction kinetics, as the current is slow to respond to the swift change in the potential. This may be attributed to a slow charge transfer step or diffusion of the MoS_4^{2-} complex toward the surface.
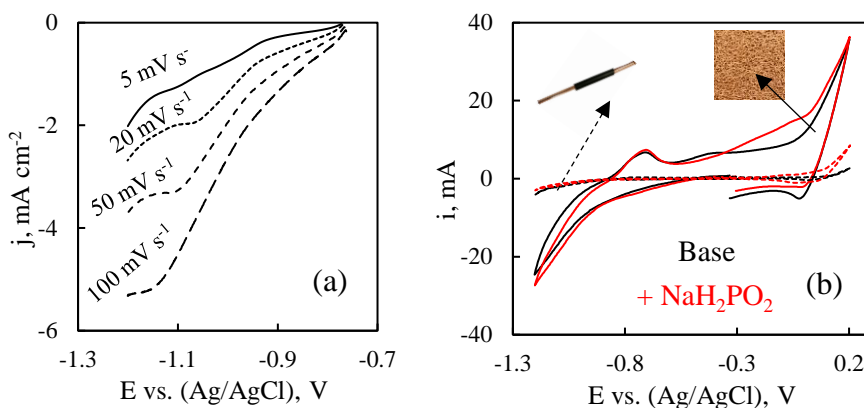

***Fig. 5**. LSV curves of MoS_2 electrodeposition on a bare Cu wire substrate in 25 mM TTM + 10% 2-propanol (a); First CV cycles at scan rate of 2 mV s^{-1} for MoS_2 electrodeposition on Cu wire electrode (geometrical area of 1 cm^2) and 3D-foam in 25 mM TTM with (black lines) and without NaH_2PO_2 (red lines) (b).*

The electrodeposition of MoS_2 films on copper foam substrates in both solutions (without and with hypophosphite) was investigated by cyclic voltammetry in order to establish a working potential range, where the dominating cathodic reaction is MoS_4^{2-} reduction to MoS_2. Firstly, CV scans

were taken on a 1 cm^2 surface area copper wire electrode, at potentials from -1.2 V to 0.2 V vs. Ag/AgCl (**Fig. 5b**).

Again, no prominent cathodic peaks were present in these cycles due to overlaying of MoS_4^{2-} reduction peaks with hydrogen evolution, which occurs across the entire potential range. At about -1 V the cathodic current begins to increase more rapidly, which reveals that MoS_4^{2-} reduction and HER are occurring. The addition of NaH_2PO_2 does not change the profile of the cycles, nor do any peaks become apparent. There is a small difference in the anodic part of the cycles, but in this system the anodic current is entirely dominated by the corrosion of the copper substrate, and the oxidation of electrodeposited MoS_2. A minor increase in the cathodic current is observed with the addition of hypophosphite, but no distinguishable reductive peaks appear. A small anodic peak at -0.68 V is seen in both cases, and is likely caused by rapid hydrogen desorption from the large surface area of the catalyst-covered electrode. The sharp increase in oxidative current at higher anodic potentials again occurs due to corrosion of the substrate.

Hence, on copper wire substrates MoS_2 films were first deposited under a potentiostatic mode, in the range of -0.8 V – -1.2 V to observe film formation nearby the reduction peak. The surface morphology of as-deposited films was observed to change with applied potential (**Fig. 6**). Thin layers that replicate the surface morphology of the substrate are obtained at low cathodic potentials. At an intermediate deposition potential of -1.0 V a rough and nodular surface structure with some cracks is formed. At even higher potentials (-1.2 V) the thick films were observed to peel off from the substrate when drying.

Electrodeposition at a constant potential of -1.0 V but for different times (200 s – 7200 s) was also chosen for further investigation. The surface morphologies of these films were slightly different: after a short deposition time of 200 s a homogeneous film had not yet formed, and only disconnected crystallite structures could be observed. After 600 seconds deposition the film was almost identical to the one obtained previously, although slight changes in deposition conditions could have resulted in what appears to be a smoother morphology. Finally, the film that had been deposited for 1800 seconds appears thick but smooth, and long cracks again propagate throughout its structure.
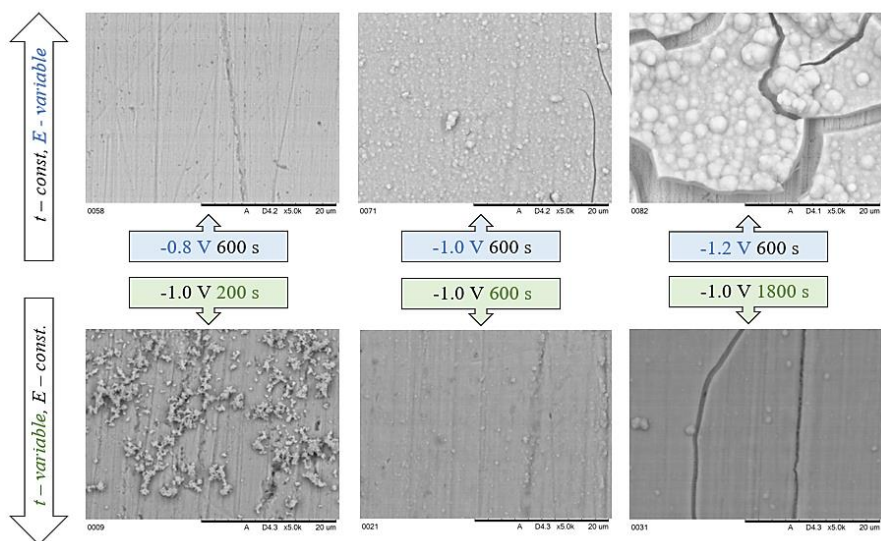
Fig. 6. *SEM images of MoS₂ films, electrodeposited potentiostatically on copper wire substrates.*

The results of experiments on copper wire substrates suggest that mild electrodeposition conditions (in this particular case ~ 1 mA cm^{-2} deposition current settles at ~ -1.0 V) favor the formation of compact, non-cracked film. For this reason, on copper foam substrates a cathodic current of 10 mA was selected. At this current, the potential settles at ~ 1.05 V (**as in Fig. 5b**) and intense HER does not occur. The films were electrodeposited at increasing charge passed through the cell (from 10 to 40 Coulombs). This range was selected in order to encompass a wider array of film thicknesses: thinner MoS$_2$ films were expected to have better adhesion to the substrate, more resistance to delamination, and have more favorable electron transfer kinetics from the catalyst/solution interface to the substrate. In contrast, thicker films may exhibit poorer physical stability due to internal stresses and weaker chemical bonding to the substrate. However, the increased catalyst loading (higher charged passed) should result in better HER catalytic activity.

In order to relate electrodeposition parameters to catalyst loading the films were weighed, thus measuring the mass of the MoS$_2$ deposits. The reductive deposition of MoS$_2$ conforms to Faraday's law – there is a linear correlation between charge passed and mass of the electrodeposited film. Up to 0.25 mg of material is deposited per 1 C. In terms of current efficiency this corresponds to ~ 32%. The amount of material deposited without and with NaH$_2$PO$_2$ is almost identical. Current efficiencies are slightly lower for the electrolyte with hypophosphite, but not by any significant degree. Therefore, the addition of NaH$_2$PO$_2$ has no effect on the kinetics or mechanism of MoS$_2$ deposition. The

catalyst loading for films, electrodeposited for a similar amount of charge without or with hypophosphite can be assumed to be identical.

A visible effect of hypophosphite is observed on the morphology of the electrodeposited MoS_2 films – the deposits grow more evenly and with less apparent roughness (**Fig. 7**). In the base electrolyte, MoS_2 appears to grow in clusters of nodules, protruding from the surface and away from the substrate, but often not connecting amongst each other. In contrast, the addition of NaH_2PO_2 causes the formation of more compact films, with MoS_2 growth occurring homogenously over a larger surface area. This change in morphology causes a decrease in the micro-level roughness of the deposits. Some cracks can be seen in the thicker MoS_2 films (e.g., deposited for 30 C), which have also been observed in our previous studies, and are directly related to the thickness and consequent tensile stress of the electrodeposited films. Fewer cracks are seen for the films, electrodeposited with hypophosphite, feasibly due to the lower stress of the deposits.

Interestingly, sodium hypophosphite provides a similar effect on the electrodeposition of various transition metal alloys. For example, when depositing a Fe-W-P film, a certain concentration of NaH_2PO_2 in the deposition solution resulted in lower stress of the film, and smaller crystallite sizes; the grain sizes would decrease when the NaH_2PO_2 concentration was increased [135]. Similarly, for Co-Ni-P electrodeposits, the amount of NaH_2PO_2 in the electrodeposition solution was observed to affect the surface morphology – the surface appeared smooth and less nodular [136].
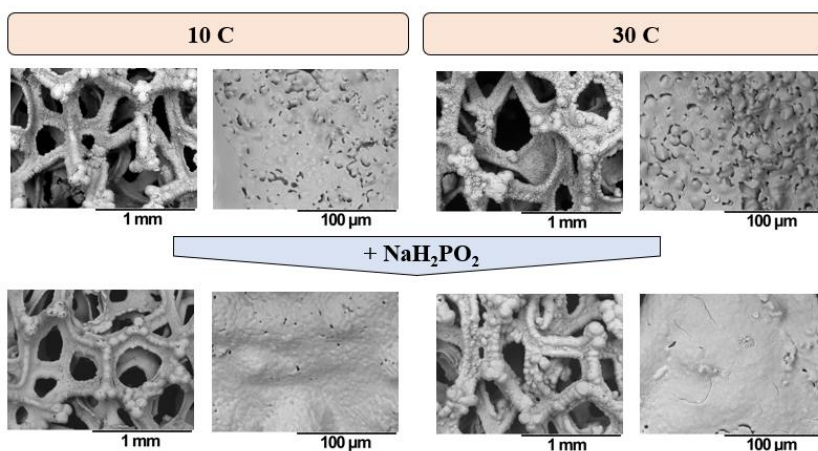

Fig. 7. SEM images of MoS$_2$ films electrodeposited at cathodic current of 10 mA on Cu-foam electrodes from electrolytes without and with sodium hypophosphite.

3.1.2 Composition and structural properties

As was suspected from LSV measurements on Cu wire substrates, the increase of the cathodic deposition potential results in higher quantities (in at. %) of Mo and S in the electrodeposits at a constant deposition time (**Fig. 8a**). Larger quantities of Mo and S can be also obtained by increasing the deposition time at lower potentials (**Fig. 8b**). The as-deposited films are thin, and therefore a strong signal of the Cu substrate is visible in the EDX analysis. However, the atomic % of Cu decreases when a larger amount of Mo and S is deposited at higher potentials or deposition times. It should be noted that a significant amount of oxygen is also present in the samples, and its relative amount increases with applied potential. This could be attributed to the following issues:

(a) Some amount of unreacted molybdate (MoO_4^{2-}) from the solution can electrodeposit alongside MoS_2

(b) Due to the oxidation of MoS_2 active centers in air.
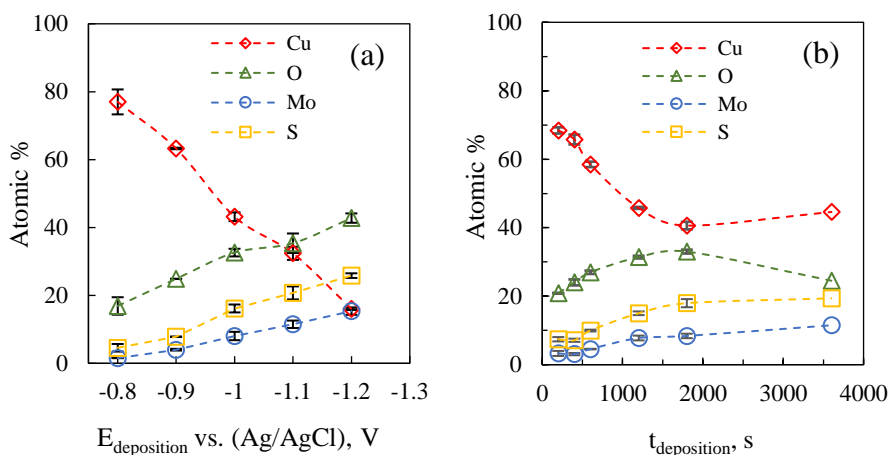

Fig. 8. *EDX compositional data for MoS$_2$ films that had been electrodeposited on a Cu wire substrate: for 600 s at different potentials (a); at -1.0 V for increasing deposition times (b).*

Similarly, for MoS$_2$ films on Cu foam substrates (**Table 5**) the elemental analysis showed that the deposited films are rather thin; therefore, a strong signal from the substrate material (Cu) was present in the EDX spectra. A significant amount of oxygen was also detected in all samples, which may be due to the same reasons as discussed above. There is no direct correlation between electrodeposition conditions and composition of MoS$_2$ films. The deposits are sulfur-deficient, and for those obtained from the base solution, the MoS$_{2-x}$ stoichiometry ranges from MoS$_{1.72}$ to MoS$_{1.87}$. Some difference in

composition is observed for the films, electrodeposited with hypophosphite. The amount of Mo and S in atomic % increases with passed charge, and the background signal of the copper substrate consequently decreases. In MoS_2 films, electrodeposited with hypophosphite, the Mo:S ratios are closer to the stoichiometric ideal – 2. The film deposited for 10 C even exhibits a sulfur surplus, which may be caused by a chemical reaction, for example the formation of copper sulfide. A small amount of phosphorus is present in the EDX spectra, but in some cases, it was smaller than the reliable detection limit deviation. It must be concluded that there exists a possibility of phosphide incorporation into the MoS_2 structure, but if so – the amount of it is near the detection limit. Because the active sites of MoS_2 for HER catalysis are sulfur vacancies, it can be suspected that the stoichiometry difference will have an effect on the electrocatalytic activity of these deposited films. Indeed, the research has shown that there is an optimal amount of point defects (active sites) that results in best HER catalytic activity [25].

Table 5. *Dependence of chemical composition of MoS_2 films on the passed charge at a cathodic current of 10 mA; films electrodeposited from electrolytes containing MoS_4^{2-} and MoS_4^{2-} + NaH_2PO_2 (denoted with *).*

Q, C	Composition, at. %							Mo : S ratio	
	Mo	**Mo***	**S**	**S***	**O**	**O***	**P***	**-**	*****
10	9.60	6.63	17.99	13.90	72.40	79.41	0.047	1.87	2.10
20	8.15	7.26	13.81	14.25	78.04	78.38	0.11	1.72	1.98
30	9.06	8.14	15.92	16.06	75.0	75.73	0.065	1.75	1.96
40	8.12	9.54	14.69	15.86	77.18	74.47	0.13	1.83	1.66

X-ray photoelectron spectra were obtained for the MoS_2 films, electrodeposited with and without NaH_2PO_2 in order to investigate the possible differences in their structure (**Fig. 9**). The sulfur 2p region is determined by a single doublet corresponding to S $2p_{1/2}$ and S $2p_{3/2}$ lines that is characteristic for the presence of the 2H-MoS_2 phase. For the MoS_2 films, electrodeposited without NaH_2PO_2 (**Fig. 9b**), the $2p_{3/2}$ maximum is seen at a binding energy of 161.9 eV. Whereas deposition with hypophosphite leads to the shift of the peak position towards slightly higher energies at 162.1 eV. Another S 2p doublet was added in the model for better fitting of the spectra. A second doublet in the S 2p region has been attributed to the existence of different S-S bonds in the material (terminal and bridging bonds) [137,138].

However, in our case the second S 2p doublet appears more similar to those that have been reported to be caused by sulfur residuals from polysulfide that may have formed in the deposition solution. Thus, it can be inferred from the spectra that the near-surface sulfur atoms exist almost entirely in one oxidation state.
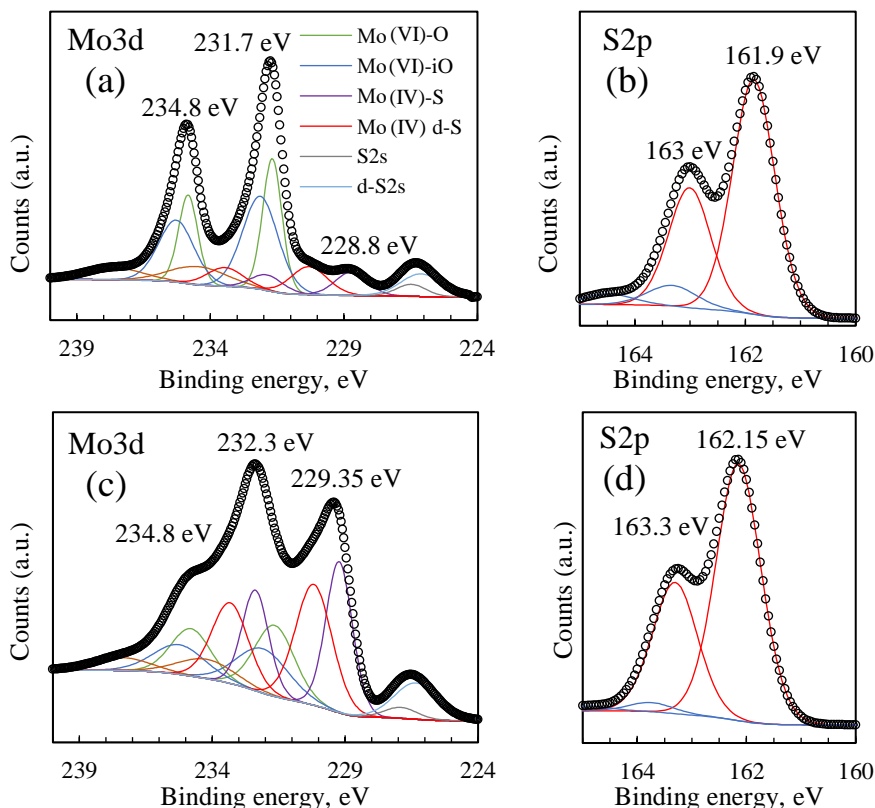

Fig. 9. XPS spectra and fitted peaks of MoS₂ films, electrodeposited on copper foams without NaH₂PO₂(a, b) and with NaH₂PO₂ (c, d).

Deconvolution of the Mo 3d region revealed that Mo exists in multiple oxidation states, and is coordinated by different elements (**Fig. 9a, c**). The films electrodeposited without hypophosphite (**Fig. 9a**) show a spectrum that is almost entirely decided by two peaks at 231.7 eV and 234.8 eV. Judging by these binding energies, these peaks likely belong to Mo(VI) oxides ($3d_{5/2}$ 232.3 eV to 232.5 eV; $3d_{3/2}$ 235.4 eV to 235.7 eV [139,140]). These oxides may have been electrodeposited from residual MoO_4^{2-} in the deposition solution, or appeared through oxidation of uncoordinated Mo sites on the surface. The peaks deconvolute into two doublets marked Mo(VI)-O and Mo(VI)-iO in Figure 9, which also suggests that the oxide exists in different states.

The peaks at binding energies of 229.35 eV and 232.3 eV have been reported to correspond to Mo^{4+} $3d_{5/2}$ and $3d_{3/2}$ components of 2H-MoS_2 (marked Mo(VI)-S) [141]. This, along with the previously discussed characteristic S 2p peaks, confirms the presence of the 2H-MoS_2 phase. The origin of the doublet ($3d_{5/2}$ 230.2 eV; $3d_{3/2}$ 233.2 eV) is ambiguous. Such binding energies correspond well to Mo(IV) oxides [139,140], which may exist in the electrodeposited film due to reasons discussed above related to Mo(VI) oxides. However, a very similar binding energy (230.7 8eV) may also be attributed to an intermediate Mo oxidation state (e.g. V) that is only partially coordinated by sulfur (with a sulfur vacancy – active site) [138,142]. The depressed, wide peaks at a very high binding energies (234.5 eV 237.8 eV) could not be attributed to any state of Mo, and are assumed to be caused by some residual compound from the solution.

XPS analysis showed that within films, electrodeposited without NaH_2PO_2, molybdenum is widely coordinated by oxygen, i.e., the film contains a lot of molybdenum oxide. This is also supported by EDX analysis, where the amount of oxygen in these films was relatively large. When electrodeposition is carried out with hypophosphite, a much stronger Mo(IV)-S bond signal is observed. Because the S 2p signal does not change in any major way, it is assumed that the material retains the same 2H-MoS_2 structure, and that the effect of NaH_2PO_2 on the electrochemical deposition of MoS_2 is mainly targeting the suppression of Mo-O bond formation, or conversely, the assistance of Mo-S bond formation.

3.1.3 HER electrocatalytic activity

The electrodeposited MoS_2 films were all tested for their ability to catalyze HER in acidic media. All experiments were carried out with freshly-prepared MoS_2, as it was found that the electrocatalytic activity for HER severely decreases after the films had been dried and stored in air (likely due to surface active site oxidation). Thus, the as-deposited films were removed from the electrolyte, rinsed with distilled water and 2-propanol, and then immediately transferred into 0.5 M H_2SO_4. The solution was used for a comprehensive characterization of the films, deposited on Cu wire substrates, consisting of EIS, HER voltametric sweeps, and galvanostatic stability experiments (**Fig. 10**). Several tendencies were revealed from the analysis.
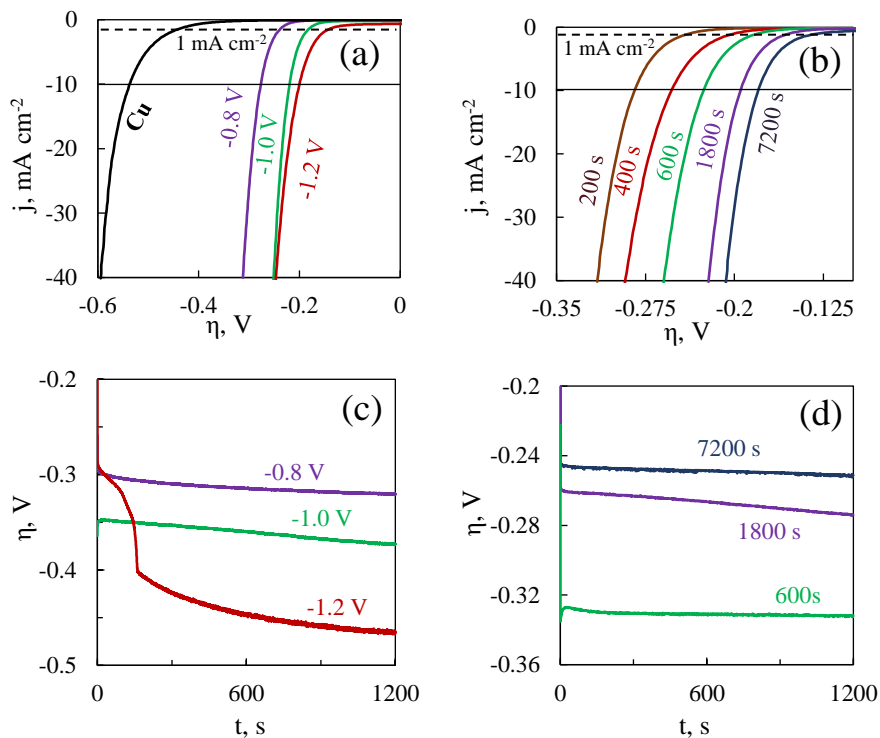
Fig. 10. *HER polarization curves and galvanostatic (-40 mA cm^{-2}) stability experiments of MoS$_2$ films, electrodeposited on copper wire: at indicated potentials for 600s (a,c); at -1.0 V (vs. Ag/AgCl) for indicated deposition time (b,d). Scan rate 10 mV s^{-1}, 0.5M H$_2$SO$_4$. Bare Cu substrate added for comparison.*

It is evident that even a thin coating of MoS$_2$ (deposited at – 0.8 V) already greatly increased HER activity compared to the bare substrate (**Fig. 10a**). An increase in the cathodic deposition potential resulted in better catalytic activity and lower onset overpotentials (measured at 1 mA cm^{-2}): -0.232 V and -0.122 V vs. RHE for MoS$_2$ deposited at -0.8 V and -1.2 V respectively. The reason for this improvement is mostly linked to the increase in catalyst loading, i.e., a higher amount of electrodeposited MoS$_2$ (as in **Fig. 8a**).

Deposition time also affects the elemental composition of the MoS$_2$ layers (**Fig 8b**), and consequently can change their catalytic activity. Taking into account SEM/EDX analysis and stability of the films, deposition at a constant potential of -1.0 V but for different times (200 s – 7200 s) was further investigated (**Fig. 10b**). Indeed, a longer deposition time had a significant effect on the MoS$_2$ films' electrocatalytic activity. The overpotential for HER (at 10 mA cm^{-2}) changed from -0.285 V to -0.180 V (vs. RHE) when the deposition time was increased from 200 s to 7200 s, which may be attributed to increasing catalyst loading. A diminishing gain in catalytic activity is observed when deposition times are increased from 1800 s to 7200 s: a limit

is reached where the electrode's total catalytic activity no longer depends on catalyst loading (deposition time).

The electrochemical stability of the MoS_2 films was evaluated by chronopotentiometry at moderately harsh working conditions of -40 mA cm^{-2} for 20 minutes (**Fig. 10c,d**). On average, the films lost around 5% activity over the measurement, but the MoS_2 film deposited at -1.2 V underwent complete destruction (peeling off from the substrate) within the first 200 s of the experiment. Thinner (short deposition time) and more compact films can lose less than 1% (in terms of overpotential) of their initial activity over the experiment. For the film deposited for 1800 s, a larger 2.9% decrease in catalytic activity was observed. Finally, the film with the longest deposition time in our experimental series (7200 s) only had a 1.3% loss from initial activity. These results show that the most electrochemically stable MoS_2 films should have either a compact, or a well-evolved and rough surface morphology.

Similar experiments were carried out on the MoS_2 films, electrodeposited on copper foam substrates. The initial potential was set close to thermodynamic equilibrium (0 V vs RHE), and a scan rate of 2 mV s^{-1} was applied. A cut-off condition of 100 mA of cathodic current was set to end the scan. In this way, three scans were recorded, and the third scan was selected for analysis (**Fig. 11a**).
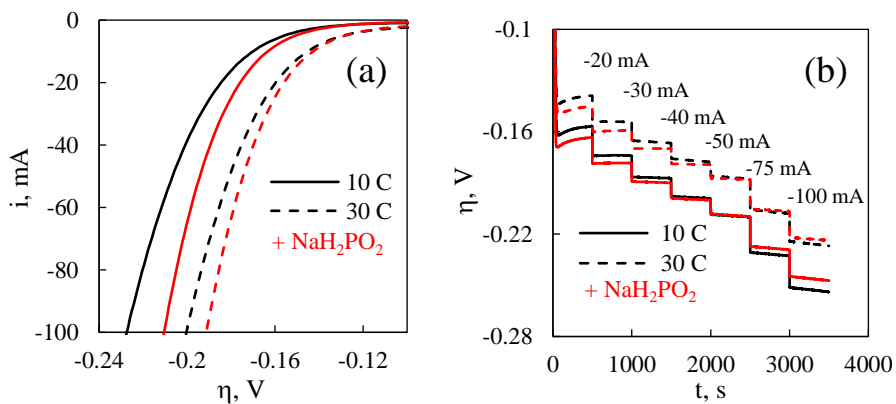

Fig. 11. *iR-corrected polarization curves of electrodeposited MoS_2 films in 0.5 M H_2SO_4 (a); Galvanostatic stability curves of MoS_2 films, electrodeposited with and without NaH_2PO_2 (b). Scan rate – 2 mV s^{-1}. (Red lines correspond to samples, deposited with NaH_2PO_2).*

Note that the cathodic current on the ordinate axis has not been normalized into geometrical surface area, because it would be incorrect for such an electrode, where current density distribution does not guarantee equal HER

turnover over the entire electrochemically active surface area. More discussion on this issue follows in the EIS section. It can be seen that MoS_2 films, electrodeposited for increased passed charge (higher catalyst loading) predictably have better total activity. The onset overpotential (arbitrary, where the HER current would begin to sharply rise) is also lower for higher-loading electrodes. Thus, a MoS_2 film electrodeposited from the base MoS_4^{2-} solution for 10 C could reach a HER cathodic current of 100 mA at an overpotential of -0.227 V. In comparison, a film electrodeposited for 10 C in the presence of NaH_2PO_2 could reach -100 mA at -0.21 V, representing a 17 mV improvement. The effect of adding sodium hypophosphite into the electrodeposition solution has a prominent effect on the electrocatalytic activity of the films – their total activity generally increases. On LSV curves, this results in lower overpotentials, required to reach the same HER current. A smaller, but similar difference is observed in all cases. Because the mass of the Cu-foam MoS_2 electrodes (catalyst loading) is alike, this must be caused by changes of the intrinsic activity of the film.

The electrochemical stability of electrodeposited MoS_2 films was tested by a galvanostatic step technique: the cathodic current was set at incrementally increasing values (from -10 mA to -100 mA), and the potential response was measured for 500 s in order to approach a steady state value (**Fig. 11b**). All examined films are stable at lower applied currents (up to -40 mA), and only a slight decrease in overpotential is observed over each 500 s step. Furthermore, MoS_2 films electrodeposited from the solution with hypophosphite possess worse catalytic activity at lower currents than in the absence of it, but at cathodic currents higher than -50 mA, the curves overlap, and the films electrodeposited with hypophosphite exhibit improved catalytic activity. At higher cathodic currents (over -50 mA) a rapid drop in measured overpotential is observed, which indicates a loss in catalytic activity. This is likely due to the cathodic corrosion, i.e. shortening of the polymeric S-Mo-S chains by cleavage of Mo-S bonds, which has been described in [138].

The catalytic parameters that had been extracted from these polarization curves are shown in **Table 6**. Tafel slopes and exchange current densities are calculated by plotting the iR-corrected logarithmic current density against overpotential (as per **eq. 6**), and applying a linear trendline where log j – E shows a linear correlation, typically at higher overpotentials. This process is trivial, and so is not shown graphically, although it must be kept in mind that Tafel slopes are predictive in nature and should be derived from as many orders of magnitude of current as possible [16]. Also note that for MoS_2 films on Cu foam substrates current densities are replaced by absolute currents. This

is due to the uncertain surface area of the electrode, and electrochemical surface area effects will instead be evaluated through EIS later.

Table 6. *A summary of the deposition conditions and resulting catalytic parameters (overpotential at 10 mA HER current, Tafel slope, and exchange current density) of the MoS$_2$ catalysts considered in these studies.*

Substrate	Applied potential V	Time s	Charge passed C	η_{10mA}, mV	Tafel slope mV dec^{-1}	j_0 μA cm^{-2}
Copper wire	Bare substrate	-	-	537	116.4	-
	-0.8		-	277	45.1	0.0077
	-0.9		-	263	49.4	0.048
	-1.0	600	-	220	45.2	0.14
	-1.1		-	205	49.2	0.70
	-1.2		-	200	65.9	9.35
		200	0.103	285	45.9	0.0064
		400	0.208	253	52.9	0.017
		600	0.317	226	45.6	0.012
		800	0.437	216	43.3	0.011
	-1.0	1000	0.529	210	42.5	0.012
		1200	0.673	205	41.9	0.013
		1800	1.05	196	40.9	0.017
		3600	2.35	185	41.6	0.035
		7200	5.03	181	44	0.080

Substrate	Applied current and settled potential V	NaH$_2$PO$_2$	Charge passed C	η_{10mA}, mV	Tafel slope, mV dec^{-1}	j_0, μA
Copper foam	Bare substrate	-	-	413	93.1	-
			10	171	47.5	2.62
			20	158	47	4.22
	- 10 mA	-	30	145	54.5	21.5
			40	145	51.4	14.9
	- 1.05 V		10	163	42.5	1.43
			20	157	47.9	5.23
		+	30	142	51.7	16.8
			40	142	49	12.3

For MoS$_2$ films on copper wire substrates an exponential relation between MoS$_2$ electrodeposition potential and HER exchange current density (j_0) was observed. When the films had been deposited for 600 s from -0.8 V to -1.2 V, j_0 increased from 0.0076 μA cm^{-2} to 9.35 μA cm^{-2}. Unfortunately, further increasing the deposition potential did not obey this exponential relation, probably because of the unfavorable changes in the film's formation that occur

due to severe hydrogen evolution at high potentials. The exchange current density also increases linearly with deposition time (at -1.0 V) in the entire investigated range up to 7200 s. This is a particularly promising result, as it implies a possibility to reach relatively high exchange current densities under mild electrodeposition conditions.

Tafel slopes for all deposited MoS_2 films generally fell within the 40 – 50 mV dec^{-1} range, showing mixed HER kinetics. As per eqs. 3 – 5 and the discussion therein, such slopes suggest a Volmer-Heyrovsky HER mechanism. One exception from the given trend was the film, deposited at -1.2 V. The Tafel slope for this sample was markedly higher at 65.9 mV dec^{-1}. The increase in the Tafel slope shows an unfavorable deviation from the dominating Volmer-Heyrovsky mechanism. This may be related to the occurrence of side reactions during electrodeposition at this relatively high potential, and the changes in the deposited MoS_2 films. The Mo : S ratio of this film was also the lowest at 1 : 1.68, and the film had a significant amount of oxygen (see **Fig. 8**). When the films had been deposited at -1.0 V but increasing durations, a minimum of 40.9 mV dec^{-1} is reached when the MoS_2 film has been deposited for 1800 s. The reason for this outcome could be linked to the formation of different active sites, or that an optimum catalyst loading is reached, where a further increase of deposition time begins to impede charge transfer in the semiconductor MoS_2 material.

On copper foam substrates the determined values for slopes are also in the 40 – 50 mV dec^{-1} range. MoS_2 films, electrodeposited with hypophosphite, have slightly lower Tafel slopes, but still do not meaningfully surpass the previously discussed MoS_2 films on wire substrates. In terms of exchange current, the values are much larger than those obtained for films on copper wire, likely owing to the much larger surface area. Only a small change of this parameter is seen upon addition of NaH_2PO_2 as i_0 decreases in most cases. However, due to the potential variance in the geometrical surface area of Cu-foam electrodes, these values are not necessarily correct representation of the intrinsic activity of the electrodeposited films.

3.1.4 Investigation of HER kinetics by EIS / Active sites

EIS has been shown to provide useful information on HER catalytic materials that is supplementary to more typical experiments like steady-state polarization, and can give insight into the mechanic or kinetic phenomena of the system under investigation [143].In these experiments the EIS spectra were obtained prior to the polarization measurements, in the same working electrolyte of 0.5 M H_2SO_4.

For MoS$_2$ films on copper wire substrates a cathodic overpotential of 0.1 V was chosen, as it represents a potential window where hydrogen evolution occurs at a low rate (as can be seen in **Fig.10b**), and a lower disturbance of the pre-electrode layer by hydrogen bubbles is expected.

Under these experimental conditions, the low-frequency current response to the potential perturbation should be caused mainly by the adsorption of H onto the active sites of the MoS$_2$ film (**eq. 3**). Because the majority of active centers are S vacancies and Mo edges (with respective free hydrogen adsorption energies of $\Delta G_H^0 \approx$ -0.095 eV, $\Delta G_H^0 \approx$ 0.115 eV [23]), specific H$^+$ adsorption had to occur during the measurements. The characteristic impedance spectra are shown in **Fig. 12**.
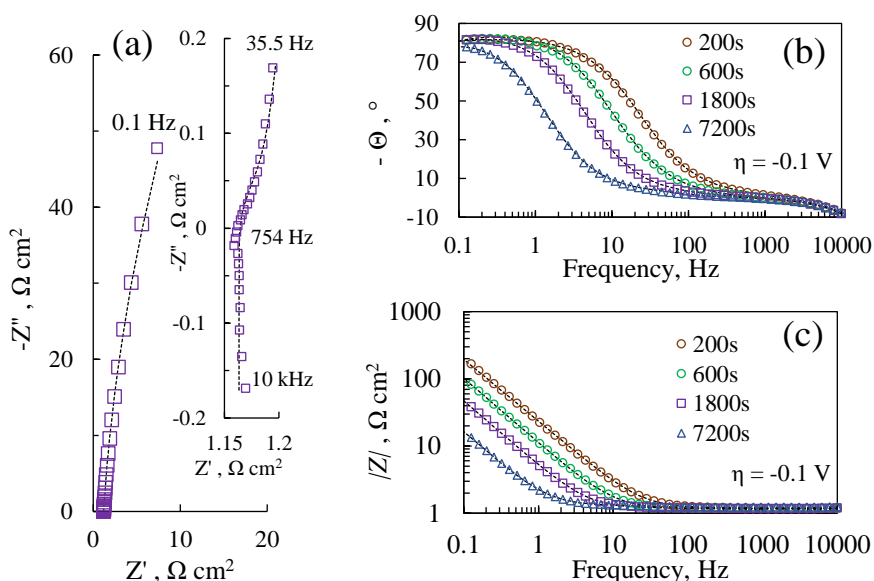

***Fig. 12.** EIS spectra obtained at overpotential -0.1 V of MoS$_2$ films, electrodeposited for different deposition times: a representative complex-plane Nyquist spectrum of a MoS$_2$ film electrodeposited for 1800 s (inset shows high frequency region) (a); the Bode impedance plots for respective films (b,c). Dashed lines represent fitted data.*

An identical high-frequency inductive response was observed for all samples (**Fig. 12a** inset). Although it did not seem to vary with electrodeposition time (and as such was likely not related to the occurring changes in the electrodeposited MoS$_2$ films), it was also taken into account when fitting the data to equivalent electrochemical circuit models. All of the impedance spectra have an almost entirely capacitive profile in the low-frequency range, but at higher frequencies ($\sim$ 1000 Hz to 100 Hz) the beginning of a small semicircle can be distinguished. As is seen from Bode

plots (**Fig. 12b,c**), a longer deposition time resulted in lower impedance magnitudes, but also a slower phase response. This confirms that the measured EIS spectra reflect the electrocatalytic activity of the MoS_2 films, as the films with the lowest impedances are also the ones that exhibit the best activity in LSV measurements.

The EIS study of MoS_2 films that had been deposited on copper foam substrates was modified – the spectra were registered over increasingly cathodic overpotentials (0 V, -0.1 V, -0.15 V, -0.175 V, -0.2 V, -0.25 V, -0.3 V) to obtain more data (in addition to Tafel analysis) on the kinetics of HER catalysis (**Fig 13**).
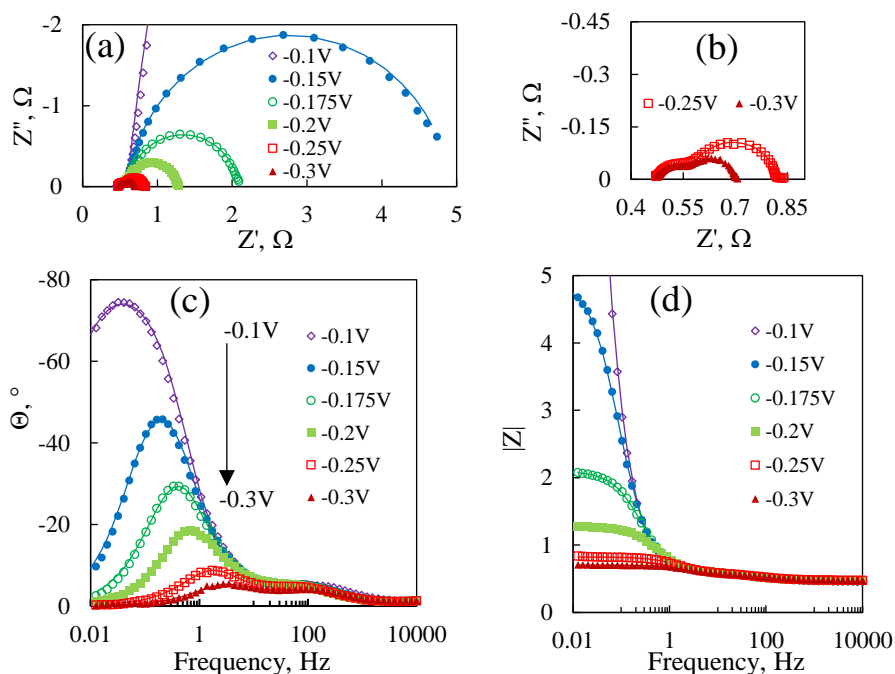

***Fig. 13**. EIS spectra of HER from 0.5 M H_2SO_4 on the electrodeposited MoS_2 film (Q= 10 C): Nyquist plots obtained at various overpotentials (a); spectra, obtained at higher overpotentials (b); Bode plots of respective overpotentials (c,d). Points – experimental data, lines represent fitting to EEC shown in **Fig. 14**.*

The impedance of the system decreases dramatically with the increase of the overpotential, owing to the intensity of HER. Two semicircles become especially pronounced from -0.15 V, when hydrogen evolution begins to occur at an increasing rate (**Fig. 13a**). At higher overpotentials the semicircles become similar in magnitude (**Fig. 13b**). If the spectra were to be registered at even higher overpotentials, only the high-frequency semicircle could be distinguished. The Bode phase plot (**Fig. 13c**) also shows two distinguishable

peaks, with the low-frequency peak shrinking in magnitude when the overpotential is increased – at higher overpotentials the response to perturbation is faster due to the increased rate of HER. Finally, the Bode magnitude plots show that at low overpotentials the system acts in a blocking manner, but as the overpotential reaches -0.3 V the system is almost completely conductive.

These spectra can be interpreted through equivalent electric circuit (EEC) fitting. The circuit used here contains two time constants in the system: τ_{HF} (determined by C_{dl} and R_{ct}) and τ_{LF} (product of C_a and R_a). This EEC, shown in **Fig. 14**, is commonly used to interpret EIS data for electrode processes involving adsorbed intermediate compounds, and it is often applied to model HER in both acidic and alkaline media [144]. To fit the spectra, shown in **Fig. 12**, an inductance element was also added, but it is inconsequential for the parameters of interest and can be omitted from further discussion.
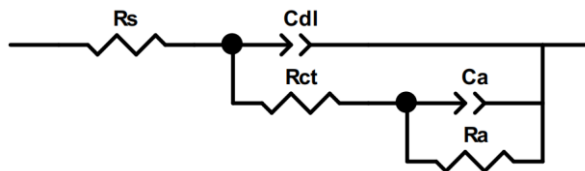

Fig. 14. *Equivalent electrical circuit, used to model impedance data. R_s – solution resistance; C_{dl} – constant phase element related to double layer capacitance; R_{ct} – charge transfer resistance; C_a – polarization capacitance; R_a -polarization resistance;*

Here the double layer capacitance C_{dl} and polarization capacitance C_a are represented by constant phase elements that account the inhomogeneity of the surface. Values of CPE were recalculated into capacitance by *Brug et al*'s formula [145]:

$$C_{dl} = T_{dl}^{\frac{1}{n}} \left(\frac{1}{R_s} + \frac{1}{R_{ct}} \right)^{1-\frac{1}{n}} \tag{26}$$

$$C_a = T_a^{\frac{1}{n}} \left(\frac{1}{R_s + R_{ct}} + \frac{1}{R_a} \right)^{1-\frac{1}{n}} \tag{27}$$

Here T_{dl} and T_a are values of the CPE_{dl} and CPE_a elements respectively.

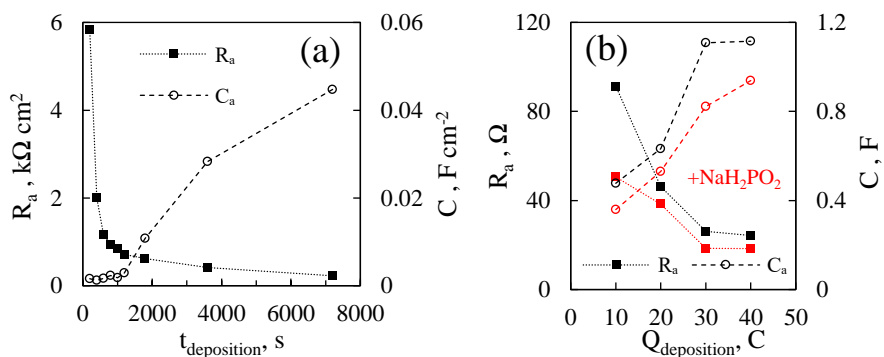After fitting, the parameters were plotted as a function of film formation conditions (**Fig. 15**)

Fig. 15. *EEC-calculated values of C_a and R_a, and their dependence on the electrodeposition time/charge of MoS_2 films: for films on Cu wire substrates (a); for films on Cu foam substrates (b) (red lines represent films that had been electrodeposited with NaH_2PO_2). Data calculated from spectra that were obtained at $\eta = -0.1$ V.*

For films on both substrates, C_a increases with deposition time/charge in a fairly linear manner. The values of C_a are defined by both the roughness of the surface and electric current response to the reversible variations of surface coverage of adsorbate under the electrode potential perturbation during HER. The apparent growth of adsorption capacitance with film deposition time seems to suggest that the longer-deposited films either adsorb more hydrogen (which could reasonably be related to a larger number of active sites), or the coverage is more uniform. Furthermore, for MoS_2 films on copper wire electrodes, C_a follows almost the exact same trend as exchange current density with deposition time (as seen in **Table 6**). When comparing the two different substrates, it can be seen that C_a on foam-deposited MoS_2 are at least 10 times larger (**Fig 15b**). Although the deposition conditions were different, and the films can't be compared directly, the difference in adsorption capacitance is another indication as to the electrocatalytically active surface area of the catalysts for which the geometrical surface are is uncertain.

The adsorption-related resistance R_a follows an exponential extinction curve, and almost plateaus at 226 Ω cm^2 for the longest deposition time film, which could be attributed to the appearance of charge transfer limitations in the growing semiconductor material. However, on foam substrates the drop in R_a is still clear when the deposition charge is increased from 10 C to 40 C. Regarding the effect of NaH_2PO_2 – the adsorption resistance is seen to decrease, which would suggest faster kinetics of HER, but C_a is also lower, and that may correspond to less hydrogen being adsorbed on the catalyst.

Regardless of whether MoS_2 was deposited on a wire electrode, or a metallic foam – the adsorption resistance follows the same relation with deposition charge; R_a decreases in an exponential decay trend (**Fig. 16a**), as

does the overpotential, needed to reach 10 mA of HER current. Although η_{10mA} is a useful parameter when comparing different catalysts, it is qualitative in nature, and it is the result rather than the cause. The inverse of adsorption resistance – R_a^{-1} – should be proportional to the reaction rate, and that is clearly seen in **Fig. 16b**, where R_a^{-1} follows the same trend as the current, measured at the same potential ($i_{\eta=0.1\,V}$). Then it stands to reason all of these trends should be related to some parameter of intrinsic activity of the films, and that is seen by plotting the exchange current i_0, obtained from Tafel analysis, against electrodeposition charge (**Fig 16c,d**). Again, the same relation is observed, and regardless of whether deposition had been carried out on a wire or a foam substrate, i_0 increases with deposition charge/catalyst loading. Coinciding C_a-Q tendencies confirm that this effect is related to the growing number of active sites.
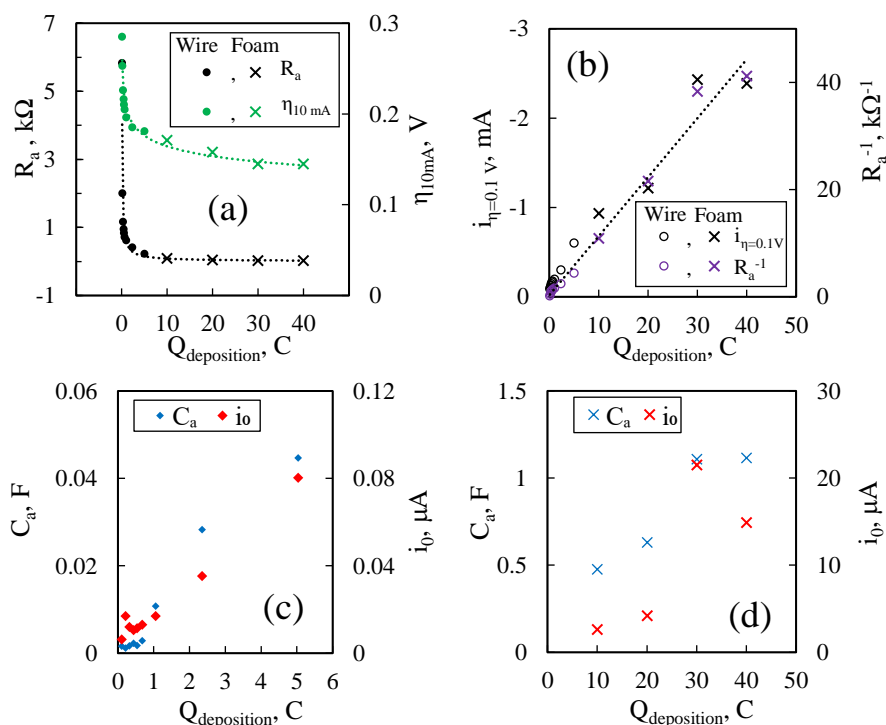

***Fig. 16.** Catalytic parameters of MoS$_2$ films, obtained by passing an increasing amount of charge during electrodeposition: R_a and η_{10mA} dependence (a); current at $\eta = 0.1$ V and R_a^{-1} dependence (b); values of C_a and i_0 as a function of deposition charge as measured on wire (c) and foam (d) electrodes. The data presented here was obtained from Tafel analysis and EIS spectra, measured at -0.1 V vs RHE.*

When the values of R_a were considered as a function of applied overpotential (for the spectra in **Fig. 13**) R_a was observed to decrease exponentially, and was the most significantly affected parameter of the

system. R_a values would decrease by several magnitudes over the measured overpotential range (for example, for a MoS_2 film, deposited for 30 C, a decrease from 26.1 Ω at -0.1 V to 0.09 Ω at -0.3 V is seen). R_a as a function of η begins to plateau at overpotentials larger than -0.2 V, and could conceivably reach a constant value. Also, the MoS_2 films, electrodeposited with NaH_2PO_2, exhibited lower R_a values than those electrodeposited in the base solution.

The electrocatalytically active surface area is not necessarily equal to the electrochemically active surface area, and attempts to normalize HER current density into electrochemically active surface area can skew the desired results. It should be noted, that there is no conventional method for active site calculation yet; research on MoS_2-based HER catalysts usually faces difficulty in finding an appropriate way for number of active site estimation. However, researchers often report the number of active sites per cm^2 to compare their synthesized materials. Therefore, a model to estimate the number of active sites attributed to the specific adsorption of H_{ads} by the application of EIS is discussed.

Firstly, to have a baseline for comparison, a calculation for a theoretical ideal catalytic film with 100% adsorbed hydrogen coverage is performed. From a geometrical point of view, an active site (sulfur vacancy) on the surface of a MoS_2 lattice has a diameter of ~ 0.5 nm [23] . Therefore, a film of 1 cm^2 would then have $5.0 \cdot 10^{14}$ active sites. Assuming complete coverage with a monolayer of H_{ads}, the charge necessary to attain this monolayer would be $\sigma = 0.08$ mC.

For the MoS_2 films, the charge necessary to attain a layer of adsorbed H was calculated from the EIS data, by taking into account only the adsorption capacitance. Values of C_a were recalculated into charge using following equation:

$$Q_a = C_a \cdot \eta \qquad (28)$$

where Q_a is the charge used to obtain a layer of H_{ads} on the MoS_2 film's surface; C_a is the adsorption capacitance; η is the overpotential applied for hydrogen evolution reaction, and at the same time for H_{ads} layer formation (-0.1 V).

It was assumed, that hydrogen adsorption is a one-electron process (**eq. 3**), and the one active site adsorbs a single H^+. Thus, the maximum number of active sites can be calculated from **eq. 29**.

$$N_{sites} = \frac{Q_a \cdot N_A}{nF} \qquad (29)$$

This yields values ranging from 10^{15} to 10^{17} sites cm^{-2}, based on deposition charge. Taking into account the difference between the real surface area and the geometric, these values are considered as being in good agreement with those obtained from geometric parameters as described above. In addition, the values estimated based on C_a data are close to those reported by other researchers working with different methods (e.g. roughness factor/capacitance calculations, anodic oxidation, etc.) to estimate active site densities for amorphous MoS_2 [14,27].

The obtained numbers of active sites were used to calculate turnover frequencies (TOF) in hydrogen molecules evolved per second per site, and to compare all catalysts (**Fig. 17**). The dependencies were recalculated from LSV curve data, and that is why they resemble them. One note that should be kept in mind is that the number of active sites is assumed to be constant throughout the entire potential range, which is almost certainly not the case. In theory, the surface coverage by adsorbed hydrogen approaches $\Theta_H = 1$ at highly negative overpotentials [28], so more active sites may begin to participate in the reaction. TOF is a measure of the intrinsic activity of the material, so from **Fig. 17a** it becomes apparent that the 1000 s deposited film is, in fact, the most active one, because it requires the lowest η to reach a certain TOF.
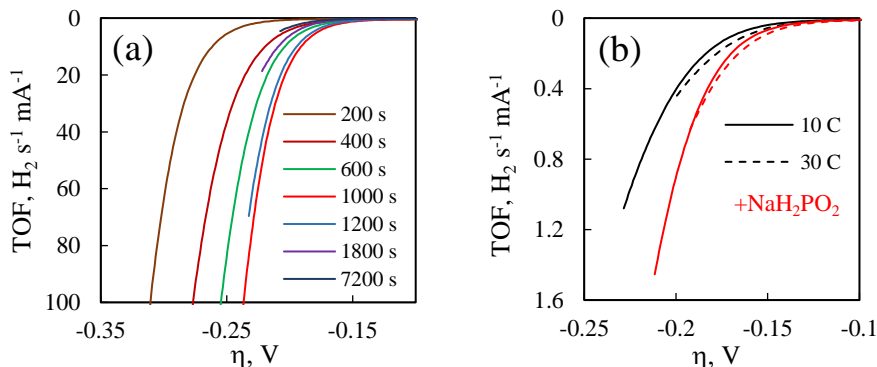

Fig. 17. *TOF per active site as a function of overpotential for the MoS_2 films, tested in this study: deposited on wire substrates (a); deposited on foam substrates with and without NaH_2PO_2 (b).*

It is also evident that, despite their seemingly excellent total activity, due to the large number of active sites the MoS_2 films that had been deposited on foam substrates reach very low TOF values (**Fig. 17b**). Furthermore, the films, deposited with NaH_2PO_2, exhibit better intrinsic activity.

Finally, these findings can again be related to all of the previously discussed data, in order to truly discover the most intrinsically effective film that had been obtained in this study. **Fig. 18** shows the TOF values that had been obtained at one overpotential $\eta = 0.2$ V, as a function of deposition charge. A distinct maximum is revealed at 0.529 C, which is the MoS_2 film deposited on a wire substrate for 1000 seconds. The low-frequency time constant ($\tau_{LF} = C_a \cdot R_a$), which represents how fast the system responds to the potential perturbation at low frequencies, displays an inverse trend. τ_{LF} reaches a minimum of ~1.48 s^{-1} for the same film. The time constant is not directly related to HER kinetics, but it is proportional. A low value means that the response to perturbation happens faster, and if the response is related to hydrogen adsorption and desorption, it must mean that this process also occurs at a faster rate. Thus, the MoS_2 film, that had been deposited on copper wire for 1000 s is conclusively the most intrinsically active in this study. It is interesting to note that the tendencies of TOF and τ_{LF} with amount of charge passed during electrodeposition are again seen to continue across both wire and metallic foam substrates.
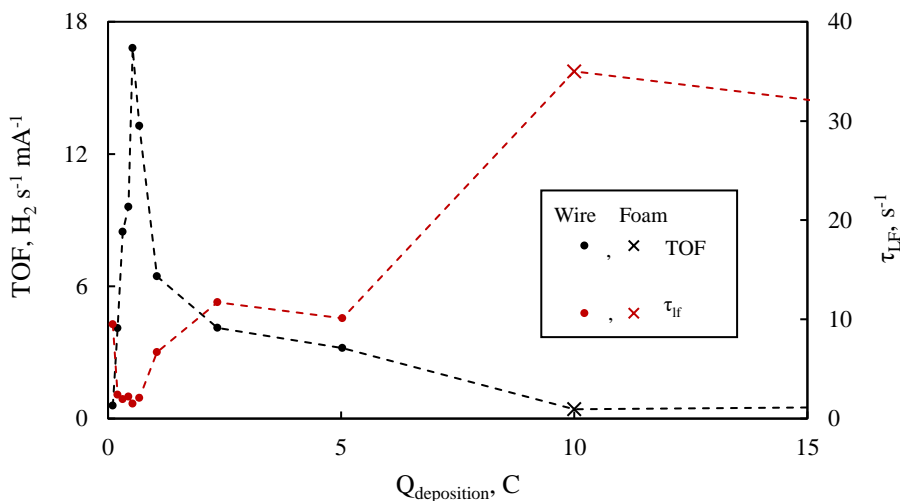

Fig. 18. TOF and τ_{LF} values as a function of deposition charge.

To conclude the study on HER catalysis by electrodeposited MoS_2 films, it is apparent that in terms of intrinsic catalytic activity there is an optimal deposition amount. However, in terms of total electrode activity, the higher catalyst loading films (-1.0 V for 7200 s on Cu wire, and the 10 C to 40 C foam electrodes) are still more effective. Further optimization of such catalysts should probably focus on cost/efficiency calculations.

3.2 WO₃ films, formed by anodization, and their photocatalytic properties

3.2.1 Investigation of WO₃ film growth

In order to compare the formation of WO_3 in different electrolytes, LSV curves on metallic tungsten electrodes were recorded in the following solutions: 1 M H_2SO_4; 1M HCl; 14 M H_3PO_4; 14 M H_3PO_4 + 1 M NH_4F, and 0.3 M oxalic acid. The obtained anodic polarization curves are shown in **Fig. 19**. The shape of the curves is similar: a broad peak, comprised from 3 more or less well-distinguished oxidation peaks, is followed by a wide passivation-dissolution plateau that extends at least up to 5 V. The oxidation peaks are the largest in 0.3 M oxalic acid and the sulfate-fluoride-hypophosphite electrolytes (**Fig. 19a**), reaching a maximum current of over 2 mA cm^{-2}. The plateau current j_{pl} is also the largest at 1.08 mA cm^{-2} – over 10 times higher than in the remaining electrolytes. The oxidative peaks completely merge into one in 85% H_3PO_4, but with the addition of NH_4F a peak at 0.78 V emerges. In the presence of ammonium fluoride oxide dissolution is facilitated by the formation of fluoride complexes with W(VI) as in **eqs. 11 and 12**. Thus, the peak current density increases slightly. Despite the interesting behavior of these peaks, under potentiostatic conditions it can be assumed that the plateau current is best representative of equilibrium conditions. Therefore, it is apparent that 0.3 M oxalic acid facilitates the dissolution of tungsten and formation of WO_3 (as per **eqs. 7-9**) at the highest rate. For that reason, films deposited in this electrolyte were selected for further analysis.
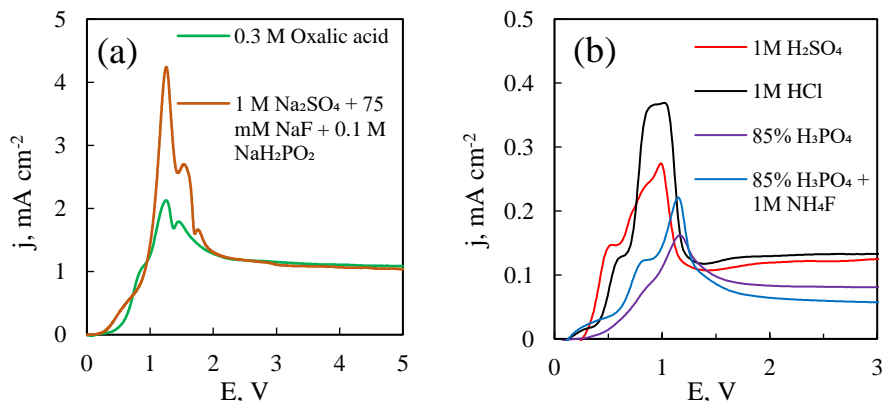

***Fig. 19.** Anodic linear sweep voltammetry scans of tungsten in various anodizing electrolytes: LSV curves in 0.3 M oxalic acid and 1 M Na₂SO₄ + 75 mM NaF + 0.1 M NaH₂PO₂ (a); LSV curves in sulfuric, hydrochloric, and phosphoric acid electrolytes (b). Scan rate – 10 mV s⁻¹.*

Another method used to investigate WO_3 film formation in was anodic electrochemical impedance spectroscopy. The experiments were carried out as described in section 2.3.2 – the film was kept at a constant potential (0.1 V to 5.0 V) for 10 minutes, after which an impedance spectrum was registered. Because the experiment was started on a fresh W electrode no WO_3 had existed on the surface prior. The measured spectra reflect not only the capacitance of a barrier oxide layer, but also effects related to WO_3 film formation. Two experimental series (obtained in 0.3 M oxalic acid and *1 M Na2SO4 + 75 mM NaF with hypophosphite*) are presented in **Fig. 20**. The impedance magnitude increases with applied potential owing to the formation of a semiconducting oxide film. But perhaps the most intriguing feature of these spectra is the intermediate to low frequency inductive loop.
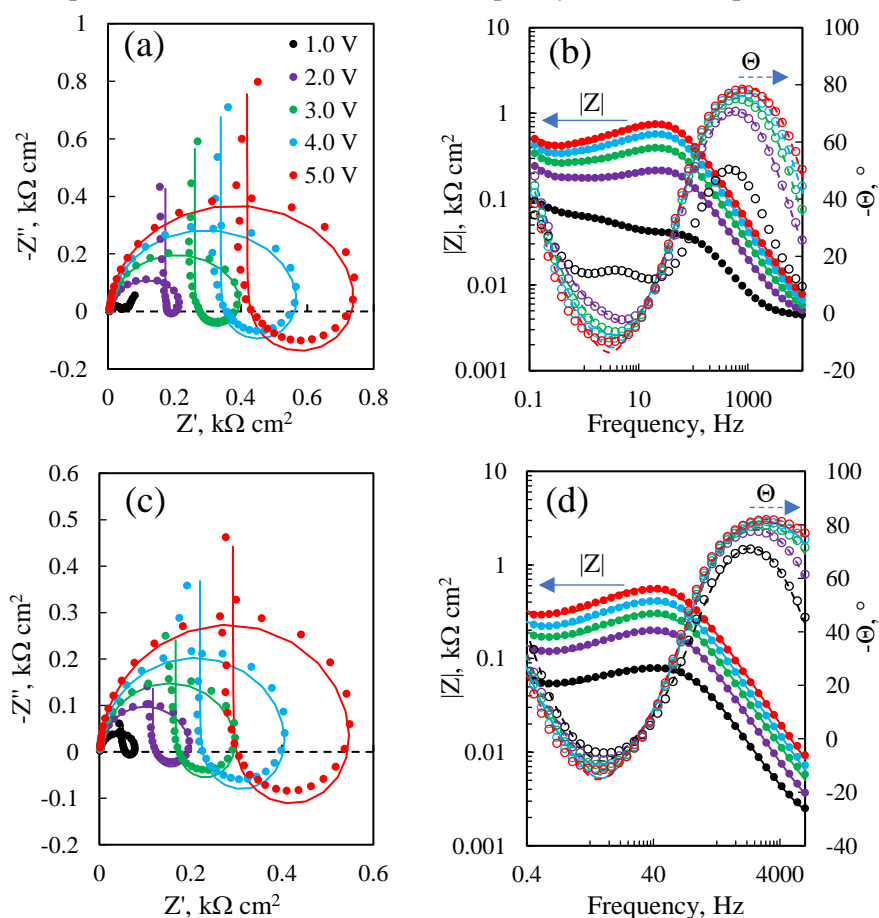

Fig. 20. *Nyquist and Bode plots obtained for tungsten anodization under various anodic potentials in electrolytes: 0.3 M oxalic acid (a,b); 1M Na2SO4 + 75 mM Na4F + 0.1 M Na2H2PO2 (c,d). Points are experimental data and solid lines are data fitted to the equivalent circuits presented in **Fig 21**.*

The entire spectrum is characterized by a capacitive time constant at high frequencies, an intermediate-frequency inductive time constant, and again capacitive behavior at low frequencies. The cause of the inductive loop lies within the mechanism of oxide film growth (the point defect model, briefly discussed in section 1.2.1). In essence, oxygen vacancies are generated at the metal/film interface and are transferred through the film, where they react with adsorbed water at the film/solution interface thus forming oxide. In oxide films oxygen vacancies are considered to be the main charge carriers. Similarly, metal vacancies are produced at the film/solution interface (by dissolution of WO_3), and are transported back toward the metal/film boundary. Accumulation of metal vacancies at the film/solution interface then accelerates the transport of oxygen vacancies, which have an opposite charge. This is what causes the pseudo-inductive behavior [146].

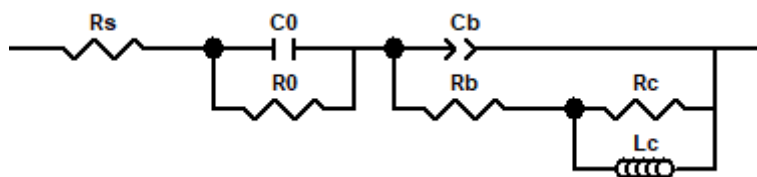These spectra were fitted to the model shown in **Fig. 21**.

Fig. 21. *Equivalent electric circuit, used to fit anodization EIS spectra.*

where R_s represents the electrolyte resistance, C_0 is faradaic pseudo-capacitance. R_0 is the resistance related to the pseudo-capacitor. C_b is the constant phase element, ascribed to the barrier (oxide) layer capacitance. R_b is a charge transfer resistance (resistance of defect/oxygen vacancy migration). R_c and L_c are the resistive and inductive elements, associated to the negative surface charge buildup at the film/solution interface.

The values of these discrete elements were plotted as a function of applied potential, which will be referred to as formation potential E_f here. CPE values were recalculated into capacitance again by **eqs. 26 and 27**. The plots are shown in **Fig. 22**. The linearity of the trends is immediately apparent in all graphs, which confirms that film growth depends linearly on applied potential, i.e., the strength of the applied electric field. The values of C_b are plotted as an inverse; this is because the oxide film can be imagined to work as a parallel plate capacitor. Then the film's thickness will be inversely related to its capacitance. Indeed, in **Fig. 22a** this relation is seen, and it can be presumed to continue past 5 V (which was the limit of the potentiostat). Because C_b^{-1} is proportional to the thickness of the oxide film, two observations can be made: although in both electrolytes linearity is observed, the barrier layers in 1 M Na_2SO_4 + 75 mM NaF are thicker than in 0.3 M oxalic acid, and the slope of

the linear trend is larger, meaning that thicker films could feasibly be obtained at the same potential. Furthermore, these considerations about film growth are confirmed by the larger charge transfer resistance R_b of films in oxalic acid (**Fig. 22b**). If R_b is thought of as resistance of the oxygen vacancy migration, then larger values correspond to impeded migration, which ultimately results in slower rate of film growth. Lastly, the parameters R_c and L, related to surface charging, also display linearity with formation potential (**Fig. 22c,d**). Their precise meaning is difficult to interpret, but it is interesting to note that the films produced in oxalic acid display significantly more inductivity.
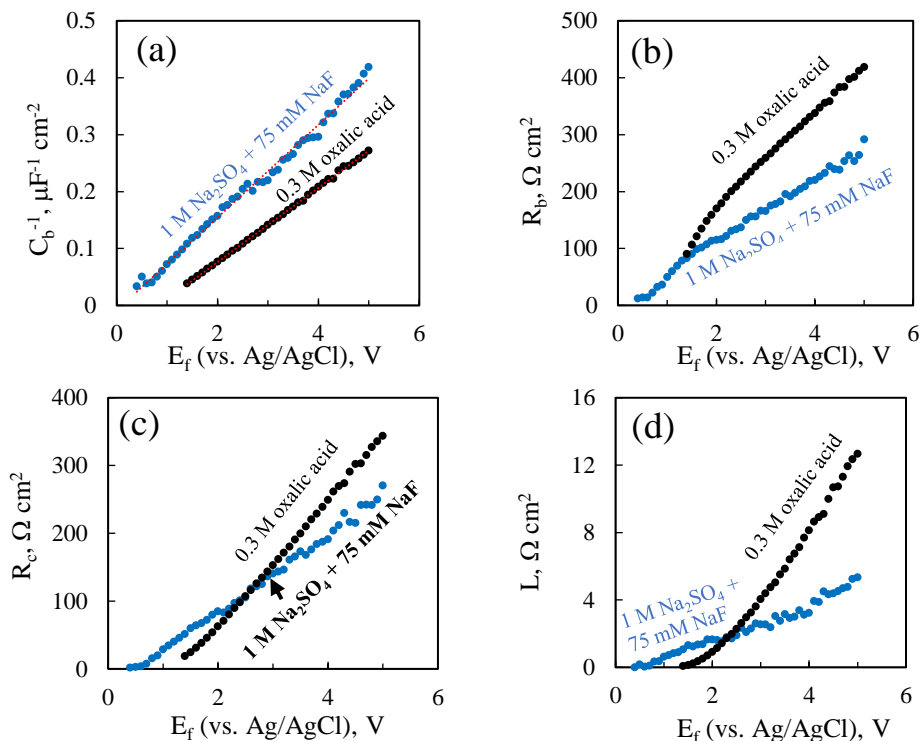

Fig. 22. *EIS fitting data as a function of formation potential in two electrolytes 0.3 M oxalic acid and 1 M Na₂SO₄ + 75 mM NaF: inverse barrier layer capacitance (a); barrier layer resistance (b); surface charge buildup related resistance (c); surface charge buildup related inductance (d).*

This type of EIS characterization was carried out in all the mentioned electrolytes, but only the discussed two (0.3 M oxalic acid and 1 M Na₂SO₄ + 75 mM NaF) were used for formation of thick WO₃ films. As it can be inferred from the anodization current densities in **Fig. 19**, dissolution of W and formation of WO₃ occurs at a much slower rate in the remaining electrolytes, and the EIS spectra reflect that.

3.2.2 Synthesis of WO₃ films by potentiostatic anodization in 0.3 M oxalic acid

WO$_3$ films had been obtained after anodization in 0.3 M oxalic acid for 30 minutes at voltages ranging from 20 V to 60 V. As can be seen in the potentiodynamic anodization curve in **Fig. 23a**, at relatively small voltages current density rises steadily until a peak (of approx. 1 mA cm^{-2}) is reached at ~ 11 V, after which the current density decreases slightly and more or less plateaus at higher voltages. The voltage in this curve was raised by increments of 0.5 V every 30 seconds, so the current density value is a reasonable representation of the steady-state current at potentiostatic conditions. The surface morphologies of the obtained films at different voltages are presented in **Fig 23b-d**.
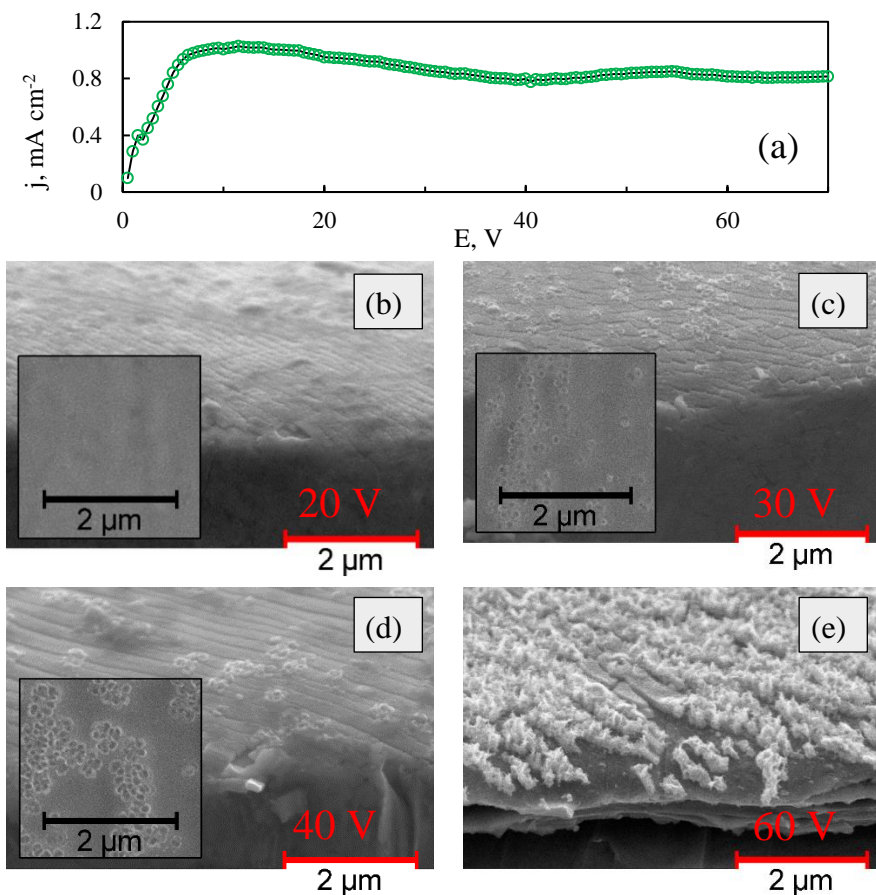

Fig. 23. *Potentiodynamic anodization curve (a) and SEM surface morphology of films that had been obtained after 30 min. of anodization in 0.3 M oxalic acid at: 20 V (b); 30 V (c); 40 V (d); 50 V (e). Insets show top-down view.*

After anodization at 20 V only a very compact film that replicates the surface morphology of the substrate is formed, and the surface has no distinct

features. Anodization at 30 V, however, yields a film that already appears rougher, more etched, and nucleation of pores becomes visible. This trend then continues, as the film that was obtained after anodization at 40 V shows even more pore nucleation. And finally, a very etched morphology forms after anodization at 60 V.

Finally, it was experimentally proven that film thickness does increase linearly with applied potential (**Fig. 24**). The experimental data was obtained by approximating film thickness from their cross-section SEM images. Overall, the films are fairly thin, and range from ~ 40 nm (obtained after anodizing at 20 V) to 116 nm (obtained after anodizing at 60 V). Moreover, this linearity agrees well with theory as discussed in chapter 1.2.1, and an anodization constant of 1.87 nm V^{-1} can be calculated.

In **Fig. 24** the dashed line relates to EIS calculations that were presented in **Fig. 22a** by assuming that the barrier layer capacitance is proportional to film thickness as per the parallel plate capacitor equation. Here C_b values were recalculated into film thickness (using relative permittivity $\varepsilon = 33.3$ that was obtained from the experimentally determined anodization constant), and the trend that had been calculated from 0 V to 5 V was extrapolated to high voltages. The fit was found to be reasonable, although with a slight underapproximation of film thickness. Even though C_b data was obtained only for low potentials (when the film would likely be of single nanometer dimensions) extrapolation demonstrably predicts the average thickness of films that are formed by anodizing at high voltages. One drawback of this analysis is that the relative permittivity must already be known, and it is known to vary with anodization conditions such as electrolyte.
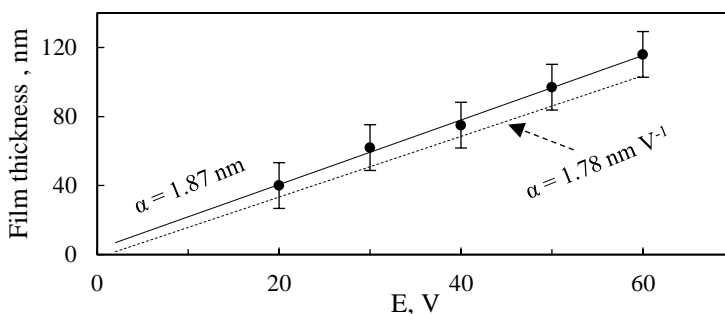

Fig. 24. *Film thickness as a function of anodizing potential in 0.3 M oxalic acid. Points are experimental data. Solid line is calculated using α = 1.87 nm V^{-1}, and dashed line is calculated from barrier layer capacitance data.*

3.2.3 Synthesis of thick WO₃ films by anodization in a Na₂SO₄ + NaF electrolyte

Thick WO_3 films were formed by galvanostatic anodization in a slightly basic (pH ~ 8) 1 M Na_2SO_4 + 75 mM NaF (with 0.1 M NaH_2PO_2) electrolyte. A current density of 25 mA cm⁻² was applied, and the solution was agitated by magnetic stirring to faster remove oxygen bubbles from the growing film. **Fig. 25a** presents a typical anodization curve, obtained under these conditions. It can be seen that over the first minute the voltage grows from near zero to 72 V, which corresponds to the growth of a compact oxide film. A very indistinct maximum of 79 V is reached after 4.5 minutes, after which the voltage very slowly decreases to ~ 74 V near the 30-minute mark. This behavior is typical (as discussed in section 1.2.1), and is caused by the competition between electric-field-induced film formation, and chemical dissolution.
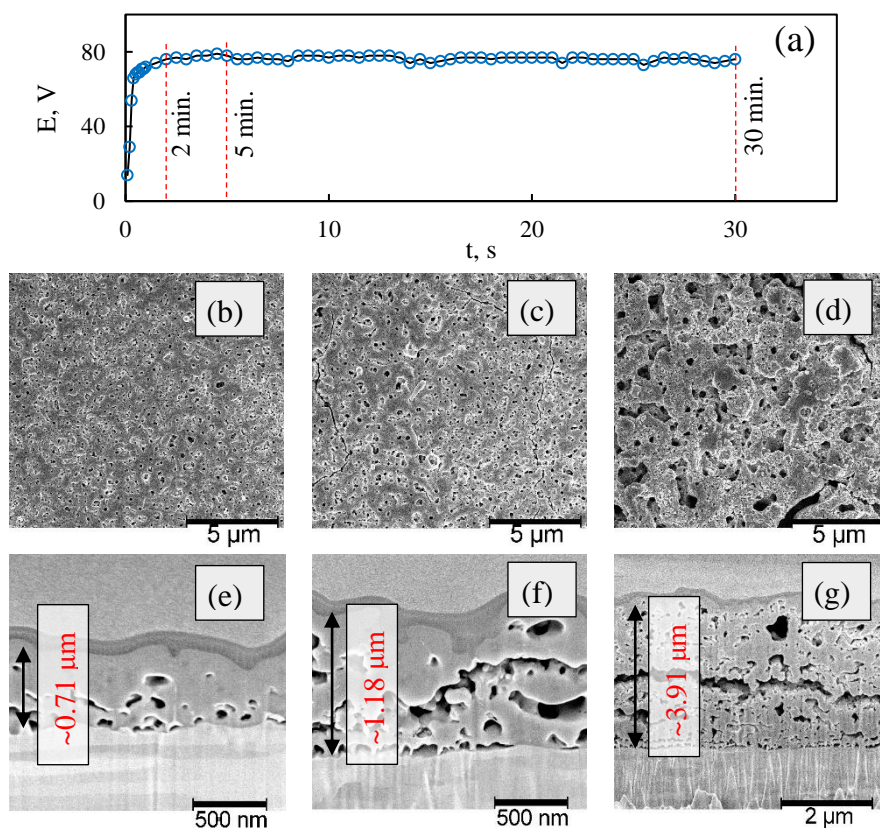

Fig. 25. *Anodization curve (a) and SEM surface morphology and FIB cross-section images of WO₃ films that had been obtained after anodization for: 2 min. (b, e), 5 min. (c, f), 30 min. (d, g). Galvanostatic conditions – 25 mA cm⁻².*

The films have a porous surface morphology, with pore diameters reaching up to several hundred nm. Little difference is seen between the films that had been obtained after anodization for 2 and 5 minutes (**Fig. 25 b,c**), but a very rough and disordered surface structure evolves after anodizing for 30 minutes (**Fig. 25d**). Cross-sectional images reveal that the porous structure extends throughout the film's structure and all the way to the substrate metal (**Fig. 25e,f,g**). The film, obtained after 2 minutes, is relatively compact, while the film that was obtained after 30 minutes is highly porous; here the pores tend to form large, empty horizontal channels rather than grow vertically. Moreover, the average thickness of the investigated samples was found to linearly depend on anodization time, although rather large deviations of thickness can be seen on different parts of the film.

XPS experiments reveal that the as-anodized film is almost entirely WO_3 with a small amount of W(V) oxide: W(VI)- 96.9 %, W(V) - 3.1% (**Fig. 26**). Two clear peaks at 38.1 eV and 35.9 eV are seen, and they deconvolute into two doublets of W(VI) ($4f_{5/2} \sim 37.8$ eV, $4f_{7/2} \sim 35.7$ eV [131,147,148]) and W(V) ($4f_{5/2}$ 37.25 eV, $4f_{7/2}$ 35.15 eV [114,149]). Regarding the W(V) signal – it is possible for W(V) to exist in the structure as a residual intermediate W_2O_5 left after anodization, but more likely this signal occurs due to the appearance of defect sites – oxygen-deficient W within the crystal lattice [150]. Moreover, in the O1s spectrum (**Fig. 26b**) the peak at 531 eV deconvolutes into three binding states that have been attributed to O-W bonds (530.8 eV), O-vacancies (531.4 eV), and O-OH bonds (532.4 eV) [109,151,152].
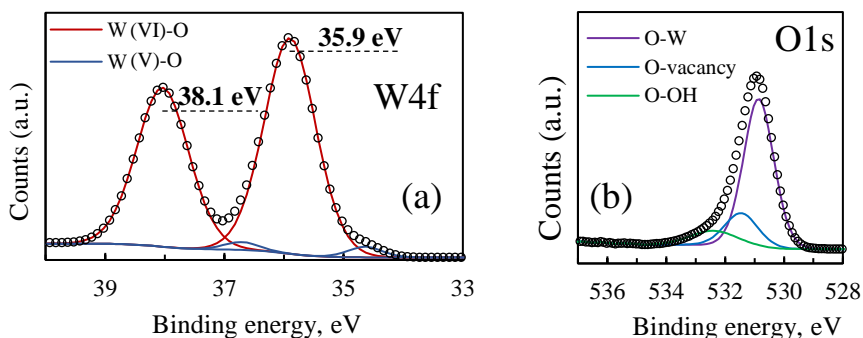

Fig. 26. *XPS W4f (a) and O1s (b) spectra of a WO₃ film, that was obtained after 5 minutes of anodization.*

3.2.4   Synthesis of WO₃ + MoSₓ composites by galvanostatic anodization

In order to form composite films that are comprised from WO_3 and MoS_x a 25 mM MoS_4^{2-} solution was prepared, and 1 M Na_2SO_4, 75 mM NaF, 0.1 M NaH_2PO_2 were added to it. As per **eq. 2**, anodic deposition of MoS_3 can occur

from MoS_4^{2-} ions. Then, two processes that determine the formation of a composite film take place at anodic potentials – the growth of a WO_3 film, and simultaneous anodic deposition of MoS_x. From the anodization curve (**Fig. 27a**) a similar behavior as previously is seen: the voltage peaks after 2.5 minutes (74 V), and drops more substantially to 63 V after 30 minutes. Again, the surface morphologies of the films that had been obtained by anodizing for 2 and 5 minutes are porous, and an even more disordered structure is observed for the film with the longest (30 minute) formation time (**Fig. 27b-d**). The overall lower anodization voltages are also reflected in the thicknesses of the films (**Fig. 27e-g**), which are 0.3 – 0.4 µm smaller than for their respective WO_3 films. Apart from causing the formation of large, globular macrostructures after long anodization times, the presence of MoS_4^{2-} in the anodization solution does not seem to have any effect on the porosity of the films.
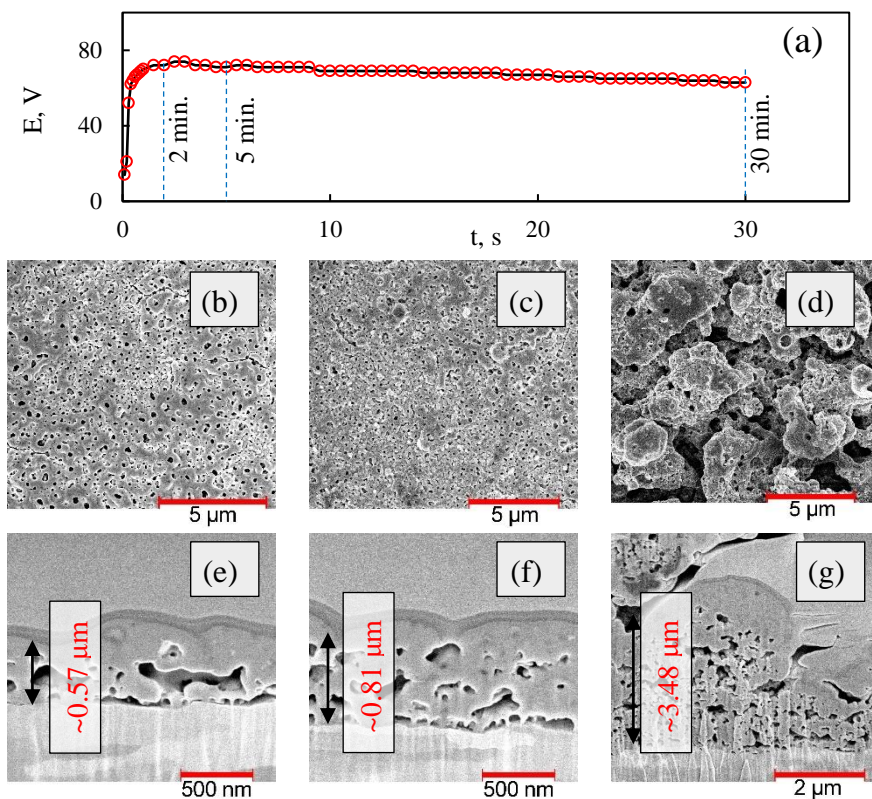

Fig. 27. Anodization curve (a) and SEM surface morphology and FIB cross-section images of WO_3+MoS_x films that had been obtained after anodization for: 2 min. (b, e), 5 min. (c, f), 30 min. (d, g). Galvanostatic conditions – 25 mA cm^{-2}.

EDX experiments showed that the amount of Mo and S in atomic % increased with anodization time, and reached 2.0 at % of Mo and 4.1 at % of

S after a 30 minute anodization. Overall, the molybdenum sulfide had deposited in non-stoichiometric ratios: $MoS_{0.4}$ (2 min.), $MoS_{0.5}$ (5 min.), and $MoS_{1.2}$ (30 min.). This large deviation from the expected MoS_3 stoichiometry is likely caused by the immediate oxidation of the MoS_3 material after its deposition. EDX mapping was also used to investigate both cross-sectional and surface composition variations. For the films that had been obtained after anodization for 2 and 5 minutes no clear MoS_x structures could be discerned. However, after 30 minutes of anodization a very rough, macrostructured surface morphology is evolved, and MoS_x clusters were observed within it. It seems that MoS_x is not dispersed throughout the depth of the film, but instead forms globules near the film's surface (**Fig. 28a**). Whereas, if it is dispersed, EDX mapping is not sensitive enough to observe these structures. Furthermore, the tendency of MoS_x to deposit in clusters is also seen from the surface morphology (**Fig. 29a**), where large Mo and S containing structures have formed at the film-solution interface. These observations lead to the conclusion that most MoS_x exists on the film's surface. This is not unexpected, because MoS_4^{2-} ions likely cannot permeate deeper into the film through its pores, and therefore they can only electrochemically interact with the surface that is readily exposed to the electrolyte.
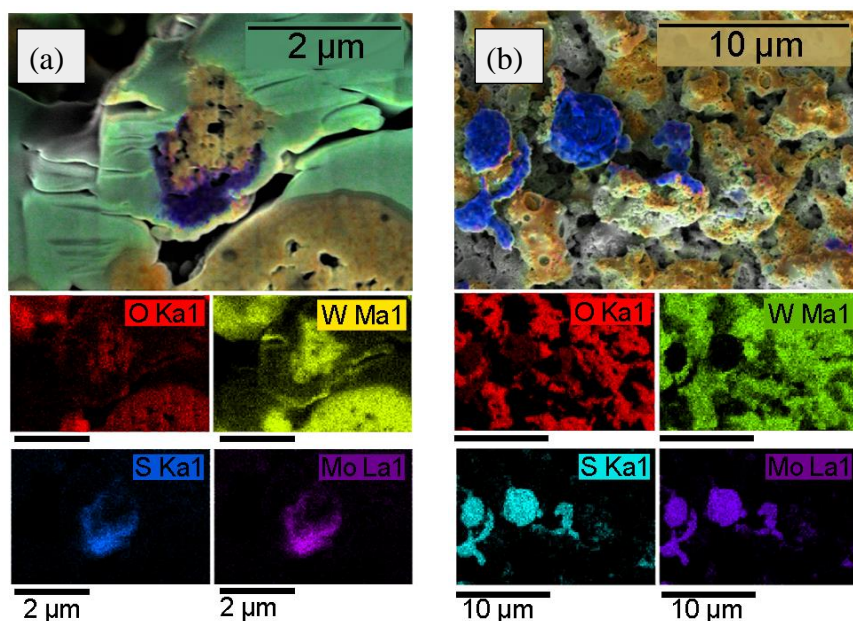

Fig. 28. *EDX mapping of a WO₃ + MoSₓ film that was formed by anodizing for 30 minutes: cross-sectional map (a), and surface morphology map (b).*

Lastly, the successful formation of a composite material was confirmed by XPS analysis. Although no MoS_x could be observed by SEM and EDX for a 5-min-WO_3+MoS_x film, the core-level Mo3d XPS spectrum (**Fig. 29a**). displayed the same characteristic peaks that had been observed for cathodically deposited MoS_2. As previously (chapter 3.1.2), the Mo3d region deconvolutes into several doublets that are related to: Mo(VI)-O bonds ($3d_{5/2}$ 232.7 eV; $3d_{3/2}$ 235.7 eV), Mo(IV)-S bonds ($3d_{5/2}$ 229.3 eV; $3d_{3/2}$ 232.1 eV), and a Mo(V) signal, which may be related to a heptavalent oxide, but also sulfur-deficient Mo/active sites ($3d_{5/2}$ 230.9 eV; $3d_{3/2}$ 234.2 eV). Interestingly, here the S2p core-level spectra deconvolute into two clear doublets, the existence of which can be attributed to terminal (S-term. $S2p_{3/2}$ 161.8 eV; $Sp_{1/2}$ 163.0 eV) and bridging (S-br. $S2p_{3/2}$ 163.2 eV; $S2p_{1/2}$ 164.2 eV) S bonds within the material [137]. Unlike for cathodically deposited MoS_2 (see **Fig. 9**), a very strong signal of the bridging sulfide bond component is seen. This observation implies a somewhat different structure of MoS_x that had been deposited anodically. Similar behaviors were reported in literature [14]. This may also have a pronounced effect on the material's use as a HER electrocatalyst – terminal sulfur bonds tend to break during hydrogen evolution, leaving a sulfur-deficient Mo/an active site. A molybdenum sulfide structure comprised mostly of bridging bonds may be less susceptible to corrosion, but also less electrocatalytically active.
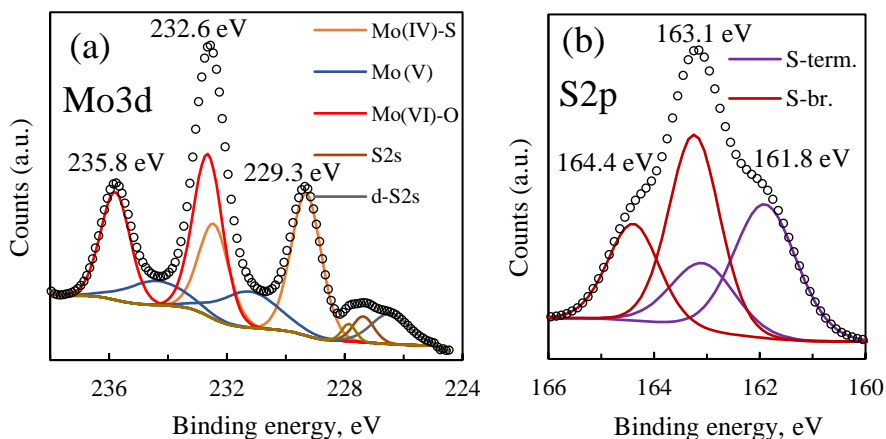

Fig. 29. Mo3d (a) and S2p (b) XPS spectra of a 5-min-WO_3-MoS_x film.

Regardless of the discussion above, the application of these films for HER catalysis was not investigated. The W4f core-level spectra of this film showed that the material is almost entirely W^{6+} oxide (99.52%), with a very small W^{5+} signal (0.48 %).

3.2.5   Modifying WO3 films by cathodic reduction and activation

As discussed in chapter 1.2.3 cathodic reduction of WO_3 in acidic media (also called intercalation of H^+) results in the formation of a tungsten bronze H_xWO_3, which has been shown to have beneficial properties for the material's semiconductor properties, including photocatalytic activity. Therefore, the WO_3 films that had been obtained in this study were also modified by applying a cathodic reduction step in-situ, before photoelectrochemical characterization. After some experimentation to find the optimal reduction conditions, it was decided to apply a potential of -0.5 V (where hydrogen evolution does not occur at a significant rate) for 300 seconds. The reduction curves for 2-min., 5-min., and 30 min. WO_3 films are shown in **Fig 30a**, and are characterized by a swift decrease of current from its initial value until a near-steady-state after 300 seconds. The differences in current densities for the films correlate well to their thicknesses, and are likely related to the film's conductivities, with the thinnest film reaching the lowest reductive currents.
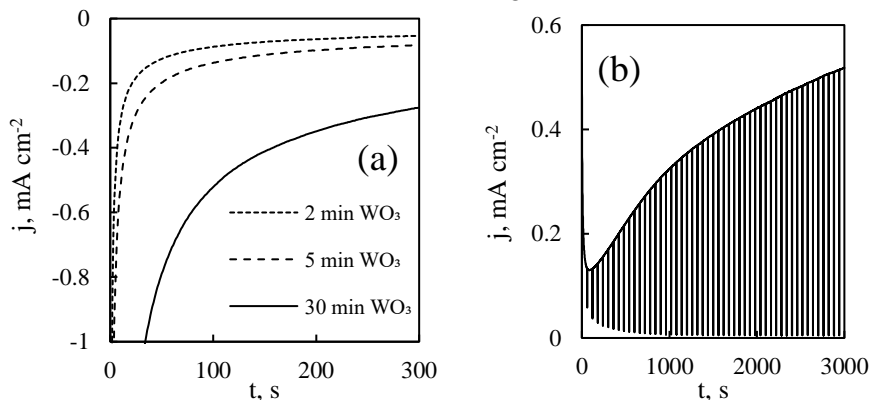

Fig. 30. *Reduction curves of WO₃ films, obtained by anodizing for different times (a) and activation curve of a 5-min-r-WO₃ film (b).*

Furthermore, it was noticed that freshly-reduced films generate relatively small photocurrents, which increase rapidly when the film is held illuminated under potentiostatic conditions. In order to find steady-state photocurrent conditions, an „activation" step was elaborated: the freshly-reduced film was held under intermittent UV illumination (60 s on, 2 s off; $I_0 = 50$ mW cm^{-2}) until the photocurrent would begin to plateau, which commonly occurred after ~ 3000 seconds. **Fig 30b** shows a typical activation curve. The short UV-off pulses give information on background Faradaic processes, and reasonably represent the dark current. As the measurement begins the dark current starts off at ~ 60 µA cm^{-2} and drops to fewer than 10 µA cm^{-2} after 1000 seconds. In contrast, j_{ph} (which is assumed to be the difference between the UV off and

UV on pulses) increases from ~0.12 mA cm^{-2} to 0.5 mA cm^{-2}. It is then a demonstrable fact that the increase in photocurrent during activation of reduced WO$_3$ films can be attributed to effects that are caused by changes within the semiconductor's structure or morphology, and not background processes such as reoxidation.

No changes in surface morphology were observed after reduction. This effect was further investigated by XPS analysis of freshly-reduced and reduced-and-activated WO$_3$ films. After reduction the signal of W(V) grows substantially (**Fig. 31a**). 18.27 % of the peak area can now be attributed to W(V) bonds and the signal of W(VI) decreases correspondingly (**Table 7**). Analysis of the respective O1s spectrum reveals a drop in O-W bonds (from 72.11 % before reduction to 55.42% after), and a double increase of the O-vacancy bond signal. Also, the O-OH signal had decreased, suggesting that the intercalated protons interact with W rather than O in the material's crystal lattice. It has been suggested that electrochemical reduction of WO$_3$ results in the formation of tungsten bronzes with an approximate stoichiometry of H$_x$WO$_3$, and the results of this measurement agree with that.
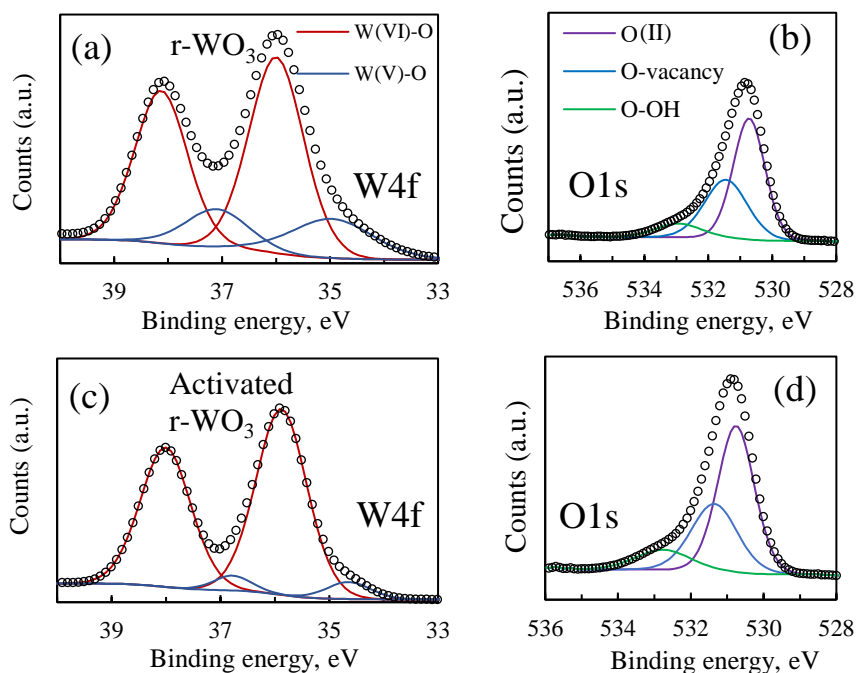

Fig. 31. *XPS spectra and fitted peaks of a WO$_3$ film formed by anodization for 5 min.: after reduction at -0.5 V for 300 s (a, b); after reduction and activation at 1.2 V, I$_0$ = 50 mW cm^{-2}, 3000 s. (c, d).*

Fig. 31c shows the W4f spectrum of an activated r-WO$_3$ film: it appears as an intermediate between plain WO$_3$ and fresh r-WO$_3$. The signal of W(V) had decreased, but the integrated peak area was still 7.13% - over two times larger than for the WO$_3$ film. However, although the amount of W(VI) had returned to near-initial levels, the O-vacancy signal remained elevated even after activation. This correlation between structure and photoactivity may be related to the emergence of an optimal amount of W(V) sites/oxygen vacancies. Too few vacancies (e.g., for plain WO$_3$) reduce the effect of them acting as electron donor dopants overall, resulting in poorer photoexcitation of charge carriers. Too many vacancies (as for fresh r-WO$_3$) act as electron traps, and promote recombination of photogenerated charge carriers.

Table 7. *Ratios of W and O bonds in as-anodized and modified WO$_3$ films, obtained from integration of XPS peak areas.*

Film	W4f		O1s		
	W(VI), %	W(V), %	O-W, %	O-vacancy, %	O-OH, %
5-min-WO$_3$	96.87	3.13	72.11	17.41	10.48
5-min-r-WO$_3$	77.07	22.93	55.42	35.77	8.81
Activated 5-min-r-WO$_3$	92.76	7.24	56.37	32.36	11.26

Then the mechanism of activation may be such: when a fresh r-WO$_3$ film is illuminated, photogeneration and transfer of charge carriers begins. Recombination inevitably occurs due to the increased number of W(V) trap sites, and the observed j_{ph} is relatively small. Over time, as this process proceeds, non-reversible recombination results in the decrease of the number of trap sites – this results in a larger j_{ph}, and corresponds to a weaker W^{5+} signal in the XPS spectrum of an activated film. Therefore, electrochemical reduction, followed by activation, can possibly be used to quite accurately tune the number of vacancies in WO$_3$ films.

3.2.6 Photocatalytic properties of WO$_3$ films

Preliminary studies on WO$_3$ prepared by anodizing in oxalic acid.

For characterization of photocatalytic activity, WO$_3$ films were obtained by anodizing potentiostatically in 0.3 M oxalic acid for 30 minutes. LSV and CA experiments were carried out with chopped on/off light pulses in order to get information about several important parameters of a photoanode. LSV scans were obtained in the 1.0 V – 2.0 V range (**Fig. 32a**), and reveal that

photocurrents increase with applied potential. As per the **eqs. 13 and 14**, this is directly related to the expanding space charge layer, and consequent increased generation/concentration of photoexcited charge carriers. Regarding anodization conditions, it is evident that the film that had been obtained by anodizing at 60 V generates by far the largest photocurrent. This may broadly relate to the film's thickness, but interestingly the film had had been obtained at 40 V generates an exceptionally small photocurrent. This must mean that the films' photocatalytic activities depend not only on their thickness, but also structure and morphology (as seen in **Fig. 23**).
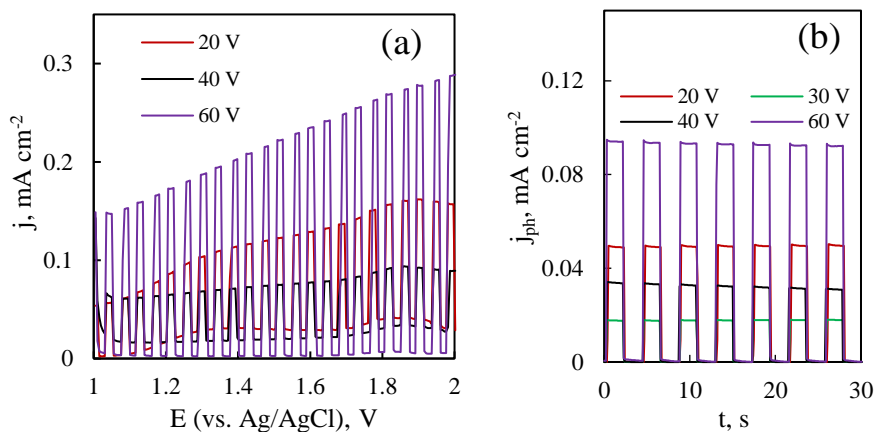

Fig. 32. *Chopped-UV LSV (a) and chronoamperometric (b) curves of films, obtained by anodization in oxalic acid at different voltages. Measured in 0.5 M Na_2SO_4. LSV Scan rate 10 mV s^{-1}, CA potential 1.0 V. $I_0 = 80$ mW cm^{-2}.*

Identical trends in terms of anodization conditions and photocatalytic activity are observed in potentiostatic light pulses (**Fig. 32b**). The largest photocurrent is generated by the film that had been obtained at 60 V (~ 0.094 mA cm^{-2}), which is also the thickest film with the roughest surface morphology. A photocurrent of ~ 0.05 mA cm^{-2} is generated by the film that was formed at 20 V – one that had a relatively compact structure and smooth morphology. It then follows that either compact or extensively porous films are best used as photoanodes, whereas intermediate structures have defects that impede their photoactivity.

Moreover, these films exhibit little to no surface recombination (difference between $j_{t=0}$ and j_{ss}), which means that all of the photogenerated holes are transferred into the electrolyte to drive the photocatalytic reaction. Despite the small photocurrents they generate, this is a very positive characteristic for photoanodes.

Photocatalytic properties of WO₃, r-WO₃, and WO₃ + MoSₓ films.

As previously, LSV with a chopped on/off UV illumination pulse was initially performed. The potential was scanned from 0.4 V up to a cut-off condition of 2 V at 2 mV s⁻¹ (**Fig. 33a,c,e**). At the onset near OCP only a small photocurrent (j_{ph}) up to ~ 10 μA cm⁻² was observed for all films, but afterwards j_{ph} rapidly grew with increasing applied potential. Here the background current was not corrected for, but it was so minimal that the entire measured current was attributed to photocurrent. This relation between $j_{ph} - E$ is expected, because as the strength of the electric field is increased, the space-charge layer within the semiconductor also expands, which allows more photogenerated charge carriers to participate in the circuit.

The j_{ph} may be expected to plateau when either: (a) the space charge layer becomes of similar dimension as the penetration depth of incident light, or (b) diffusion limitations begin hindering charge transfer. This phenomenon does not occur at least until 2.0 V showing that the films have a rather large operating potential range. LSV measurements demonstrate that thinner (2min- and 5 min-WO₃) films generate the strongest photocurrents. In contrast, the longest anodization time (thickest film) yields a photoanode with very poor photocatalytic properties (**Fig. 33a,c,e red lines**).The highly disordered structure of thicker films is not conducive to efficient charge transfer, and this reflects in the near-zero photocatalytic activity of this film. Namely, 2min-WO₃ produces a maximum j_{ph} = *0.46 mA cm⁻²*, whereas 30min-WO₃ has a maximum j_{ph} = *0.045 mA cm⁻²*. Intermediate anodization times (10, 20 minutes) resulted in films which fell within the same decreasing activity trend.

An inverse effect was observed for r-WO₃ films (**Fig. 33a,c,e blue lines**). Note, that the r-WO₃ LSV curves shown here were registered after an activation step as described in **chapter 3.2.5**. Although the overall highest photocurrent was generated by the film obtained after 5 minutes, in terms of relative improvement versus their non-reduced counterparts the films with longer anodization times benefitted the most. After reduction, water permeates into the film and protons intercalate into the near-surface WO₃ structure, forming a more conductive HₓWO₃ tungsten bronze [107]. As the structure becomes more conductive photogenerated electrons reach the back contact faster; this results in faster photogenerated charge transfer kinetics in LSV and steady-state measurements. It is also highly likely that reduction decreases the number of defects that act as electron or hole traps in this material, thus increasing photon conversion efficiency [111]. Both of these effects result in a much higher measured photocurrent. Thus, the electrochemical reduction

and activation treatment increased the activity of 30min-r-WO$_3$ film over 10 times, whereas the 2min-r-WO$_3$ film showed only a marginal improvement.

The composite films behaved similarly, but generated higher photocurrents than their WO$_3$ counterparts (**Fig. 33a,c,d, yellow lines**). The main difference observed here was that the composites (especially 30-min-WO$_3$+MoS$_x$) had a significant anodic background current, likely related to the oxidation of the MoS$_x$ material.
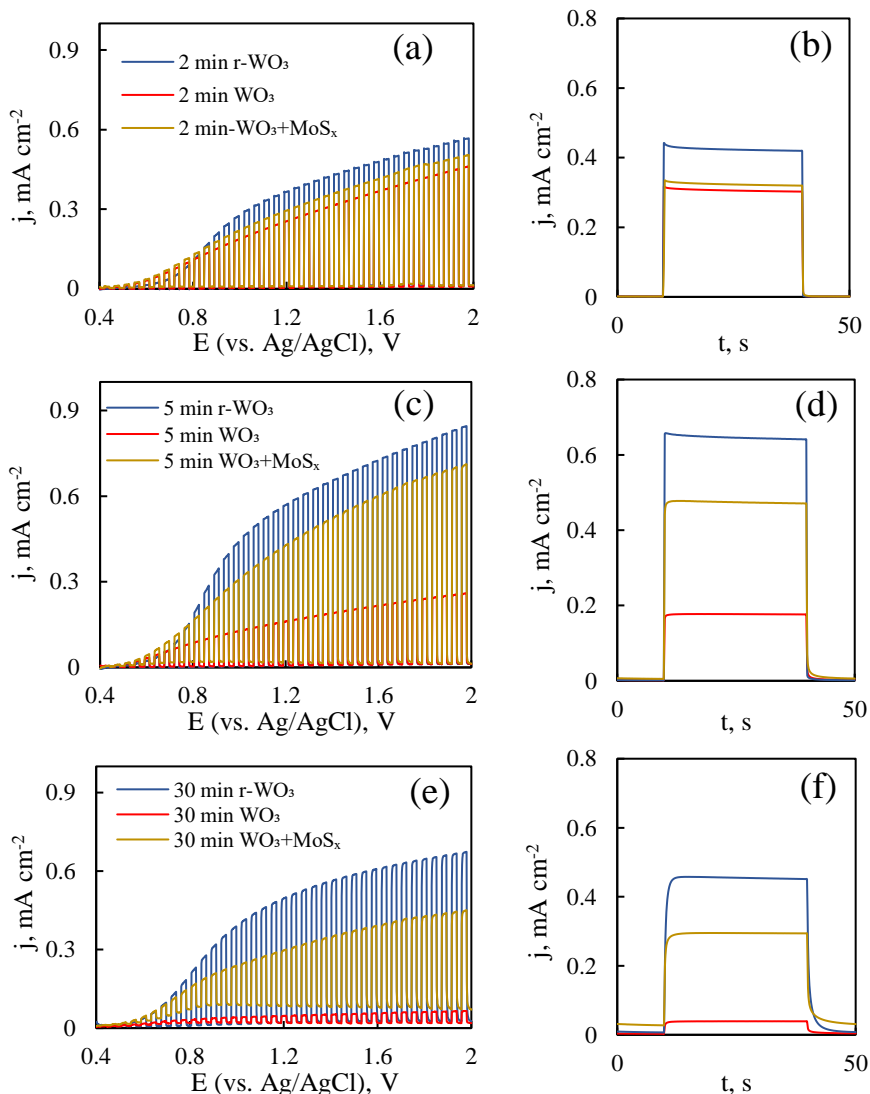

Fig. 33. *Linear sweep voltammetry chopped-UV measurements and chronoamperometric light on/off pulses of WO$_3$, r-WO$_3$, and WO$_3$ + MoS$_x$ films that had been obtained after anodization for 2 minutes (a, b), 5 minutes (c,d), and 30 minutes (e,f). Scan rate 2 mV s^{-1}, I$_0$ = 50 mW cm^{-2}.*

Potentiostatic UV on/off pulses at 1.2 V were applied in order to obtain information on $j_{t=0}$ (the instantaneous photocurrent) and j_{ss} (the steady state photocurrent). The most rudimentary interpretation of a photocurrent pulse profile is that the difference between $j_{t=0}$ *and* j_{ss} is proportional to the amount of minority charge carriers that recombine at the semiconductor's surface, i.e. transfer efficiency [153]. However, it is evident from **Fig. 33b,d,f** that only the films obtained after short anodizations exhibit the initial "overshoot". Even in this case j_{ss} is approached rapidly, and the difference can be effectively disregarded. In contrast, the 30-min films take several seconds to reach a steady-state photocurrent, indicating slow photogenerated charge transfer. The transfer and recombination kinetics will be further elucidated using non-stationary photoelectrochemical methods. The slight decrease of j_{ph} over the duration of the pulse also shows that the thinner films are less photoelectrochemically stable. This could be caused by non-reversible electron-hole recombination and the depletion of the space charge layer, but it could also be related to electro- or photo-corrosion of the films under anodic conditions.

In order to compare the photocatalytic activities of all films consider in this study, the obtained j_{ss} values from the potentiostatic pulses were recalculated into IPCE by **eq. 15**. The conversion efficiencies increase with applied potential as does the steady-state photocurrent, and their trends conclusively show that r-WO$_3$ films exhibit better photon conversion efficiencies over the entire measured potential range. **Table 8** presents IPCE values obtained from steady state photocurrent pulses measured at 1.2 V. For WO$_3$ films photon conversions trend towards lower values as the anodization time is increased, and the most effective film is 2-min-WO$_3$. After reduction and activation, conversion efficiencies increase for all films, but as was shown earlier the effect is most pronounced for the films that had been less photocatalytically active before. The largest overall IPCE value of 4.35% was reached with a 5-min-r-WO$_3$ film. Such photon conversion efficiencies are substantial as for as-deposited films, and the effect of cathodic reduction is considerable. The WO$_3$+MoS$_x$ films are not as photoactive as r-WO$_3$ films, but they are still a substantial improvement over plain WO$_3$. The 5-min-WO$_3$+MoS$_x$ film reaches the highest IPCE of this series – 3.1%. However, it is interesting that the 30-min-WO$_3$+MoS$_x$ film is substantially more photoactive than the comparable WO$_3$ film, suggesting that, much like reduction, modification with MoS$_x$ also increases the conductivity or charge separation efficiency of the material. Because IPCE typically decreases with increasing I_0, even larger efficiencies would be reached when using lower light intensities.

Table 8. IPCE % values calculated from potentiostatic UV on/off pulse data measured at 1.2 V for WO₃, r-WO₃, and WO₃+MoSₓ films obtained by anodizing at 25 mA cm⁻² and for varying times.1 M Na₂SO₄ pH 2, I₀ = 50 mW cm⁻².

$t_{anodization}$, min	j_{ss}, mA cm⁻²			IPCE, %		
	WO_3	$r\text{-}WO_3$	WO_3+MoS_x	WO_3	$r\text{-}WO_3$	WO_3+MoS_x
2	0.301	0.418	0.315	2.04	2.84	2.16
5	0.175	0.640	0.456	1.19	4.35	3.10
30	0.036	0.444	0.266	0.246	3.02	1.80

The potentiostatic curves presented in **Fig. 34** show the behavior of measured current under constant illumination. For WO_3 and WO_3+MoS_x films a near-steady-state photocurrent is reached almost immediately, after which the current begins decreasing slowly but continuously. In accordance with previous measurements, the WO_3+MoS_x film generates a larger photocurrent than the WO_3 film, although here the difference is not as large, possibly due to slight differences that could have occurred during anodization. However, for the r-WO_3 films the photocurrent behaves in an entirely different manner. A strong discharge current is observed, and a minimum is reached after ~ 180 seconds. As can be seen in **Fig. 30b**, the dark current is also relatively high at this point. Afterwards, the current density begins to increase and only approaches a steady state after ~ 2 hours of operation. Reduction of composite films was also experimented with, and r-WO_3+MoS_x were found to display the same tendencies. Regardless, due to their functional similarity to r-WO_3 they will be excluded from further discussion.

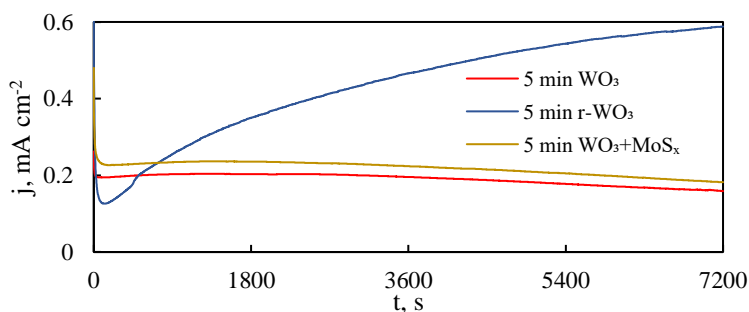*Fig. 34. Potentiostatic steady-state photocurrent curves of WO₃, r-WO₃, and WO₃+MoSₓ films that had been obtained after anodizing for 5 minutes. Obtained at 1.2 V and I₀ = 50 mA cm⁻².*

3.2.7 Photo-electrochemical impedance spectroscopy study

PEIS spectra were obtained with a constant light intensity of 50 mW cm⁻² at increasingly anodic applied potentials up to 2 V. A good understanding of

the system under investigation is crucial for interpretation of impedance spectra. Polarization data (**Fig. 33**) shows that under dark conditions no Faradaic processes occur on WO_3 films, and the same is assumed for the reduced and activated films. This means that the photogenerated charge transfer kinetics within the space charge layer will decide the low frequency response of the PEIS spectra of this system. The WO_3+MoS_x films, on the other hand, had a small anodic current that could probably be attributed to oxidation of MoS_x. However, the signal in PEIS is caused by the modulation of the semiconductor's photoconductivity, so a background oxidative current should have little effect on the resulting spectra.

A collection of representative PEIS spectra is presented in **Fig. 35**. From the Nyquist coordinates it is apparent that the WO_3 impedance response draws a depressed semicircle in the complex plane (**Fig. 35a**). The width of this semicircle is smallest for the most conductive films (i.e., 2min-WO_3), and the magnitude of the film's impedance increases with anodization time. Although the complex plane seems to display one semicircle, a closer look at the Bode coordinates reveals that the response is in fact comprised from two distinct time constants (**Fig. 35b**), which are only well distinguishable for 5min-WO_3 and 30min-WO_3. Only the low-frequency component could be extracted for the 2min-WO_3 film.

The electrochemical reduction and activation process seems to work by increasing the conductivity of the films, as is confirmed by their PEIS spectra (**Fig. 35c, d**). The impedance magnitudes of r-WO_3 decrease several times when compared to their respective non-reduced films. As was the case with j_{ph} measurements, the effect is most significant for the least-conductive 30min-WO_3 film. It is also interesting to note that from the Bode spectra it appears that, while reduction has little effect on the low frequency range, it strongly suppresses the high frequency response. In PEIS high frequencies can often be attributed to capacitances caused by the charge and discharge of the double layer and intermediate surface states, and this may be an indication that the r-WO_3 material has more favorable adsorption/desorption kinetics of OER intermediates because the high frequency response is more in phase with the perturbation.

Lastly, the PEIS spectra of WO_3+MoS_x films largely resembled those of the r-WO_3 films. Overall, much smaller impedance magnitudes than for plain WO_3 are seen in accordance with the films' enhanced photocatalytic activities. The low frequency response is characterized by a depressed semicircle (**Fig. 35e**), but a significant high-frequency element becomes apparent from Bode coordinates (**Fig. 35d**). As before, its cause is the charge and discharge of the surface that is in contact with the electrolyte [91].
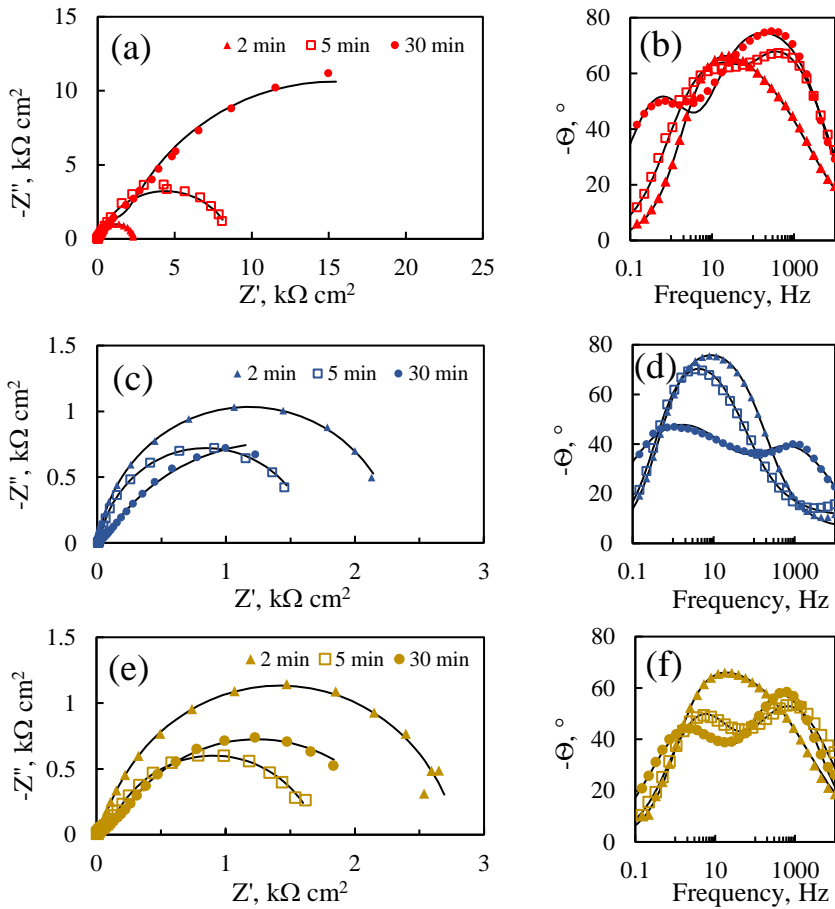
Fig. 35. *PEIS spectra in Nyquist and Bode coordinates of WO_3 (a,b), r-WO_3 (c,d), and WO_3+MoS_x (e,f) films that have been formed by anodizing for 2, 5, and 30 minutes. Spectra obtained at $I_0 = 50$ mW cm^{-2} and 1.2 V. Solid lines show fits to the equivalent circuit in **Fig. 37**.*

In a typical full characterization of a film the PEIS spectra were registered at incrementally increasing anodic potentials up to 2.0 V. LSV measurements had shown that in this range j_{ph} grows with applied potential, but interestingly the system's impedance also increases (**Fig. 36**). This means that the semiconductor material becomes less conductive even though a higher generated photocurrent is observed. Technically this behavior can be related to the $j_{ph} - E$ curves that can be inferred from the "UV on" parts of **Fig. 33**. A sharper rise in j_{ph} is observed at lower potentials, and the increase trends toward a plateau as the potential is swept anodically. Because the PEIS response is generated by integrating a small part of the $j_{ph} - E$ curve under perturbation by a set potential amplitude, a steeper curve will result in more

integrated current – a smaller impedance. These considerations can be further elaborated by applying equivalent circuit fitting.
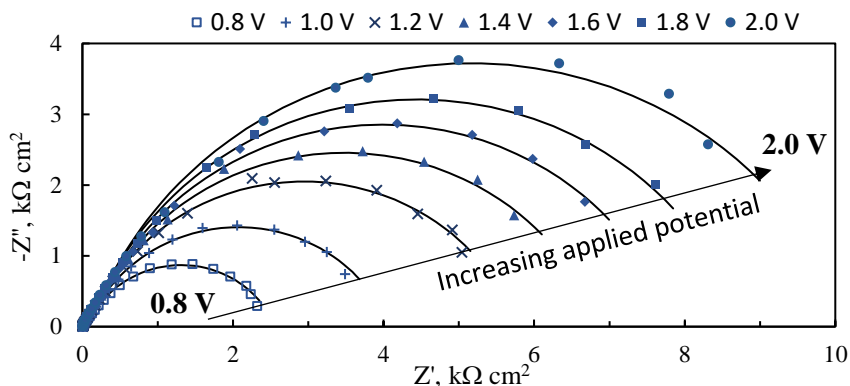

Fig. 36. *PEIS spectra of 5min-WO₃ film in dependence on the anodic potential. Solid lines show fits to the equivalent circuit in* ***Fig. 37***.

The measured spectra were processed by fitting them to an equivalent electrical circuit (EC), where a single time constant is represented by an RC element with a capacitor connected in parallel to a resistor. Because two time constants are generally observed, the EC must have two RC elements. This results in an EC that is commonly used in electrochemical impedance modeling, and has been frequently applied to fit the spectra of photoanodes (**Fig. 37**).
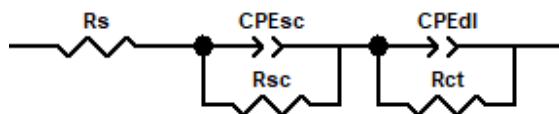

Fig. 37. *Equivalent electrical circuit, used to model PEIS data. R_s – solution resistance; CPE_{dl} is the double layer capacitance represented by a constant phase element to account for surface inhomogeneity, but it can overlap with a capacitance that is caused by the charge and discharge of surface states. R_{ct} is the associated charge transfer resistance. CPE_{sc} and R_{sc} are related to the semiconductor's space charge layer.*

CPE_{sc} should be proportional to the layer's width, provided that the depletion zone acts as an insulating layer. The nature of R_{sc} requires a deeper explanation. Broadly speaking, a resistance is a measure of the electrical force that a charge carrier must overcome in order to move through an electrical field of certain strength. R_{sc} may be thought of as the electrical resistance of the space charge layer between the point where a charge carrier is generated and where it exits the layer. When the photoanode is illuminated, a flux of holes (that is equal to the flux of incident photons multiplied by a conversion

coefficient) begins moving in the direction of the semiconductor/electrolyte interface. Therefore, R_{sc} must be a measure of this flux.

The circuit's parameters were plotted as a function of applied potential, and these trends were then compared to examine whether the increased photoactivity of r-WO$_3$ and WO$_3$+MoS$_x$ over plain films could be attributed to any of them. R_{sc} values are seen to increase linearly with the applied potential (**Fig. 38a**), reflecting the increasing magnitude of the spectra in **Fig. 36**. This is a peculiar observation, as it implies that the system is becoming less conductive while the steady-state photocurrent increases. $1/R_{sc}$, which should be in some way representative of photogenerated charge carrier transfer, peaks at 0.8 V and then drops with applied potential in stark contrast with the increasing steady-state photocurrent (**Fig. 38b-d**).
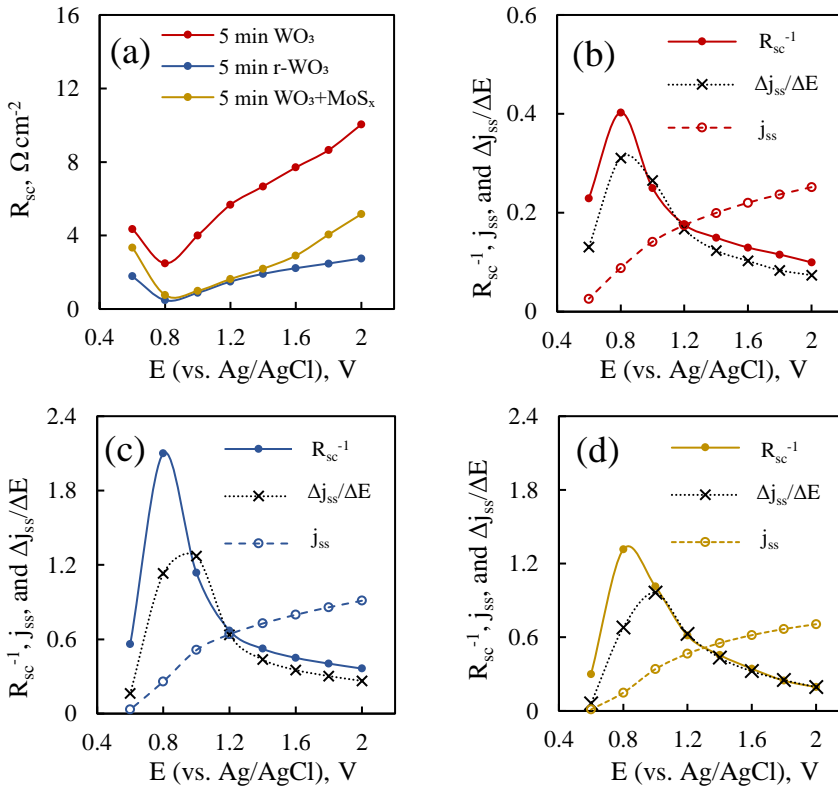
Fig. 38. *Results of the EIS fitting data for WO$_3$ (red lines) r-WO$_3$ (blue lines), and WO$_3$+MoS$_x$ (yellow lines) films presented as trends over applied potential: the space-charge resistance (a), steady state photocurrent and modeled R_{sc} for WO$_3$ (b), r-WO$_3$ (c), and WO$_3$+MoS$_x$ (d).*

If the incident photon flux is constant, and bias potential is increased (i.e., the space charge layer expands as per **eq. 14**), the photogenerated charge

carrier flux should also increase. All this points towards that R_{sc} is not a direct measure of the flux. Instead, it is related to the change of the flux over bias potential – $\Delta\varphi_{h+}/\Delta E$. Values of j_{ss} that had been obtained from steady state UV pulse measurements were used to calculate the rudimentary derivative values of $\Delta j_{ss}/\Delta E$, which are presented as a function of applied potential in **Fig. 38b-d**. It can be seen that, although experimental errors could have distorted the results, the same decreasing trend is observed. Moreover, this relation between the charge carrier flux and applied electric field strength is effectively photoconductivity as measured in mA V^{-1} cm^{-2}. It then follows that this decrease in conductivity is what determines the R_{sc} parameter.

The physical cause of this phenomenon can be traced to the balance between the expanding space charge layer and decreasing charge carrier density. As the photogenerated charge carriers transfer away (e^- towards the back contact, and h^+ towards the electrolyte) an insulating depletion region forms, resulting in a measurable capacitance. As the depletion layer widens, the capacitance decreases (**Fig. 39a**).
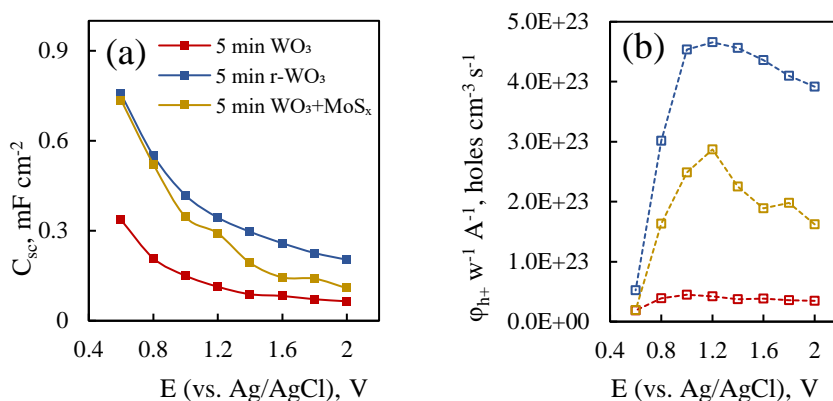
Fig. 39. Semiconductor properties of WO₃ (red lines), r-WO₃ (blue lines), and WO₃ + MoSₓ (yellow lines) films in dependence on applied potential: space charge layer capacitance (a), and calculated photoconductivity (b).

If C_{sc} can be considered a reasonable approximation of the capacitance of the space charge layer, then its width W should be proportional to $1/C_{sc}$ as per the parallel plate capacitor equation. If the relative permittivity ε_r were to be known, the width of the depletion zone could be calculated. The ε_r of WO₃ is known to vary based on electrodeposition conditions, but for illustration purposes a value of 33.3 (obtained for WO₃ films formed by anodization in 0.3 M oxalic acid in chapter 3.2.2) will be considered.

Then the width and volume of the space charge layer is calculated, and the values of charge carrier density are presented as a function of applied potential in **Fig. 39b**. It is evident that the charge carrier density reaches a peak at a

certain potential, which is ~ 1 V to 1.2 V for all three films. After this, the charge carrier density begins to decrease linearly as the space charge layer continues to expand. It is also worth noting that this peak almost exactly corresponds to where the observed steady state photocurrents intersect the calculated $1/R_{sc}$ trends in **Fig. 38b-d**. It may then be concluded that the steady state photocurrent is equal to the photoconductivity when the hole density within the space charge layer is at a maximum. Functionally, j_{ph} continues to rise with further increasing potential, as its magnitude depends on the minority charge carrier flux rather than conductivity.

Therefore, analysis and fitting of the low-frequency PEIS response reveals information about the photoconductivity of photoanodes (e^- - h^+ pair photogeneration) rather than steady state photocurrent. Although, as demonstrated, at a certain potential $j_{ss} = R_{sc}^{-1}$. In accordance with steady-state measurements, the PEIS results confirm the enhanced photocatalytic activity of r-WO_3 and WO_3+MoS_x films over plain WO_3. From the results of these experiments, this increase in photocatalytic activity can be attributed to increased charge carrier photogeneration. The high-frequency elements (C_{dl} and R_{ct}) were not analyzed in detail. It was noticed that R_{ct} increases with applied potential until it peaks (which corresponds to a small background current peak that had been observed in LSV curves), suggesting that this parameter is most likely related to the anodic corrosion of W or WO_3. And C_{dl} was noticed to have a strong diffusive element at low overpotentials (where the n of CPE_{dl} was near 0.5), which probably indicates a complex interaction between the Helmholtz capacitance and charge/discharge of intermediate surface states.

3.2.8 Intensity modulated photocurrent spectroscopy study

IMPS was used to complement PEIS results, as it provides additional information on photon conversion efficiency and hole transfer kinetics. Initially, measurements were carried out at increasing light intensities (I_0: 10 to 60 mW cm^{-2} at increments of 10 mW cm^{-2}). Under potentiostatic conditions the width of the space charge layer should remain constant, as it is mostly dependent on the bias potential. According to the Gärtner equation (**eq 13**) then the increase in j_{ph} should be related to the flux of photogenerated charge carries within the space charge layer, which is equal to the incident photon flux multiplied by a conversion coefficient.

The IMPS spectra shown in **Fig. 40** exhibit some unique characteristics. For one, the spectra begin in the third quadrant of the complex coordinate plane. This is an experimental fact that has also been observed for Fe, Ti, and W oxides [154–156], and its origin is the high-frequency charge/discharge of

the double layer. All of the spectra then intercept the H" axis at 417 Hz (at which the phase shift equals -90º), after which substantial low frequency semicircles begin.
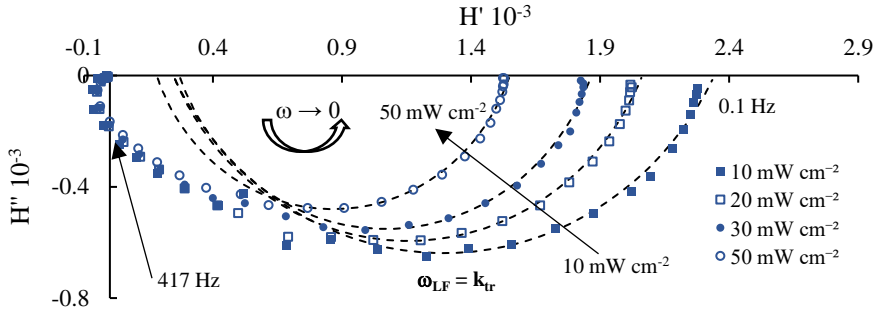

Fig. 40. *IMPS spectra obtained at 1.2 V in dependence on UV light intensities (10% modulation amplitude). Measured on 5min-r-WO₃ film. Dashed lines represent semicircle fits.*

It is immediately apparent that there is no surface recombination at this applied potential – at low frequencies the spectra trend towards intercept with the H' axis as the phase nears 0. According to IMPS theory, the low frequency semicircle is expected to reach a maximum at a certain frequency which is equal to the sum of both transfer constants ($\omega_{LF} = k_{tr} + k_{rec}$). If no recombination is experimentally observed, then $k_{tr} \gg k_{rec}$, and $\omega_{LF} = k_{tr}$ [89]. That is to say, the entire IMPS response, comprised from two semicircles, will be confined to the fourth quadrant of the complex coordinate plane. This is almost exactly what is observed in the obtained spectra – the low frequency semicircle decreases in magnitude with increasing I_0, while the high frequency response is not significantly altered by light intensity.

However, although they appear as semicircles, they could not be modeled with a single CPE element, likely due to interference from the high-frequency response. In order to better distinguish the signal that occurs due to hole transfer, the following procedure for processing IMPS spectra was adopted: a semicircular fitting with a simple $R_1(CPE-R_2)$ equivalent circuit was applied to the low-frequency response. From the obtained values an entire semicircle was simulated on the complex plane plot. The values of ω_{LF} and $H'_{\omega \to 0}$ were obtained from this simulated semicircle that corresponds to the low frequency response. Note that here the parameters of the equivalent circuit do not have a physical meaning as they would in EIS. These observations point to the conclusion that, much like in electrochemical impedance spectroscopy, if two time constants are different by enough magnitudes, non-stationary spectroscopy methods will allow the discernment of one or both of them. In this case τ_s is impossible to calculate, but τ_{LF} is. The validity of this approach

is shown in **Fig. 41** by comparing various parameters that had been obtained from steady-state, PEIS, and IMPS experiments.

The steady-state photocurrent increases linearly with I_0 for all studied films (**Fig. 41a**). This is the first indication as to the mechanism of water oxidation: it has been demonstrated that this behavior is related to whether the photoelectrochemical reaction occurs through direct or indirect (i.e. hydroxyl radical assisted) hole transfer [157,158]. In this case, a linear relation of j_{ph} to the light intensity is an indication of direct hole transfer.
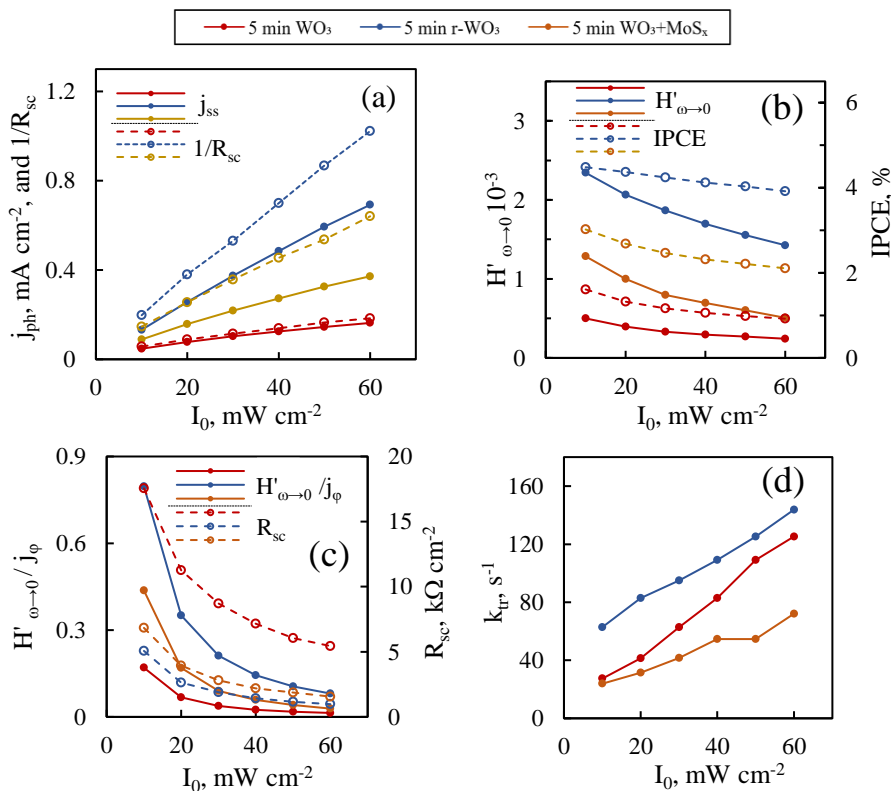
Fig. 41. *Analysis data of the IMPS spectra for WO$_3$ (red lines), r-WO$_3$ (blue lines), and WO$_3$+MoS$_x$ (yellow lines) in dependence on applied illumination intensity: steady-state photocurrent and R_{sc}^{-1} (a); trends of the low frequency intercept with the real axis and IPCE (b); trends of the normalized low frequency intercept and Rsc, obtained from PEIS data (c); transfer constants, obtained from IMPS (d). Data measured for 5min films, at 1.2 V.*

From parallel PEIS experiments it was determined that at 1.2 V for a WO$_3$ film, $1/R_{sc}$ values are almost equal to the observed steady state photocurrent. Conversely, for r-WO$_3$ and WO$_3$+MoS$_x$ films, $1/R_{sc}$ values were larger throughout. This can be related to the observations made in **Fig. 38**, where it was demonstrated that at a certain potential the photoconductivity $(1/R_{sc})$

equals j_{ss}. As was discussed earlier, R_{sc} is a measure of the semiconductor's conductivity owing to the photogenerated charge carrier flux. The potentiostatic mode keeps the strength of the electric field effectively constant, and therefore the changes in the charge carrier flux are directly related to the increasing incident photon flux, as per the Gärtner equation. As the hole flux increases at a constant potential, the conductivity and $1/R_{sc}$ is observed to grow linearly with I_0. The difference between j_{ph} and $1/R_{sc}$ then becomes even more remarkable: for the WO_3 films - collected e^- results in one h^+ joining the flux because $j_{ph} \approx 1/R_{sc}$, but for the r-WO_3 films - collected e^- yields ~ 1.41 to 1.49 h^+ based on I_0.

The second important parameter of IMPS spectra is the low-frequency intercept with the real axis. The real axis of an IMPS plot is fundamentally related to quantum efficiency, i.e., the ratio between the photogenerated current and the incident photon flux. The so-called external quantum efficiency (EQE, functionally identical to IPCE) is defined as:

$$EQE(\lambda) = \frac{j_e(\lambda)}{q\varphi(\lambda)} = \frac{j_e(\lambda)}{j_\varphi(\lambda)} \tag{30}$$

where j_e is the collected electrical current, and j_φ is the spectral flux expressed in the units of current, q is the elementary charge.

If an IMPS spectrum were to be normalized by assuming that the maximum observed value of the real axis H' equals 1, then the low frequency intercept with the real axis would give the transfer efficiency. However, if the spectrum were to be normalized by the incident photon flux or not normalized at all, then the low frequency intercept should be proportional to the EQE.

At low frequencies (as $\Theta \rightarrow 0$) the collected current approaches steady state, and the low frequency intercept should be proportional to the IPCE values that were calculated from steady-state photocurrent measurements. Indeed, for the non-normalized H spectra that were presented in **Fig. 40,** it is observed that $H'_{\omega \rightarrow 0}$ values decrease with I_0 with the similar tendency as for IPCE (**Fig. 41b**). However, these values are dimensionless and demonstrably cannot be equated to steady state photocurrent. Here the enhanced photon conversion efficiency of reduced and composite films is again seen, as the intercept values of the modified films are 2 to 5 times larger than those of plain WO_3.

Another observation was made when normalizing the presented $H'_{\omega \rightarrow 0}$ values by j_φ. The normalized $H'_{\omega \rightarrow 0} / j_\varphi$ values decreased by a power law that was not entirely proportional to IPCE (**Fig. 41c**). In fact, the only other

parameter within the system that would exhibit such a trend with I_0 was R_{sc}, obtained from parallel PEIS measurements under identical conditions. Of course, if $H'_{\omega\to0} \sim j_{ss}/j_\varphi$, then $H'_{\omega\to0}/j_\varphi$ will be proportional to $1/j_{ss}$ (which is directly related to R_{sc} as discussed earlier). These results are interesting, and they connect the various parameters obtained by PEIS and IMPS. In practice this means that while the low frequency intercept is proportional to conversion efficiency, the normalized intercept is more proportional to photoconductivity.

Finally, the transfer constants of WO_3, r-WO_3, and WO_3+MoS_x films were found to increase with I_0 in moderately linear trends (**Fig. 41d**). The k_{tr} of the WO_3 film ranged from 27.3 s^{-1} to 125.3 s^{-1}, whereas for the r-WO_3 film it was almost double at lower intensities from 62.8 s^{-1} to 143.8 s^{-1}. For composite films the transfer constants were lower than for unmodified WO_3 (23.8 s^{-1} to 72.1 s^{-1}). Thus, modification of WO_3 by reduction increases photoconductivity and the rate of hole injection into the electrolyte, resulting in overall enhanced photocatalytic water splitting properties. Meanwhile, WO_3+MoS_x films also exhibit better charge carrier photogeneration and separation, but suffer from hindered hole transfer. This may limit their effectiveness for photocatalysis.

The following conclusions have been made about applying IMPS analysis to these films: photocatalytic activity in terms of steady-state photocurrent is directly proportional to $1/R_{sc}$ that is obtainable by equivalent circuit fitting of PEIS spectra. Also, the low-frequency intercept $H'_{\omega\to0}$ is proportional to EQE, and larger H' values correspond to enhanced photon conversion efficiencies. Further implementation of this analysis is shown in **Fig. 42**. Here, the presented spectra had been obtained at different bias potentials. A significant difference is observed for the low frequency intercept $H'_{\omega\to0}$ – its values increase as the applied potential is raised towards more anodic values. Recalling the previous discussion, this must mean that better photon conversion efficiency is achieved at higher potentials. Conversely, ω_{LF} decreases, which is not apparent from the profile of the spectra, but will be discussed in more detail later on.
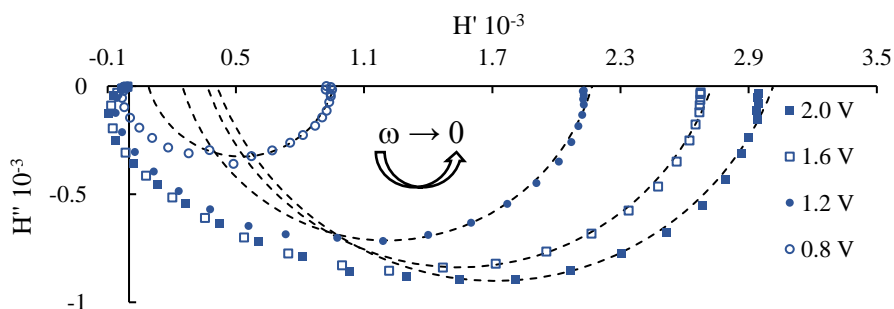
Fig. 42. *IMPS spectra obtained at I_0 = 50 mW cm^{-2} and 1.2 V in dependence on applied potential for 5min-r-WO3 film.*

The IMPS spectra of films that had been anodized for different times are particularly intriguing, and are presented in **Fig. 43**, but without fitting. For the films that had been formed by shorter anodizing durations (2, 5 minutes) the high frequency response overlaps the low frequency signal, as a broad semicircle is observed in the first half of the spectrum. This complicates estimation of ω_{LF} (for example, for the 2min-r-WO$_3$ film in **Fig. 43b** the low-frequency signal is completely indistinguishable). Modeling by simulation and extrapolation of the low frequency response yielded usable data in most other cases.

Designation of the low frequency extremum is a known issue in IMPS analysis, and interpretation can vary by researcher. The method used in this study may result in an over- or under-approximation of the parameters, but it provides consistency of data acquisition.

Furthermore, these films may also exhibit some recombination as is signaled by the appearance of a trend toward low frequency semicircles in the first quadrant, but these recombination signals are negligible and have been disregarded from broader data analysis. The low frequency intercepts with the real axis show that 2min-WO$_3$ and 5min-WO$_3$ films reach better photon conversion efficiencies, which fall drastically when the anodization time is extended to 30 minutes (**Fig. 43a**). As expected, the r-WO$_3$ films have larger low frequency intercept values owing to their enhanced conversion efficiencies (**Fig. 43b**). The 30min-r-WO$_3$ film in particular shows significant improvement over 30min-WO$_3$. The composite films follow largely the same trends, with 2min-WO$_3$+MoS$_x$ and 5min-WO$_3$+MoS$_x$ having the largest conversion efficiencies (**Fig. 43c**), but it is again noteworthy that the 30min-WO$_3$+MoS$_x$ film exhibits much higher conversion efficiency than the respective plain WO$_3$ film. These results broadly correspond to all of the previous discussion about the effect of anodization time and photoactivity – shorter anodizing times yield more photoactive films, but modification by

either compositing with MoS_x or cathodic reduction enable the formation of relatively photoactive thick films.
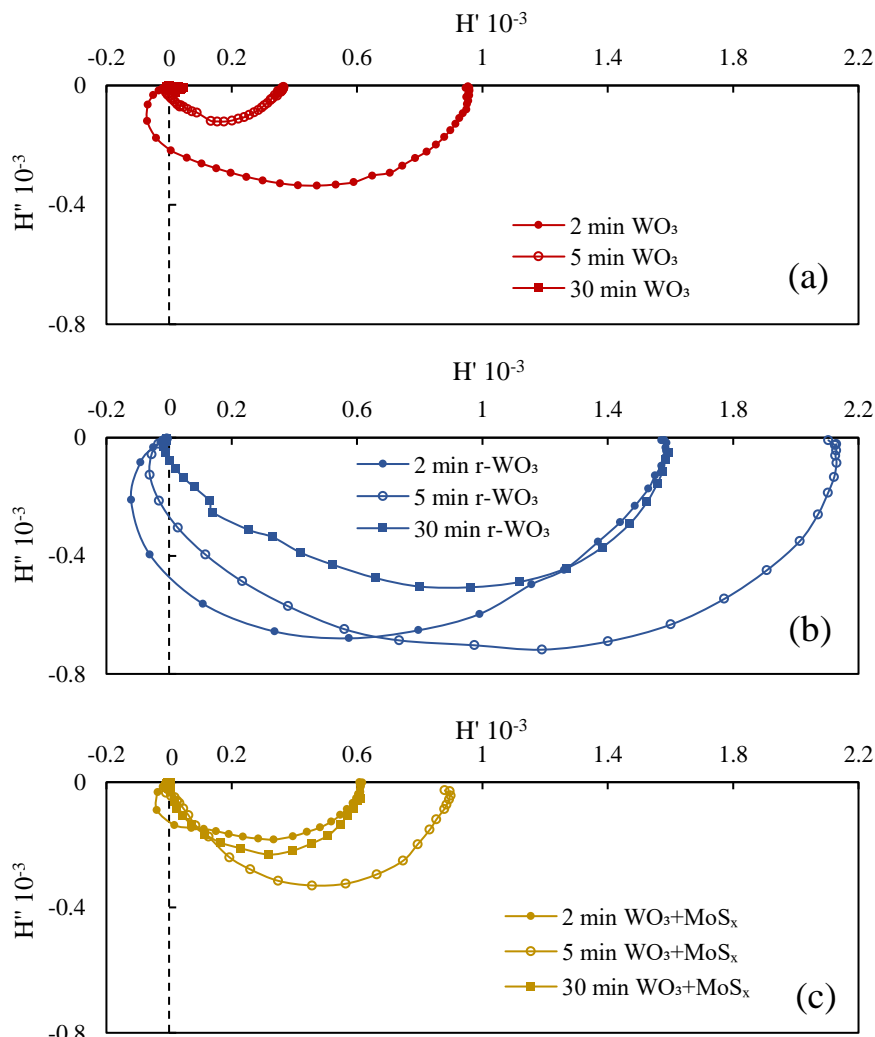
Fig. 43. *IMPS spectra obtained at $I_0 = 50$ mW cm^{-2} and 1.2 V in dependence on anodization time for WO_3 (a), r-WO_3 (b), and WO_3+MoS_x (c) films.*

The relation between applied potential and transfer kinetics/conversion efficiency must also be discussed. IMPS analysis shows that as bias potential is increased the photon conversion efficiency also increases, which is in agreement with steady state measurements. To illustrate these tendencies, as well as to compare WO_3, r-WO_3, and WO_3+MoS_x films, **Fig. 44** contains the values of low frequency intercepts with the real axis, as well as transfer rate constant values that were obtained directly from ω_{lf}. It is seen that $H'_{\omega \to 0}$

increase with applied potential (**Fig. 44a**), and the intercept values of modified films are overall larger, showing better photon conversion efficiency and directly relating to the observed difference in steady state photocurrents. In contrast, here the transfer rate constants k_{tr} of r-WO$_3$ and WO$_3$+MoS$_x$ are smaller than that of the plain WO$_3$ film. Moreover, k_{tr} decrease steadily throughout the entire potential range. It has been suggested that this behavior can be related to the mechanism of oxygen evolution through either mobile or immobile intermediate surface states [159]. If k_{tr} increases with applied potential it would suggest that oxygen evolution occurs through coupling of two adjacent oxygen-containing intermediates. Otherwise, the trend of k_{tr} would point towards a mechanism where oxygen evolution occurs through a single immobile active site which reacts with other photogenerated holes and adsorbed OH$^-$ species. Then k_{tr}, obtained from IMPS, may be related to $j_{ph} - I_0$ measurements (as in **Fig. 41a**), which also give an indication as to whether hole transfer proceeds through indirect (mobile) or direct (immobile) steps. In this case the $k_{tr} - E$ and $j_{ph} - I_0$ behavior of all films agree and strongly suggest that water oxidation proceeds through direct hole transfer.
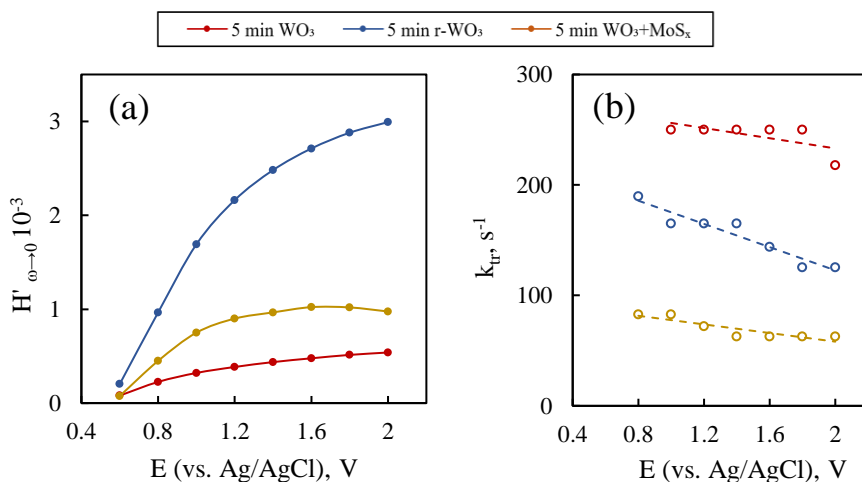

Fig. 44. *Low frequency intercepts (a) and transfer rate constants (b) as a function of applied potential for WO$_3$, r-WO$_3$, and WO$_3$+MoS$_x$ films.*

3.3 Summary

The studies presented in this dissertation focused on two distinct but inseparable aspects of catalytic water splitting – the hydrogen evolution reaction and the oxygen evolution reaction.

Efficient HER electrocatalysts in acidic media were prepared by electrodepositing MoS_2 on copper substrates: a device-based approach of depositing catalytic films on metallic foams was shown to enable the construction of electrodes with excellent total catalytic activity, regardless of geometrical surface area considerations. Such electrodes could be used in cells where finite volume is an issue. Although larger than typical laboratory electrodes, these were still much smaller versions of what could feasibly be used for industrial applications, and issues may still arise when scaling up.

OER was examined from the perspective of photocatalysis. Anodization is a simple and versatile way to form WO_3 films with various parameters like thickness, porosity, and even composition. Due to its bandgap, the material's absorbance is maximal for near-UV light, but a small portion of the visible light spectrum can also be used for photoexcitation. Obviously, although laboratory conditions are selected to be optimal for the investigated material, utilization of direct sunlight is the ultimate objective of photocatalysts. Modifications like compositing with MoS_x or cathodic reduction decrease the amount of energy needed for photoexcitation of charge carriers, so that longer wavelengths (more of the visible light spectrum) could be used.

A complete photocatalytic water splitting cell would be a self-contained device with two catalytic electrodes immersed in a reservoir for water, and an electric field applied across the cell. Some engineering issues like evolved gas collection or water circulation/replenishment would need to be optimized, but overall, such devices are guaranteed to play a role in humanity's future energy industries.

CONCLUSIONS

1. a) MoS_2 films were synthesized on Cu wire (flat) and foam (3D) substrates by electrodeposition. Depending on the deposition time films having sulfur-deficiency ($MoS_{1.72}$ to $MoS_{1.87}$) were obtained on flat electrode. 3D scaled substrate increased films adhesion under developed optimum deposition conditions. The presence of NaH_2PO_2 in the bath results in the films with Mo:S ratio close to stoichiometric MoS_2 that was also confirmed by XPS.

b) The catalytic activity of MoS_2 cathodes for HER obtained on wire and foam substrates related complex dependence on the extrinsic and intrinsic parameters (catalyst loading vs. per-site activity): overpotential for HER decreases with increasing catalyst loading (deposition time), but for lowest Tafel slopes and TOFs (per-site activity) the deposition time should not exceed 1000 s. Moreover, the films deposited with NaH_2PO_2 were noticeably more catalytically active.

2. a) The WO_3 and WO_3+MoS_x films were obtained by anodization in dependence on electrolyte, voltage and anodization time. The material's stoichiometry was: WO_3, with a small W(V)-O signal and WO_3+MoS_x having S2p spectra with a strong S-bridging bond signal. Moreover, EDX mapping revealed that the MoS_x material is mostly incorporated on the WO_3 structure's surface and with Mo:S ratio close to 1.

b) The increased photocatalytic activity for OER were obtained for thinner films (shorter anodization times): $IPCE_{5min-WO3} = 1.19$ %, $IPCE_{5min-WO3+MoSx} = 3.1$ %. Moreover, by H^+ intercalation (cathodic reduction & activation) the photocatalytic activity of WO_3 films can be enhanced even exceeding composites films: $IPCE_{5min-r-WO3}$ reaches 4.35 %. This can be related to the elevated signal of O-vacancy after H^+ intercalation.

3. a) The impedance spectra revealed that the HER activity of MoS_2 films is related to the adsorption resistance, while pseudocapacitance is proportional to the number of active sites. Moreover, regardless of intrinsic activity, 3D electrodes are more suited for scaled-up applications.

b) A PEIS study showed that photocatalytic performance of WO_3 and WO_3+MoS_x is related to the charge carrier photoexcitation within the space charge layer, i.e., R_{sc}.

c) IMPS data showed that H^+ intercalation enhanced higher rate of hole transfer into the electrolyte, while composites have lower k_{tr} values, which may limit their effectiveness as OER photocatalysts.

REFERENCES

[1] E. Stura, C. Nicolini, New nanomaterials for light weight lithium batteries, Analytica Chimica Acta. 568 (2006) 57–64. https://doi.org/10.1016/j.aca.2005.11.025.

[2] G. Jeong, H. Kim, J.H. Park, J. Jeon, X. Jin, J. Song, B.-R. Kim, M.-S. Park, J.M. Kim, Y.-J. Kim, Nanotechnology enabled rechargeable Li–SO$_2$ batteries: another approach towards post-lithium-ion battery systems, Energy Environ. Sci. 8 (2015) 3173–3180. https://doi.org/10.1039/C5EE01659B.

[3] K. Wong, S. Dia, Nanotechnology in Batteries, Journal of Energy Resources Technology. 139 (2017) 014001. https://doi.org/10.1115/1.4034860.

[4] H. Tributsch, J.C. Bennett, Electrochemistry and photochemistry of MoS2 layer crystals. I, Journal of Electroanalytical Chemistry and Interfacial Electrochemistry. 81 (1977) 97–111. https://doi.org/10.1016/S0022-0728(77)80363-X.

[5] I. Song, C. Park, H.C. Choi, Synthesis and properties of molybdenum disulphide: from bulk to atomic layers, RSC Adv. 5 (2015) 7495–7514. https://doi.org/10.1039/C4RA11852A.

[6] B. Hinnemann, P.G. Moses, J. Bonde, K.P. Jørgensen, J.H. Nielsen, S. Horch, I. Chorkendorff, J.K. Nørskov, Biomimetic Hydrogen Evolution: MoS$_2$ Nanoparticles as Catalyst for Hydrogen Evolution, J. Am. Chem. Soc. 127 (2005) 5308–5309. https://doi.org/10.1021/ja0504690.

[7] P. Afanasiev, Synthetic approaches to the molybdenum sulfide materials, Comptes Rendus Chimie. 11 (2008) 159–182. https://doi.org/10.1016/j.crci.2007.04.009.

[8] E.A. Ponomarev, M. Neumann-Spallart, G. Hodes, C. Lévy-Clément, Electrochemical deposition of MoS2 thin films by reduction of tetrathiomolybdate, Thin Solid Films. 280 (1996) 86–89. https://doi.org/10.1016/0040-6090(95)08204-2.

[9] R.N. Bhattacharya, C.Y. Lee, F.H. Pollak, D.M. Schleich, Optical study of amorphous MoS3: Determination of the fundamental energy gap, Journal of Non-Crystalline Solids. 91 (1987) 235–242. https://doi.org/10.1016/S0022-3093(87)80306-X.

[10] G. Laperriere, B. Marsan, D. Belanger, Preparation and characterization of electrodeposited amorphous molybdenum sulfide, Synthetic Metals. 29 (1989) 201–206. https://doi.org/10.1016/0379-6779(89)90900-4.

[11] C.G. Morales-Guio, X. Hu, Amorphous Molybdenum Sulfides as Hydrogen Evolution Catalysts, Acc. Chem. Res. 47 (2014) 2671–2681. https://doi.org/10.1021/ar5002022.

[12] D. Bélanger, G. Laperriére, B. Marsan, The electrodeposition of amorphous molybdenum sulfide, Journal of Electroanalytical Chemistry. 347 (1993) 165–183. https://doi.org/10.1016/0022-0728(93)80086-W.

[13] D. Belanger, G. Laperriere, F. Girard, D. Guay, G. Tourillon, Physicochemical characteristics of electrochemically deposited molybdenum sulfide and polypyrrole-tetrathiomolybdate/molybdenum trisulfide composite electrodes, Chem. Mater. 5 (1993) 861–868. https://doi.org/10.1021/cm00030a024.

[14] D. Merki, S. Fierro, H. Vrubel, X. Hu, Amorphous molybdenum sulfide films as catalysts for electrochemical hydrogen production in water, Chem. Sci. 2 (2011) 1262–1267. https://doi.org/10.1039/C1SC00117E.

[15] K. Kakaei, M.D. Esrafili, A. Ehsani, Alcohol Oxidation and Hydrogen Evolution, in: Interface Science and Technology, Elsevier, 2019: pp. 253–301. https://doi.org/10.1016/B978-0-12-814523-4.00007-1.

[16] S. Fletcher, Tafel slopes from first principles, J Solid State Electrochem. 13 (2009) 537–549. https://doi.org/10.1007/s10008-008-0670-8.

[17] J.O. Bockris, E.C. Potter, The Mechanism of the Cathodic Hydrogen Evolution Reaction, J. Electrochem. Soc. 99 (1952) 169. https://doi.org/10.1149/1.2779692.

[18] J.K. Nørskov, T. Bligaard, A. Logadottir, J.R. Kitchin, J.G. Chen, S. Pandelov, U. Stimming, Trends in the Exchange Current for Hydrogen Evolution, J. Electrochem. Soc. 152 (2005) J23. https://doi.org/10.1149/1.1856988.

[19] S. Trasatti, Work function, electronegativity, and electrochemical behaviour of metals, Journal of Electroanalytical Chemistry and Interfacial Electrochemistry. 39 (1972) 163–184. https://doi.org/10.1016/S0022-0728(72)80485-6.

[20] C.G. Morales-Guio, Nanostructured hydrotreating catalysts for electrochemical hydrogen evolution, Chem Soc Rev. (2014) 15.

[21] P. Raybaud, J. Hafner, G. Kresse, S. Kasztelan, H. Toulhoat, Ab Initio Study of the H2–H2S/MoS2 Gas–Solid Interface: The Nature of the Catalytically Active Sites, (n.d.) 18.

[22] T.F. Jaramillo, K.P. Jorgensen, J. Bonde, J.H. Nielsen, S. Horch, I. Chorkendorff, Identification of Active Edge Sites for Electrochemical H2 Evolution from MoS2 Nanocatalysts, Science. 317 (2007) 100–102. https://doi.org/10.1126/science.1141483.

[23] G. Li, D. Zhang, Q. Qiao, Y. Yu, D. Peterson, A. Zafar, R. Kumar, S. Curtarolo, F. Hunte, S. Shannon, Y. Zhu, W. Yang, L. Cao, All The Catalytic Active Sites of MoS $_2$ for Hydrogen Evolution, J. Am. Chem. Soc. 138 (2016) 16632–16638. https://doi.org/10.1021/jacs.6b05940.

[24] Z. Lin, B.R. Carvalho, E. Kahn, R. Lv, R. Rao, H. Terrones, M.A. Pimenta, M. Terrones, Defect engineering of two-dimensional transition metal dichalcogenides, 2D Mater. 3 (2016) 022002. https://doi.org/10.1088/2053-1583/3/2/022002.

[25] L. Li, Z. Qin, L. Ries, S. Hong, T. Michel, J. Yang, C. Salameh, M. Bechelany, P. Miele, D. Kaplan, M. Chhowalla, D. Voiry, Role of Sulfur Vacancies and Undercoordinated Mo Regions in MoS $_2$ Nanosheets

toward the Evolution of Hydrogen, ACS Nano. 13 (2019) 6824–6834. https://doi.org/10.1021/acsnano.9b01583.

[26] D. Merki, H. Vrubel, L. Rovelli, S. Fierro, X. Hu, Fe, Co, and Ni ions promote the catalytic activity of amorphous molybdenum sulfide films for hydrogen evolution, Chem. Sci. 3 (2012) 2515. https://doi.org/10.1039/c2sc20539d.

[27] J.D. Benck, Z. Chen, L.Y. Kuritzky, A.J. Forman, T.F. Jaramillo, Amorphous Molybdenum Sulfide Catalysts for Electrochemical Hydrogen Production: Insights into the Origin of their Catalytic Activity, ACS Catal. 2 (2012) 1916–1923. https://doi.org/10.1021/cs300451q.

[28] A. Lasia, Mechanism and kinetics of the hydrogen evolution reaction, International Journal of Hydrogen Energy. 44 (2019) 19484–19518. https://doi.org/10.1016/j.ijhydene.2019.05.183.

[29] H. Vrubel, T. Moehl, M. Grätzel, X. Hu, Revealing and accelerating slow electron transport in amorphous molybdenum sulphide particles for hydrogen evolution reaction, Chem. Commun. 49 (2013) 8985. https://doi.org/10.1039/c3cc45416a.

[30] M.-L. Tremblay, M.H. Martin, C. Lebouin, A. Lasia, D. Guay, Determination of the real surface area of powdered materials in cavity microelectrodes by electrochemical impedance spectroscopy, Electrochimica Acta. 55 (2010) 6283–6291. https://doi.org/10.1016/j.electacta.2009.11.006.

[31] O. Reid, F.S. Saleh, E.B. Easton, Determining electrochemically active surface area in PEM fuel cell electrodes with electrochemical impedance spectroscopy and its application to catalyst durability, Electrochimica Acta. 114 (2013) 278–284. https://doi.org/10.1016/j.electacta.2013.10.050.

[32] S.K. Ghosh, T. Bera, O. Karacasu, A. Swarnakar, J.G. Buijnsters, J.P. Celis, Nanostructured MoSx-based thin films obtained by electrochemical reduction, Electrochimica Acta. 56 (2011) 2433–2442. https://doi.org/10.1016/j.electacta.2010.10.065.

[33] J. Gao, B. Li, J. Tan, P. Chow, T.-M. Lu, N. Koratkar, Aging of Transition Metal Dichalcogenide Monolayers, ACS Nano. 10 (2016) 2628–2635. https://doi.org/10.1021/acsnano.5b07677.

[34] S. Kc, R.C. Longo, R.M. Wallace, K. Cho, Surface oxidation energetics and kinetics on MoS$_2$ monolayer, Journal of Applied Physics. 117 (2015) 135301. https://doi.org/10.1063/1.4916536.

[35] J. Martincová, M. Otyepka, P. Lazar, Is Single Layer MoS$_2$ Stable in the Air?, Chem. Eur. J. 23 (2017) 13233–13239. https://doi.org/10.1002/chem.201702860.

[36] L. Wu, N.Y. Dzade, M. Yu, B. Mezari, Unraveling the Role of Lithium in Enhancing the Hydrogen Evolution Activity of MoS2: Intercalation versus Adsorption, ACS Energy Letters. (2019) 8.

[37] X. Lin, J. Ni, Charge and magnetic states of Mn-, Fe-, and Co-doped monolayer MoS $_2$, Journal of Applied Physics. 116 (2014) 044311. https://doi.org/10.1063/1.4891495.

[38] E. Arslan, Comparison of structure and tribological properties of MoS2-Ti films deposited by biased-dc and pulsed-dc, Progress in Organic Coatings. (2012) 5.

[39] A.A. Tedstone, D.J. Lewis, P. O'Brien, Synthesis, Properties, and Applications of Transition Metal-Doped Layered Transition Metal Dichalcogenides, Chem. Mater. 28 (2016) 1965–1974. https://doi.org/10.1021/acs.chemmater.6b00430.

[40] S.Y. Wang, T.S. Ko, C.C. Huang, D.Y. Lin, Y.S. Huang, Optical and electrical properties of MoS $_2$ and Fe-doped MoS $_2$, Jpn. J. Appl. Phys. 53 (2014) 04EH07. https://doi.org/10.7567/JJAP.53.04EH07.

[41] J. Deng, Triggering the electrocatalytic hydrogen evolution activity of the inert two-dimensional MoS2 surface via single-atom metal doping, Environmental Science. (2015) 8.

[42] D. Mosconi, P. Till, L. Calvillo, T. Kosmala, D. Garoli, D. Debellis, A. Martucci, S. Agnoli, G. Granozzi, Effect of Ni Doping on the MoS2 Structure and Its Hydrogen Evolution Activity in Acid and Alkaline Electrolytes, Surfaces. 2 (2019) 531–545. https://doi.org/10.3390/surfaces2040039.

[43] Q. Liu, Q. Liu, X. Kong, Anion Engineering on Free-Standing Two-Dimensional MoS $_2$ Nanosheets toward Hydrogen Evolution, Inorg. Chem. 56 (2017) 11462–11465. https://doi.org/10.1021/acs.inorgchem.7b01886.

[44] H. Huang, Hierarchically nanostructured MoS2 with rich in-plane edges as a high-performance electrocatalyst for the hydrogen evolution reaction, Journal of Materials Chemistry A. (2016) 10.

[45] V.H.V. Quy, E. Vijayakumar, P. Ho, J.-H. Park, J.A. Rajesh, J. Kwon, J. Chae, J.-H. Kim, S.-H. Kang, K.-S. Ahn, Electrodeposited MoS2 as electrocatalytic counter electrode for quantum dot- and dye-sensitized solar cells, Electrochimica Acta. 260 (2018) 716–725. https://doi.org/10.1016/j.electacta.2017.12.023.

[46] W. Teng, Y. Wang, H. Huang, X. Li, Y. Tang, Enhanced photoelectrochemical performance of MoS $_2$ nanobelts-loaded TiO $_2$ nanotube arrays by photo-assisted electrodeposition, Applied Surface Science. 425 (2017) 507–517. https://doi.org/10.1016/j.apsusc.2017.06.297.

[47] W. Jian, Arrays of ZnO/MoS2 nanocables and MoS2 nanotubes with phase engineering for bifunctional photoelectrochemical and electrochemical water splitting, (n.d.) 34.

[48] Z. Guan, Remarkable enhancement in solar hydrogen generation from MoS2-RGO/ZnO composite photocatalyst by constructing a robust electron transport pathway, (n.d.) 37.

[49] D. Wang, X. Zhang, Y. Shen, Z. Wu, Ni-doped MoS_2 nanoparticles as highly active hydrogen evolution electrocatalysts, RSC Adv. 6 (2016) 16656–16661. https://doi.org/10.1039/C6RA02610A.

[50] Z. Zhang, W. Li, M.F. Yuen, T.-W. Ng, Y. Tang, C.-S. Lee, X. Chen, W. Zhang, Hierarchical composite structure of few-layers MoS_2 nanosheets supported by vertical graphene on carbon cloth for high-performance hydrogen evolution reaction, Nano Energy. 18 (2015) 196–204. https://doi.org/10.1016/j.nanoen.2015.10.014.

[51] N. Zhang, W. Ma, F. Jia, T. Wu, D. Han, L. Niu, Controlled electrodeposition of CoMoSx on carbon cloth: A 3D cathode for highly-efficient electrocatalytic hydrogen evolution, International Journal of Hydrogen Energy. 41 (2016) 3811–3819. https://doi.org/10.1016/j.ijhydene.2015.12.173.

[52] A. Ambrosi, M. Pumera, Templated Electrochemical Fabrication of Hollow Molybdenum Sulfide Microstructures and Nanostructures with Catalytic Properties for Hydrogen Production, ACS Catal. 6 (2016) 3985–3993. https://doi.org/10.1021/acscatal.6b00910.

[53] Y. Yan, Vertically oriented MoS2 and WS2 nanosheets directly grown on carbon cloth as efficient and stable 3-dimensional hydrogen-evolving cathodes, Journal of Materials Chemistry A. (2015) 5.

[54] Z. Lu, W. Zhu, X. Yu, H. Zhang, Y. Li, X. Sun, X. Wang, H. Wang, J. Wang, J. Luo, X. Lei, L. Jiang, Ultrahigh Hydrogen Evolution Performance of Under-Water "Superaerophobic" MoS_2 Nanostructured Electrodes, Adv. Mater. 26 (2014) 2683–2687. https://doi.org/10.1002/adma.201304759.

[55] C. Li, X. Bo, M. Li, L. Guo, Facile electrodeposition fabrication of molybdenum-tungsten sulfide on carbon cloth for electrocatalytic hydrogen evolution, International Journal of Hydrogen Energy. 42 (2017) 15479–15488. https://doi.org/10.1016/j.ijhydene.2017.05.046.

[56] Z. Chen, D. Cummins, B.N. Reinecke, E. Clark, M.K. Sunkara, T.F. Jaramillo, Core–shell MoO_3–MoS_2 Nanowires for Hydrogen Evolution: A Functional Design for Electrocatalytic Materials, Nano Lett. 11 (2011) 4168–4175. https://doi.org/10.1021/nl2020476.

[57] Y. Li, H. Wang, L. Xie, Y. Liang, G. Hong, H. Dai, MoS_2 Nanoparticles Grown on Graphene: An Advanced Catalyst for the Hydrogen Evolution Reaction, J. Am. Chem. Soc. 133 (2011) 7296–7299. https://doi.org/10.1021/ja201269b.

[58] B. Guo, K. Yu, H. Li, H. Song, Y. Zhang, X. Lei, H. Fu, Y. Tan, Z. Zhu, Hollow Structured Micro/Nano MoS_2 Spheres for High Electrocatalytic Activity Hydrogen Evolution Reaction, ACS Appl. Mater. Interfaces. 8 (2016) 5517–5525. https://doi.org/10.1021/acsami.5b10252.

[59] J. Benson, M. Li, S. Wang, P. Wang, P. Papakonstantinou, Electrocatalytic Hydrogen Evolution Reaction on Edges of a Few Layer Molybdenum Disulfide Nanodots, ACS Appl. Mater. Interfaces. 7 (2015) 14113–14122. https://doi.org/10.1021/acsami.5b03399.

[60] D. Voiry, M. Salehi, R. Silva, T. Fujita, M. Chen, T. Asefa, V.B. Shenoy, G. Eda, M. Chhowalla, Conducting MoS2 Nanosheets as Catalysts for Hydrogen Evolution Reaction, Nano Lett. (2013) 6.

[61] T. Bak, J. Nowotny, M. Rekas, C.C. Sorrell, Photo-electrochemical hydrogen generation from water using solar energy. Materials-related aspects, International Journal of Hydrogen Energy. 27 (2002) 991–1022. https://doi.org/10.1016/S0360-3199(02)00022-8.

[62] K.J. Patel, C.J. Panchal, V.A. Kheraj, M.S. Desai, Growth, structural, electrical and optical properties of the thermally evaporated tungsten trioxide (WO3) thin films, Materials Chemistry and Physics. 114 (2009) 475–478. https://doi.org/10.1016/j.matchemphys.2008.09.071.

[63] S.K. Gullapalli, R.S. Vemuri, C.V. Ramana, Structural transformation induced changes in the optical properties of nanocrystalline tungsten oxide thin films, Appl. Phys. Lett. (2014) 4.

[64] R.S. Vemuri, K.K. Bharathi, S.K. Gullapalli, C.V. Ramana, Effect of Structure and Size on the Electrical Properties of Nanocrystalline WO$_3$ Films, ACS Appl. Mater. Interfaces. 2 (2010) 2623–2628. https://doi.org/10.1021/am1004514.

[65] H. Qi, J. Wolfe, D. Wang, H.J. Fan, D. Fichou, Z. Chen, Triple-layered nanostructured WO$_3$ photoanodes with enhanced photocurrent generation and superior stability for photoelectrochemical solar energy conversion, Nanoscale. 6 (2014) 13457–13462. https://doi.org/10.1039/C4NR03982C.

[66] D.D. Macdonald, E. Sikora, J. Sikora, The kinetics of growth of the passive ®lm on tungsten in acidic phosphate solutions, (n.d.) 11.

[67] J.M. Macak, H. Tsuchiya, A. Ghicov, K. Yasuda, R. Hahn, S. Bauer, P. Schmuki, TiO2 nanotubes: Self-organized electrochemical formation, properties and applications, Current Opinion in Solid State and Materials Science. 11 (2007) 3–18. https://doi.org/10.1016/j.cossms.2007.08.004.

[68] V. Karastoyanov, M. Bojinov, Anodic oxidation of tungsten in sulphuric acid solution—Influence of hydrofluoric acid addition, Materials Chemistry and Physics. 112 (2008) 702–710. https://doi.org/10.1016/j.matchemphys.2008.06.029.

[69] E. Widenkvist, R.A. Quinlan, B.C. Holloway, H. Grennberg, U. Jansson, Synthesis of Nanostructured Tungsten Oxide Thin Films, Crystal Growth & Design. 8 (2008) 3750–3753. https://doi.org/10.1021/cg800383c.

[70] D.D. Macdonald, S.R. Biaggio, H. Song, Steady-State Passive Films: Interfacial Kinetic Effects and Diagnostic Criteria, J. Electrochem. Soc. 139 (1992) 170–177. https://doi.org/10.1149/1.2069165.

[71] V.P. Parkhutik, V.I. Shershulsky, Theoretical modelling of porous oxide growth on aluminium, J. Phys. D: Appl. Phys. 25 (1992) 1258–1263. https://doi.org/10.1088/0022-3727/25/8/017.

[72] N.R. de Tacconi, C.R. Chenthamarakshan, G. Yogeeswaran, A. Watcharenwong, R.S. de Zoysa, N.A. Basit, K. Rajeshwar, Nanoporous TiO$_2$ and WO$_3$ Films by Anodization of Titanium and Tungsten

Substrates: Influence of Process Variables on Morphology and Photoelectrochemical Response [†], J. Phys. Chem. B. 110 (2006) 25347–25355. https://doi.org/10.1021/jp064527v.

[73] K. Syrek, L. Zaraska, M. Zych, G.D. Sulka, The effect of anodization conditions on the morphology of porous tungsten oxide layers formed in aqueous solution, Journal of Electroanalytical Chemistry. 829 (2018) 106–115. https://doi.org/10.1016/j.jelechem.2018.09.054.

[74] C.W. Lai, S. Sreekantan, Fabrication of WO3 nanostructures by anodization method for visible-light driven water splitting and photodegradation of methyl orange, Materials Science in Semiconductor Processing. 16 (2013) 303–310. https://doi.org/10.1016/j.mssp.2012.10.007.

[75] Y. Chai, C.W. Tam, K.P. Beh, F.K. Yam, Z. Hassan, Porous WO3 formed by anodization in oxalic acid, J Porous Mater. 20 (2013) 997–1002. https://doi.org/10.1007/s10934-013-9675-5.

[76] Y. Chai, F.K. Yam, Z. Hassan, Stability of the anodic growth porous tungsten oxide in different solutions, in: Penang, Malaysia, 2015: p. 070036. https://doi.org/10.1063/1.4915754.

[77] N. Mukherjee, M. Paulose, O.K. Varghese, G.K. Mor, C.A. Grimes, Fabrication of nanoporous tungsten oxide by galvanostatic anodization, J. Mater. Res. 18 (2003) 2296–2299. https://doi.org/10.1557/JMR.2003.0321.

[78] M. Zych, K. Syrek, L. Zaraska, G.D. Sulka, Improving Photoelectrochemical Properties of Anodic WO3 Layers by Optimizing Electrosynthesis Conditions, Molecules. 25 (2020) 2916. https://doi.org/10.3390/molecules25122916.

[79] R.M. Fernández-Domene, R. Sánchez-Tovar, B. Lucas-Granados, G. Roselló-Márquez, J. García-Antón, A simple method to fabricate high-performance nanostructured WO 3 photocatalysts with adjusted morphology in the presence of complexing agents, Materials & Design. 116 (2017) 160–170. https://doi.org/10.1016/j.matdes.2016.12.016.

[80] X. Zhu, L. Liu, Y. Song, H. Jia, H. Yu, X. Xiao, X. Yang, Oxygen evolution and porous anodic alumina formation, Materials Letters. 62 (2008) 4038–4040. https://doi.org/10.1016/j.matlet.2008.05.062.

[81] J. Cao, Z. Gao, C. Wang, H.M. Muzammal, W. Wang, Q. Gu, C. Dong, H. Ma, Y. Wang, Morphology evolution of the anodized tin oxide film during early formation stages at relatively high constant potential, Surface and Coatings Technology. 388 (2020) 125592. https://doi.org/10.1016/j.surfcoat.2020.125592.

[82] W.W. Gärtner, Depletion-Layer Photoeffects in Semiconductors, Phys. Rev. 116 (1959) 84–87. https://doi.org/10.1103/PhysRev.116.84.

[83] W.L. Kwong, H. Qiu, A. Nakaruk, P. Koshy, C.C. Sorrell, Photoelectrochemical Properties of WO3 Thin Films Prepared by Electrodeposition, Energy Procedia. 34 (2013) 617–626. https://doi.org/10.1016/j.egypro.2013.06.793.

[84] W.L. Kwong, N. Savvides, C.C. Sorrell, Electrodeposited nanostructured WO3 thin films for photoelectrochemical applications, Electrochimica Acta. 75 (2012) 371–380. https://doi.org/10.1016/j.electacta.2012.05.019.

[85] B. Yang, P.R.F. Barnes, W. Bertram, V. Luca, Strong photoresponse of nanostructured tungsten trioxide films prepared via a sol–gel route, J. Mater. Chem. 17 (2007) 2722–2729. https://doi.org/10.1039/B702097J.

[86] S.J. Hong, H. Jun, J.S. Lee, Nanocrystalline WO3 film with high photo-electrochemical activity prepared by polymer-assisted direct deposition, Scripta Materialia. 63 (2010) 757–760. https://doi.org/10.1016/j.scriptamat.2010.05.021.

[87] V.S. Vidyarthi, M. Hofmann, A. Savan, K. Sliozberg, D. König, R. Beranek, W. Schuhmann, A. Ludwig, Enhanced photoelectrochemical properties of WO3 thin films fabricated by reactive magnetron sputtering, International Journal of Hydrogen Energy. 36 (2011) 4724–4731. https://doi.org/10.1016/j.ijhydene.2011.01.087.

[88] V.D. Mihailetchi, J. Wildeman, P.W.M. Blom, Space-Charge Limited Photocurrent, Phys. Rev. Lett. 94 (2005) 126602. https://doi.org/10.1103/PhysRevLett.94.126602.

[89] S. Ravishankar, A. Riquelme, S.K. Sarkar, M. Garcia-Batlle, G. Garcia-Belmonte, J. Bisquert, Intensity-Modulated Photocurrent Spectroscopy and Its Application to Perovskite Solar Cells, J. Phys. Chem. C. 123 (2019) 24995–25014. https://doi.org/10.1021/acs.jpcc.9b07434.

[90] E.A. Ponomarev, L.M. Peter, A generalized theory of intensity modulated photocurrent spectroscopy (IMPS), Journal of Electroanalytical Chemistry. 396 (1995) 219–226. https://doi.org/10.1016/0022-0728(95)04115-5.

[91] D.J. Fermín, E.A. Ponomarev, L.M. Peter, A kinetic study of CdS photocorrosion by intensity modulated photocurrent and photoelectrochemical impedance spectroscopy, Journal of Electroanalytical Chemistry. 473 (1999) 192–203. https://doi.org/10.1016/S0022-0728(99)00109-6.

[92] D. Klotz, D.S. Ellis, H. Dotan, A. Rothschild, Empirical in operando analysis of the charge carrier dynamics in hematite photoanodes by PEIS, IMPS and IMVS, Phys. Chem. Chem. Phys. 18 (2016) 23438–23457. https://doi.org/10.1039/C6CP04683E.

[93] C. Zachäus, F.F. Abdi, L.M. Peter, R. van de Krol, Photocurrent of BiVO$_4$ is limited by surface recombination, not surface catalysis, Chem. Sci. 8 (2017) 3712–3719. https://doi.org/10.1039/C7SC00363C.

[94] M. Antuch, P. Millet, A. Iwase, A. Kudo, The role of surface states during photocurrent switching: Intensity modulated photocurrent spectroscopy analysis of BiVO4 photoelectrodes, Applied Catalysis B: Environmental. 237 (2018) 401–408. https://doi.org/10.1016/j.apcatb.2018.05.011.

[95] I. Rodríguez-Gutiérrez, E. Djatoubai, J. Su, A. Vega-Poot, G. Rodríguez-Gattorno, F.L. Souza, G. Oskam, An intensity-modulated photocurrent

spectroscopy study of the charge carrier dynamics of WO3/BiVO4 heterojunction systems, Solar Energy Materials and Solar Cells. 208 (2020) 110378. https://doi.org/10.1016/j.solmat.2019.110378.

[96] F. Amano, S. Koga, Influence of light intensity on the steady-state kinetics in tungsten trioxide particulate photoanode studied by intensity-modulated photocurrent spectroscopy, Journal of Electroanalytical Chemistry. 860 (2020) 113891. https://doi.org/10.1016/j.jelechem.2020.113891.

[97] M. Yagi, S. Maruyama, K. Sone, K. Nagai, T. Norimatsu, Preparation and photoelectrocatalytic activity of a nano-structured WO3 platelet film, Journal of Solid State Chemistry. 181 (2008) 175–182. https://doi.org/10.1016/j.jssc.2007.11.018.

[98] W. Li, Photoelectrochemical and physical properties of WO3 films obtained by the polymeric precursor method, I n t e r n a t i o n a l j o u r n a l o f h y d r o g e n e n e r g y. (n.d.) 9.

[99] J. Yang, W. Li, J. Li, D. Sun, Q. Chen, Hydrothermal synthesis and photoelectrochemical properties of vertically aligned tungsten trioxide (hydrate) plate-like arrays fabricated directly on FTO substrates, (2012) 9.

[100] Y. Chai, C.W. Tam, K.P. Beh, F.K. Yam, Z. Hassan, Effects of thermal treatment on the anodic growth of tungsten oxide films, Thin Solid Films. 588 (2015) 44–49. https://doi.org/10.1016/j.tsf.2015.04.033.

[101] C.Y. Ng, K. Abdul Razak, Z. Lockman, Effect of annealing temperature on anodized nanoporous WO3, J Porous Mater. 22 (2015) 537–544. https://doi.org/10.1007/s10934-015-9924-x.

[102] S. Ismail, C.Y. Ng, E. Ahmadi, K.A. Razak, Z. Lockman, Segmented nanoporous WO3 prepared via anodization and their photocatalytic properties, J. Mater. Res. 31 (2016) 8.

[103] J. Wang, E. Khoo, P.S. Lee, J. Ma, Synthesis, Assembly, and Electrochromic Properties of Uniform Crystalline WO$_3$ Nanorods, J. Phys. Chem. C. 112 (2008) 14306–14312. https://doi.org/10.1021/jp804035r.

[104] J. Wang, E. Khoo, P.S. Lee, J. Ma, Controlled Synthesis of WO$_3$ Nanorods and Their Electrochromic Properties in H$_2$SO$_4$ Electrolyte, J. Phys. Chem. C. 113 (2009) 9655–9658. https://doi.org/10.1021/jp901650v.

[105] J.Z. Ou, S. Balendhran, M.R. Field, D.G. McCulloch, A.S. Zoolfakar, R.A. Rani, S. Zhuiykov, A.P. O'Mullane, K. Kalantar-zadeh, The anodized crystalline WO3 nanoporous network with enhanced electrochromic properties, Nanoscale. 4 (2012) 5980. https://doi.org/10.1039/c2nr31203d.

[106] K.J. Patel, C.J. Panchal, M.S. Desai, P.K. Mehta, An investigation of the insertion of the cations H+, Na+, K+ on the electrochromic properties of the thermally evaporated WO3 thin films grown at different substrate

temperatures, Materials Chemistry and Physics. 124 (2010) 884–890. https://doi.org/10.1016/j.matchemphys.2010.08.021.

[107] L.D. Mell, J.T. Maloy, B.M. Bezilla, M.S. Thesis, The Electrochromic Processat W03 Electrodes Prepared by Vacuum Evaporation and Anodic Oxidation of W, 126 (n.d.) 9.

[108] S.J. Calero, P. Ortiz, A.F. Oñate, M.T. Cortés, Effect of proton intercalation on photo-activity of WO3 anodes for water splitting, International Journal of Hydrogen Energy. 41 (2016) 4922–4930. https://doi.org/10.1016/j.ijhydene.2015.12.155.

[109] S.Q. Yu, Y.H. Ling, J. Zhang, F. Qin, Z.J. Zhang, Efficient photoelectrochemical water splitting and impedance analysis of WO 3−x nanoflake electrodes, International Journal of Hydrogen Energy. 42 (2017) 20879–20887. https://doi.org/10.1016/j.ijhydene.2017.01.177.

[110] L. Zhang, W. Wang, S. Sun, D. Jiang, Near-infrared light photocatalysis with metallic/semiconducting H x WO 3 /WO 3 nanoheterostructure in situ formed in mesoporous template, Applied Catalysis B: Environmental. 168–169 (2015) 9–13. https://doi.org/10.1016/j.apcatb.2014.12.018.

[111] Y. Liu, J. Li, W. Li, H. He, Y. Yang, Y. Li, Q. Chen, Electrochemical Doping Induced In Situ Homo-species for Enhanced Photoelectrochemical Performance on WO3 Nanoparticles Film Photoelectrodes, Electrochimica Acta. 210 (2016) 251–260. https://doi.org/10.1016/j.electacta.2016.05.165.

[112] R. Solarska, B.D. Alexander, A. Braun, R. Jurczakowski, G. Fortunato, M. Stiefel, T. Graule, J. Augustynski, Tailoring the morphology of WO3 films with substitutional cation doping: Effect on the photoelectrochemical properties, Electrochimica Acta. 55 (2010) 7780–7787. https://doi.org/10.1016/j.electacta.2009.12.016.

[113] Y. Li, Z. Tang, J. Zhang, Z. Zhang, Enhanced photocatalytic performance of tungsten oxide through tuning exposed facets and introducing oxygen vacancies, Journal of Alloys and Compounds. 708 (2017) 358–366. https://doi.org/10.1016/j.jallcom.2017.03.046.

[114] Y. Hu, L. Hao, Y. Zhang, X. Ping, T. Liu, Q. Zhao, S. Guan, Y. Lu, Defect concentration regulation in nanoflower-like WO3 film and its influence on photocatalytic activity, J Mater Sci: Mater Electron. (2021). https://doi.org/10.1007/s10854-021-05605-2.

[115] J. Guo, Y. Li, S. Zhu, Z. Chen, Q. Liu, D. Zhang, W.-J. Moon, D.-M. Song, Synthesis of WO 3 @Graphene composite for enhanced photocatalytic oxygen evolution from water, RSC Adv. 2 (2012) 1356–1363. https://doi.org/10.1039/C1RA00621E.

[116] A. Cordero-García, G. Turnes Palomino, L. Hinojosa-Reyes, J.L. Guzmán-Mar, L. Maya-Teviño, A. Hernández-Ramírez, Photocatalytic behaviour of WO3/TiO2-N for diclofenac degradation using simulated solar radiation as an activation source, Environ Sci Pollut Res. 24 (2017) 4613–4624. https://doi.org/10.1007/s11356-016-8157-0.

[117] Karthick. S, Sumisha. A, Haribabu. K, Performance of tungsten oxide/polypyrrole composite as cathode catalyst in single chamber microbial fuel cell, Journal of Environmental Chemical Engineering. 8 (2020) 104520. https://doi.org/10.1016/j.jece.2020.104520.

[118] D.M. Soares, R. Vicentini, A.C. Peterlevitz, C.B. Rodella, L.M. da Silva, H. Zanin, Tungsten oxide and carbide composite synthesized by hot filament chemical deposition as electrodes in aqueous-based electrochemical capacitors, Journal of Energy Storage. 26 (2019) 100905. https://doi.org/10.1016/j.est.2019.100905.

[119] X.V. Le, T.L.A. Luu, H.L. Nguyen, C.T. Nguyen, temperature by compositing carbon nanotubes with tungsten oxide nanobricks, (2019) 8.

[120] W.L. Kebede, D.-H. Kuo, K.E. Ahmed, H. Abdullah, Dye degradation over the multivalent charge- and solid solution-type n-MoS2/p-WO3 based diode catalyst under dark condition with a self-supporting charge carrier transfer mechanism, Advanced Powder Technology. 31 (2020) 2629–2640. https://doi.org/10.1016/j.apt.2020.04.028.

[121] S. Singh, N. Dogra, S. Sharma, A sensitive H2S sensor using MoS2/WO3 composite, Materials Today: Proceedings. 28 (2020) 8–10. https://doi.org/10.1016/j.matpr.2019.12.104.

[122] Facile sol-gel fabrication of MoS2 bulk, flake and quantum dot for electrochromic device and their enhanced performance with WO3, Electrochimica Acta. (2020) 9.

[123] G. Li, J. Hou, W. Zhang, P. Li, G. Liu, Y. Wang, K. Wang, Graphene-bridged WO3/MoS2 Z-scheme photocatalyst for enhanced photodegradation under visible light irradiation, Materials Chemistry and Physics. 246 (2020) 122827. https://doi.org/10.1016/j.matchemphys.2020.122827.

[124] D. Wei, Y. Ding, Z. Li, Noble-metal-free Z-Scheme MoS2–CdS/WO3–MnO2 nanocomposites for photocatalytic overall water splitting under visible light, International Journal of Hydrogen Energy. 45 (2020) 17320–17328. https://doi.org/10.1016/j.ijhydene.2020.04.160.

[125] A. Beyhaqi, Q. Zeng, S. Chang, M. Wang, S.M. Taghi Azimi, C. Hu, Construction of g-C3N4/WO3/MoS2 ternary nanocomposite with enhanced charge separation and collection for efficient wastewater treatment under visible light, Chemosphere. 247 (2020) 125784. https://doi.org/10.1016/j.chemosphere.2019.125784.

[126] M. Mojaddami, A. Simchi, Robust water splitting on staggered gap heterojunctions based on WO3\WS2–MoS2 nanostructures, Renewable Energy. 162 (2020) 504–512. https://doi.org/10.1016/j.renene.2020.08.016.

[127] Y. Zeng, Degradation of bisphenol a using peroxymonosulfate activated by WO3@MoS2/Ag hollow nanotubes photocatalyst, (2019) 9.

[128] H. Gong, Preparation and supercapacitive property of molybdenum disulfide (MoS2) nanoflake arrays- tungsten trioxide (WO3) nanorod

arrays composite heterojunction: A synergistic effect of one-dimensional and two-dimensional nanomaterials, (n.d.) 27.

[129] S.R. Biaggio, R.C. Rocha-Filho, J.R. Vilche, F.E. Varela, L.M. Gassa, A study of thin anodic WO3 films by electrochemical impedance spectroscopy, Electrochimica Acta. 42 (1997) 1751–1758. https://doi.org/10.1016/S0013-4686(96)00375-1.

[130] S. Berger, H. Tsuchiya, A. Ghicov, P. Schmuki, High photocurrent conversion efficiency in self-organized porous WO3, Appl. Phys. Lett. 88 (2006) 203119. https://doi.org/10.1063/1.2206696.

[131] M. Yang, N.K. Shrestha, P. Schmuki, Thick porous tungsten trioxide films by anodization of tungsten in fluoride containing phosphoric acid electrolyte, Electrochemistry Communications. 11 (2009) 1908–1911. https://doi.org/10.1016/j.elecom.2009.08.014.

[132] S. Ismail, K.A. Razak, P.W. Jing, Z. Lockman, A.M. Hashim, V.K. Arora, Tungsten Oxide Nanoporous Structure Synthesized Via Direct Electrochemical Anodization, in: Kuala Lumpur, (Malaysia), 2011: pp. 21–24. https://doi.org/10.1063/1.3586946.

[133] T. Zhu, M.N. Chong, E.S. Chan, Nanostructured Tungsten Trioxide Thin Films Synthesized for Photoelectrocatalytic Water Oxidation: A review, ChemSusChem. 7 (2014) 2974–2997. https://doi.org/10.1002/cssc.201402089.

[134] Y. Liu, Photoelectrochemical properties and photocatalytic activity of nitrogen-doped nanoporous WO3 photoelectrodes under visible light, Applied Surface Science. (2012) 8.

[135] N. Thangaraj, K. Tamilarasan, D. Sasikumar, Effect of current density on electrodeposited ferrous tungsten thin films, APPL PHYS. 52 (2014) 4.

[136] D.-Y. Park, N.V. Myung, M. Schwartz, K. Nobe, Nanostructured magnetic CoNiP electrodeposits: structure–property relationships, Electrochimica Acta. 47 (2002) 2893–2900. https://doi.org/10.1016/S0013-4686(02)00160-3.

[137] J. Kibsgaard, T.F. Jaramillo, F. Besenbacher, Building an appropriate active-site motif into a hydrogen-evolution catalyst with thiomolybdate [Mo3S13]22 clusters, NATURE CHEMISTRY. 6 (2014) 6.

[138] P.D. Tran, T.V. Tran, M. Orio, S. Torelli, Q.D. Truong, K. Nayuki, Y. Sasaki, S.Y. Chiam, R. Yi, I. Honma, J. Barber, V. Artero, Coordination polymer structure and revisited hydrogen evolution catalytic mechanism for amorphous molybdenum sulfide, NATURE MATERIALS. (n.d.) 8.

[139] J.-G. Choi, L.T. Thompson, XPS study of as-prepared and reduced molybdenum oxides, Applied Surface Science. 93 (1996) 143–149. https://doi.org/10.1016/0169-4332(95)00317-7.

[140] J. Baltrusaitis, Generalized molybdenum oxide surface chemical state XPS determination via informed amorphous sample model, Applied Surface Science. (2015) 11.

[141] G. Eda, H. Yamaguchi, D. Voiry, T. Fujita, M. Chen, M. Chhowalla, Photoluminescence from Chemically Exfoliated MoS $_2$, Nano Lett. 11 (2011) 5111–5116. https://doi.org/10.1021/nl201874w.

[142] A. Syari'ati, S. Kumar, A. Zahid, A. Ali El Yumin, J. Ye, P. Rudolf, Photoemission spectroscopy study of structural defects in molybdenum disulfide (MoS $_2$) grown by chemical vapor deposition (CVD), Chem. Commun. 55 (2019) 10384–10387. https://doi.org/10.1039/C9CC01577A.

[143] E.B. Castro, M.J. de Giz, E.R. Gonzalez, J.R. Vilche', An electrochemical impedance study on the kinetics and mechanism of the hydrogen evolution reaction on nickel molybdenite electrodes, (n.d.) 9.

[144] A. Lasia, Electrochemical Impedance Spectroscopy and its Applications, Springer New York, New York, NY, 2014. https://doi.org/10.1007/978-1-4614-8933-7.

[145] G.J. Brug, A.L.G. van den Eeden, M. Sluyters-Rehbach, J.H. Sluyters, The analysis of electrode impedances complicated by the presence of a constant phase element, Journal of Electroanalytical Chemistry and Interfacial Electrochemistry. 176 (1984) 275–295. https://doi.org/10.1016/S0022-0728(84)80324-1.

[146] M. Bojinov, The ability of a surface charge approach to describe barrier film growth on tungsten in acidic solutions, Electrochimica Acta. 42 (1997) 3489–3498. https://doi.org/10.1016/S0013-4686(97)00037-6.

[147] C.S. Blackman, I.P. Parkin, Atmospheric Pressure Chemical Vapor Deposition of Crystalline Monoclinic WO $_3$ and WO $_{3 - x}$ Thin Films from Reaction of WCl $_6$ with O-Containing Solvents and Their Photochromic and Electrochromic Properties, Chem. Mater. 17 (2005) 1583–1590. https://doi.org/10.1021/cm0403816.

[148] W. Li, J. Li, X. Wang, S. Luo, J. Xiao, Q. Chen, Visible light photoelectrochemical responsiveness of self-organized nanoporous WO3 films, Electrochimica Acta. 56 (2010) 620–625. https://doi.org/10.1016/j.electacta.2010.06.025.

[149] G. Wang, Y. Ling, H. Wang, X. Yang, C. Wang, J.Z. Zhang, Y. Li, Hydrogen-treated WO3 nanoflakes show enhanced photostability, Energy Environ. Sci. 5 (2012) 6180. https://doi.org/10.1039/c2ee03158b.

[150] L. Cheng, Y. Hou, B. Zhang, S. Yang, J.W. Guo, L. Wu, H.G. Yang, Hydrogen-treated commercial WO3 as an efficient electrocatalyst for triiodide reduction in dye-sensitized solar cells, Chem. Commun. 49 (2013) 5945. https://doi.org/10.1039/c3cc42206b.

[151] M. Vasilopoulou, A. Soultati, D.G. Georgiadou, T. Stergiopoulos, L.C. Palilis, S. Kennou, N.A. Stathopoulos, D. Davazoglou, P. Argitis, Hydrogenated under-stoichiometric tungsten oxide anode interlayers for efficient and stable organic photovoltaics, J. Mater. Chem. A. 2 (2014) 1738–1749. https://doi.org/10.1039/C3TA13975A.

[152] S.Y. Lee, G. Shim, J. Park, H. Seo, Tunable polaron-induced coloration of tungsten oxide *via* a multi-step control of the physicochemical property

for the detection of gaseous F, Phys. Chem. Chem. Phys. 20 (2018) 16932–16938. https://doi.org/10.1039/C8CP00158H.

[153] M. Mokhtarimehr, S.A. Tatarkova, Photocurrent transients of thin-film solar cells, J. Opt. Soc. Am. B. 34 (2017) 1705. https://doi.org/10.1364/JOSAB.34.001705.

[154] R. Peat, L.M. Peter, A study of the passive film on iron by intensity modulated photocurrent spectroscopy, Journal of Electroanalytical Chemistry and Interfacial Electrochemistry. 228 (1987) 351–364. https://doi.org/10.1016/0022-0728(87)80117-1.

[155] A. Goossens, Intensity-modulated photocurrent spectroscopy of thin anodic films on titanium, Surface Science. (1996) 10.

[156] M. Rodríguez-Pérez, I. Rodríguez-Gutiérrez, A. Vega-Poot, R. García-Rodríguez, G. Rodríguez-Gattorno, G. Oskam, Charge transfer and recombination kinetics at WO3 for photoelectrochemical water oxidation, Electrochimica Acta. 258 (2017) 900–908. https://doi.org/10.1016/j.electacta.2017.11.140.

[157] T.L. Villarreal, R. Gómez, M. Neumann-Spallart, N. Alonso-Vante, P. Salvador, Semiconductor Photooxidation of Pollutants Dissolved in Water: A Kinetic Model for Distinguishing between Direct and Indirect Interfacial Hole Transfer. I. Photoelectrochemical Experiments with Polycrystalline Anatase Electrodes under Current Doubling and Absence of Recombination, J. Phys. Chem. B. 108 (2004) 15172–15181. https://doi.org/10.1021/jp049447a.

[158] I. Mora-Seró, T.L. Villarreal, J. Bisquert, Á. Pitarch, R. Gómez, P. Salvador, Photoelectrochemical Behavior of Nanostructured TiO $_2$ Thin-Film Electrodes in Contact with Aqueous Electrolytes Containing Dissolved Pollutants: A Model for Distinguishing between Direct and Indirect Interfacial Hole Transfer from Photocurrent Measurements, J. Phys. Chem. B. 109 (2005) 3371–3380. https://doi.org/10.1021/jp045585o.

[159] T.A. Kandiel, Mechanistic investigation of water oxidation on hematite photoanodes using intensity-modulated photocurrent spectroscopy, Journal of Photochemistry and Photobiology A: Chemistry. 403 (2020) 112825. https://doi.org/10.1016/j.jphotochem.2020.112825.

SANTRAUKA

Foto-/elektrokatalizinių MoS₂ ir WO₃ plonų sluoksnių elektrocheminis nusodinimas ir pritaikymas vandens skaidymo katalizei

ĮVADAS

Šiuo metu Europos Sąjunga yra užsibrėžusi tikslą iki 2030-ųjų metų beveik trečdalį (27%) bendrijos šalių suvartojamos elektros energijos pagaminti iš atsinaujinančių išteklių. Atsinaujinančiais šaltiniais įprastai vadinami tie, kuriuos galima atkurti per pakankamai trumpą laiko tarpą, arba tie, kurie yra iš esmės neišsenkantys – pavyzdžiui saulės ar vėjo energija. Pastarieji energijos šaltiniai jau dabar plačiai naudojami, tačiau norint iš tiesų pasauliniu lygmeniu pereiti prie atsinaujinančios energetikos netolimoje ateityje reikės didelių pastangų pritaikant jau esamą infrastruktūrą arba kuriant naują. Pagamintą elektros energiją galima nesunkiai tiekti į vietinius ar tarptautinius tinklus. Kita vertus, pritaikyti vidaus degimo variklius, kad šie galėtų naudoti ne angliavandenių pagrindo skystą kurą, nepraktiška ar net neįmanoma.

Atsinaujinantys energijos šaltiniai dažnai veikia nepastoviai, jų efektyvumas priklauso nuo paros meto ar klimato sąlygų. Todėl itin aktualu tampa energijos kaupimas ir saugojimas. Paprasčiausias ir kol kas labiausiai paplitęs elektros energijos kaupimo būdas yra baterija: įprastos ličio jonų baterijos energetinis tankis yra ~ 152 W·h kg^{-1}, tačiau nanostruktūrizavimo būdu gali būti gerokai padidintas iki bent 690 W·h kg^{-1}. Palyginimui, benzino ir dyzelio energetiniai tankiai siekia apie 13 000 W·h kg^{-1}, o vandenilio – 30 000 W·h kg^{-1}

Būtent dėl šio išskirtinai didelio gravimetrinio (o suspaustoms dujoms ir volumetrinio) energetinio tankio tikimasi, kad vandenilis bus plačiau naudojamas energetikoje. Tačiau 2019 metais tik 4% ES pagaminto vandenilio buvo „švarus", t.y. pagamintas neišskiriant taršių šalutinių produktų. Bene geriausias būdas švariai gaminti vandenilį yra elektrolizė – vandens skaidymas elektros energija į H₂ ir O₂ dujas. Be abejo, ar technologija ras platų pritaikymą priklauso nuo jos sąnaudų kainos. 2020 metais Bloomberg paskelbti skaičiavimai teigė, jog šiuo metu elektrolizės būdu pagamintas vandenilis kainuoja nuo 2,5$ iki 4.5$ už kilogramą. Palyginimui – kitais būdais gaminamo vandenilio kaina apie 1,1$ už kilogramą. Tikimasi, kad pingant elektrolizės būdu gamintam vandeniliui iki 2030 metų šios kainos išsilygins, o 2050 metais elektrolizės būdu gautas vandenilis kainuotų tik 0,7$ – 1.6$ už kilogramą.

Jeigu energetikos pramonėje vandeniliui atsiras paklausa, tada jo gamyba vandens elektrolizės būdu tikrai taps svarbia vandenilio ekonomikos dalimi. Pagaminto vandenilio kaina susidėtų iš sunaudotos elektros energijos, žaliavos (vandens), ir elektrolizės celės kainų. Paprastos medžiagos (pvz. plienas) yra pigios, tačiau nepakankamai efektyvios. Celės efektyvumą galima padidinti naudojant katalizatorius; šių kaina didesnė, bet jie gerokai padidina celės efektyvumą.

Dėl to vandens skilimo katalizę tyrinėjančioje mokslo sferoje šiuo metu intensyviai vykdomi tyrimai, siekiant sukurti kuo pigesnius ir efektyvesnius katalizatorius. Elektrolizinę celę sudaro du elektrodai – katodas, prie kurio vyksta vandenilio skyrimosi reakcija, ir anodas, prie kurio vyksta deguonies skyrimosi reakcija. Taurieji metalai (pvz. platina, paladis) itin gerai katalizuoja vandenilio skyrimosi reakciją, tačiau jų kaina neleidžia jų naudoti plačiu mastu. Deguonies skyrimosi reakciją gerai taip pat gerai katalizuoja brangiųjų metalų, tokių kaip rutenis ar iridis, oksidai. Pigesnių alternatyvų ieškoma būtent šioms medžiagoms.

Tyrimai šioje srityje, žinoma, tęsis dar ilgai. Dalis medžiagų, kurios šiuo metu laikomos labai perspektyviomis foto- ar elektrokatalizėje, iš tiesų buvo susintetintos dar prieš kelis dešimtmečius. Molibdeno disulfidas (MoS_2) ir volframo trioksidas (WO_3) yra du tokie pavyzdžiai. MoS_2 buvo laikytas inertine ir neįdomia medžiaga, kol nebuvo atrasta, kad tam tikrose šios medžiagos struktūrose esantys aktyvus centrai turi bene optimalią vandenilio adsorbcijos laisvąją energiją. WO_3 sulaukė platesnio susidomėjimo kai pradėta ieškoti oksidų, pasižyminčių panašiomis elektrocheminėmis savybėmis kaip TiO_2, bet turinčių mažesnį draustinės juostos plotį. Šios medžiagos ir buvo išsamiai tirtos šioje disertacijoje.

Darbo tikslai:

Šio darbo tikslas buvo elektrochemiškai susintetinti foto-/elektrokatalizinius MoS_2, WO_3, bei naujus WO_3+MoS_2 plonus medžiagų sluoksnius. Taip pat parinkti tokias sluoksnių elektrocheminio nusodinimo ar modifikavimo sąlygas, kurias naudojant būtų pasiektas didžiausias įmanomas katalizinis aktyvumas.

Darbo uždaviniai yra:

1. Elektrochemiškai susintetinti MoS_2, WO_3, ir WO_3+MoS_x plonus sluoksnius atitinkamai katodinio nusodinimo ir anodavimo būdais. Šiuos sluoksnius optimizuoti, reguliuojant proceso parametrus: katalizinės medžiagos kiekį, elektrolito sudėtį, aktyvių centrų kiekį/aktyvumą.

2. Nustatyti sąryšį tarp elektrocheminio nusodinimo sąlygų, gautų katalizinių sluoksnių struktūrinių ir morfologinių ypatybių, bei foto-/elektrocheminio aktyvumo.

3. Stacionariais ir nestacionariais metodais (EIS, PEIS, IMPS) ištirti elektrocheminius procesus ir apibūdinti gautus katalizinius sluoksnius ir įvertinti jų pritaikomumą.

Mokslinis naujumas

Pritaikant heterogeninę elektrokatalizę sumažinamas elektrocheminės reakcijos aktyvacijos barjeras ir padidinamas jos greitis; tokiu būdu procesui įvykti sunaudojama daug mažiau energijos. Būtent todėl katalizė tokia svarbi efektyviam elektrocheminiam vandens skaidymui į O_2 ir H_2. Katalizinių medžiagų įvairovė yra didelė, tačiau kiekvienas katalizatorius atitinka tam tikrą paskirtį. MoS_2 struktūroje egzistuoja aktyvūs centrai kuriuose lengvai adsorbuojamas H^+, todėl ši medžiaga naudojama vandenilio skyrimosi reakcijos katalizei. Šiuos aktyvius centrus galima toliau modifikuoti, siekiant dar optimalesnio Mo – H ryšio energijos susidarymo. WO_3 draustinės juostos plotis atitinka dalį regimosios šviesos spektro energijos, todėl ši medžiaga yra perspektyvus fotokatalizatorius. Ją galima toliau modifikuoti optimizuojant struktūroje esančių defektų koncentraciją, arba siekiant dar labiau sumažinti draustinės juostos plotį (pvz. susintetinant WO_3 ir MoS_2 kompozitą).

Apibūdinant heterogeninius katalizatorius dažnai neįvertinamas elektrochemiškai aktyvus paviršiaus plotas ir lieka neaišku, kokie išmatuoti parametrai geriausiai apibūdina susintetintą katalizatorių. Šiuose tyrimuose, derinant stacionarius ir nestacionarius elektrocheminius metodus, nustatyti parametrai, kurie gali būti naudojami objektyviai apibūdinti tam tikrus katalizinių medžiagų parametrus. Vandenilio skyrimosi reakcijos katalizatoriams (MoS_2) apskaičiuota adsorbcijos talpa nepriklauso nuo medžiagos paviršiaus ploto. Pasiūlytas būdas iš šios talpos apskaičiuoti aktyvių centrų skaičių. WO_3 fotokatalizatorius galima apibūdinti panašiu parametru – fotolaidžiu, kuris priklauso nuo fotogeneruotų krūvio pernašos dalelių koncentracijos. Taigi, šių tyrimų rezultatai yra žingsnis link praktinių ir fundamentinių heterogeninės foto-/elektrokatalizės principų sujungimo.

EKSPERIMENTŲ METODIKA

Jei nenurodyta kitaip, visi elektrocheminiai eksperimentai vykdyti Metrohm µAutolab Type III ir Autolab 302N potenciostatais. Potencialai pateikti sotaus Ag/AgCl palyginamojo elektrodo skalėje.

MoS$_4^{2-}$ pradmens tirpalo ruošimas. MoS$_4^{2-}$ elektrolitas paruoštas maišant ir rūgštinant (NH$_4$)$_6$Mo$_7$O$_{24}$·4H$_2$O ir 60 % Na$_2$S·xH$_2$O tokiais santykiais, kad galutiniame tirpale būtų gauta 25 mM MoS$_4^{2-}$ koncentracija. Galutinio elektrolito pH buvo ~ 8. Vykdant nusodinimą ant vario vielos į tirpalą pridėta 2-propanolio, kad jo masės dalis būtų 10%. Vykdant nusodinimą ant vario putų, į tirpalą pridėta 0,1 M Na$_2$SO$_4$ ir, pasirinktinai, 0,1 M NaH$_2$PO$_2$.

MoS$_2$ plonų sluoksnių elektrocheminis nusodinimas. Šiuose tyrimuose MoS$_2$ sluoksniai buvo katodiškai nusodinti ant vario vielos ir metalinių vario putų substratų. Elektrodai buvo nuvalyti, plauti ultragarso vonelėje 2-propanolyje, prieš nusodinimą įmerkti į 2 M H$_2$SO$_4$ siekiant nutirpinti paviršiuje esančius oksidus, tada gerai nuskalauti distiliuotu vandeniu. Vykdant nusodinimą ant vario vielos, MoS$_{2-x}$ ploni sluoksniai buvo nusodinami 600 s keičiant potencialą (nuo -0,8 V iki -1,2 V) arba esant -1,0 V ir keičiant trukmę (200 s – 7200 s). Vykdant nusodinimą ant vario putų buvo suformuoti 2 x 2 x 0,13 cm elektrodai ir susukti į cilindro formą. Nusodinimas vykdytas galvanostatiškai (nustatant – 10 mA srovę), ir keičiant trukmę/pratekėjusį krūvį (1000 s – 4000 s / 10 C – 40 C). Vario putų elektrodai taip pat buvo pasverti prieš ir po nusodinimo, taip sužinant nusėdusio MoS$_{2-x}$ masę.

WO$_3$ ir WO$_3$ + MoS$_x$ plonų sluoksnių sintezė anodavimo būdu. Anodavimas vykdytas potenciostatiškai ir galvanostatiškai, bei skirtinguose elektrolituose (1 M HCl, 1 M H$_2$SO$_4$, 14 M H$_3$PO$_4$, 14 M H$_3$PO$_4$ + 1 M NH$_4$F, 0.3 M oksalo rūgštyje, 1 M Na$_2$SO$_4$ + 75 mM NaF + 0,1 M NaH$_2$PO$_2$). Anoduojant esant aukštoms įtampoms naudotas Consort EV 245 potenciostatas. Elektrodai anodavimui buvo paruošti iš metalinio volframo (>99,5%): 1 cm^2 paviršiaus ploto viela, arba 1 x 1 cm plokštelė. Prieš eksperimentus plokštelės buvo poliruotos, įmerktos į koncentruotą NaOH siekiant nutirpinti paviršiaus oksidus, plautos acetone ar 2-propanolyje ultragarso vonioje, ir nuskalautos distiliuotu vandeniu. Anodavimai vykdyti esant žemiems ir aukštiems potencialams. Esant žemiems potencialams tirta WO$_3$ augimo kinetika. Esant aukštiems potencialams sintetinti sluoksniai fotoelektrocheminiams tyrimams.

0,3 M oksalo rūgšties elektrolite WO$_3$ sluoksniai buvo sintetinti vykdant potenciostatinį anodavimą 30 minučių, esant potencialams nuo 10 V iki 60 V.

1 M Na$_2$SO$_4$ + 75 mM NaF + 0,1 M NaH$_2$PO$_2$ elektrolite anodavimas vykdytas galvanostatiškai (25 mA cm^2 srovės tankiu), keičiant trukmę nuo 2 iki 30 minučių. WO$_3$ + MoS$_x$ kompozito ploni sluoksniai sintetinti tokiu pat būdu, tačiau į aukščiau minėtą elektrolitą pridėjus 25 mM MoS$_4^{2-}$.

MoS₂ plonų sluoksnių katalizinio aktyvumo tyrimas. Po elektrocheminio nusodinimo, MoS_2 plonais sluoksniais padengti elektrodai buvo nuskalauti distiliuotu vandeniu ir nedžiovinant perkelti į 0,5 M H_2SO_4 elektrolitą, kuriame vykdytas katalizinio aktyvumo apibūdinimas. Tiriant vario vielos elektrodus, įprasta eksperimentinė seka buvo tokia: atviros grandinės potencialo nusistovėjimas, elektrocheminio impedanso spektro (EIS) užrašymas esant -0,32 V (- 0,1 V pagal RHE), 10-ies poliarizacinių kreivių nubrėžimas (10 mV s^{-1} potencialo skleidimo greičiu) ir stabilumo matavimas (galvanosatiškai esant 40 mA cm^{-2} katodinės srovės tankiui). Poliarizacinėms kreivėms atlikta *iR* (ominio kritimo) korekcija. EIS spektrai registruoti 10 kHz – 0,1 Hz diapazone, naudojant 20 mV amplitudę. Tiriant MoS_2 sluoksnius, nusodintus ant vario putų elektrodų, poliarizacinės kreivės brėžtos 2 mV s^{-1} greičiu, o EIS spektrai registruoti esant skirtingiems potencialams (pagal RHE: 0 V, -0,1 V, -0,15 V, -0,175 V, -0,2 V, -0,25 V, -0,3 V). Elektrocheminio impedanso spektrai interpretuoti modeliuojant ekvivalentines elektrines schemas.

WO₃ sluoksnių augimo kinetikos tyrimas EIS būdu. EIS spektrai registruoti esant nuo 0 iki 5 V potencialams, žingsniais kas 0,1 V. Elektrodas laikytas 10 minučių esant kiekvienam potencialo žingsniui, ir po šio laiko užrašytas impedanso spektras 10 kHz – 0,01 Hz dažnių diapazone. Tokiu būdu buvo gauti impedanso spektrai, nusakantys WO_3 sluoksnio augimą.

WO₃ sluoksnių fotokatalizinio efektyvumo tyrimas. Tyrimams naudota tiesinė voltamperometrija (LSV), chronoamperometrija, foto-EIS, ir moduliuojamo intensyvumo fotosrovės spektroskopija. Naudota kvarcinė celė ir apšvietimas iš priekio. Tyrimai atlikti naudojant „Autolab Optical Bench" sistemą, su kalibruojamu 365 nm bangos ilgio šviesos diodu. Tiriant 0,3 M oksalo rūgštyje potenciostatiškai sintetintus WO_3 sluoksnius naudotas 0,5 M Na_2SO_4 elektrolitas. Tiriant 1 M Na_2SO_4 + 75 mM NaF + 0,1 M NaH_2PO_2 (+ 25 mM MoS_4^{2-}) sintetintus WO_3 ir WO_3+MoS_x sluoksnius, naudotas 0,1 M Na_2SO_4 elektrolitas, kuris parūgštintas iki pH 2. Foto-EIS spektrai registruoti 10 kHz – 0,1 Hz dažnių srityje, esant potencialams nuo 0,4 V iki 2,0 V. Moduliuojamo intensyvumo fotosrovės spektrai registruoti tokioje pačioje dažnių srityje, moduliuojant srovės šaltinio intensyvumą (50 mW cm^{-2}) 10 % amplitude. Siekiant pagerinti WO_3 sluoksnių fotokatalizines savybes, atlikta katodinės redukcijos ir anodinės aktyvacijos procedūra: elektrodas redukuotas esant -0,5 V 300s, po to aktyvuotas esant 1,2 V ir UV apšvietai 3000 sekundžių.

Morfologija, struktūra, sudėtis. Paviršiaus morfologija tirta skenuojančiu elektroniniu mikroskopu (Hitachi TM 3000 ir Hitachi S-3400N). Cheminė sudėtis tirta Hitachi TM 3000 su integruotu EDX moduliu. XPS analizės atliktos Kratos Axis Supra spektrometru. Skersinių pjūvių tyrimai fokusuoto galio jonų pluoštelio metodu (FIB) atlikti Helios Nanolab 650 sistema.

REZULTATŲ APTARIMAS

MoS₂ plonų sluoksnių elektrocheminis nusodinimas ant vario ir metalinių putų substratų

Ant abiejų substratų atlikus LSV ir ciklinės voltamperometrijos (CV) tyrimus pastebėta, jog MoS_2 katodinio nusodinimo kreivėse nėra ryškių smailių, ir kad procesas vyksta kartu su vandenilio skyrimusi (5 pav., 41 p.). Atliekant nusodinimą ant vario putų taip pat tirta reduktoriaus natrio hipofosfito įtaka, tačiau šis priedas iš esmės nepakeitė CV kreivių profilio. Atliekant potenciostatinį MoS_2 nusodinimą ant vario vielos substratų pastebėta, kad esant neigiamesniam potencialui (pvz. -1,2 V) arba prailginus nusodinimą (pvz. nuo 600 s iki1800 s) gaunami suskilinėję sluoksniai (6 pav., 43 p.). Todėl tolimesniems nusodinimams parinktas vidutinis -1,0 V potencialas. Atliekant MoS_2 nusodinimą ant vario putų substratų buvo naudotos galvanostatinės sąlygos (-10 mA) ir nusodinimas atliekamas kol per sistemą pratekėjo nuo 10 C iki 40 C. Šiuo atveju MoS_2 sluoksniai buvo gana gerai prikibę prie substrato, o atliekant nusodinimą su NaH_2PO_2 priedu pastebėta, kad paviršiaus morfologija tampa lygesnė (7 pav., 44 p.).

EDX tyrimai atskleidė, jog atliekant nusodinimą esant tai pačiai trukmei, tačiau neigiamesniam potencialui, arba esant tam pačiam potencialui bet ilgesnei trukmei, gauto sluoksnio sudėtyje didėja Mo ir S kiekiai (8 pav., 45 p.). Visi gauti sluoksniai yra nestechiometriniai ir jų formulė būtų MoS_{2-x}. Kai nusodinimas vykdytas ant vario putų substratų, nusodintų sluoksnių Mo ir S santykiai siekė nuo $MoS_{1,72}$ iki $MoS_{1,87}$. Nusodinimo metu elektrolite esant NaH_2PO_2, susintetintų MoS_{2-x} sluoksnių stechiometrija buvo artimesnė MoS_2 (5 lentelė, 46 p.). XPS tyrimais nagrinėta ant vario putų nusodintų MoS_2 sluoksnių analizė. Nustatyta, kad MoS_2 sluoksniuose gana daug Mo^{6+}-O ryšių, t.y. MoO_3, bet jei nusodinimas atliktas elektrolite su NaH_2PO_2, matomas daug stipresnis Mo^{4+}- S ryšio signalas (9 pav., 47 p.).

MoS₂ sluoksnių katalizinio aktyvumo vandenilio skyrimosi reakcijai tyrimas

10 pav. 49 p., pavaizduotos voltamperometrinės ir chronoamperometrinės kreivės, gautos ant vario vielos nusodintiems MoS_2 sluoksniams. Akivaizdu,

kad didesniu kataliziniu aktyvumu pasižymi sluoksniai, nusodinti arba 600 s ir -1,2 V potencialui, arba 7200 s ir -1,0 V potencialui. Tokiu būdu gauta, kad. katalizinis efektyvumas koreliuoja su nusodintu katalizatoriaus kiekiu. Taip pat išmatuotas šių sluoksnių stabilumas galvanostatinėmis sąlygomis. Analogiški matavimai atlikti ir naudojant ant vario putų nusodintus MoS_2 sluoksnius (11 pav. 50 p.), kuriuose didesniu vandenilio skyrimosi reakcijos kataliziniu aktyvumu taip pat pasižymi ilgiau sodinti sluoksniai. Kita vertus, kai MoS_2 sluoksniai sintetinti elektrolite esant NaH_2PO_2, jų kataliznis aktyvumas didesnis. Manoma, kad toks efektas pastebimas dėl medžiagos vidinio aktyvumo pagerėjimo. Įvairūs katalizatorius apibūdinantys parametrai kaip Tafelio nuolinkio kampas bei mainų srovė yra pateikti 6 lentelėje (52 p.). Apskaičiuoti Tafelio nuolinkio kampai siekė nuo 40 iki 60 mV dec^{-1}, o tai reiškia, kad vandenilio skyrimasis vyksta pagal Volmer-Heyrovsky mechanizmą.

Vandenilio skyrimosi reakcijos kinetikos ir aktyvių centrų tyrimas EIS būdu

EIS buvo naudota tikintis objektyviau įvertinti gana skirtingų katalizinių elektrodų ypatybes. Spektrai registruoti tame pačiame tirpale, kaip ir prieš tai aptartas katalizinio aktyvumo charakterizavimas. EIS spektrai kurie buvo gauti ant vario vielos nusodintiems MoS_2 sluoksniams pavaizduoti 12 pav., (54 p.) ir juose matyti, jog ilgiau nusodinti sluoksniai turi mažesnius impedansus ir lėtesnį fazės atsaką. EIS spektrai gauti ant vario putų nusodintiems sluoksniams (13 pav., 55 p.) akivaizdžiai parodo, kad sistemos impedansas sparčiai mažėja keliant viršįtampį. Kompleksinėse koordinatėse matomi du pusapskritimiai – aukšto dažnio atsakas ir žemo dažnio atsakas. Būtent žemo dažnio pusapskritimis labiausiai priklauso nuo viršįtampio, todėl jis pagrinde apibūdina sistemos kinetiką.

Šie spektrai modeliuoti naudojant ekvivalentinę schemą pavaizduotą 14 pav. (56 p.), kuri susideda iš tirpalo varžos (R_s), dvigubo sluoksnio talpos (C_{dl}), krūvio pernašos varžos (R_{ct}), adsorbcijos pseudotalpos (C_a), bei adsorbcijos varžos (R_a). Įvertinta modeliavimo būdu apskaičiuotų parametrų priklausomybė nuo nusodinimo trukmės / per sistemą pratekėjusio krūvio: C_a parametras tiesiogiai didėja didinant nusodinimo laiką, o R_a parametras eksponentiškai mažėja (15 pav., 57 p.).

Apjungiant vario vielos ir metalinių putų elektrodus bei EIS rezultatus pastebėta, kad gauti parametrai priklauso nuo nusodinimo metu per sistemą pratekėjusio krūvio. R_a parametro eksponentinis kritimas nepriklauso nuo to, ar MoS_2 sluoksnis buvo susintetintas ant vario vielos ar putų elektrodų; analogiška tendencija pastebėta ir viršįtampiui, kurio reikia norint pasiekti 10

mA vandenilio skyrimosi srovę η_{10mA} (16 pav. a, 58 p.). Panašios tendencijos atsiskleidžia ir nagrinėjant kitus parametrus – C_a, i_0, $i_{\eta=0,1V}$ (16 pav., b, c, d, 58 p.). Tiriant šių parametrų priklausomybę nuo viršįtampio nustatyta, kad didinant viršįtampį R_a mažėja logaritmiškai. Jei MoS_2 sluoksniai nusodinami elektrolite esant NaH_2PO_2, jų R_a vertės yra mažesnės. Galiausiai, laikant, jog pseudotalpa C_a yra tiesiogiai susijusi su vandenilio adsorbcijos reakcija, C_a vertės panaudotos apskaičiuoti kiek aktyvių centrų yra susintetintuose MoS_2 sluoksniuose. Buvo laikyta, kad vienas aktyvus centras adsorbuoja vieną H^+, ir kad H^+ adsorbcija yra vieno elektrono procesas. Toliau, pagal 28 ir 29 lygtis apskaičiuotas aktyvių centrų kiekis $N_{centr.}$ Gautos vertės siekė nuo 10^{15} iki 10^{17} centrų per cm^{-2}, ir buvo panašios į literatūroje skelbiamas vertes.

Iš gautų aktyvių centrų kiekio verčių paskaičiuota kiek išsiskyrusio vandenilio molekulių tenka vienam aktyviam centrui per sekundę tekant 1 mA srovei (TOF – skyrimosi dažnis). Tokiu būdu prieš tai gautos poliarizacinės kreivės buvo perskaičiuotos, ir nubrėžtos TOF – viršįtampio priklausomybės (17 pav. 60p.). Jos skiriasi nuo prieš tai aptartų poliarizacinių kreivių tuo, kad jose atsiskleidžia ne bendras elektrodo aktyvumas, o fundamentalus medžiagos aktyvumas. Akivaizdu, jog MoS_2 sluoksnis nusodintas per 1000 s esant -1,0 V ant vario vielos yra pats aktyviausias, nes jis pasiekia aukščiausias TOF vertes esant mažiausiems viršįtampiams. Taipogi matoma, kad bendrai aktyviausi buvo nusodinti sluoksniai per 600 s iki 1200 s.

Visi rezultatai vėl susieti tarpusavyje, atidedant TOF (apskaičiuoto esant 0,2 V viršįtampiui) priklausomybę nuo nusodinimo metu pratekėjusio krūvio (18 pav., 61 p.). Šioje kreivėje išryškėja aiški tendencija iki maksimumo, kuris gautas būtent 1000 s nusodintam sluoksniui. Dydis, kuris atvirkščiai proporcingas TOF – žemo dažnio laiko konstanta τ_{LF} ($\tau_{LF} = C_a \cdot R_a$) turi priešingą tendenciją ir pasiekia minimumą.

Tokiu būdu atskirtas medžiagos aktyvumas nuo elektrodo aktyvumo. Visgi aktyviausi elektrodai vandenilio skyrimosi reakcijos katalizei yra gaunami ant vario putų elektrolizuojant 7200 s esant -1,0 V, , praleidžiant nuo 10 C iki 40 C elektros kiekį.

WO_3 sluoksnių sintezės tyrimas

Siekiant ištirti WO_3 sluoksnių sintezės ir augimo pobūdį, poliarizacinės kreivės nustatytos skirtinguose anodavimo elektrolituose (19 pav., 62p.). Visų kreivių profilis panašus – pasiekiama anodinė smailė (skirtinguose elektrolituose geriau ar prasčiau išsiskiria 3 smailės), po kurios srovės tankis nukrenta ir stabilizuojasi. Sąlyginai dideli anodavimo srovės tankiai pastebėti 0,3 M oksalo rūgšties ir 1 M Na_2SO_4 + 75 mM NaF + 0,1 M NaH_2PO_2 elektrolituose. Tai parodo spartesnį volframo tirpimo greitį. WO_3 sluoksnių

formavimosi kinetikos tyrimui taip pat naudota EIS. Spektrai buvo matuoti kaip aprašyta eksperimentinėje dalyje. Iš 20 pav. (63 p.) matyti, jog sistemos impedansas didėja esant didesniam anodiniam potencialui; spektruose taip pat išryškėja indukcinė kilpa.

Šie spektrai buvo modeliuoti ekvivalentine elektrine schema (21 pav., 64 p.), kurią sudaro: elektrolito varža R_s, Faradėjinė pseudotalpa C_0 ir su ja susieta varža R_0, oksido sluoksnio talpa C_b, krūvio pernašos/defektų migracijos varža R_b, bei R_c ir L_c – indukciniai elementai, atsirandantys dėl prie paviršiaus susikaupiančių priešingo krūvio jonų. Nagrinėta šių elementų priklausomybė nuo potencialo (22 pav., 65 p.), kurioje matoma kaip kinta keli esminiai parametrai. C_b ir R_b yra tiesiogiai susiję su sluoksnio storiu, taigi jų tiesinė priklausomybė nuo potencialo parodo, kad sluoksnio storis tiesiogiai priklauso nuo potencialo. Taip pat įdomu pastebėti, jog su induktyvumu susiję parametrai rodo panašias tendencijas.

WO$_3$ plonų sluoksnių sintezė anodavimo būdu

0,3 M oksalo rūgštyje anodavimas vykdytas potenciostatiškai, esant įtampoms nuo 20 V iki 60 V. Anodavimas visais atvejais vykdytas 30 minučių. Anodavimo kreivėje (23 pav., 66 p.) matyti, jog srovės tankis pasiekia maksimumą esant ~ 10 V, o toliau keliant įtampą nežymiai krenta. Susintetintų plonų WO$_3$ sluoksnių SEM atvaizdai pateikti 23 pav. b-d, ir jose matyti, kad anoduojant esant 20 V gaunamas gana kompaktiškas sluoksnis, o vykdant anodavimą esant 60 V gaunamas storesnis, grubus, mikrostrukūrizuotas sluoksnis. Iš skersinių pjūvių analizės nustatyta, jog sluoksnio storis iš tiesų tiesiškai priklauso nuo anodavimo įtampos (24 pav., 67 p.).

1 M Na$_2$SO$_4$ + 75 mM NaF + 0,1 M NaH$_2$PO$_2$ elektrolite anodavimas vykdytas galvanostatiškai esant 25 mA cm^{-2} srovės tankiui; anodavimo trukmė buvo nuo 2 iki 30 minučių. Šiame elektrolite gautoje galvanostatinio anodavimo kreivėje (25 pav., a, 68 p.) matyti, jog per pirmas 2 minutes pasiekiama ~ 80 V įtampa, kuri beveik nekinta viso proceso metu. Gautų WO$_3$ sluoksnių storiai tiesiogiai priklauso nuo anodavimo trukmės, ir siekia nuo 0,71 μm iki 3,91 μm. Jų paviršiaus morfologija poringa, o skerspjūvio nuotraukos parodo, jog sluoksnių vidinė struktūra taip pat poringa (25 pav., b-g, 68 p.). XPS spektruose matomas itin stiprus W^{+6} - O ryšių signalas (96,9%), ir galima teigti, jog ši medžiaga yra beveik grynas WO$_3$. Tačiau matomas ir silpnas W^{5+} signalas (3,1 %), kuris taip pat yra itin reikšmingas, nes atitinka defektus/deguonies vakansijas medžiagos struktūroje.

1 M Na₂SO₄ + 75 mM NaF + 0,1 M NaH₂PO₂ + 25 mM MoS₄²⁻ elektrolite galvanostatinio anodavimo būdu sintetinti WO_3+MoS_x kompozito ploni sluoksniai. Kadangi kaip pavaizduota 2-oje reakcijoje iš MoS_4^{2-} jonų anodiškai gali skirtis MoS_3, anodavimo metu vyksta WO_3 sluoksnio augimas ir MoS_3 anodinis nusėdimas. Tokio anodavimo kreivė pavaizduota 27 pav., a (70 p.) ir joje matyti, kad per ~ 2 minutes pasiekiama maksimali įtampa (74 V), kuri po 30 minučių nukrenta iki 63 V. Kaip ir prieš tai, anodavimas vykdytas esant 25 mA cm⁻² srovės tankiui ir nuo 2 iki 30 minučių. Sluoksnių morfologija ir giluminė struktūra taip pat yra poringa (27 pav., b-g, 70 p.). EDX būdu gauti elementų žemėlapiai patvirtina, kad po 30 minučių anodavimo gautų kompozitų struktūrose išties yra Mo ir S (28 pav., 71p.), tačiau pagrinde sluoksnio paviršiuje. XPS analizė taip pat patvirtina MoS_x įsiterpimą į WO_3 sluoksnį, matomi signalai iš Mo^{+6}-O ir Mo^{+4}-S ryšių (29 pav., 72 p.).

WO₃ plonų sluoksnių modifikavimas katodinės redukcijos ir anodinės aktyvacijos būdu

WO_3 yra elektrochrominė medžiaga, o tai reiškia, jog į jos struktūrą gali interkaliuotis maži jonai (pvz. H^+) taip pakeičiant medžiagos struktūrą į H_xWO_3. Anodavimo būdu gauti WO_3 ploni sluoksniai buvo modifikuojami redukuojant juos 300 s esant -0,5 V potencialui. (30 pav., a, 73 p.). Pastebėta, kad redukuotų sluoksnių fotosrovės stipriai išauga po tam tikro laiko. Dėl to po redukcijos visada vykdyta aktyvacija, pertraukiamai apšviečiant redukuotą sluoksnį esant 1,2 V potencialui. Tokia aktyvacija vykdyta 3000 s, ir pavyzdinė aktyvacijos kreivė pateikta 30 pav. b. Tik redukuotų bei redukuotų ir aktyvuotų WO_3 sluoksnių XPS analizė parodė, jog po redukcijos stipriai išauga W^{+6} - O ir O-vakansija signalai (31 pav., a, b, 74 p.), o po aktyvacijos W^{5+} signalas sumažėja, tačiau O-vakansija signalas išlieka panašus (31 pav., c, d). Rezultatai taip pat pateikti 7-oje lentelėje (75 p.). Manoma, kad būtent dėl padidėjusio (optimalesnio) deguonies vakansijų kiekio pagerėja sluoksnio fotoelektrocheminės savybės.

WO₃ plonų sluoksnių fotokatalizinės savybės

0,3 M oksalo rūgštyje susintetintų sluoksnių fotokatalizinės savybės tirtos LSV ir CA metodais, pritaikant pertraukiamą apšvietimą (32 pav., 75 p.). Nors tendencija nebuvo vienareikšmiška, storesni sluoksniai (gauti anoduojant esant aukštesnėms įtampoms) generavo didesnes fotosroves. Esant 60 V gautas sluoksnis pasiekė 0,094 mA cm⁻² matuojant 80 mW cm⁻² šviesos intensyvumu esant 1,0 V. Kaip ir galima tikėtis, fotosrovės tankis didėja skleidžiant potencialą anodine kryptimi.

1 M Na₂SO₄ + 75 mM NaF + 0,1 M NaH₂PO₂ (+ 25 mM MoS₄²⁻) elektrolite $1\ M\ Na_2SO_4 + 75\ mM\ NaF + 0{,}1\ M\ NaH_2PO_2\ (+ 25\ mM\ MoS_4^{2-})$ *elektrolite sintetintų WO₃, WO₃+MoSₓ, ir redukuotų r-WO₃ sluoksnių* fotokatalizinės savybės ištirtos išsamiau. Visų pirma, tiesinės voltmetrijos kreivės su pertraukiamais šviesos impulsais brėžtos nuo 0,4 V iki 2,0 V, 2 mV s⁻¹ potencialo skleidimo greičiu. Šioje potencialų srityje fotosrovė kyla nuo ~ 10 μA cm⁻² (esant 0,4 V) iki daugiau nei 0,8 mA cm⁻² (esant 2,0 V). Poliarizacinės ir chronoamperometrinės kreivės, priklausančios skirtingo anodavimo laiko WO₃, r-WO₃, ir WO₃+MoSₓ sluoksniams, pavaizduotos 33 pav. (78 p.). Iš jų matyti, kad nemodifikuoto WO₃ didžiausia fotosrovė priklauso po 2 anodavimo minučių susintetintam sluoksniui. Abu modifikavimo būdai – redukcija ir kompozito ko-nusodinimas, gerokai padidina susintetintų sluoksnių fotokatalizines savybes. Didžiausia fotosrove iš tirtų mėginių pasižymėjo po 5 minučių anodavimo gautas ir redukuotas r-WO₃ sluoksnis. Taipogi pastebėta, kad teigiama redukcijos įtaka itin ryški mažai fotokataliziškai aktyviems sluoksniams (pvz. gautam po 30 minučių anodavimo). 8-oje lentelėje pateiktos esant 1,2 V gautos fotosrovių vertės ir apskaičiuoti fotonų konversijos efektyvumai.

Įvertintas ir fotokatalizinių plonų sluoksnių stabilumas, palaikant gana ilgą 2 valandų apšvietimo laiką (34 pav., 80 p.). Čia matyti, kad WO₃ ir WO₃+MoSₓ sluoksnių fotosrovė pradeda pastebimai kristi po ~1800 sekundžių, o r-WO₃ sluoksnio fotosrovė stabiliai auga iki 7200 sekundžių ribos.

Foto-elektrocheminio impedanso spektroskopija

Foto-EIS spektrai buvo matuojami kaip aprašyta eksperimentinėje dalyje, esant 50 mW cm⁻² pastoviam apšvietimui. WO₃, r-WO₃, ir WO₃+MoSₓ ploniems sluoksniams, gautiems po skirtingo anodavimo laiko, gauti spektrai pateikti 35 pav. (82 p.). Iš esmės visi spektrai sudaryti iš dviejų pusapskritimių (Bode koordinatėse stebimi 2 maksimumai), tačiau tam tikriems mėginiams neįmanoma išskirti aukšto dažnio signalo. Bendrai matoma, kad sistemos impedanso dydis koreliuoja su fotosrovės matavimų rezultatais – r-WO₃ ir WO₃+MoSₓ sistemų impedansai gerokai mažesni nei lygintinų WO₃ sistemų. Matuojant sistemos foto-EIS priklausomybę nuo potencialo pastebėta, kad didinant anodinį potencialą žemo dažnio signalas smarkiai išauga (36 pav., 83 p.), t.y. sistemos impedansas didėja. Šie rezultatai buvo interpretuoti elektrine ekvivalentine schema, pavaizduota 37 pav. (84 p.), kuri susideda iš tirpalo varžos R_s, erdvinio krūvio srities talpos ir varžos (CPE$_{sc}$, R_{sc}), bei dvigubo sluoksnio varžos (CPE$_{dl}$) ir krūvio pernašos varžos (R_{ct}). Įvertinus šių parametrų priklausomybę nuo matavimo potencialo pastebėta, kad R_{sc}^{-1} su fotosrove tiesiogiai nekoreliuoja. Iš tiesų šis parametras yra proporcingas (o

esant tam tikram potencialui ir lygus) sistemos fotolaidžiui $\Delta j_{ss}/\Delta E$ (38 pav., 84 p.). Darant prielaidą, kad erdvinio krūvio sritį galima modeliuoti kaip plokščią kondensatorių, iš C_{sc} verčių apskaičiuotas sluoksnio storis, ir tada apskaičiuota fotogeneruotų krūvininkų koncentracija (39 pav., 85 p.). Ši koncentracija didėja iki tam tikro potencialo, kuriame pasiekia maksimumą, o po to pradeda kristi. Būtent tai ir nulemia iš foto-EIS duomenų nustatytą fotolaidžio kritimą.

Moduliuojamo intensyvumo fotosrovės spektroskopija

Šio metodo esmė yra ta, kad laikomas pastovus potencialas, o tam tikra amplitude moduliuojamas apšvietimo intensyvumas I_0. Tokiu būdu galima tirti krūvininkų fotogeneraciją pačioje erdvinio krūvio srityje. Spektrai kurie buvo gauti esant skirtingiems I_0 pavaizduoti 40-ame pav. (87 p.), ir juose matomas ryškus žemo dažnio signalo mažėjimas esant didesniems šviesos intensyvumams, o tai rodo mažesnius fotonų konversijos efektyvumus. Taip pat iš tokių spektrų įmanoma nustatyti, ar sistemą limituoja paviršiaus elektronų ir skylučių rekombinacija. Šiuo atveju, kadangi žemų dažnių srityje nematomas perėjimas į teigiamas H'' vertes, rekombinacijos nėra.

Įvairūs parametrai iš IMPS ir foto-EIS analizių, atliktų WO_3, r-WO_3, ir WO_3+MoS_x ploniems sluoksniams, yra lyginami 41-ame paveiksle (88 p.). Tendencijos vėl atskleidžia, kad geriausiu kataliziniu aktyvumu (fotosrove, fotolaidžiu, konversijos efektyvumu, ir net skylučių pernašos kinetika) pasižymi r-WO_3 sluoksniai. Spektre žemo dažnio susikirtimas su H' ašimi atitinka konversijos efektyvumą, o iš žemo dažnio signalo pusapskritimio maksimalaus taško kampinio dažnio galima paskaičiuoti skylučių pernašos konstantą k_{tr}.

Kadangi susikirtimo su H' ašimi vertė yra proporcinga fotonų konversijos efektyvumui, nenuostabu, jog keliant potencialą spektrų profilis platėja (42 pav., 91 p.). Esant žemiems potencialams (0,8 V) matoma, jog žemų dažnių srityje gali susiformuoti nedidelis rekombinaciją rodantis signalas, tačiau jo vienareikšmiškai nebelieka esant didesniems potencialams (1,2 V – 2,0 V). Taip pat sulyginti IMPS spektrai, užrašyti po skirtingo anodavimo laiko susintetintiems WO_3, r-WO_3, ir WO_3 + MoS_x ploniems sluoksniams (43 pav., 92 p.). Iš šių spektrų vėl matyti, kad r-WO_3 ir WO_3+MoS_x pasižymi geresnėmis fotokatalizinėmis savybėmis (t.y. didesniu fotonų konversijos efektyvumu).

Įvertintos žemo dažnio susikirtimo su H' ašimi ir k_{tr} priklausomybės nuo potencialo. H' – E priklausomybės iš esmės atkartoja poliarizacines fotosrovės kreives, o k_{tr} vertės stabiliai mažėja esant didesniam potencialui. Tai parodo, jog deguonies skyrimasis vyksta per nejudrų aktyvų centrą.

IŠVADOS

1. a) Elektrocheminio nusodinimo metodu ant vario vielos ir metalinių putų substratų buvo susintetinti MoS_2 ploni sluoksniai. Gautų ant vario vielos sluoksnių stechiometrija priklausė nuo nusodinimo sąlygų ($MoS_{1,72}$ – $MoS_{1,87}$). MoS_2 sluoksniai, kurie buvo nusodinti ant vario putų, pasižymėjo geresniu sukibimu su pagrindu. Elektrocheminio nusodinimo metu elektrolite esant NaH_2PO_2 priedo gaunami ploni sluoksniai, kurių Mo:S santykis artimesnis MoS_2. Tai patvirtina ir XPS duomenys.

b) Susintetintų MoS_2 sluoksnių katalizinis vandenilio skyrimosi reakcijos aktyvumas priklausė nuo medžiagos vidinių ir išorinių savybių (nusodinto katalizatoriaus kiekio ir aktyvių centrų aktyvumo). Viršįtampis, reikalingas pasiekti 10 mA vandenilio skyrimosi srovę, mažėja didinant nusodinto katalizatoriaus kiekį. Žemiausi Tafelio nuolinkio kampai pasiekti kai sluoksnio nusodinimo trukmė buvo 1000 s. MoS_2 ploni sluoksniai, nusodinti tirpale esant NaH_2PO_2, buvo kataliziškai aktyvesni.

2. a) Anodavimo būdu susintetinti WO_3 ir WO_3+MoS_x ploni sluoksniai. Gautos medžiagos stechiometrija yra WO_3, tačiau stebėtas ir nežymus W^{5+}-O signalas. WO_3+MoS_x kompozito S2p spektruose pastebėtas stiprus tiltelinės sieros signalas. EDX žemėlapių tyrimai atskleidė, kad MoS_x įsiterpęs priepaviršiniame WO_3 sluoksnyje, ir kad Mo : S santykis yra artimas 1.

b) Geresniu deguonies skyrimosi fotokataliziniu aktyvumu pasižymėjo plonesni (susintetinti esant trumpesnei anodavimo trukmei) sluoksniai. WO_3 plonų sluoksnių katalizinis aktyvumas gerokai padidėja po elektrocheminės redukcijos (protonų interkaliacijos). Tai susieta su padidėjusiu O-vakansijų signalu.

3. a) Elektrocheminio impedanso spektroskopija atskleidė, kad MoS_2 sluoksnių vandenilio skyrimosi reakcijos katalizinis aktyvumas vienareikšmiškai susijęs su adsorbcijos varža. Adsorbcijos pseudotalpa buvo panaudota siekiant apskaičiuoti aktyvių centrų skaičių.

b) Foto elektrocheminio impedanso spektroskopijos tyrimais nustatyta, kad WO_3 ir WO_3+MoS_x plonų sluoksnių fotokatalizinis aktyvumas tiesiogiai proporcingas fotogeneruotų krūvininkų koncentracijai erdvinio krūvio srityje.

c) Moduliuojamo intensyvumo fotosrovės spektroskopijos tyrimai parodė, kad po H^+ interkaliacijos ir aktyvacijos galimai padidėja fotogeneruotų skylučių pernaša į elektrolitą.

ACKNOWLEDGEMENTS

First and foremost I would like to express my my thanks to my academic supervisor Prof. Dr. Henrikas Cesiulis and my academic consultant – Assoc. Prof. Dr. Natalia Tsyntsaru. I am very grateful for both the guidance and freedom they have provided during my studies, as well as the many opportunities to travel, learn abroad, and in result to grow as a person and a researcher. I'm also thankful for the many hours of editorial work that they have put into my research documents.

A special thank you should be extended to my international colleagues that I have had the pleasure of working with over the years: from Belarus, Moldova, and the United States of America. I appreciate their hospitality and always making me feel welcome. My time spent with them, whether in an academic or personal capacity, has definitely reflected on this thesis in a very positive manner.I hope these friendships that we have built will last for many years to come.

I would also like to acknowledge my colleagues from the Department of Physical Chemistry – in particular the ones I was closest with, and with whom I have ended up sharing most of my scientific career. Even though our paths were different we found much common ground, and had many fruitful discussions. After all, as is said in *Proverbs 27:17* „*Iron sharpens iron, and one man sharpens another*".

Finally, thank you to my friends and family for their support and persistent interest in my studies. I expect this thesis will finally clarify any unanswered questions.

ARTICLE I

Synthesis, electrochemical impedance spectroscopy study and photoelectrochemical behaviour of as-deposited and annealed WO$_3$ films

R. Levinas, N. Tsyntsaru, M. Lelis, H. Cesiulis

Synthesis, electrochemical impedance spectroscopy study and photoelectrochemical behaviour of as-deposited and annealed WO$_3$ films

R. Levinas[a], N. Tsyntsaru[a,b,*,1], M. Lelis[c], H. Cesiulis[a]

[a] Vilnius University, Naugarduko str. 24, Vilnius, Lithuania
[b] Institute of Applied Physics of ASM, Academiei str. 5, Chisinau, Republic of Moldova
[c] Lithuanian Energy Institute, Kaunas, Lithuania

A R T I C L E   I N F O

A B S T R A C T

WO$_3$ films have been obtained by anodization of tungsten in the different acidic electrolytes (HCl, H$_2$SO$_4$, H$_3$PO$_4$, H$_3$PO$_4$ + NH$_4$F) and at various applied potentials. Electrochemical impedance spectroscopy was used to investigate film formation and to characterize the obtained oxide films. The equivalent electric circuits modelling reactive and blocking behaviour are provided and discussed. It was found, that oxide film capacitance decreases linearly with increasing anodization potential. The relative permittivity of tungsten oxide films varies from 31 to 56 depending on the acid used. A relatively high rate of the film formation ($1.87 \, nm \, V^{-1}$) and increased resistance against oxide breakdown can be achieved for tungsten oxide obtained from 0.3 M oxalic acid bath. Compact oxide films are formed at the potentials ranged from 10 V to 30 V, whereas increasing of anodization voltage to 60 V resulted in the formation of disordered, porous structures due to surface etching. Semiconductor properties were determined by Mott-Schottky analysis. Photoelectrochemical properties of as-deposited and annealed at 600 °C WO$_3$ films were determined in a Na$_2$SO$_4$ solution under pulsed and constant UV irradiation. It was determined that annealed WO$_3$ films in comparison to as-deposited films are more stable and generate substantially higher photelectrochemical currents.

© 2016 Elsevier Ltd. All rights reserved.

1. Introduction

Semiconductor materials have been always an area of particular interest. Most transition metal oxides exhibit semiconductor properties and are widely used in both industry and science. Currently, research on the rarer metal oxides (such as tungsten or molybdenum) remains important, especially in the increasingly vital solar energy conversion field. Anodization is a convenient and effective way to form an oxide film, because the anodic dissolution of metallic tungsten is followed by immediate formation of WO$_3$. One of the first models explaining the formation of WO$_3$ is the so-called Point Defect Model (PDM) [1,2]. It states that the formation of the oxide layer occurs via transfer of oxygen vacancies (point defects) from the metal | oxide interface, across the growing oxide layer, to the oxide | electrolyte interface, at which the

vacancies are consumed. According to the PDM, the film thickness depends on the applied anodization potential. The interpretation of electrochemical impedance spectra in the frame of elaborated kinetic models or equivalent electric circuits is a powerful tool to investigate the formation mechanism of thin films [3–5].

The presence of a pseudo-inductive loop in the impedance spectra at intermediate frequencies indicates point defect interaction during the film growth and dissolution processes. A kinetic model, including the recombination reaction between positively and negatively charged point defects at the film/solution interface, as well as an elaborated kinetic scheme for tungsten diffusion through the film, mediated by cation vacancies, have been proposed. It is assumed that AC modulation of the space-charge layer within the oxide, and the compensating surface charge cause the relaxation phenomenon that results in inductance presence in the impedance spectrum [6].

The formation of a porous oxide layer occurs through equilibrium between electrochemical film formation and chemical dissolution. As the oxide dissolves, pits form on its surface and merge into porous structures [7]. Varieties of acidic media, as well

* Corresponding author at: Institute of Applied Physics of ASM, Academiei str. 5, Chisinau, Republic of Moldova.
  E-mail addresses: tintaru@phys.asm.md, ashra_nt@yahoo.com (N. Tsyntsaru).
[1] ISE member, ORCID ID 0000-0002-9813-2460.

as combinations with fluoride ions which dissolve tungsten via a different pathway, have been used for anodizing tungsten [8–13]. Oxide films obtained at different conditions (potential, pH, anodization duration and electrolyte used) exhibit different surface morphology, thickness, and porosity. Thus, their photocatalytic properties can vary in a broad range [13,14–18]. For commercial use, stable films are highly desirable. However, in many electrolytes WO_3 is susceptible to photocorrosion. A decrease of 74% in photocurrent density of electrodeposited films was noticed [19], after which the photocurrent remains constant for a long time. A significantly smaller drop of 39% was found for films, prepared via the polymeric precursor method [20] and 28.4% for vertically aligned plate-like arrays [21].

The stability of anodized WO_3 films can be further increased by thermal annealing [17–22]. This is likely caused by changes in crystallinity of the as-anodized films (from amorphous to monoclinic/orthorhombic). Temperatures above 400 °C seem to decay surface porosity, but increase the overall thickness of the porous layer.

It was found that the photoelectrochemical properties of WO_3 films strongly depend on the film thickness. A decrease of measured optical band gap (from 2.96 eV to 2.50 eV) was observed for electrodeposited WO_3 films with thickness increase (respectively 168 nm to 431 nm) [23].

Further growth of film thickness (>600) nm leads to a diminution in photocurrent conversion efficiency [24]. It was proposed that for films thinner than 500 nm the surface band gap component dominates. Whereas for thicker films (>500 nm) it is the bulk band gap component that determines the photocurrent. Thicker films may also have increased resistivity, larger distance of charge carrier diffusion, and greater possibility of electron-hole pair recombination [25]. Multiple studies have shown that the limiting factor of the WO_3 film's photocatalytic properties is the generation of charge carriers by photons [26,27] and therefore a linear relation between illumination intensity and generated photocurrent was determined. The present study was devoted to the synthesis, electrochemical impedance spectroscopy (EIS) study and photoelectrochemical behaviour of as-deposited and annealed WO_3 films.

2. Experimental

All electrodes were prepared from pure W (99.95%, Alfa Aesar): (a) plates of 1 cm × 1 cm dimensions were used for structural analysis and photocurrent measurements; (b) wire of 1 cm^2 surface area was used for voltammetry and electrochemical impedance spectroscopy. Prior to experiments, the electrodes were polished, degreased in acetone in the ultrasonic bath and rinsed with distilled water. Based on previous research [2,3,8–13], several electrolytes have been selected, and are presented in Table 1. All measurements were carried out using programmable potentiostat Autolab 302N and NOVA software. For high-voltage anodization, a Consort EV 245 galvanostat/potentiostat was used.

Table 1
Electrolytes and conditions of the EIS study.

Electrolyte	Anodization potential range	No. of steps	Duration of each step
1 M HCl	0.1 V–5.0 V	50	10 min.
1 M H_2SO_4			
14 M H_3PO_4			
14 M H_3PO_4 + 1 M NH_4F			
0.3 M oxalic acid			

2.1. Tungsten oxidation at relatively low anodic potentials

Polarization curves were obtained by linear sweep voltammetry in the 0–5 V potential range at scan rate of 50 mV s^{-1}. A two-electrode cell with a stainless steel coil of significantly larger surface area (∼30 cm^2) was used as counter electrode. It was considered that the possible potential shift during the measurement would be negligible compared to the applied voltage.

Electrochemical impedance spectra were registered as follows: an automated program has been set up to increase the potential in steps of 0.1 V (see Table 1). During each of these step, the electrode was kept at corresponding anodization potential for 10 min (a steady-state current has been settled within this period), then EIS spectrum was registered in the 10 kHz–0.01 Hz frequency range at perturbation amplitude of ±5 mV. In this way, a continuous growth of the oxide film could be examined *in situ*. Measurements were conducted in a two-electrode cell. Due to the bigger electrode area and large capacitance of the counter electrode, the measured impedance belonged entirely to the working electrode.

The obtained EIS data quality and causality was confirmed by applying Kramers-Kronig procedure integrated into the NOVA software. The determined residuals were very small for the real part of the impedance (up to 0.8%), and their distribution appears to be random. Larger residuals occur on the imaginary part; their appearance coincides with the frequency range that exhibits inductance in the spectrum. Even so, only a few points are particular outliers, and generally the residuals are also within the vicinity of 1%. The sum of squares of the relative residuals reflects the compliance to Kramers-Kronig transforms, because the overall sums of residuals, χ^2 were ranged from 10^{-6} to 10^{-4} dependently of solution.

Mott-Schottky plots were calculated based on the EIS data obtained. For these experiments the impedance of the working electrode was measured at one frequency of 1 kHz (±5 mV amplitude) and at anodic potentials from 1.2 V to 0.1 V. After measurement of each point, the oxide layer was regenerated for one minute at a constant potential 1 ÷ 5 V. The capacitance was calculated by fitting of the obtained results with a RC circuit. This given frequency (1 kHz) is within the range when the capacitance can be attributed to the barrier layer only. Moreover, this frequency was used to compare our results with other published data.

2.2. Tungsten oxidation at relatively high anodic potentials

WO_3 films were obtained by anodization in a two-electrode cell for 30 min at voltages ranged from 10 to 60 V in 0.3 M oxalic acid. Surface morphology was evaluated with Hitachi S-3400N scanning electron microscope. The thickness of obtained oxide films was measured based on cross-section images.

Photocurrents were measured in a three-electrode quartz cell, with a stainless steel counter electrode and a saturated Ag/AgCl reference electrode. A 0.5 M Na_2SO_4 electrolyte was selected. Measurements were carried out by means of Autolab Optical Bench system with a calibrated UV LED (365 nm) and light intensities up to 80 mW cm^{-2} connected to Autolab N3012 potentiostat. To compare as-deposited and annealed WO_3 films, samples were obtained by anodizing in 0.3 M oxalic acid at applied potential of 35 V for 30 min, then have been thermally treated for 3 h at 600 °C with a temperature ramp-up speed of 130–145 °C min^{-1}.

3. Results and discussion

3.1. Tungsten oxidation at relatively low anodic potentials

In order to compare the formation of WO_3 in different electrolytes, potentiodynamic anodic curves for tungsten electrode

were recorded in following solutions: 1 M H_2SO_4, 1 M HCl, 14 M H_3PO_4, 14 M H_3PO_4 + 1 M NH_4F, and 0.3 M oxalic acid. Obtained anodic polarization curves for tungsten in various solutions are shown in Fig. 1. The shape of the curves is similar: a broad peak is followed by a wide passivation-dissolution plateau that extends at least up to 5 V. The peak is less pronounced in phosphoric acid with and without the addition of ammonium fluoride. In the presence of ammonium fluoride oxide dissolution is somehow facilitated by the formation of fluoride complexes with W(VI), and peak current density increases slightly.

The polarization curves obtained in H_2SO_4 and HCl acids have similar shapes as in phosphoric acid solutions, but the peak current values are slightly larger. In the case of oxalic acid (Fig. 1), the highest peak and plateau current densities are observed: j_{peak} = 3.0 mA cm^{-2} and j_{pl} = 1.3 mA cm^{-2}.

3.1.1. Electrochemical impedance spectroscopy study

In order to reveal the different anodization behaviour of tungsten in the investigated electrolytes the electrochemical impedance spectroscopy was used. The EIS spectra and the equivalent electric circuits that best fit to the obtained spectra, are given in Figs. 2 and 3, respectively. The shapes of Nyquist and Bode plots differ, and represent either reactive (H_3PO_4 solutions) or blocking (HCl and $H_2C_2O_4$ solutions) systems in accordance with classification based on the impedance behaviour at the low frequencies and provided in [28]. For reactive systems, when frequency approaches 0, the impedance magnitude reaches a finite value [29]. Phase angle also approaches 0, showing that the current and potential are in phase. The system is then conductive to direct current. Such behaviour can be seen on the Bode plots (see Fig. 2a and b) of impedance in phosphoric acid solutions. Blocking systems, however, completely prevent passing of direct current. It follows that when frequency approaches zero, imaginary part of impedance, Z_{im}, approaches $-\infty$. Tungsten passivation in hydrochloric and oxalic acids reveals a strong capacitive response at the low frequencies (Fig. 2c and d).

The impedance magnitudes decrease in the following order of acids: H_3PO_4 > H_3PO_4 + HF > HCl > $H_2C_2O_4$, as it can be predicted from the potentiodynamic curves. Notably, the shapes of the Nyquist and Bode plots depend on the chemical composition of the solution and anodization potential. The increase in impedance magnitude with increasing anodization potential in all studied cases can probably be explained by the increasing film thickness in these systems.

In addition, in the range of intermediate frequencies a pseudo-inductive response is visible in the studied potential range (at 1 V
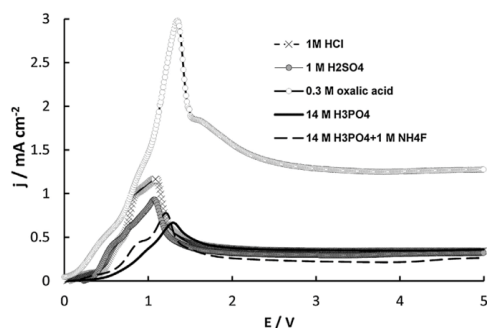
and higher) that can be ascribed to the relaxation phenomena at the oxide film/solution interface [4]. The differences that arise between impedance spectra in the investigated solutions are caused by the specific kinetics of WO_3 formation in chemically dissimilar solutions. The anodization of tungsten oxide in aqueous electrolytes is a complicated reaction, but can be represented as:

$$W + 3H_2O \rightarrow WO_3 + 6H^+ + 6e^- \qquad (1)$$

Then, partial dissolution of formed WO_3 occurs in acidic media [2]:

$$WO_3 + 2H^+ \rightarrow WO_2^{2+} + H_2O \qquad (2)$$

The addition of NH_4F to the solution promotes three reactions, which can occur simultaneously: (i) tungsten oxide formation – Eq. (1); (ii) tungsten dissolution through the oxide [6], because of increased defectiveness of the outermost layer of the oxide – Eq. (3); and (iii) WO_3 dissolution – Eq. (4). The last two reactions result in the formation of tungsten and fluoride complexes:

$$W + nF^- \rightarrow [WF_n]^{(n-6)} + 6e^- \qquad (3)$$

$$WO_3 + 6H^+ + nF^- \rightarrow [WF_n]^{(n-6)} + 3H_2O \qquad (4)$$
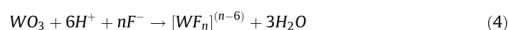
When the mentioned reactions occur under AC perturbation of small amplitude, the H_3PO_4 and H_3PO_4 + NH_4F systems behave as reactive at the low frequencies (Fig. 2a and b), and impedance spectra fit well to the equivalent circuit shown in Fig. 3a. The constant phase element (CPE) in the equivalent electric circuits used to fit obtained spectra represents the imperfection of double layer capacitance. In general, the impedance of CPE is given by:

$$Z(\omega) = \frac{1}{Q}(j\omega)^{-n} \qquad (5)$$

where Q is a constant, and $0 < n < 1$.

After adding NH_4F to the H_3PO_4 electrolyte (Fig. 2c) a substantial decrease (6–10 times) in the system impedance is obtained (see Fig. 2a and b). It is caused by the electrochemical dissolution of W leading to the formation of complexes in the solution according to the reaction (3). In addition, the value of coefficient n (see Eq. (5)) decreases from 1 to 0.92 probably due to increased defectiveness of the oxide film in the presence of F$^-$-ions.

EIS spectra obtained in HCl and oxalic acid solutions (Fig. 2c and d) are of similar shape, and demonstrate blocking behaviour at the low frequencies. Probably, in these systems the concentration of WO_2^{2+} formed in the reaction (2) reaches the point of supersaturation and an extra oxide layer of $WO_3 \cdot 2H_2O$ is formed by the following reaction [30]:

$$WO_2^{2+} + 3H_2O \rightarrow WO_3 \cdot 2H_2O + 2H^+ \qquad (6)$$
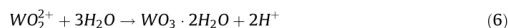
Therefore, the electric equivalent circuit used to fit these impedance spectra contains the additional RC element connected in series (Fig. 3b) which is marked as "R2" and "C0", and fitting to this equivalent circuit is shown in Fig. 2c and d.

Based on the impedance fitting results and taking into account the physical meaning of the elements of equivalent electric circuits, it is possible to estimate the thickness of oxide layers formed at relatively low anodization potentials. The capacitive behaviour can be related to the thickness and the dielectric properties of the oxide film. However, in order to be able to separate the barrier layer capacitance (C_1) from the pseudoca-pacitance (C_0) we needed to look into this phenomenon. A zone bordering the oxide | electrolyte interface (the space-charge zone) can either accumulate or deplete charge under effect of the AC signal. Then a compensating surface charge will build up from the electrolyte. It is evident that this process will alternate along
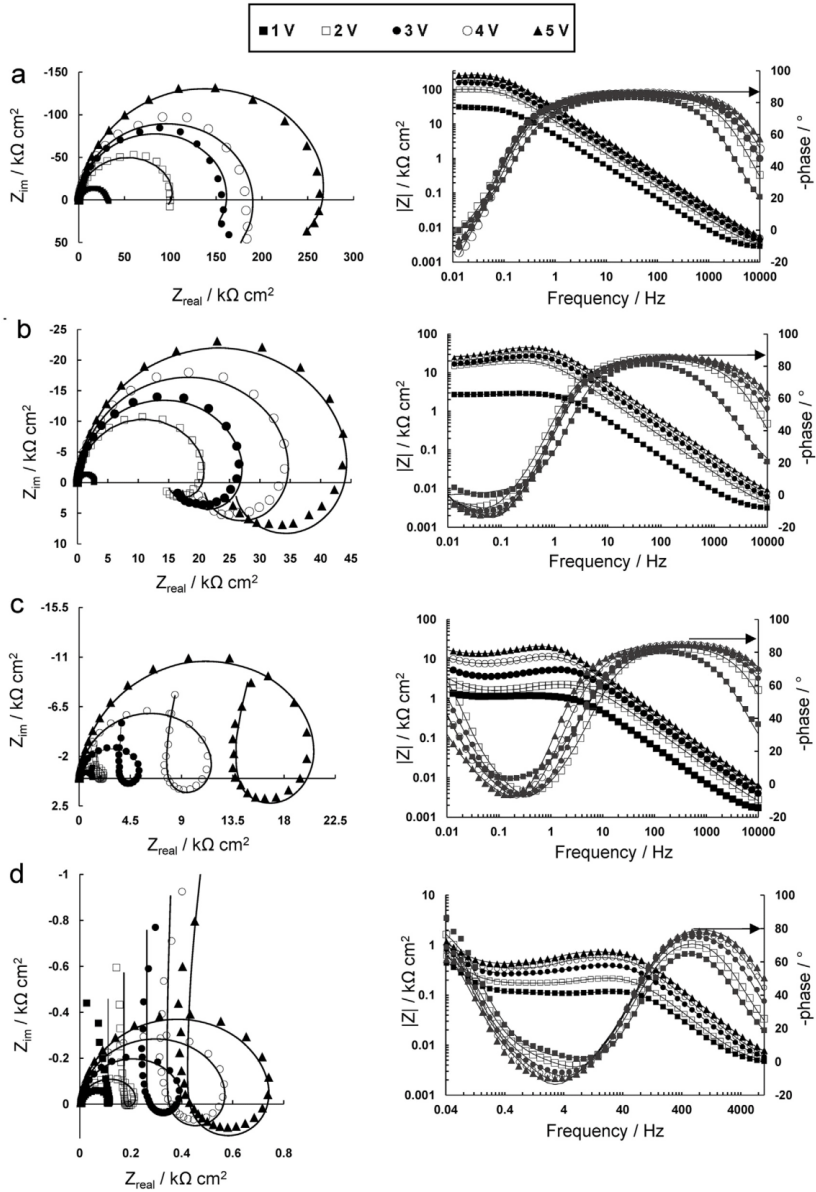

Fig. 1. Potentiodynamic curves for tungsten anodization in the investigated solutions; potential scan rate 50 mV s^{-1}.

Fig. 2. Nyquist and Bode plots obtained for tungsten anodization at various potentials (indicated on the top) in the electrolytes: 14 M H_3PO_4 (a); 14 M H_3PO_4 + 1 M NH_4F (b); 1 M HCl (c); 0.3 M oxalic acid (d). Points are experimental data and solid lines are fitting results to the equivalent circuits (Fig. 3).

with the AC phase. Hence, a time-dependent capacitor appears at the low frequency range.

The values of equivalent electric circuit elements depending on the potential are shown in Fig. 4. With formation potential increasing, the oxide become thicker and both the capacitance of the barrier layer (C_1) and pseudocapacitance (C_0) decreases. Simultaneously, the charge transfer resistance (R_3) increases linearly because the charge carriers have to migrate a larger
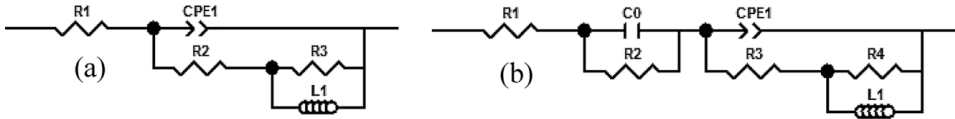
Fig. 3. Equivalent electrical circuits used to fit data shown in Fig. 2. (a): R_1 is the electrolyte resistance; CPE$_1$ is a constant phase element and ascribed to oxide layer capacitance; R_2 is the charge transfer resistance; R_3 is ascribed to resistance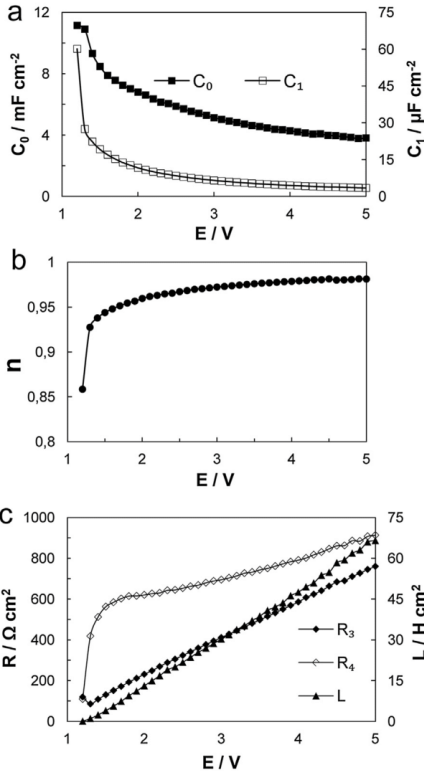 of the space-charge zone. L_1 is the inductance. (b): R_1 is the electrolyte resistance; C_0 is pseudo-capacitance; R_2 is the resistance of the pseudo-capacitor; CPE$_1$ is ascribed to oxide layer capacitance; R_3 is a charge transfer resistance; R_4 is the resistance of the space-charge zone; L_1 is the inductance.

Fig. 4. The values of the elements of equivalent electric circuit describing tungsten anodization in 0.3 M oxalic acid as a function of anodizing potential. (a) C_0 and C_1 vs E; (b) n vs E; (c) L vs E.

distance; the increase in resistance of the space charge layer (R_4) and in inductivity (L) can also be attributed to the larger film thickness.

It has been proposed that the compact oxide layer could be modelled as a parallel plate capacitor, thus the capacitance of the barrier film should be inversely proportional to the distance between the plates, or in this case to the thickness of the film [3,5]:

$$C_1 = \frac{\varepsilon_r \varepsilon_0}{L} \tag{7}$$

where ε_r and ε_0 is the apparent relative permitivity of the oxide film and the permittivity of vacuum, respectively; L is the thickenss of obtained oxide film.

On the other hand, the thickness increases with applied potential (E_F) proportionally to a coefficient α, which is also called the anodizing or formation ratio. Hence, the thickness can be expressed by a linear equation:

$$L = \alpha(E_F - E_0) \tag{8}$$

where α is the anodizing ratio; E_F is the applied formation potential; E_0 is the starting potential of the oxide film formation.

Combining these two equations results in a linear dependence of the inverse capacitance on the film formation potential, and slope of this dependence is equal to $\frac{\alpha}{\varepsilon_r \varepsilon_0}$:

$$\frac{1}{C_1} = \frac{\alpha}{\varepsilon_r \varepsilon_0}(E_F - E_0) \tag{9}$$

It was found that tungsten oxide layer capacitance is represented by the CPE (see. Figs. 3 and 4), and the capacitance values were recalculated into effective capacitances, C_b, using the following equation [31]:

$$C_b = Q^{\frac{1}{n}} R_f^{\frac{1-n}{n}} \tag{10}$$

where R_f is the oxide layer resistance; Q and n are defined in Eq. (5).

The plots of the inverse capacitance on the applied potential for all investigated electrolytes are shown in Fig. 5.

They are linear as it is predicted by Eq. (9), but slopes depend on the electrolyte used. The slope is higher in the case of HCl, H$_2$SO$_4$ and oxalic acid, than for phosphoric acid solutions. If the relative permittivity is assumed to be constant for the entire range of the applied potentials 1÷5 V, then according to Eq. (7) the capacitance decreases due to thickness increase. However, the estimation of film thickness from capacitance measurements is not straightforward. Most of the researchers are finding the constant of relative permittivity or are using other independent methods for thickness estimation. In this study the method reported in [3] was applied, and the indicated averaged value of the anodization ratio $\alpha = 1.78$ nm V^{-1} was used for calculations using Eq. (9). The calculated constants of relative permittivity are presented in Table 2 and estimated thickness of oxide layers vs anodization potential is shown in Fig. 6. Obviously, using of α as an average value results in some smoothing out of the results, although the differences between thickness of films formed in phosphoric acid and other electrolytes are seen clearly.

3.1.2. Semiconductor properties of obtained WO$_3$ films

Semiconductor properties have been determined for tungsten oxide films obtained in 0.3 M oxalic acid using Mott-Schottky equation:

$$\frac{1}{C_{SC}^2} = \left(\frac{2}{q\varepsilon_r\varepsilon_0 N_D}\right)\left((V_F - V_{FB}) - \frac{kT}{q}\right) \tag{11}$$
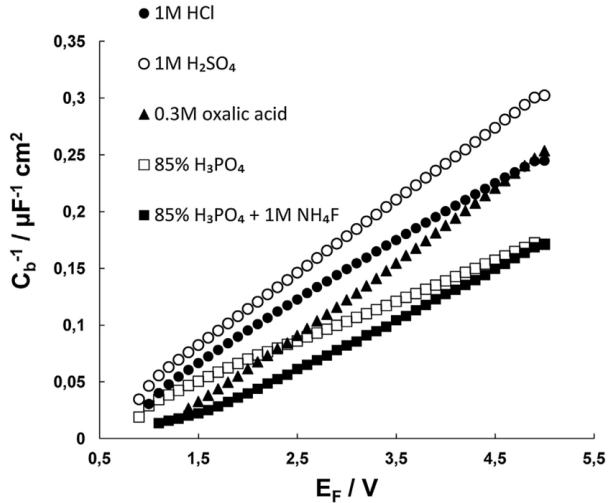
Fig. 5. The dependence of the inverse oxide layer capacity on the formation potential.

Table 2
Values of relative permittivity (ε_r) of WO_3 films in the investigated solutions.

Solution	ε_r
HCl	37.9
H_2SO_4	31.2
0.3 M oxalic acid	31.6; (33.3)[a]
14MH_3PO_4	55.9

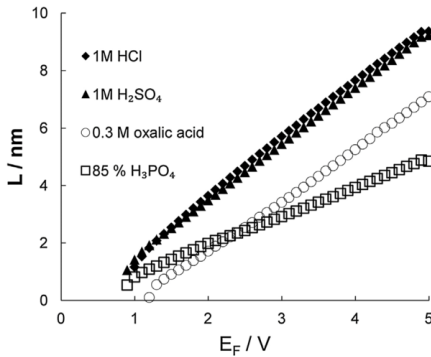[a] Value is calculated based on the experimentally obtained $\alpha = 1.87$ nm V^{-1}.

Fig. 6. The thickness of oxide films vs anodization potential in the investigated solutions.

where C_{SC} is the space-charge layer capacitance; q is the elementary charge; N_D is the donor density; V_F and V_{FB} are the oxide film formation potential and flat band potential, respectively.

In our case C_{SC} is equivalent to C_I (Fig. 3). The Mott-Schottky plots shown in Fig. 7 were plotted based on the electrochemical impedance data obtained at the decreasing potential values from
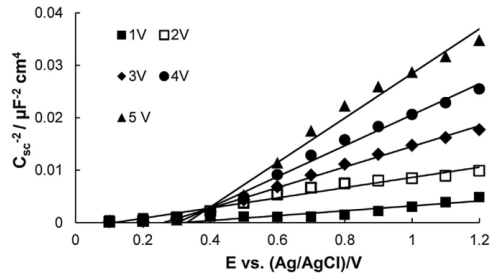

Fig. 7. Mott-Schottky plots for tungsten oxide films obtained in 0.3 M oxalic acid at various potentials.

1.2 V to 0.1 V. After measurement of each point, the oxide layer was regenerated for one minute at a constant potential of 1 V–5 V. The capacitance was calculated through fitting with a typical RC circuit, because at 1 kHz neither pseudocapacitance nor inductance should distort the fitting data.

The shape of plots reveals, that the obtained WO_3 is an n-type semiconductor. The interception of the trend lines with the ordinate gives the value of the flat band potential, while the donor density can be calculated from the slope of the plots. The results of these calculations are presented in Table 3, and show that both donor density and flat band potential vary with anodization

Table 3
Data of Mott-Schottky analysis.

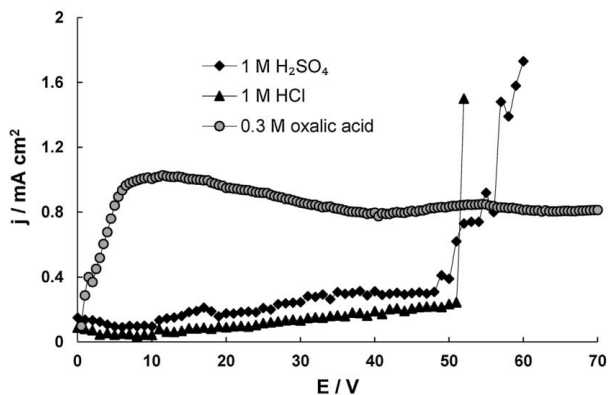| E_F, V	V_{FB} vs. Ag/AgCl, V	N_D, cm^{-3}
2	0.179	3.9 10^{20}
3	0.260	2.4 10^{20}
4	0.302	1.6 10^{20}
5	0.371	1.1 10^{20}

Fig. 8. Film thickness as a function of anodizing potential in 0.3 M oxalic acid solution. Points are experimental data; solid line is calculated using α=1.87 nm V^{-1}; and dashed line is calculated based on the data shown in Fig. 6.

potential. The drop in donor density can be related to the increase in film thickness; and the bulk donor concentration must decrease with increase in oxide volume. With rising formation potential from 2 V to 5 V the flat band potential shifts from 0.179 V to 0.371 V vs Ag/AgCl. Clearly, a change occurs in the oxide band structure, which may have an effect on its photoelectrochemical properties.

3.2. Tungsten oxidation at relatively high anodic potentials

High anodization potentials have been applied in order to obtain thicker tungsten oxide films, which are more suitable for photoelectrochemical behaviour study. Due to limited rate of tungsten oxide growth in phosphoric solutions (Fig. 6), only
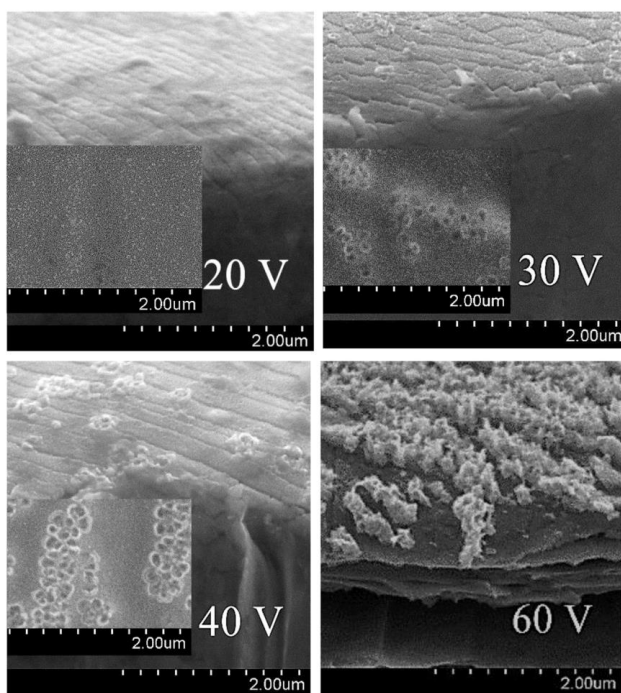

Fig. 9. Anodic polarization curve of tungsten in 0.3 M oxalic acid, 1 M HCl, and 1 M H$_2$SO$_4$.

132

sulphuric, hydrochloric and oxalic acids have been used for anodization at the high potentials. Stationary polarization curves of tungsten anodization in investigated acidic solutions are shown in Fig. 8. The relatively high anodization potentials up to 70 V without film breakdown can be applied only in the oxalic acid, while the oxide layers obtained in 1 M H_2SO_4 and 1 M HCl solutions are not stable already at ~50 V. Also, the anodization current densities are much lower in these solutions than in oxalic acid.

Therefore, only WO_3 films obtained in oxalic acid have been further investigated. SEM images of these films obtained at relatively high anodization potentials are shown in Fig. 9. It was observed that at formation potential of 10–20 V a compact oxide film is obtained, which covers the entire surface uniformly. At formation potentials of 30–40 V, due to partial surface etching, nanoporous structures on the compact oxide layer are formed. However, the coverage of ordered nanoporous layer was not uniform (Fig. 9, inset images). At anodization potential of 60 V almost the entire surface of oxide film was affected by etching (Fig. 9).

The thicknesses of the anodized films obtained at high anodization potentials were estimated from SEM images of the film cross-sections (Fig. 10, scatter points). The linear correlation between anodization potential and the resulted film thickness is observed. Based on these experimental data the anodization ratio $\alpha = 1.87$ nm V^{-1} was determined in the oxalic acid solution. This value was introduced into Eq. 8 to calculate the trend-line that was extended to the lower potentials as well (Fig. 10 solid line).

The obtained value for anodization ratio is slightly higher than reported in [3] $\alpha = 1.78$ nm V^{-1}, which was determined as an average value for several electrolytes, and can result in underestimation of oxide film thickness. Thus, the comparison of the trend-lines, obtained by extrapolation of the data presented in Fig. 6 for oxalic acid (Fig. 10, dashed line) and experimental data (Fig. 10 solid line), reveals the difference in the estimation of the film thickness. Moreover, based on experimentally determined value of α, the relative permittivity for tungsten oxide obtained from oxalic acid solution has been updated from 31. 6 to 33.3 (Table 2).

3.3. Photoelectrochemical properties of as-deposited and annealed WO_3 films

It has been reported [14] that the band gap of WO_3 lies within the range of 2.6 eV to 3.0 eV, therefore the strongest light absorbance shall occur in the ultraviolet range. Photoelectrochemical properties of obtained tungsten oxide films in 0.3 M oxalic acid were investigated. Fig. 11 shows linear sweep voltammetry curves obtained in the presence and without UV irradiation in a Na_2SO_4 solution for as-anodized sample. There is a small peak at ~−0.2 V,
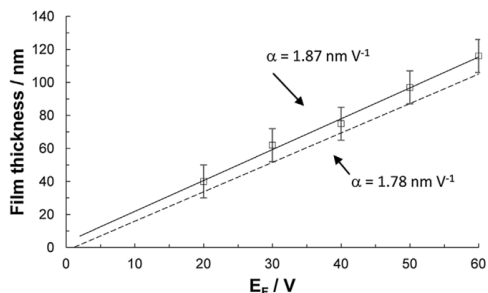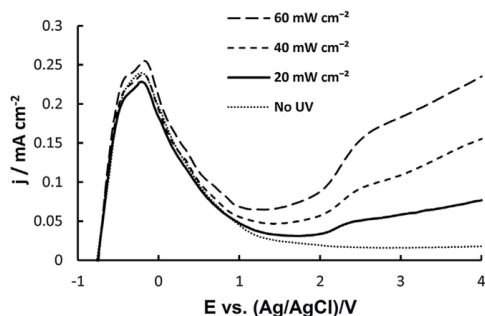
Fig. 11. Photocurrents of WO_3 obtained by anodizing for 30 min at 30 V in a 0.3 M oxalic acid solution. Photocurrents were measured in 0.5 M Na_2SO_4. Potential sweep rate 50 mV s^{-1}.

and its position and height do not depend on the UV irradiation intensity. It can likely be related to the oxidation of some remaining un-oxidized tungsten through the formed oxide film. An increase in photocurrent is observed at potentials >1 V, where the photo-electrochemical splitting of water begins to occur. Further increasing of potential yields progressively stronger photocurrents. The increase of UV irradiation intensity also linearly increases the photocurrent density at any given potential.

Chronoamperometric measurements under pulsed UV irradiation with 2 s on-off intervals have also been carried out on the obtained oxide films, and data are presented in Fig. 12. The highest photocurrent density (0.11 mA cm^{-2}) was observed for the film anodized at 80 V. According to the previously discussed results, this film would be the thickest and has the highest specific surface area. Although, some discrepancy can be seen at lower voltages, where changes in the surface structure might have had an effect, generally the bigger anodization voltage the larger is the photocurrent.

Although, the stability of WO_3 layers has not been a major task of this study, the film degradation was noticed. Namely, a change in film colour was detected during prolonged measurements and some films even can dissolve. Furthermore, after 200 s the photocurrent decreased by 10–20 μA cm^{-2} in most cases. In order to overcome the film stability issue, the annealing was performed

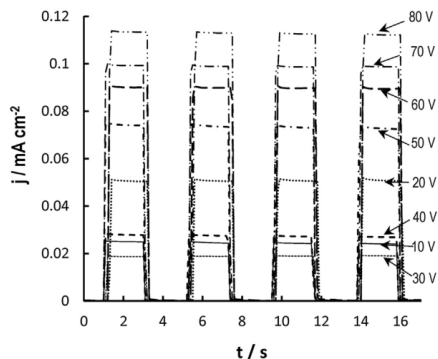**Fig. 10.** SEM images of WO_3 films, obtained by 30 min anodization of tungsten in 0.3 M oxalic acid solution.

Fig. 12. Photocurrents of WO_3 films, obtained in 0.3 M oxalic acid for 30 min at different formation potentials. UV intensity is 80 mW cm^{-2}. Measured in 0.5 M Na_2SO_4 at 1 V anodic potential.
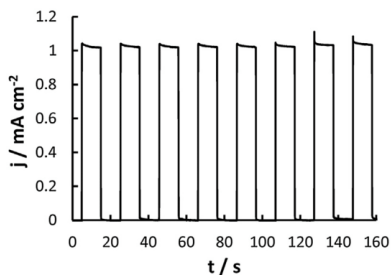
Fig. 13. Photocurrent of annealed WO_3 film measured in 0.5 M Na_2SO_4 at 1 V anodic potential; UV intensity is 80 mW cm^{-2}; on-off interval is10 s.

as it increases the amount of oxygen vacancies and thus free electrons in the oxide, as well as improves the crystallinity [17]. The effects of annealing have been discussed in [12,17], where it was found that the indirect band gap of WO_3 decreases almost linearly when annealing temperature increases from 300 °C to 500 °C. Consequently the photoelectrochemical properties of oxides improves [19].

Annealing of the WO_3 films obtained at potential of 35 V for 30 min was carried out for 3 h at 600 °C and the temperature ramp-up speed of 130–145 °C min^{-1}. The measured photocurrents of these films are presented in Fig. 13. Annealed films showed faster response to UV illumination and higher photocurrents (up to 1 mA cm^{-2}) compared to as-deposited films generating photocurrent of ∼0.11 mA cm^{-2}.

The films also exhibit higher resistance to photocorrosion, because no decrease of photocurrent during the measurement was observed. Results of voltammetric measurements (Fig. 14) reveal that the photocurrent onset potential shifts to the lower anodic values after annealing due to possible changes in crystal structure. Also, an increase in photocurrent from 0.37 mA cm^{-2} at 0.5 V–1.95 mA cm^{-2} at 2.4 V is observed. Thus, irradiation of annealed WO_3 films at higher potentials could result in enhanced photocatalytic behaviour for water splitting.

4. Conclusions

The comprehensive investigation of as-deposited and annealed WO_3 films obtained by tungsten anodization in the different acidic
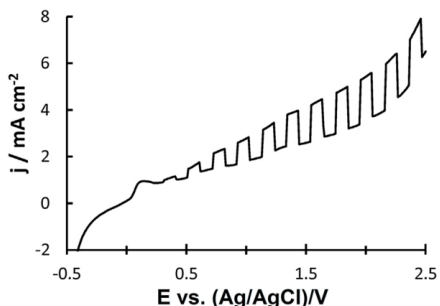

Fig. 14. Polarization curve of annealed WO_3 under pulsed UV irradiation obtained in 0.5 M Na_2SO_4; UV intensity is 80 mW cm^{-2}; on-off interval is 10 s; potential sweep rate − 10 mV s^{-1}.

solutions (1 M H_2SO_4, 1 M HCl, 14 M H_3PO_4, 14 M H_3PO_4 + 1 M NH_4F, 0.3 M oxalic acid) was carried out. Highest anodization currents of tungsten oxide formation were obtained for 0.3 M oxalic acid solution. The anodization behaviour of tungsten in the investigated electrolytes was studied by the electrochemical impedance spectroscopy. Electrochemical impedance magnitudes at the low frequency range decrease in the following order: $H_3PO_4 > H_3PO_4 + HF > HCl > H_2C_2O_4$. The lowest charge transfer resistances are obtained for oxalic acid that is in conformity with voltammetric data.

In addition, in the range of intermediate frequencies a pseudo-inductive response is visible, that can be ascribed to the relaxation phenomena at the oxide film/solution interface. The shapes of the Nyquist and Bode plots depend on the chemical composition of the solution and the anodization potential. Blocking (HCl and $H_2C_2O_4$) or reactive (H_3PO_4) behaviour was revealed based on EIS study. Also, Mott-Schottky analysis has been performed in order to evaluate semiconductor properties of the obtained films and was shown that both donor density and flat band potential vary with anodization potential.

A compact oxide film deposits at lower anodization potentials (<20 V), and some irregular, porous structures are formed at higher anodization potentials. The thickness of WO_3 formed in 0.3 M oxalic acid linearly depends on the anodization potential, and could reach 120 nm obtained at 60 V. The anodization ratio α = 1.87 nm V^{-1} and relative permittivity equal to 33.3 were determined for oxalic acid electrolyte.

Photoelectrochemical behaviour of as-deposited and annealed WO_3 films has been evaluated. The highest photocurrents are generated by films obtained at higher anodizing potentials (60 V–80 V). Annealing at 600 °C significantly improves the stability of oxide layer and increases the photocurrent. Thus, annealed WO_3 films manifest performed photocatalytic behaviour for water splitting in comparison to as-deposited.

References

[1] D.D. Macdonald, Steady-State Passive Films, J. Electrochem. Soc. 139 (1992) 170, doi:http://dx.doi.org/10.1149/1.2069165.
[2] D.D. Macdonald, The kinetics of growth of the passive film on tungsten in acidic phosphate solutions, Electrochim. Acta 43 (1998) 2851–2861, doi:http://dx.doi.org/10.1016/S0013-4686(98)00026-7.
[3] S. Biaggio, R. Rocha-Filho, J. Vilche, A study of thin anodic WO_3 films by electrochemical impedance spectroscopy, Electrochim. Acta 42 (1997) 1751–1758.
[4] M. Bojinov, The ability of a surface charge approach to describe barrier film growth on tungsten in acidic solutions, Electrochim. Acta 42 (1997) 3489–3498, doi:http://dx.doi.org/10.1016/S0013-4686(97)00037-6.
[5] M. Metikoš-Huković, Z. Grubač, The growth kinetics of thin anodic WO_3 films investigated by electrochemical impedance spectroscopy, J. Electroanal. Chem. 556 (2003) 167–178, doi:http://dx.doi.org/10.1016/S0022-0728(03)00342-5.
[6] V. Karastoyanov, M. Bojinov, Anodic oxidation of tungsten in sulphuric acid solution-Influence of hydrofluoric acid addition, Mater. Chem. Phys. 112 (2008) 702–710, doi:http://dx.doi.org/10.1016/j.matchemphys.2008.06.029.
[7] N.R. De Tacconi, C.R. Chenthamarakshan, G. Yogeeswaran, A. Watcharenwong, R.S. De Zoysa, N.A. Basit, K. Rajeshwar, Nanoporous TiO$_2$ and WO_3 films by anodization of titanium and tungsten substrates: Influence of process variables on morphology and photoelectrochemical response, J. Phys. Chem. B 110 (2006) 25347–25355, doi:http://dx.doi.org/10.1021/jp064527v.
[8] S. Berger, H. Tsuchiya, A. Ghicov, P. Schmuki, High photocurrent conversion efficiency in self-organized porous WO_3, Appl. Phys. Lett. 88 (2006) 203119, doi:http://dx.doi.org/10.1063/1.2206696.
[9] M. Yang, N.K. Shrestha, P. Schmuki, Thick porous tungsten trioxide films by anodization of tungsten in fluoride containing phosphoric acid electrolyte, Electrochem. Commun. 11 (2009) 1908–1911, doi:http://dx.doi.org/10.1016/j.elecom.2009.08.014 S.
[10] S. Ismail, K.A. Razak, P.W. Jing, Z. Lockman, Tungsten oxide nanoporous structure synthesized via direct electrochemical anodization, AIP Conf. Proc. (2011) 21–24, doi:http://dx.doi.org/10.1063/1.3586946.

[11] N. Mukherjee, M. Paulose, O.K. Varghese, G.K. Mor, C.A. Grimes, Fabrication of nanoporous tungsten oxide by galvanostatic anodization, J. Mater. Res. 18 (2003) 2296–2299, doi:http://dx.doi.org/10.1557/JMR 2003, 0321.

[12] T. Zhu, M.N. Chong, E.S. Chan, Nanostructured tungsten trioxide thin films synthesized for photoelectrocatalytic water oxidation: A review, Chem. Sus. Chem. 7 (2014) 2974–2997, doi:http://dx.doi.org/10.1002/cssc.201402089.

[13] Y. Liu, Y. Li, W. Li, S. Han, C. Liu, Photoelectrochemical properties and photocatalytic activity of nitrogen-doped nanoporous WO_3 photoelectrodes under visible light, Appl. Surf. Sci. 258 (2012) 5038–5045, doi:http://dx.doi.org/10.1016/j.apsusc.2012.01.080.

[14] R.M. Fernández-Domene, R. Sánchez-Tovar, B. Lucas-Granados, J. García-Antón, Improvement in photocatalytic activity of stable WO_3 nanoplatelet globular clusters arranged in a tree-like fashion: Influence of rotation velocity during anodization, Appl. Catal. B Environ. 189 (2016) 266–282, doi:http://dx.doi.org/10.1016/j.apcatb.2016.02.065.

[15] F. Di Quarto, A. Di Paola, C. Sunseri, Semiconducting properties of anodic WO3 amorphous films, Electrochim. Acta 26 (1981) 1177–1184, doi:http://dx.doi.org/10.1016/0013.

[16] S. Caramori, V. Cristino, L. Meda, A. Tacca, R. Argazzi, C.A. Bignozzi, Efficient anodically grown WO_3 for photoelectrochemical water splitting, Energy Procedia 22 (2011) 127–136, doi:http://dx.doi.org/10.1016/j.egypro.2012.05.214.

[17] Y. Chai, C.W. Tam, K.P. Beh, F.K. Yam, Z. Hassan, Effects of thermal treatment on the anodic growth of tungsten oxide films, Thin Solid Films 588 (2015) 44–49, doi:http://dx.doi.org/10.1016/j.tsf.2015.04.033.

[18] S. Ismail, C. Ng, E. Ahmadi, K. Razak, Segmented nanoporous WO_3 prepared via anodization and their photocatalytic properties, J. Mater. Res. (2016), doi:http://dx.doi.org/10.1557/jmr.2016.71.

[19] M. Yagi, S. Maruyama, K. Sone, K. Nagai, T. Norimatsu, oPreparation and photoelectrocatalytic activity of a nano-structured WO_3 platelet film, J. Solid State Chem. 181 (2008) 175–182, doi:http://dx.doi.org/10.1016/j.jssc.2007.11.018.

[20] W. Li, J. Li, X. Wang, J. Ma, Q. Chen, Photoelectrochemical and physical properties of WO_3 films obtained by the polymeric precursor method, Int. J. Hydrogen Energy 35 (2010) 13137–13145, doi:http://dx.doi.org/10.1016/j.ijhydene.2010.09.011.

[21] J. Yang, W. Li, J. Li, D. Sun, Q. Chen, Hydrothermal synthesis and photoelectrochemical properties of vertically aligned tungsten trioxide (hydrate) plate-like arrays fabricated directly on FTO substrates, J. Mater. Chem. 22 (2012) 17744, doi:http://dx.doi.org/10.1039/c2jm33199c.

[22] C.Y. Ng, K. Abdul Razak, Z. Lockman, Effect of annealing temperature on anodized nanoporous WO_3, J. Porous Mater. 22 (2015) 537–544, doi:http://dx.doi.org/10.1007/s10934-015-9924-x.

[23] W.L. Kwong, H. Qiu, A. Nakaruk, P. Koshy, C.C. Sorrell, Photoelectrochemical properties of WO_3 thin films prepared by electrodeposition, Energy Procedia 34 (2013) 617–626, doi:http://dx.doi.org/10.1016/j.egypro.2013.06.793.

[24] W.L. Kwong, N. Savvides, C.C. Sorrell, Electrodeposited nanostructured WO_3 thin films for photoelectrochemical applications, Electrochim. Acta 75 (2012) 371–380, doi:http://dx.doi.org/10.1016/j.electacta.2012.05.019.

[25] B. Yang, P.R.F. Barnes, W. Bertram, V. Luca, Strong photoresponse of nanostructured tungsten trioxide films prepared via a sol-gel route, J. Mater. Chem. 17 (2007) 2722, doi:http://dx.doi.org/10.1039/b702097j.

[26] H. Wang, T. Lindgren, J. He, A. Hagfeldt, S.-E. Lindquist, Photolelectrochemistry of Nanostructured WO_3 Thin Film Electrodes for Water Oxidation: Mechanism of Electron Transport, J. Phys. Chem. B 104 (2000) 5686–5696, doi:http://dx.doi.org/10.1021/jp0002751.

[27] N. Naseri, S. Yousefzadeh, E. Daryaei, A.Z. Moshfegh, Photoresponse and H_2 production of topographically controlled PEG assisted sol-gel WO_3 nanocrystalline thin films, Int. J. Hydrogen Energy 36 (2011) 13461–13472, doi:http://dx.doi.org/10.1016/j.ijhydene.2011.07.129.

[28] M.E. Orazem, B. Tribollet, Electrochemical Impedance Spectroscopy, Wiley New York, 2008 523 pp.

[29] M.E. Orazem, N. Pebere, B. Tribollet, Enhanced graphical representation of electrochemical impedance data, J. Electrochem. Soc. 153 (2006) B129–B136, doi:http://dx.doi.org/10.1149/1.2168377.

[30] C. Ng, C. Ye, Y.H. Ng, R. Amal, Flower-shaped tungsten oxide with inorganic fullerene-like structure: synthesis and characterization, Cryst. Growth Des. 10 (2010) 3794–3801.

[31] B. Hirschorn, M.E. Orazem, B. Tribollet, V. Vivier, I. Frateur, M. Musiani, Determination of effective capacitance and film thickness from constant-phase-element parameters, Electrochim Acta 55 (2010) 6218–6227, doi:http://dx.doi.org/10.1016/j.electacta.2009.10.065.

ARTICLE II

Insights into electrodeposition and catalytic activity of

MoS₂ for hydrogen evolution reaction electrocatalysis

R. Levinas, N. Tsyntsaru, H. Cesiulis

Electrochimica Acta 317 (2019) 427-436

Insights into electrodeposition and catalytic activity of MoS$_2$ for hydrogen evolution reaction electrocatalysis

Ramunas Levinas [a, *, 1], Natalia Tsyntsaru [a, b, 1], Henrikas Cesiulis [a]

[a] Faculty of Chemistry and Geosciences, Vilnius University, Naugarduko str. 24, Vilnius, Lithuania
[b] Institute of Applied Physics of ASM, 5 Academiei str., Chisinau, Republic of Moldova

A R T I C L E   I N F O

A B S T R A C T

MoS$_{2-x}$ films were electrodeposited cathodically onto copper rod substrates from a solution, containing MoS$_4^{2-}$ as the common Mo and S ion precursor. The catalyst loading was varied by adjusting electrodeposition conditions — applied potential and deposition time. A typical set of HER electrocatalyst experiments (polarization, Tafel slope analysis) carried out in 0.5 M H$_2$SO$_4$ was applied on the deposited MoS$_{2-x}$ films. Analysis of surface morphology (SEM) and chemical composition (EDS) were also performed. Electrochemical impedance spectroscopy in the same acidic media was used to evaluate the catalyst-solution interface and the interfacial kinetics (by calculating double layer capacitance and charge transfer resistance), as well as to characterize the hydrogen adsorption process (adsorption capacitance and resistance). A linear correlation between electrodeposition time and double layer capacitance was observed. However, the charge transfer resistance was found to decrease until it plateaued at longer deposition times. The MoS$_{2-x}$ film, deposited for 7200 s at −1.0 V (vs. Ag/AgCl), reached 10 mA cm^{-2} HER current at −0.18 V (vs. RHE), and represented the best result of this study. Electrochemical impedance spectroscopy (EIS) was further applied to evaluate the subtle changes in the MoS$_{2-x}$ films' semiconductor properties after HER stability tests (at −40 mA cm^{-2}), and to estimate the number of active sites on the material. EIS, in comparison to cyclic voltammetry or roughness factor calculations, is a completely nondestructive method that can be applied to accurately assess the system under investigation.

1. Introduction

Contemporary research into renewable energy always faces a common issue, namely: what can be used as an energy carrier from production to consumption. Hydrogen is considered as a potential alternative to hydrocarbons [1], but for a true breakthrough in hydrogen fuel cells more effective methods of H$_2$ generation and storage must be discovered. Photo- or electrochemical water splitting can be a source of clean H$_2$ fuel, but the process is hindered by unfavourable kinetics, and for efficient, large-scale application a catalyst is required [2].

Molybdenum sulphide compounds have been an object of research since at least 1977 [3—5], and have been thoroughly investigated for their semiconductor, photo-, and electrochemical properties. Extensive review papers have also been published

recently [6—8].

Their electrocatalytic properties towards the hydrogen evolution reaction were elucidated in an attempt to mimic the effects of biological enzymes [9]. In their seminal work, B. Hinnemann et al. proposed that an ideal catalyst would have a free energy of adsorbed H of $\Delta G_0^H \approx 0$. In other words, hydrogen evolution catalysis would obey the Sabatier principle: the chemical interactions between the catalyst and the substrate should be "just right"; that is, neither too strong nor too weak. A sufficient understanding of the various active centres is important when working with any heterogeneous catalysis, and this was also the case with molybdenum sulphide. Early research showed, that bulk MoS$_2$ (i.e. the basal plane) is a poor HER catalyst [10]. It became known later that edge sites are one of the active sites for H$_2$ evolution [11], and that HER activity would scale with their amount in the catalyst. However, when comparing edge-site-rich MoS$_2$ flakes with a monolayer film, it was found that the film exhibited much better HER activity, which led to proof of the importance of different active sites — sulphur vacancies ($\Delta G_0^H \approx -0.095$ eV) [12]. Currently, the active sites of MoS$_2$ are thought to be Mo edge sites

* Corresponding author.
  E-mail address: ramunas.levinas@chf.vu.lt (R. Levinas).
[1] ISE member.

$(\Delta G^H_0 \approx 0.115 \, eV)$, S vacancies, and grain boundaries $(\Delta G^H_0 \approx 0.181-0.566 \, eV)$. The basal plane is effectively inert at $\Delta G^H_0 \approx 1.218 \, eV$. It may also be important to mention that not all commercially available MoS_2 is equal, as it was found that the HER properties of MoS_2, obtained from different suppliers, varies greatly due to different methods of preparation [13].

Coatings of unique compositions, crystallographic structures, surface morphologies, and catalytic properties, have been synthesized using chemical vapour deposition [14,15], hydro- or solvothermal deposition [16—18], the increasingly popular chemical exfoliation method, electrodeposition [19—23], and more. Incorporation of naturally-occurring molybdenite has also been shown to greatly enhance the HER catalytic properties of electrodeposited Ni films in alkaline media [24]. Electrodeposited molybdenum disulphide films consist of nonstoichiometric, amorphous MoS_{2-x} that is particularly active towards HER [25,26]. However, they are less stable in comparison to crystalline MoS_2 materials [27]. Some of the earlier studies on the electrodeposition of MoS_2 have reported the method involving a cathodic reduction of aqueous ammonium tetrathiomolybdate $((NH_4)_2MoS_4)$ [28]. It was found, that electrodeposition begins at $-0.9 \, V$ (vs. SCE) and reaches a maximum of 30% current efficiency at $-1.2 \, V$ to $-1.4 \, V$, then decreases at more negative potentials due to hydrogen evolution. A linear correlation was found between the electrodeposited film thickness and the charge passed through the cell. On the other hand, oxidative deposition of tetrathiomolybdate solutions at anodic potentials yields the formation of MoS_3 [4,5], which also has attractive electrochemical properties. A mixture of MoS_2 and MoS_3 has been electrodeposited by applying a potential cycling method between cathodic and anodic deposition modes, resulting in a MoS_{2+x} film possessing mixed electrocatalytic capabilities [29].

The stability of electrodeposited MoS_2 seems to be an often-omitted issue. Although most research reports satisfactory or even excellent electrochemical stability, some authors have reported that thicker films (>1 μm) peeled off from the substrate [28,30], and that cracks could appear during drying. Furthermore, for a MoS_2 monolayer (grown by CVD and aged for 1 year) XPS analysis showed that the Mo/S ratio decreased from 1 /2 to 1 /1.05 due to oxidation of sulphide sites [31]. Calculations based on Density Functional Theory (DFT) revealed, that on a S-deficient MoS_2 surface the kinetic O_2 dissociative adsorption barrier is relatively low, meaning that the oxidation (passivation) of active sites is thermodynamically favourable [32]. Edge sites and grain boundaries were also found to be susceptible to oxidation, and it was theorized, that the misfit between the MoS_2 and MoO_3 lattices may be the cause of the mechanical stress that causes MoS_2 cracking [33].

Ultimately, during recent years strides have been made in the understanding of amorphous MoS_{2-x} compounds. Raman spectroscopy experiments have unravelled different S—S bonds in electrodeposited MoS_2, representing bridging/shared and terminal disulphide bonds. It was revealed that the structure of MoS_2 is a polymer, composed of $[Mo_3S_{13}]^{2-}$ clusters connected via disulphide ligands [34]. This structure is currently thought to explain the empirically observed peculiarities of amorphous MoS_2: the unprecedented HER electrocatalytic activity (the active unsaturated Mo^{IV} sites/sulphur vacancies have a favourable ΔG^H_0), the reductive activation of some MoS_2 compounds (removal of terminal disulphide ligands, resulting in more unsaturated Mo^{IV} sites), and the cathodic corrosion (shortening of the polymer chains). Taking into account what was mentioned above, the present research is devoted to extending the knowledge into the electrodeposition of MoS_2, and its catalytic activity for hydrogen evolution reaction.

2. Experimental

Electrolyte preparation. Molybdenum disulphide films were electrodeposited from a solution containing a common precursor of Mo^{6+} and S^{2-} ions — tetrathiomolybdate (TTM/MoS_4^{2-}). In order to prepare the electrolyte, ammonium heptamolybdate tetrahydrate $((NH_4)_6Mo_7O_{24}*4H_2O)$ and 60% sodium sulphide hydrate (Na_2S*xH_2O) were mixed in a ratio of $Mo /S = 1 /4$. The sulfidation of molybdate ions (MoO_4^{2-}) to tetrathiomolybdate is a four-step reaction, where each step is reversible, and the total reaction can be represented as follows:

$$MoO_4^{2-} + 4HS^- + 4H^+ \leftrightarrow MoS_4^{2-} + 4H_2O \qquad (1)$$
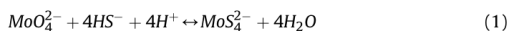
The pH of the mixture was ~12, and it was acidified up to pH of 7 with sulfuric acid to push the reaction equilibrium towards the product side and to favour the formation of MoS_4^{2-} over the intermediates. The reference indicator of MoS_4^{2-} formation was the solution colour changing to a deep red. 25 ml of 2-propanol was added to the electrolyte in order to decrease surface tension and increase wettability of the working electrode. The final electrolyte composition contained: $C_{MoS_4^{2-}} = 0.025 \, M + 10\%$ of 2-propanol. The pH was kept weakly alkaline (pH ~ 8) to prevent precipitation of insoluble MoS_3.

MoS_2 electrodeposition. All electrochemical measurements were carried out using a standard three-electrode cell set-up (potentiostat/galvanostat Metrohm μAutolab Type III). Unless specified otherwise, all potentials were referenced to Ag/AgCl. The copper rod substrates were prepared to have a $1 \, cm^2$ working surface area. They were first polished with a commercial detergent, then immersed in $2 \, M \, H_2SO_4$ to dissolve surface oxides, rinsed with distilled water, and finally degreased with 2-propanol. Initially, linear sweep voltammetry measurements were carried out to determine the electrodeposition potential range in the investigated electrolyte. MoS_{2-x} films were deposited under potentiostatic mode, at various cathodic potentials ($-0.8 \, V$ to - $1.2 \, V$); or at constant potential ($-1.0 \, V$), but for different deposition times (200 s—7200 s). The surface morphology and chemical composition of the electrodeposited MoS_{2-x} films were evaluated using a Hitachi TM 3000 Scanning Electron Microscope with an integrated EDX module.

Electrocatalytic activity measurements. To measure the electrocatalytic activity towards hydrogen evolution, the as-deposited MoS_2 films were rinsed with distilled water and immediately transferred to a $0.5 \, M \, H_2SO_4$ solution. A multi-faceted characterization of the obtained MoS_2 films towards HER consisted of the following measurements: a) open circuit potential (OCP) determination; b) electrochemical impedance spectroscopy (EIS) at $-0.32 \, V$ vs. Ag/AgCl ($-0.1 \, V$ vs. RHE); c) ten linear sweep voltammetry (LSV) curves at $10 \, mV \, s^{-1}$ from OCP to - $40 \, mA \, cm^{-2}$ cut-off condition; d) stability measurement for 20 min at $-40 \, mA \, cm^{-2}$.

Registering an electrochemical impedance spectrum before electrocatalytic measurements served two purposes: it allowed analysis of the catalyst in a non-destructive way, and supplied an accurate value of electrolyte resistance (for iR correction). Accordingly, all polarization curves were corrected for the iR drop.

In addition, EIS was used to estimate the H^+ adsorption and double layer capacitances (C_a and C_{dl}) of the electrodeposited MoS_{2-x} films. The cathodic overpotential for EIS recording was chosen to be not far from Nernst potential ($-0.1 \, V$). HER polarization experiments showed that at this overpotential range the reaction of hydrogen evolution occurs slowly. EIS spectra were measured in the range 10 kHz - 0.1 Hz. An amplitude of 20 mV was used based on the data of performed Kronig-Kramers analysis.

3. Results and discussion

3.1. Cathodic electrodeposition of MoS2

To develop a necessary understanding of the chosen system, linear sweep voltammetry (LSV) measurements at increasing potential scan rates were performed. The cathodic deposition of MoS_2 occurs according to Eq. (2):

$$[MoS_4]^{2-} + 2e^- + 2H_2O \rightarrow MoS_2 + 2HS^- + 2OH^- \tag{2}$$
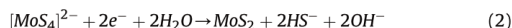
The open circuit potential was chosen as the starting point and the potential was scanned toward −1.2 V (Fig. 1). At a low scan rate (5 mV s^{-1}) no clear reduction peaks can be distinguished. MoS_{2-x} electrodeposition occurs alongside hydrogen evolution. When the potential scan rate is increased to 20 mV s^{-1} and more, a small peak in the reduction region (−1.0 V to −1.15 V) becomes apparent, after which further cathodic current increase results in hydrogen evolution. The peak shift towards more cathodic values with increased potential scan rate suggests slow reaction kinetics, as the current is slow to respond to the swift change in the potential. This may be attributed to a slow charge transfer step or diffusion, but the detailed kinetics of this reaction were not the objective of this study.

Hence, MoS_{2-x} films were deposited under a potentiostatic mode, in the range of −0.8 V to −1.2 V to observe film formation nearby the reduction peak. The surface morphology and chemical composition of as-deposited films depends on the potential applied (Fig. 2). Thin layers that replicate the surface morphology of the substrate are obtained at low cathodic potentials (Fig. 2a). At an intermediate deposition potential of −1.0 V a rough and nodular surface structure with some cracks is formed (Fig. 2b). At even higher potentials (−1.2 V) the deposited films were observed to peel off from the substrate when drying. As was expected from LSV, the increase of the cathodic deposition potential results in higher quantities (in at. %) of Mo and S in the electrodeposits at a constant deposition time (Fig. 2c). Larger quantities of Mo and S can be also obtained by increasing the deposition time (Fig. 2d). Thus, by increasing the deposition time it is possible to carry out electrodeposition at lower potentials, in order to avoid intense hydrogen evolution. As it was mentioned, the as-deposited films are thin, and therefore a strong signal of the Cu substrate is visible in the EDX
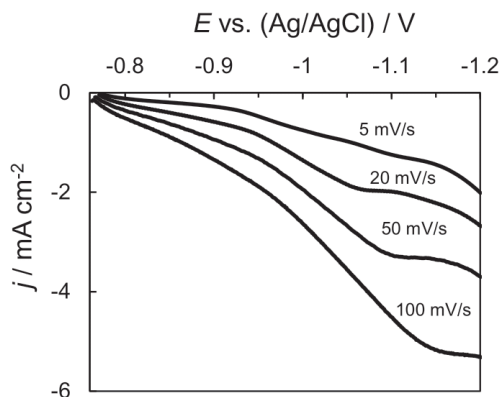
analysis. However, the atomic % of Cu decreases when a larger amount of Mo and S is deposited at higher potentials or deposition times (Fig. 2c and d). It should be noted, that a significant amount of oxygen is also present in the samples, and its relative amount increases with applied potential. This could be attributed to the following issues: a) some amount of unreacted molybdate from the solution can electrodeposit alongside MoS_{2-x}; b) due to the oxidation of MoS_{2-x} active centres in air.

3.2. Electrocatalytic activity for hydrogen evolution reaction
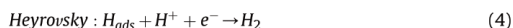
3.2.1. Influence of electrodeposition potential

The electrodeposited MoS_{2-x} films were all characterized in terms of their ability to catalyse the hydrogen evolution reaction in acidic media. All experiments were carried out with freshly-prepared MoS_{2-x}, as it was found that the electrocatalytic activity for HER severely decreases after the films had been dried and stored in air (likely due to surface active site oxidation). Thus, the as-deposited films were removed from the electrolyte, rinsed with distilled water and 2-propanol, and then immediately transferred into 0.5 M H_2SO_4. The solution was used for a comprehensive characterization of the obtained films (as described in the experimental section), consisting of EIS, HER voltammetric sweeps, and galvanostatic stability experiments (Fig. 3). Several tendencies were revealed from the analysis.

It is evident that even a thin coating of MoS_{2-x} (deposited at −0.8 V) already greatly increased HER activity compared to the bare substrate (Fig. 3a). An increase in the cathodic deposition potential resulted in better catalytic activity and lower onset overpotentials (measured at 1 mA cm^{-2}): 0.232 V and −0.122 V vs. RHE for MoS_{2-x} deposited at −0.8 V and −1.2 V respectively. The reason for this improvement is mostly likely due to the increase in catalyst loading, i.e. a higher amount of electrodeposited MoS_{2-x}, or a lesser amount of Cu in EDX spectra. A more in-depth analysis of the catalytic activity follows in section 3.3.

The hydrogen evolution rate depends both on the chemical composition of a cathode and surface morphology. An exponential relation between MoS_{2-x} electrodeposition potential and HER exchange current density (j_0) was observed (Fig. 3b). Although the average thickness of the films deposited at −1.0 V to −1.2 V does not differ significantly from each other, the increase in j_0 is evident. Unfortunately, further increasing of the deposition potential did not obey this exponential relation, probably because of the unfavourable changes in the film's formation that occur due to severe hydrogen evolution.

Another result showing the impact of electrodeposition potential on the intrinsic activity of the film is the calculated HER Tafel slope (Fig. 3c). The mechanism of cathodic hydrogen evolution occurs through a few intermediate stages, and each of these can be rate limiting:

$$Volmer : H^+ + e^- \rightarrow H_{ads} \tag{3}$$

$$Heyrovsky : H_{ads} + H^+ + e^- \rightarrow H_2 \tag{4}$$

$$Tafel : H_{ads} + H_{ads} \rightarrow H_2 \tag{5}$$

If the Volmer adsorption reaction is the rate limiting step, a Tafel slope of 120 mV dec^{-1} would be expected. If either the Heyrovsky or Tafel recombination steps are rate limiting, the Tafel slope would be 40 or 30 mV dec^{-1}. For the investigated samples, Tafel slopes generally fell within the 40–50 mV dec^{-1} range, showing mixed HER kinetics. One exception from the given trend was the MoS_{2-x} film, deposited at −1.2 V. The Tafel slope for this sample was markedly higher at 65.9 mV dec^{-1} (Fig. 3c). The increase in the Tafel

Fig. 1. LSV curves of MoS_{2-x} electrodeposition on a bare Cu wire substrate in 25 mM TTM +10% 2-propanol.
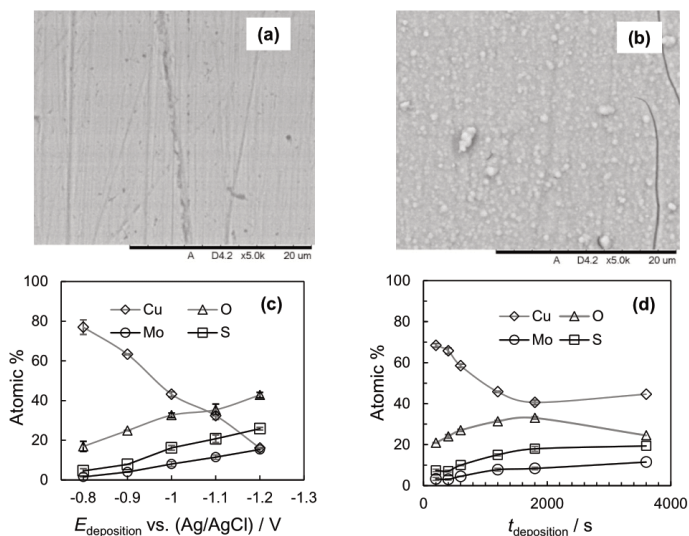
Fig. 2. SEM images of the surface morphology of MoS$_{2-x}$ films, electrodeposited for 600 s at −0.8 V and −1.0 V respectively (a, b). Influence of applied potential at fixed deposition time of 600 s (c) and deposition time at fixed potential of −1.0 V (d) on composition of MoS$_{2-x}$ films electrodeposited on copper.
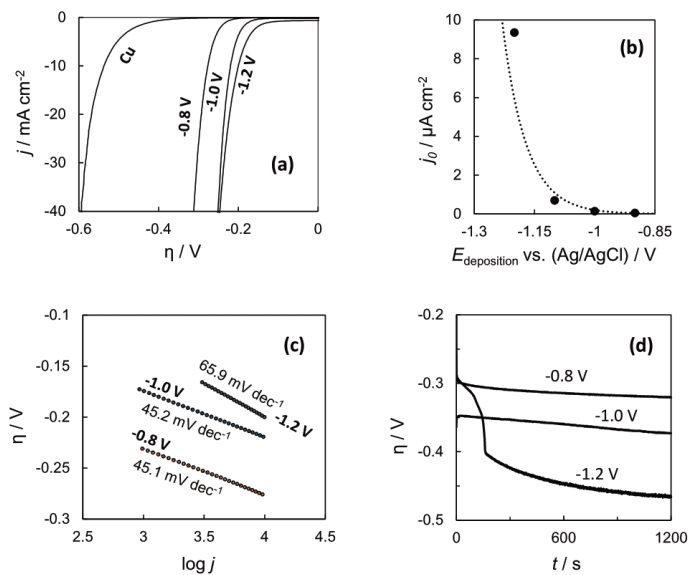

Fig. 3. Hydrogen evolution electrocatalysis data: 10th cycle of HER polarization curve of MoS$_{2-x}$ films, electrodeposited at indicated potentials for 600s, scan rate 10 mV s^{-1}, 0.5 M H$_2$SO$_4$. Bare Cu substrate added for comparison (a); HER exchange current density as a function of MoS$_{2-x}$ electrodeposition potential (b); Tafel slopes of the respective samples (c); Galvanostatic (−40 mA cm^{-2}) stability experiments (d) — see details in the text.

slope shows an unfavourable deviation from the dominating Volmer-Heyrovsky or Volmer-Tafel HER mechanism. This may be related to the occurrence of side reactions during electrodeposition at this relatively high potential, and the changes in the deposited

MoS$_{2-x}$ films. The Mo: S ratio of this film was also the lowest at 1:1.68.

Finally, the electrochemical stability of the MoS$_{2-x}$ films was evaluated by chronopotentiometry at moderately harsh working

conditions of $-40\,\mathrm{mA\,cm^{-2}}$ for 20 min (Fig. 3d). On average, the films lost around 5% activity over the measurement, but MoS_{2-x} film deposited at $-1.2\,V$ underwent complete destruction (peeling off from the substrate) within the first 200 s of the experiment. These experiments show that, although electrodeposition at higher potentials seems to yield films with better electrocatalytic activity, their stability is unacceptable.

3.2.2. Influence of deposition time

Deposition time also affects the elemental composition of the MoS_{2-x} layers (Fig. 2 b), and consequently can change their catalytic activity. Taking into account SEM/EDX analysis and stability of the films, deposition at a constant potential of $-1.0\,V$ but for different times (200 s—7200 s) was chosen for further investigation (Fig. 4). Indeed, a longer deposition time had a significant effect on the MoS_{2-x} films' electrocatalytic activity. The overpotential for HER (at $10\,\mathrm{mA\,cm^{-2}}$) changed from $-0.285\,V$ to $-0.180\,V$ (vs. RHE) when the deposition time was increased from 200 s to 7200 s (Fig. 4a), which may be attributed to increasing catalyst loading. However, a diminishing gain in catalytic activity is observed when deposition times are increased from 1800 s to 7200 s. A limit is reached where the electrode's total catalytic activity no longer depends on catalyst loading.

The exchange current density increases linearly with deposition time in the entire investigated range up to 7200 s (Fig. 4b). This is a particularly promising result, as it implies a possibility to reach relatively high exchange current densities under mild electrodeposition conditions. The Tafel slopes of these samples also show an interesting behaviour (Fig. 4c). A minimum of $42.5\,\mathrm{mV\,dec^{-1}}$ is reached when the MoS_{2-x} film has been deposited for 1800 s. The reason for this outcome could be linked to the formation of

different active sites, or that an optimum catalyst loading is reached, where a further increase of deposition time begins to impede charge transfer in the semiconductor MoS_{2-x} material.

The electrochemical stability of these films does not necessarily correlate to their catalytic activity. Stability tests under the previously described conditions showed that thinner (short deposition time) and more compact films can lose less than 1% (in terms of overpotential) of their initial activity over the experiment. For the film deposited for 1800 s, a larger 2.9% decrease in catalytic activity was observed. Finally, the film with the longest deposition time in our experimental series (7200 s) only had a 1.3% loss from initial activity. These results show that the most electrochemically stable MoS_{2-x} films should have either a compact, or a well-evolved and rough surface morphology.

An electrodeposited MoS_{2-x} film with the highest electrocatalytic activity for HER was compared with that of other MoS_2 and WS_2 based materials, synthesized by various methods (Table 1). It should be pointed out, that due to difficulties in assessing the electrocatalytically active surface area most reported current densities are normalized to a geometric surface area. Usually bigger catalyst loading results in better catalytic activity. In addition, composites with high-surface-area substrates (e.g. carbon cloth, nanowires) have been reported to exhibit the best catalytic activity and stability.

3.3. Electrochemical impedance spectroscopy

3.3.1. Catalyst-solution interface evaluation

EIS has been shown to provide useful information on HER catalytic materials that is supplementary to more typical experiments like steady-state polarization, and can give insight into the
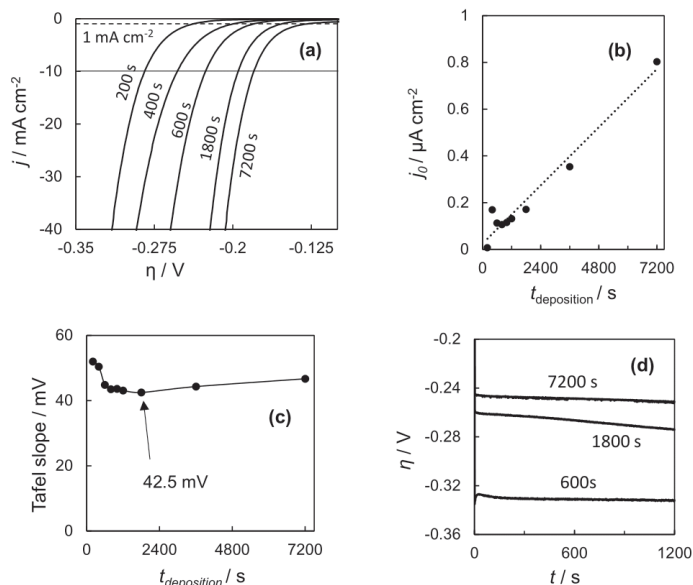

Fig. 4. iR-corrected 10th HER polarization curve of MoS_{2-x} films, electrodeposited at $-1.0\,V$ (vs. Ag/AgCl) for indicated deposition time (a), scan rate $10\,\mathrm{mV\,s^{-1}}$, $0.5\,\mathrm{M\,H_2SO_4}$; HER exchange current density as a function of deposition time (b); Relation between electrodeposition time and HER tafel slope (c); galvanostatic stability measurement (at $-40\,\mathrm{mA\,cm^{-2}}$) curves (d).

Table 1
Comparison of key HER catalytic parameters for WS_2 and MoS_2 based catalysts.

Catalyst	j/mA cm^{-2}	$-E_j$/mV	Tafel slope/mV dec^{-1}	Synthesis method	Reference
Ni—MoS_2	10	310	47	Hydrothermal	[35]
GO/WS_2		180	67	Electrodeposition	[36]
VG/CC/MoS_2		78	53	Hydrothermal	[37]
CC/$CoMoS_x$		100	70	Electrodeposition	[38]
GC/MoS_2 film		202	48	Electrodeposition	[39]
CC/MoS_2	86	250	50	Solvothermal	[40]
Ti/MoS_2	30	250	—	Hydrothermal	[41]
CC/WS_2	42	300	68	Thermolysis	[42]
rGO/WS_2	23	300	58	Hydrothermal	[43]
CC/Mo—W—S	10	198	54	Electrodeposition	[44]
MoO_3—MoS_2		254	—	CVD/sulfidization	[45]
Amorph. MoS_3		242	—	Electrodeposition	[25]
Exfol. MoS_2		207	—	Liquid exfoliation	[46]
MoS_{2-x}		180	44	Electrodeposition	This work

mechanic or kinetic phenomena of the system under investigation [47]. In this study, the EIS spectra were obtained prior to the polarization measurements, in the same working electrolyte of 0.5 M H_2SO_4. A cathodic overpotential of −0.1V was chosen, as it represents a potential window where the Faradaic reaction (hydrogen evolution) occurs at a low rate, and a lower disturbance of the pre-electrode layer by hydrogen bubbles is expected.

Under these experimental conditions, the low-frequency current response to the potential perturbation should be caused mainly by the adsorption of H onto the active sites of the MoS_{2-x} film. Because the majority of active centres are S vacancies and Mo edges (with respective free hydrogen adsorption energies of $\Delta G^H_0 \approx -0.095$ eV, $\Delta G^H_0 \approx 0.115$ eV [12]), specific H^+ adsorption had to assert during measurements by EIS and further characterization of the catalyst-solution interface. The characteristic impedance spectra are shown in Fig. 5. An identical high-frequency inductive response was observed for all samples. Although it did not seem to vary with electrodeposition time (and as such was likely not related to the occurring changes in the electrodeposited MoS_{2-x} films), it was also taken into account when fitting the data to equivalent electrochemical circuit models.

All of the impedance spectra have an almost entirely capacitive profile in the low-frequency range, but at higher frequencies (~1000 Hz—100 Hz) the beginning of a small semicircle can be distinguished (see Fig. 5a and insert). As is seen from Bode plots (Fig. 5b and c), a longer deposition time resulted in lower impedance magnitudes. When a thicker layer of a semiconductor is deposited, an opposite result would be expected − the impedance magnitude should increase. It confirms that the measured EIS spectra reflect the electrocatalytic activity of the MoS_{2-x} films. However, in order to model the spectra using discrete elements, both the double layer and adsorption capacitances should be taken into account. Therefore, the equivalent electric circuit (EEC) used for fitting has to involve elements attributed to the capacitance of the double electric layer (C_{dl}) and capacitance describing the specific adsorption of hydrogen onto the active sites of MoS_{2-x} film (C_a). Thus, the results were fitted to the EEC shown in Fig. 6.

This EEC has been often used to model reactions with a consecutive adsorption step. The inductance element has been added in order to fit the spectrum in the entire measured frequency range. The quality of the fit was evaluated by the chi-square and lowest sum of squares tests, by checking the randomness of the fit residuals, low relative standard deviations (normally less than 5%), and applying statistical F-test and t-test analysis. The model was found to fit the spectra well and conforms the requirements of performed statistical tests.

A constant phase element (CPE$_a$, Fig. 6) fits the experimental data better than a simple capacitance element; the obtained values of T were recalculated into capacitance, C_a, using Brug et al.'s formula, Eq. (6) [48]:

$$C_a = T_a^{\frac{1}{n}} \left(\frac{1}{R_s + R_{ct}} + \frac{1}{R_a} \right)^{1-\frac{1}{n}} \tag{6}$$

where T_a is the parameter related to the electrode capacitance, n is the constant phase exponent; R_s, R_{ct} and R_a are uncompensated, charge transfer, and adsorption resistances, respectively.

This EEC describes an EIS spectrum that has two time constants. The process occurring at high frequencies is characterized by (C_{dl}−R_{ct}), and the corresponding time constant is τ_1. Here C_{dl} is the double-layer capacitance, and R_{ct} is the charge transfer resistance of the Faradaic process. The (CPE_a-R_a) circuit represents the low frequency time constant τ_2. Its presence is caused by the hydrogen adsorption reaction. Some variation becomes evident when the time constants are plotted against the electrodeposition time of the MoS_{2-x} films (Fig. 7). The high frequency time constant τ_1 approaches a maximum of 0.067 s, and the low frequency τ_2 reaches a minimum of 1.48 s for the film electrodeposited for 1000 s, and is lowest for films that have been deposited for 400—1200 s. This tendency broadly corresponds to the change in Tafel slope. As it is seen in Fig. 4d, although the total electrode activity increases with deposition time, part of that increase should be attributed to changes in the electrocatalytically active surface area rather than the intrinsic activity of the material.

The variations of the double layer capacitance C_{dl}, adsorption capacitance C_a, and adsorption resistance R_a are presented in Fig. 8. Both C_{dl} and C_a increase with deposition time, but the double layer capacitance at shorter deposition times remains larger than C_a. Such high values of C_{dl} are defined by a large real area of the obtained surface in comparison with the flat geometric surface area. Therefore, it is even higher than C_a, whose values are defined by both the roughness of the surface and electric current response to the reversible variations of surface coverage of adsorbate under the electrode potential perturbation during faradaic hydrogen evolution process.

However, when the films have been deposited for 1800 s and longer, the adsorption capacitance grows larger than C_{dl}. This is likely related to an increase in the number of active sites, and a consequent increase of coverage of the electrode surface by H_{ads}. The adsorption-related resistance R_a follows an exponential extinction curve, and almost plateaus at 226 Ω cm^2 for the longest deposition time film, which could be attributed to the appearance of charge transfer limitations in the growing MoS_{2-x} film.

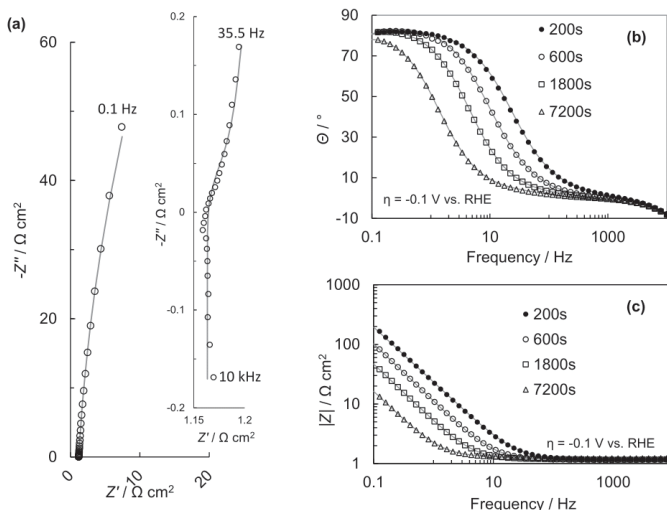This can be further related to the observed limit in HER

Fig. 5. EIS spectra obtained at overpotential −0.1 V of MoS$_{2-x}$ films, electrodeposited for different deposition times: a representative complex-plane Nyquist spectrum of a MoS$_{2-x}$ film electrodeposited for 1800 s (inset shows high frequency region) (a); the Bode impedance plots for respective films (b, c). Lines represent fitted data.
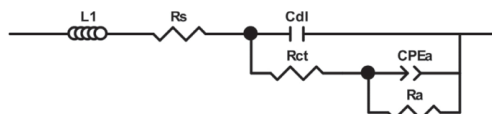

Fig. 6. Equivalent electric circuit used for EIS data fitting. L$_1$ − inductance element. R$_s$ − electrolyte resistance; C$_{dl}$ − element representing double layer capacitance; R$_{ct}$ − Faradaic charge transfer resistance; CPE$_a$ − constant phase element of the adsorption reaction; R$_a$ − adsorption resistance.
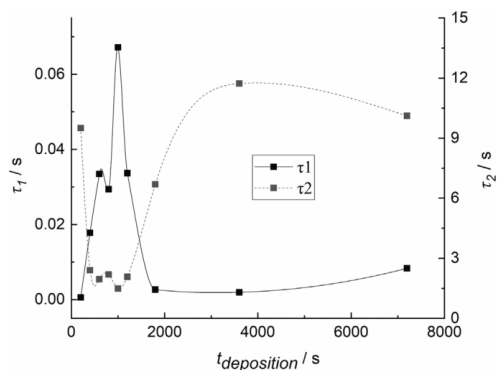
Fig. 7. The variation of time constants τ_1 (high frequency) and τ_2 (low frequency) with electrodeposition time.

electrocatalytic activity for the investigated films. With increasing film deposition time, the η$_{10mA}$ (overpotential at 10 mA cm^{-2} of HER current) and HER onset overpotential reach a plateau (Fig. 9). Thus, although further catalyst loading by electrodeposition is possible, the gain in electrocatalytic activity remains almost constant. In order to construct a more active electrode for HER electrocatalysis, it would be best to choose an optimal deposition time that results in better intrinsic activity, and increase the surface area of the substrate.

3.3.2. Electrochemical stability

The EIS methodology has also been applied to characterize the film and the catalyst-solution interface before and after stability tests (20 min under galvanostatic conditions at −40 mA cm^{-2}). A first EIS spectrum was generated prior to the test, and the second after, in the same electrolyte and applied conditions. The procedure allowed tracking any changes in the surface morphology, structure, or composition of the catalyst, by evaluating the differences in the impedance spectra. Indeed, a small but detectable signal was observed. Namely, the impedance magnitudes |Z| and phase angles θ increased slightly after stability tests. The changes of the double layer and adsorption capacitances, as well as the charge transfer resistance, were estimated using the same EEC shown in Fig. 6. C$_{dl}$ was found to decrease slightly after the stability test, which likely shows a decrease of the electrochemically active surface area. However, the R$_a$ increased up to several hundred ohms for some samples. This correlates with the cathodic corrosion of amorphous MoS$_{2-x}$ in the form of shortening [Mo$_3$S$_{13}$]$^{2-}$ polymer chains that has been hypothesized in Ref. [34]. A disrupted polymeric structure would indeed result in a hindered charge transfer step. These EIS results correspond well with the voltammetric stability curves (Fig. 4d). The capacitance of the specifically adsorbed species also changes after stability tests, and C$_a$ was seen to increase slightly. The increase in adsorption capacitance is likely caused by another phenomenon related to the polymeric structure − the removal of terminal disulphide ligands, which results in the appearance of
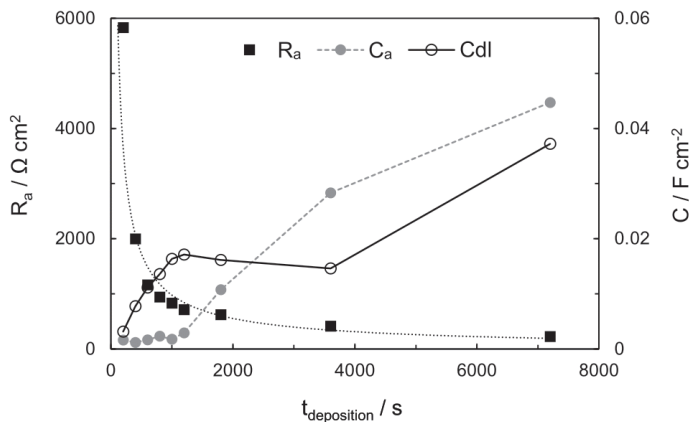
Fig. 8. EEC-calculated values of C_{dl}, C_a and R_a, and their dependence on the electrodeposition time of MoS_{2-x} films.
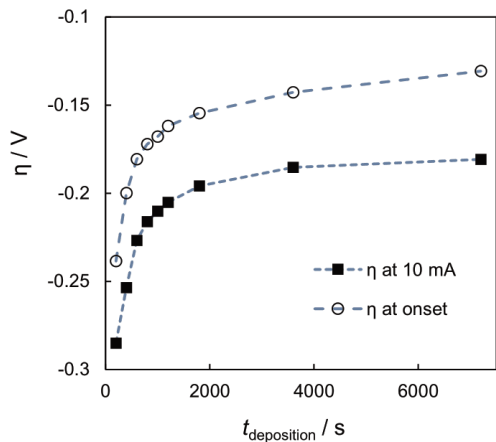

Fig. 9. HER onset overpotential (at $-1\,mA\,cm^{-2}$) and overpotential, needed to reach $10\,mA\,cm^{-2}$ of HER current, as a function of electrodeposition time.

new active sites (unsaturated Mo^{IV} sites). These experiments prove that, under vigorous hydrogen evolution conditions, the MoS_{2-x} films actually gain some active sites, but lose electrocatalytically active surface area and charge transfer conductivity, which limits the overall HER electrocatalytic activity of the material.

3.3.3. Estimation of electrocatalytically active sites

The electrocatalytically active surface area is not necessarily equal to the electrochemically active surface area, and attempts to normalize HER current density into electrochemically active surface area can skew the desired results. It should be noted, that there is no conventional method for active site calculation yet; research on MoS_2-based HER catalysts usually faces difficulty in finding an appropriate way for number of active site estimation. However, researchers often report the number of active sites per cm^2 to compare their synthesized materials. Therefore, a following model to estimate the number of active sites attributed to the specific adsorption of H_{ads} by the application of EIS is discussed.

Firstly, to have a baseline for comparison, a calculation for a theoretical ideal catalytic film with 100% adsorbed hydrogen coverage is performed. From a geometrical point of view, an active site (sulphur vacancy) on the surface of a MoS_{2-x} lattice has a diameter of ~0.5 nm [12]. Therefore, a film of $1\,cm^2$ would then have $5.0 \cdot 10^{14}$ active sites. Assuming complete coverage with a monolayer of H_{ads}, the charge necessary to attain this monolayer would be $\sigma = 0.08\,mC$.

For the MoS_2 films, the charge necessary to attain a layer of adsorbed H was calculated from the EIS data, by taking into account only the adsorption capacitance. Values of C_a were recalculated into charge using following equation:

$$Q_a = C_a \eta \tag{7}$$

where Q_a is the charge used to obtain a layer of H_{ads} on the MoS_{2-x} film's surface; C_a is the adsorption capacitance; η is the over-potential applied for hydrogen evolution reaction, and at the same time for H_{ads} layer formation ($-0.1\,V$).

It was assumed, that hydrogen adsorption is a one-electron process (Eq. (3)), and the one active site adsorbs a single H^+. Thus, the maximum number of active sites can be calculated from Equation (8).

$$N_{sites} = \frac{Q_a * N_A}{nF} \tag{8}$$

This yields values ranging from 10^{15} to 10^{16} sites cm^{-2} (see Table 2). Taking into account the difference between the real surface area and the geometric, these values are considered as being in good agreement with those obtained from geometric parameters as described above. In addition, the values estimated based on C_a data are close to those reported by other researchers working with different methods (e.g. roughness factor/capacitance calculations,

Table 2
Adsorption charge and active site calculation data.

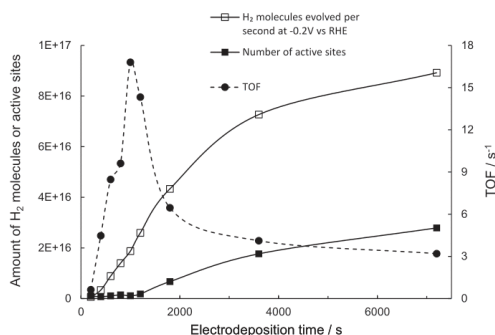| $t_{deposition}$/s	Q_a/mC cm^{-2}	$N_{active\ sites} \cdot 10^{15}$/sites cm^{-2}
200	0.22	1.02
600	0.183	1.05
1200	0.317	1.81
3600	3.19	17.7
7200	5.05	27.9

Fig. 10. Number of active sites and HER turnover frequencies at -0.2 V vs. RHE of MoS$_{2-x}$ films, electrodeposited for different times (200 s–7200 s).

anodic oxidation, etc) to estimate active site densities for amorphous MoS$_{2-x}$ [25,49].

The turnover frequencies (number of hydrogen molecules evolved per active site per second) for the films were compared at an overpotential of -0.2 V (Fig. 10). Active site number values per 1 cm^2 of the geometric area of the deposits were calculated from EIS data as described previously. The number of H$_2$ molecules evolved per second was calculated from respective current densities at overpotential -0.2 V, assuming that hydrogen evolution is a two-electron process. A maximum of turnover frequencies (TOF) of 15.3 s^{-1} was calculated for the MoS$_{2-x}$ film, electrodeposited for 1000 s. Although the films, deposited for longer times (up to 7200 s) have better total activity, probably because of an optimum point in deposition time for per-site activity. These data also correspond well to the results presented in Fig. 4c, where the films deposited for 400 s–1800 s had the lowest Tafel slopes ranging from 42 to 44 mV dec^{-1}. A Tafel slope close to 40 mV dec^{-1} suggests that hydrogen evolution occurs through a Volmer-Heyrovsky mechanism, and that the electrochemical desorption (Heyrovsky) step is rate limiting [50,51]. The calculated turnover frequencies are in agreement with these data: the highest TOFs correspond to the lowest Tafel slopes. In addition, comparing the results with the time constants presented in Fig. 7, the same correlation is seen: the lowest adsorption time constants correspond to the highest turnover frequencies. The agreement between polarization and electrochemical impedance experiments again confirms the validity of using EIS to approximate the number of active sites on electrodeposited MoS$_{2-x}$.

Electrochemical impedance spectroscopy can be proposed as a simple way to determine various HER electrocatalyst properties: from activity and stability to the number of active sites and/or turnover frequency. Under carefully chosen electrochemical conditions, it is an entirely non-destructive method that can be seamlessly included in the experimental procedure and provide valuable data on the film/solution interface.

4. Conclusions

Nonstoichiometric MoS$_{2-x}$ films were electrodeposited on copper substrates from a MoS$_4^{2-}$ ion solution under potentiostatic conditions (-0.8 V to -1.2 V). It was found that electrodeposition at -1.0 V vs. Ag/AgCl provided more stable films, and this potential was taken as a reference to study the influence of the deposition time (200 s–7200 s) on the electrocatalytic activity of as-deposited

films. A MoS$_{2-x}$ film, deposited for 7200 s, was comparable in terms of HER electrocatalytic activity to some of the best reported in the field so far (-0.18 V vs. RHE at 10 mA cm^{-2}). However, charge transfer limitations within the semiconductor lattice were found to limit catalytic activity. Under galvanostatic stability testing conditions (-40 mA cm^{-2}) the film lost ~1,3% of its initial activity over a period of 20 min. The loss in activity has been hypothesized to be caused by a shortening of polymeric [Mo$_3$S$_{13}$]$^{2-}$ chains. Electrochemical impedance spectroscopy measurements confirmed this, showing an increase in charge transfer resistance after the stability tests. EIS was also applied to estimate the active site density on the electrodeposited MoS$_{2-x}$. Values in the range of $10^{15} \div 10^{16}$ active sites cm^{-2} were obtained. The number of active sites increased with deposition time, and followed the same trend as the exchange current density.

References

[1] M.S. Dresselhaus, I.L. Thomas, Alternative energy technologies, Nature 414 (2001) 332–337, https://doi.org/10.1038/35104599.
[2] M.G. Walter, E.L. Warren, J.R. McKone, S.W. Boettcher, Q. Mi, E.A. Santori, N.S. Lewis, Solar water splitting cells, Chem. Rev. 110 (2010) 6446–6473, https://doi.org/10.1021/cr1002326.
[3] H. Tributsch, J.C. Bennett, Electrochemistry and photochemistry of MoS$_2$ layer crystals. I, J. Electroanal. Chem. 81 (1977) 97–111, https://doi.org/10.1016/S0022-0728(77)80363-X.
[4] R.N. Bhattacharya, C.Y. Lee, F.H. Pollak, D.M. Schleich, Optical study of amorphous MoS$_3$: determination of the fundamental energy gap, J. Non-Cryst. Solids 91 (1987) 235–242, https://doi.org/10.1016/S0022-3093(87)80306-X.
[5] G. Laperriere, B. Marsan, D. Belanger, Preparation and characterization of electrodeposited amorphous molybdenum sulfide, Synth. Met. 29 (1989) 201–206, https://doi.org/10.1016/0379-6779(89)90900-4.
[6] A.S. Aliyev, M. Elrouby, S.F. Cafarova, Electrochemical synthesis of molybdenum sulfide semiconductor, Mater. Sci. Semicond. Process. 32 (2015) 31–39, https://doi.org/10.1016/j.mssp.2015.01.006.
[7] Z. He, W. Que, Molybdenum disulfide nanomaterials: structures, properties, synthesis and recent progress on hydrogen evolution reaction, Appl. Mater. Today. 3 (2016) 23–56, https://doi.org/10.1016/j.apmt.2016.02.001.
[8] J. Theerthagiri, R.A. Senthil, B. Senthilkumar, A. Reddy Polu, J. Madhavan, M. Ashokkumar, Recent advances in MoS$_2$ nanostructured materials for energy and environmental applications — a review, J. Solid State Chem. 252 (2017) 43–71, https://doi.org/10.1016/j.jssc.2017.04.041.
[9] B. Hinnemann, P.G. Moses, J. Bonde, K.P. Jørgensen, J.H. Nielsen, S. Horch, I. Chorkendorff, J.K. Nørskov, Biomimetic hydrogen evolution: MoS$_2$ nanoparticles as catalyst for hydrogen evolution, J. Am. Chem. Soc. 127 (2005) 5308–5309, https://doi.org/10.1021/ja0504690.
[10] W. Jaegermann, H. Tributsch, Interfacial properties of semiconducting transition metal chalcogenides, Prog. Surf. Sci. 29 (1988) 1–167, https://doi.org/10.1016/0079-6816(88)90015-9.
[11] T.F. Jaramillo, K.P. Jørgensen, J. Bonde, J.H. Nielsen, S. Horch, I. Chorkendorff, Identification of active edge sites for electrochemical H$_2$ evolution from MoS$_2$ nanocatalysts, Science 317 (2007) 100–102, https://doi.org/10.1126/science.1141483.
[12] G. Li, D. Zhang, Q. Qiao, Y. Yu, D. Peterson, A. Zafar, R. Kumar, S. Curtarolo, F. Hunte, S. Shannon, Y. Zhu, W. Yang, L. Cao, All the catalytic active sites of MoS$_2$ for hydrogen evolution, J. Am. Chem. Soc. 138 (2016) 16632–16638, https://doi.org/10.1021/jacs.6b05940.
[13] X.J. Chua, S.M. Tan, X. Chia, Z. Sofer, J. Luxa, M. Pumera, The origin of MoS$_2$ significantly influences its performance for the hydrogen evolution reaction due to differences in phase purity, Chem. Eur J. 23 (2017) 3169–3177, https://doi.org/10.1002/chem.201605343.
[14] X. Wang, H. Feng, Y. Wu, L. Jiao, Controlled synthesis of highly crystalline MoS$_2$ flakes by chemical vapor deposition, J. Am. Chem. Soc. 135 (2013) 5304–5307, https://doi.org/10.1021/ja4013485.
[15] Y. Zhan, Z. Liu, S. Najmaei, P.M. Ajayan, J. Lou, Large-area vapor-phase growth and characterization of MoS$_2$ atomic layers on a SiO$_2$ substrate, Small 8 (2012) 966–971, https://doi.org/10.1002/smll.201102654.
[16] X. Zeng, W. Qin, Synthesis of MoS$_2$ nanoparticles using MoO$_3$ nanobelts as precursor via a PVP-assisted hydrothermal method, Mater. Lett. 182 (2016) 347–350, https://doi.org/10.1016/j.matlet.2016.07.026.
[17] T. Wang, J. Li, G. Zhao, Synthesis of MoS$_2$ and MoO$_3$ hierarchical

nanostructures using a single-source molecular precursor, Powder Technol. 253 (2014) 347—351, https://doi.org/10.1016/j.powtec.2013.12.005.

[18] F. Ye, H. Li, H. Yu, S. Chen, X. Quan, Hydrothermal fabrication of few-layer MoS₂ nanosheets within nanopores on TiO₂ derived from MIL-125(Ti) for efficient photocatalytic H₂ evolution, Appl. Surf. Sci. 426 (2017) 177—184, https://doi.org/10.1016/j.apsusc.2017.07.087.

[19] L.C. Wang, S.K. Bao, J. Luo, Y.H. Wang, Y.C. Nie, J.P. Zou, Efficient exfoliation of bulk MoS₂ to nanosheets by mixed-solvent refluxing method, Int. J. Hydrogen Energy 41 (2016) 10737—10743, https://doi.org/10.1016/j.ijhydene.2016.03.206.

[20] X. Chia, A.Y.S. Eng, A. Ambrosi, S.M. Tan, M. Pumera, Electrochemistry of nanostructured layered transition-metal dichalcogenides, Chem. Rev. 115 (2015) 11941—11966, https://doi.org/10.1021/acs.chemrev.5b00287.

[21] H. Lin, J. Wang, Q. Luo, H. Peng, C. Luo, R. Qi, R. Huang, J. Travas-Sejdic, C.G. Duan, Rapid and highly efficient chemical exfoliation of layered MoS₂ and WS₂, J. Alloy. Comp. 699 (2017) 222—229, https://doi.org/10.1016/j.jallcom.2016.12.388.

[22] H. Ma, Z. Shen, S. Ben, Understanding the exfoliation and dispersion of MoS₂ nanosheets in pure water, J. Colloid Interface Sci. 517 (2018) 204—212, https://doi.org/10.1016/j.jcis.2017.11.013.

[23] H. Liu, L. Xu, W. Liu, B. Zhou, Y. Zhu, L. Zhu, X. Jiang, Production of mono- to few-layer MoS₂ nanosheets in isopropanol by a salt-assisted direct liquid-phase exfoliation method, J. Colloid Interface Sci. 515 (2018) 27—31, https://doi.org/10.1016/j.jcis.2018.01.023.

[24] L.B. Albertini, A.C.D. Angelo, E.R. Gonzalez, A nickel molybdenite cathode for the hydrogen evolution reaction in alkaline media, J. Appl. Electrochem. 22 (1992) 888—892, https://doi.org/10.1007/BF01023735.

[25] D. Merki, S. Fierro, H. Vrubel, X. Hu, Amorphous molybdenum sulfide films as catalysts for electrochemical hydrogen production in water, Chem. Sci. 2 (2011) 1262—1267, https://doi.org/10.1039/c1sc00117e.

[26] D. Merki, H. Vrubel, L. Rovelli, S. Fierro, X. Hu, Fe, Co, and Ni ions promote the catalytic activity of amorphous molybdenum sulfide films for hydrogen evolution, Chem. Sci. 3 (2012) 2515—2525, https://doi.org/10.1039/c2sc20539d.

[27] J.D. Benck, T.R. Hellstern, J. Kibsgaard, P. Chakthranont, T.F. Jaramillo, Catalyzing the hydrogen evolution reaction (HER) with molybdenum sulfide nanomaterials, ACS Catal. 4 (2014) 3957—3971.

[28] E.A. Ponomarev, M. Neumann-Spallart, G. Hodes, C. Lévy-Clément, Electrochemical deposition of MoS₂ thin films by reduction of tetrathiomolybdate, Thin Solid Films 280 (1996) 86—89, https://doi.org/10.1016/0040-6090(95)08204-2.

[29] H. Vrubel, X. Hu, Growth and activation of an amorphous molybdenum sulfide hydrogen evolving catalyst, ACS Catal. 3 (2013) 2002—2011, https://doi.org/10.1021/cs400441u.

[30] S.K. Ghosh, T. Bera, O. Karacasu, A. Swarnakar, J.G. Buijnsters, J.P. Celis, Nanostructured MoSx-based thin films obtained by electrochemical reduction, Electrochim. Acta 56 (2011) 2433—2442, https://doi.org/10.1016/j.electacta.2010.10.065.

[31] J. Gao, B. Li, J. Tan, P. Chow, T.M. Lu, N. Koratkar, Aging of transition metal dichalcogenide monolayers, ACS Nano 10 (2016) 2628—2635, https://doi.org/10.1021/acsnano.5b07677.

[32] S. KC, R.C. Longo, R.M. Wallace, K. Cho, Surface oxidation energetics and kinetics on MoS₂ monolayer, J. Appl. Phys. 117 (2015) 135301, https://doi.org/10.1063/1.4916536.

[33] J. Martincová, M. Otyepka, P. Lazar, Is single layer MoS₂ stable in the air? Chem. Eur J. (2017) 13233—13239, https://doi.org/10.1002/chem.201702860.

[34] P.D. Tran, T.V. Tran, M. Orio, S. Torelli, Q.D. Truong, K. Nayuki, Y. Sasaki, S.Y. Chiam, R. Yi, I. Honma, J. Barber, V. Artero, Coordination polymer structure and revisited hydrogen evolution catalytic mechanism for amorphous molybdenum sulfide, Nat. Mater. 15 (2016) 640—646, https://doi.org/10.1038/nmat4588.

[35] D. Wang, X. Zhang, Y. Shen, Z. Wu, Ni-doped MoS₂ nanoparticles as highly active hydrogen evolution electrocatalysts, RSC Adv. 6 (2016) 16656—16661, https://doi.org/10.1039/C6RA02610A.

[36] Z. Pu, Q. Liu, A.M. Asiri, A.Y. Obaid, X. Sun, One-step electrodeposition fabrication of graphene film-confined WS₂ nanoparticles with enhanced electrochemical catalytic activity for hydrogen evolution, Electrochim. Acta 134 (2014) 8—12, https://doi.org/10.1016/j.electacta.2014.04.092.

[37] Z. Zhang, W. Li, M.F. Yuen, T.W. Ng, Y. Tang, C.S. Lee, X. Chen, W. Zhang, Hierarchical composite structure of few-layers MoS₂ nanosheets supported by vertical graphene on carbon cloth for high-performance hydrogen evolution reaction, Nano Energy 18 (2015) 196—204, https://doi.org/10.1016/j.nanoen.2015.10.014.

[38] N. Zhang, W. Ma, F. Jia, T. Wu, D. Han, L. Niu, Controlled electrodeposition of CoMoS_x on carbon cloth: a 3D cathode for highly-efficient electrocatalytic hydrogen evolution, Int. J. Hydrogen Energy 41 (2016) 3811—3819, https://doi.org/10.1016/j.ijhydene.2015.12.173.

[39] A. Ambrosi, M. Pumera, Templated electrochemical fabrication of hollow molybdenum sulfide microstructures and nanostructures with catalytic properties for hydrogen production, ACS Catal. 6 (2016) 3985—3993, https://doi.org/10.1021/acscatal.6b00910.

[40] Y. Yan, B. Xia, N. Li, Z. Xu, A. Fisher, X. Wang, Vertically oriented MoS₂ and WS₂ nanosheets directly grown on carbon cloth as efficient and stable 3-dimensional hydrogen-evolving cathodes, J. Mater. Chem. A. 3 (2015) 131—135, https://doi.org/10.1039/C4TA04858J.

[41] Z. Lu, W. Zhu, X. Yu, H. Zhang, Y. Li, X. Sun, X. Wang, H. Wang, J. Wang, J. Luo, X. Lei, L. Jiang, Ultrahigh hydrogen evolution performance of under-water "superaerophobic" MoS₂ nanostructured electrodes, Adv. Mater. 26 (2014) 2683—2687, https://doi.org/10.1002/adma.201304759.

[42] T.Y. Chen, Y.H. Chang, C.L. Hsu, K.H. Wei, C.Y. Chiang, L.J. Li, Comparative study on MoS₂ and WS₂ for electrocatalytic water splitting, Int. J. Hydrogen Energy 38 (2013) 12302—12309, https://doi.org/10.1016/j.ijhydene.2013.07.021.

[43] J. Yang, D. Voiry, S.J. Ahn, D. Kang, A.Y. Kim, M. Chhowalla, H.S. Shin, Two-dimensional hybrid nanosheets of tungsten disulfide and reduced graphene oxide as catalysts for enhanced hydrogen evolution, Angew. Chem. Int. Ed. 52 (2013) 13751—13754, https://doi.org/10.1002/anie.201307475.

[44] C. Li, X. Bo, M. Li, L. Guo, Facile electrodeposition fabrication of molybdenum-tungsten sulfide on carbon cloth for electrocatalytic hydrogen evolution, Int. J. Hydrogen Energy 42 (2017) 15479—15488, https://doi.org/10.1016/j.ijhydene.2017.05.046.

[45] Z. Chen, D. Cummins, B.N. Reinecke, E. Clark, M.K. Sunkara, T.F. Jaramillo, Core—shell MoO₃ —MoS₂ nanowires for hydrogen evolution: a functional design for electrocatalytic materials, Nano Lett. 11 (2011) 4168—4175, https://doi.org/10.1021/nl2020476.

[46] D. Voiry, M. Salehi, R. Silva, T. Fujita, M. Chen, T. Asefa, V.B. Shenoy, G. Eda, M. Chhowalla, Conducting MoS₂ nanosheets as catalysts for hydrogen evolution reaction, Nano Lett. 13 (2013) 6222—6227, https://doi.org/10.1021/nl403661s.

[47] E.B. Castro, M.J. De Giz, E.R. Gonzalez, J.R. Vilche, An electrochemical impedance study on the kinetics and mechanism of the hydrogen evolution reaction on nickel molybdenite electrodes, Electrochim. Acta 42 (1997) 951—959, https://doi.org/10.1016/S0013-4686(96)00272-1.

[48] G.J. Brug, A.L.G. van den Eeden, M. Sluyters-Rehbach, J.H. Sluyters, The analysis of electrode impedances complicated by the presence of a constant phase element, J. Electroanal. Chem. 176 (1984) 275—295, https://doi.org/10.1016/S0022-0728(84)80324-1.

[49] J.D. Benck, Z. Chen, L.Y. Kuritzky, A.J. Forman, T.F. Jaramillo, Amorphous molybdenum sulfide catalysts for electrochemical hydrogen production: insights into the origin of their catalytic activity, ACS Catal. 2 (2012) 1916—1923, https://doi.org/10.1021/cs300451q.

[50] B.E. Conway, B.V. Tilak, Interfacial processes involving electrocatalytic evolution and oxidation of H2, and the role of chemisorbed H, Electrochim. Acta 47 (2002) 3571—3594, https://doi.org/10.1016/S0013-4686(02)00329-8.

[51] L. Liao, J. Zhu, X. Bian, L. Zhu, M.D. Scanlon, H.H. Girault, B. Liu, MoS2 formed on mesoporous graphene as a highly active catalyst for hydrogen evolution, Adv. Funct. Mater. 23 (2013) 5326—5333, https://doi.org/10.1002/adfm.201300318.

ARTICLE III

The Characterisation of Electrodeposited MoS2 Thin Films on a Foam-Based Electrode for Hydrogen Evolution

R. Levinas, N. Tsyntsaru, H. Cesiulis

Catalysts 2020, 10, 1182

Article

The Characterisation of Electrodeposited MoS₂ Thin Films on a Foam-Based Electrode for Hydrogen Evolution

Ramunas Levinas [1,*] , Natalia Tsyntsaru [1,2] and Henrikas Cesiulis [1]

[1]   Faculty of Chemistry and Geosciences, Vilnius University, Naugarduko str. 24, 03225 Vilnius, Lithuania;
      ashra_nt@yahoo.com (N.T.); henrikas.cesiulis@chf.vu.lt (H.C.)
[2]   Institute of Applied Physics of ASM, 5 Academiei str., 2028 Chisinau, Moldova
[*]   Correspondence: ramunas.levinas@chf.vu.lt; Tel.: +370-64875762

check for
updates

Abstract: Molybdenum sulphide is an emerging precious-metal-free catalyst for cathodic water splitting. As its active sites catalyse the Volmer hydrogen adsorption step, it is particularly active in acidic media. This study focused on the electrochemical deposition of MoS₂ on copper foam electrodes and the characterisation of their electrocatalytic properties. In addition, the electrodeposition was modified by adding a reducing agent—sodium hypophosphite—to the electrolyte. To reveal the role of hypophosphite, X-ray photoelectron spectroscopy (XPS) analysis was carried out in addition to scanning electron microscopy (SEM) and energy-dispersive X-ray spectroscopy (EDX). MoS₂ films, electrodeposited at various charges passed through the cell (catalyst loadings), were tested for their catalytic activity towards hydrogen evolution in 0.5 M H₂SO₄. Polarisation curves and Tafel slope analysis revealed that the electrodeposited MoS₂ films are highly active. Namely, Tafel slopes fell within the 40–50 mV dec⁻¹ range. The behaviour of as-deposited films was also evaluated by electrochemical impedance spectroscopy over a wide overpotential range (0 to −0.3 V), and two clear time constants were distinguished. Through equivalent electrical circuit analysis, the experimental data were fitted to the appropriate model, and the obtained values of the circuit components were examined as a function of overpotential. It was found that the addition of NaH₂PO₂ into the electrodeposition solution affects the intrinsic activity of the material. Finally, a method is proposed to approximate the number of active sites from impedance data.

Keywords: molybdenum sulphide; electrodeposition; hydrogen evolution reaction; water splitting; electrocatalysis; electrochemical impedance spectroscopy; active sites

1. Introduction

Within the field of renewable energy generation, storage and transportation, H₂ is considered a feasible energy carrier due to its significant gravimetric energy density when compared to carbon-based fuels [1]. However, the most widely used industrial-scale hydrogen production method currently is the steam reforming process, where hydrocarbons react with steam, yielding H₂ and CO₂ [2]. An excellent alternative—electrochemical water splitting—is a phenomenon that has been observed since as early as 1789 [3,4]. With the application of sufficient overpotential on an electrode in an aqueous solution, the H₂O molecules spontaneously split into H₂ and O₂. The cathodic half-reaction is called the hydrogen evolution reaction (HER) [5].

The mechanism of HER in acidic solutions consists of three steps: electrochemical hydrogen adsorption (Volmer reaction), followed by electrochemical (Heyrovsky reaction) and/or chemical (Tafel reaction) hydrogen desorption [6]. The rate of HER therefore depends on the adsorption

energy of atomic hydrogen. The so-called "volcano plots" were the first attempt to systemically show correlation between M-H bond energy and HER rate, in terms of exchange current density, and explained the empirically-observed fact that platinum is the best heterogeneous HER catalyst [7–9]. Contemporary volcano plots exchange the M-H bond energy for adsorption energy (ΔG_{ad}), calculated by density function theory (DFT) [10], but show the same general trend. Although the theory is sound, difficulties arise, for example, when characterising easily oxidising metals [11].

With this knowledge-based approach in mind, research into feasible alternatives to platinum for HER electrocatalysis has focused on noble-metal-free catalysts: transition metal sulphides, selenides, phosphides, nitrides and carbides, all of which have been comprehensively covered in multiple review papers [12–15]. In particular, it was found that the free adsorption energy of hydrogen onto MoS_2 was close to that of Pt [16]. This led to further application of MoS_2 as a HER catalyst. The catalytically active sites were found to be the edge sites ($\Delta G^0_H \sim 0.115$ eV), sulphur vacancies ($\Delta G^0_H \sim -0.095$ eV) and grain boundaries [17,18]. Nanoclusters of $[Mo_3S_{13}]^{2-}$ demonstrated excellent HER catalytic activity [19]. The structure of amorphous MoS_{2-x} was later elucidated to consist of such $[Mo_3S_{13}]^{2-}$ building blocks, joined into a polymeric chain; the implications of this structure are that amorphous MoS_{2-x} can corrode cathodically, shortening the polymeric chain, but also creating new unsaturated Mo^{IV} active sites for H_2 evolution [20].

MoS_2 films and structures can be obtained by numerous methods, the pros and cons of which have been considered extensively in review papers [21,22]. Among those methods, electrochemical deposition is of particular interest, as it is a relatively inexpensive and fast way to obtain MoS_2 films on electrode surfaces. Cathodic electrodeposition from an ammonium tetrathiomolybdate (($NH_4)_2MoS_4$) solution yields amorphous MoS_{2-x} films, which can attain crystallinity upon annealing [23,24]. Crystalline MoS_2 materials are typically more electrochemically stable [25], but amorphous films have greater HER electrocatalytic activity due to their rough, nanostructured surface morphology, and consequently higher density of defect (active) sites [26,27].

Different methods to improve the catalytic activity of transition metal dichalcogenides such as MoS_2 have been proposed. Doping with lithium, transition metals or even anionic nitrogen has been shown to have various effects on MoS_2, including an enhanced catalytic activity when compared with the unmodified material [28–31]. Some methods focus on nanostructurisation to reveal a maximum amount of active sites [32], while others combine MoS_2 with electro- or photoactive materials to form functional composites with combined properties [33].

Earlier, our group reported on the HER electrocatalytic activity of electrodeposited MoS_{2-x} films and the application of electrochemical impedance spectroscopy (EIS) to characterise them [34]. EIS can provide kinetic information additional to steady-state measurements and allows the determination of reaction rate constants [6], charge transfer kinetics [35] and double layer capacitance, which is proportional to the electrocatalytically active surface area [36,37]. As the method itself is non-destructive, it excels in the characterisation of heterogeneous electrocatalysis.

As a continuation of our previous investigations on MoS_2 synthesis and application for HER electrocatalysis, this study focused on the aspects of engineering of an electrode with a relatively large geometric surface area and increasing the intrinsic per-site activity. In addition, we investigated the influence of sodium hypophosphite (NaH_2PO_2) as a chemical reducing agent on electrodeposition, the films' structure and their HER activity.

2. Results

2.1. MoS2 Electrodeposition

The electrodeposition of MoS_2 films in both solutions (without and with hypophosphite) was investigated by cyclic voltammetry to establish a working potential range, where the dominating cathodic reaction is MoS_4^{2-} reduction to MoS_2. Firstly, CV scans were taken on a 1 cm^2 surface area copper rod electrode, at potentials from −1.2 to 0.2 V vs. Ag/AgCl (Figure 1). No prominent cathodic

peaks are present in these cycles due to overlaying of MoS_4^{2-} reduction peaks with hydrogen evolution, which occurs across the entire potential range. At about −1 V, the cathodic current begins to increase more rapidly, which reveals that MoS_4^{2-} reduction and hydrogen evolution are occurring. The addition of NaH_2PO_2 does not change the profile of the cycles, nor do any peaks become apparent. There is a small difference in the anodic part of the cycles, but in this system the anodic current is entirely dominated by the corrosion of the copper substrate, and the oxidation of electrodeposited MoS_2. CVs performed on the Cu-foam electrodes have a slight difference in the cathodic profile of the curves. A minor increase in the current is observed with the addition of hypophosphite, but no distinguishable reductive peaks appear. A small anodic peak at −0.68 V is seen in both cases and is likely caused by rapid hydrogen desorption from the large surface area and catalyst-covered electrode. The sharp increase in oxidative current at higher anodic potentials again occurs due to above-discussed reasons.
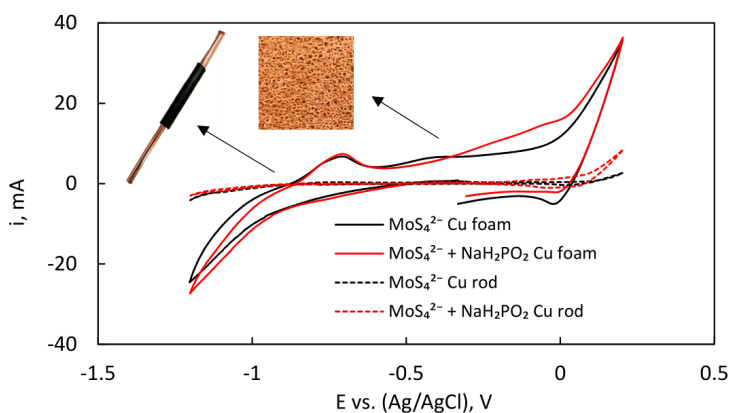

Figure 1. First CV cycles at scan rate of 2 mV s^{-1} for MoS_2 electrodeposition on Cu rod electrode (geometrical area of 1 cm^2) and 3D-foam.

All further research was conducted on the Cu-foam electrodes, prepared as described in Section 3.2. Galvanostatic conditions were chosen for the electrodeposition, because reductive peaks were not visible in CV, and the geometrical surface area of the substrates is uncertain. Therefore, a cathodic current of 10 mA corresponding to a potential, where intense hydrogen evolution does not yet occur, was selected. At this current, the potential settles at ~1.05 V, which is almost identical to the one we used for potentiostatic deposition in the precluding research [34]. The films were electrodeposited at increasing charges passed through the cell (from 10 to 40 C). This range was selected to encompass a wider array of film thicknesses: thinner MoS_2 films (10–20 C) were expected to have better adhesion to the substrate, more resistance to delamination and more favourable electron transfer kinetics from the catalyst/solution interface to the substrate. In contrast, thicker films may exhibit poorer physical stability due to internal stresses and weaker chemical bonding to the substrate. However, the increased catalyst loading (higher charged passed) should result in better HER catalytic activity.

To relate electrodeposition parameters to catalyst loading, the films, electrodeposited for discrete amounts of charge passed, were weighed, thus measuring the mass of the MoS_2 deposits. The reductive deposition of MoS_2 conforms to Faraday's law—there is a linear correlation between charge passed and mass of the electrodeposited film. Up to 0.25 mg of material is deposited per 1 C. In terms of current efficiency, this corresponds to ~32%, which is a known limit for MoS_4^{2-} electroreduction [24]. However, a decrease in current efficiency was observed with increasing charge up to 40 C. This can be caused by the formation of an active electrocatalytic film, which catalyses simultaneous hydrogen

evolution, and in turn inhibits MoS$_2$ electrodeposition. The current efficiency then drops to ~23%. It must be noted that the amount of material deposited without and with NaH$_2$PO$_2$ is almost identical. The calculated efficiencies are slightly lower for the electrolyte with hypophosphite, but not by any significant degree. Therefore, the addition of NaH$_2$PO$_2$ has no effect on the kinetics or mechanism of reductive MoS$_2$ deposition. The actual catalyst loading for films, electrodeposited for a similar amount of charge without or with hypophosphite, can be assumed to be identical. For that reason, the changes in the films' structure, morphology and catalytic activity discussed below have to be attributed to changes in the intrinsic properties of the MoS$_2$ films and not extrinsic parameters, e.g., catalyst loading.

2.2. Composition and Surface Morphology

The MoS$_2$ films, electrodeposited without and with NaH$_2$PO$_2$ were examined by SEM, and their chemical composition was determined by EDX. A visible effect of hypophosphite is observed on the morphology of the electrodeposited MoS$_2$ films. The deposits grow more evenly and with less apparent roughness (Figure 2). In the base electrolyte, MoS$_2$ appears to grow in clusters of nodules, protruding from the surface and away from the substrate, but often not connecting amongst each other. This leaves empty gaps in the film and creates disorder in the structure. In contrast, the addition of NaH$_2$PO$_2$ causes the formation of more compact films. There are fewer disconnected nodules, and MoS$_2$ growth occurs homogenously over a larger surface area. Overall, this change in morphology would certainly cause a decrease in the micro-level roughness of the deposits. Some cracks can be seen in the thicker MoS$_2$ films (e.g., deposited at 30 C), which have also been observed in our previous studies, and are directly related to the thickness and consequent tensile stress of the electrodeposited films. Fewer cracks are seen for the films, electrodeposited with hypophosphite, feasibly due to the lower stress of the deposits.
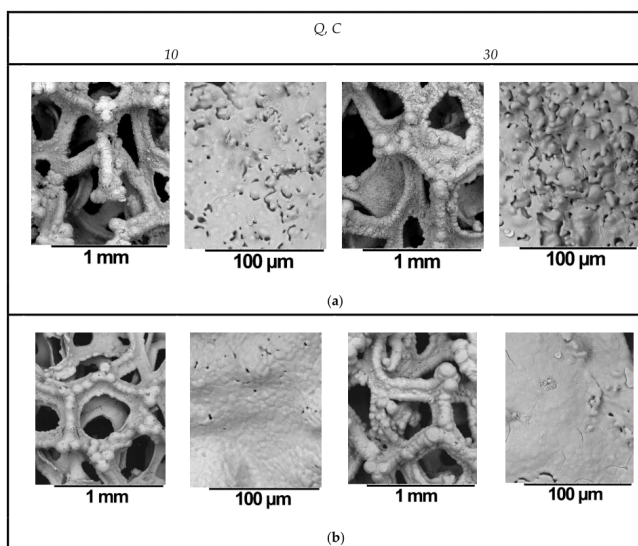

Figure 2. SEM images (low and high magnifications) of electrodeposited MoS2 films at cathodic current of 10 mA on Cu-foam electrodes from electrolytes: (**a**) without sodium hypophosphite; and (**b**) with sodium hypophosphite. Here, Q marks the cathodic charge in coulombs for which the films were electrodeposited (10 and 30 C).

Interestingly, sodium hypophosphite provides a similar effect on the electrodeposition of various transition metal alloys. For example, when depositing a Fe-W-P film, a certain concentration of NaH_2PO_2 in the deposition solution resulted in lower stress of the film and smaller crystallite sizes; the grain sizes decreased when the NaH_2PO_2 concentration was increased [38]. Similarly, for Co-Ni-P electrodeposits, the amount of NaH_2PO_2 in the electrodeposition solution was observed to affect the surface morphology—the surface appeared smooth and less nodular [39].

The elemental analysis showed that deposited MoS_2 films are rather thin; therefore, a strong signal from the substrate material (Cu) is present in the EDX spectra (Table 1). A significant amount of oxygen is also detected in all samples, which may be due to surface oxidation that has been documented to occur, as MoS_2 active sites readily oxidise when the film is left to dry in the open air.

Table 1. Dependence of chemical composition of MoS_2 films on the passed charge at a cathodic current of 10 mA; films electrodeposited from electrolytes containing MoS_4^{2-}, and MoS_4^{2-} + NaH_2PO_2 (denoted with *).

Q, C	Composition, at %									Mo: S Ratio
	Mo	Mo *	S	S *	O	O *	P	P *		*
10	9.60	6.63	17.99	13.90	72.40	79.41		0.047	1.87	2.10
20	8.15	7.26	13.81	14.25	78.04	78.38	-	0.11	1.72	1.98
30	9.06	8.14	15.92	16.06	75.0	75.73		0.065	1.75	1.96
40	8.12	9.54	14.69	15.86	77.18	74.47		0.13	1.83	1.66

There is no direct correlation between electrodeposition conditions and composition of MoS_2 films. The deposits are sulphur-deficient, and, for those obtained from the base solution, the MoS_{2-x} stoichiometry ranges from $MoS_{1.72}$ to $MoS_{1.87}$. Some difference in composition is observed for the films, electrodeposited with hypophosphite. The amount of Mo and S in atomic per cent increases with passed charge, and the background signal of the copper substrate consequently decreases. In MoS_2 films, electrodeposited with hypophosphite, the Mo:S ratios are closer to the stoichiometric. The film deposited for 10 C even exhibits a sulphur surplus, which may be caused by a chemical reaction, for example the formation of copper sulphide. A small amount of phosphorus is present in the EDX spectra, but, in some cases, it was smaller than the reliable detection limit deviation. It must be concluded that there exists a possibility of phosphide incorporation into the MoS_2 structure, but, if so, its amount is near the detection limit. Because the active sites of MoS_2 for HER catalysis are sulphur vacancies, it can be suspected that the stoichiometry difference will have an effect on the electrocatalytic activity of these deposited films. Indeed, the research has shown that there is an optimal amount of point defects (active sites) that results in best HER catalytic activity [40].

2.3. X-ray Photoelectron Spectroscopy

X-ray photoelectron spectra were obtained for the MoS_2 films, electrodeposited with and without NaH_2PO_2, to investigate the possible differences in their structure (Figure 3). The sulphur 2p region is determined by a single doublet corresponding to S $2p_{1/2}$ and S $2p_{3/2}$ lines that is characteristic for the presence of the 2H-MoS_2 phase. For the MoS_2 films, electrodeposited without NaH_2PO_2 (Figure 3b), the $2p_{3/2}$ maximum is seen at a binding energy of 161.9 eV, whereas deposition with hypophosphite leads to the shift of the peak position towards slightly higher energies at 162.1 eV. Another S 2p doublet was added in the model for better fitting of the spectra. A second doublet in the S 2p region has been attributed to the existence of different S-S bonds in the material (terminal and bridging bonds) [19,20]. However, in our case, the second S 2p doublet appears more similar to those that have been reported to be caused by sulphur residuals from polysulphide that may have formed in the deposition solution. Thus, it can be inferred from the spectra that the near-surface sulphur atoms exist almost entirely in one oxidation state.
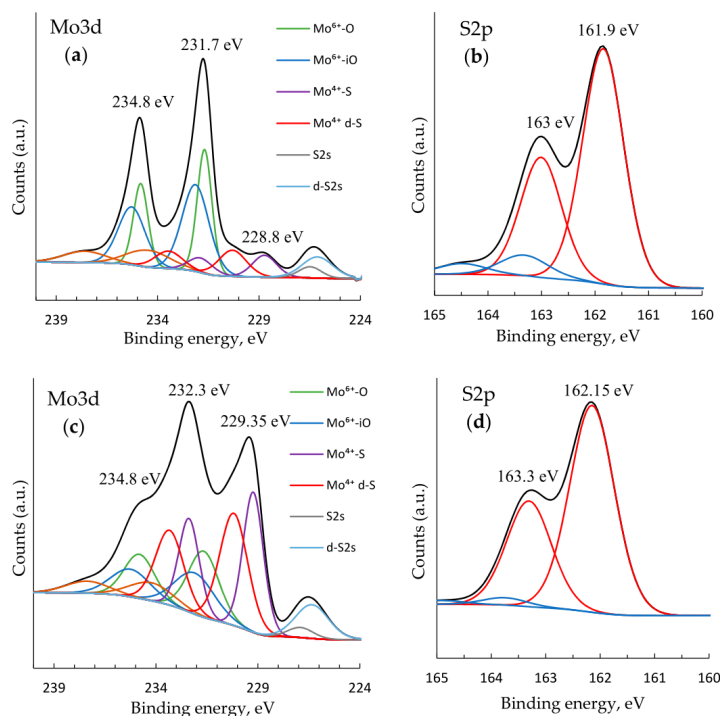
Figure 3. XPS spectra and fitted peaks of MoS$_2$ films, electrodeposited on copper foams: (**a**,**b**) without NaH$_2$PO$_2$; and (**c**,**d**) with NaH$_2$PO$_2$.

Deconvolution of the Mo 3d region revealed that Mo exists in multiple oxidation states, and is coordinated by different elements (Figure 3a,c). The films electrodeposited without hypophosphite (Figure 3a) show a spectrum that is almost entirely decided by two peaks at 231.7 eV and 234.8 eV. Judging by these binding energies, these peaks likely belong to Mo^{6+} oxides (3d$_{5/2}$ 232.3–232.5 eV; 3d$_{3/2}$ 235.4–235.7 eV [41–43]). These oxides may have been electrodeposited from residual MoO$_4{}^{2-}$ in the deposition solution, or appeared through oxidation of uncoordinated Mo sites on the surface. The peaks deconvolute into two doublets marked Mo^{6+}-O and Mo^{6+}-iO in Figure 3, which also suggests that the oxide exists in different states.

The peaks at binding energies of 229.35 and 232.3 eV have been reported to correspond to Mo^{4+} 3d$_{5/2}$ and 3d$_{3/2}$ components of 2H-MoS$_2$ (marked Mo^{4+}-S) [44]. This, along with the previously discussed characteristic S 2p peaks, confirms the presence of the 2H-MoS$_2$ phase. The origin of the doublet (3d$_{5/2}$ 230.2 eV; 3d$_{3/2}$ 233.2 eV) is ambiguous. Such binding energies correspond well to Mo^{4+} oxides [41,42], which may exist in the electrodeposited film due to reasons discussed above related to Mo^{6+} oxides. However, a very similar binding energy (230.76 eV) may also be attributed to an intermediate Mo oxidation state (e.g., 5+) that is only partially coordinated by sulphur (with a sulphur vacancy—active site) [20,45]. The depressed, wide peaks at a very high binding energies (234.5–237.8 eV) could not be attributed to any state of Mo and are assumed to be caused by some residual compound from the solution.

XPS analysis showed that within films, electrodeposited without NaH_2PO_2, molybdenum is widely coordinated by oxygen, i.e., the film contains a lot of molybdenum oxide. This is also supported by EDX analysis, where the amount of oxygen in these films was relatively large. When electrodeposition is carried out with hypophosphite, a much stronger Mo^{4+}-S bond signal is observed. Because the S 2p signal does not change in any major way, it is assumed that the material retains the same $2H$-MoS_2 structure, and that the effect of NaH_2PO_2 on the electrochemical deposition of MoS_2 is mainly targeting the suppression of Mo-O bond formation, or, conversely, the assistance of Mo-S bond formation.

2.4. Electrocatalytic Activity for HER

The most common and conventionally informative way to characterise the electrocatalytic activity of an electrode is linear sweep voltammetry (LSV) in a wide overpotential range. As MoS_2 is a catalyst in acidic media, the electrodeposited films were studied by LSV in 0.5 M H_2SO_4. The initial potential was set close to thermodynamic equilibrium (0 V vs. SHE), and a scan rate of 2 mV s^{-1} was applied. A cut-off condition of 100 mA of cathodic current was set to end the scan. In this way, three scans were recorded, and the third scan was selected for analysis (Figure 4a). Note that the cathodic current on the ordinate axis has not been normalised into geometrical surface area, because it would be incorrect for such an electrode, where current density distribution does not guarantee equal HER turnover over the entire electrochemically active surface area. More discussion on this issue follows in the Section 2.5. It can be seen that MoS_2 films, electrodeposited for increased passed charge (higher catalyst loading) predictably have better total activity. The onset overpotential (arbitrary, where the HER current would begin to sharply rise) is also lower for higher-loading electrodes. Thus, a MoS_2 film electrodeposited from the base MoS_4^{2-} solution for 10 C could reach a HER cathodic current of 100 mA at an overpotential of −0.227 V. In comparison, a film electrodeposited for 10 C in the presence of NaH_2PO_2 could reach −100 mA at −0.21 V, representing a 17-mV improvement. The effect of adding sodium hypophosphite into the electrodeposition solution has a prominent effect on the electrocatalytic activity of the films—their total activity generally increases. On LSV curves, this results in lower overpotentials, required to reach the same HER current. A smaller, but similar difference is observed in all cases. Because the mass of the Cu-foam MoS_2 electrodes (catalyst loading) is alike, this must be caused by changes of the intrinsic activity of the film.
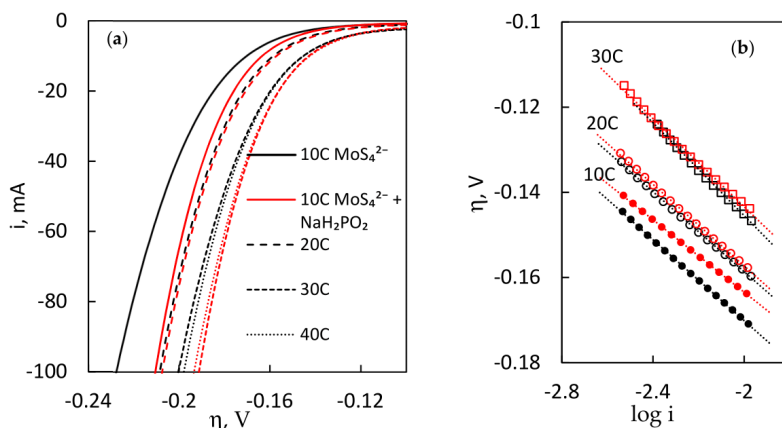

Figure 4. (**a**) iR-corrected polarisation curves of electrodeposited MoS_2 films in 0.5 M H_2SO_4; and (**b**) Tafel slopes of the respective films, with scan rate −2 mV s^{-1}. (Red lines correspond to samples, deposited with NaH_2PO_2).

Two more important parameters characterising the electrocatalytic HER activity of the MoS_2 films are the Tafel slope and exchange current. The Tafel slopes are shown in Figure [4]b, and the corresponding values are presented in Table [2]. The determined values for slopes (40–50 mV dec^{-1}) are commonly reported for MoS_2-based electrodes and materials, where HER undergoes via mixed Volmer–Heyrovsky kinetics. MoS_2 films, electrodeposited with hypophosphite, have slightly lower Tafel slopes. For exchange current, only a small change of this parameter is seen upon addition of NaH_2PO_2 as I_0 decreases in most cases. However, due to the potential variance in the geometrical surface area of Cu-foam electrodes, these values are not necessarily correct representations of the intrinsic activity of the electrodeposited films.

Table 2. Electrocatalytic activity parameters of the electrodeposited MoS_2 films from electrolytes containing $MoS_4{}^{2-}$, and $MoS_4{}^{2-}$ + NaH_2PO_2 (denoted with *).

Q, C.		10	20	30	40
Tafel slope		47.5	47	54.5	51.4
η, mV dec^{-1}	*	42.5	47.9	51.7	49.0
Exchange current		2.62	4.22	21.5	14.9
I_0, µA	*	1.43	5.23	16.8	12.3

The electrochemical stability of electrodeposited MoS_2 films was tested by a galvanostatic step technique: the cathodic current was set at incrementally increasing values (from -10 to -100 mA), and the potential response was measured for 500 s in order to approach a steady state value (Figure [5]). In terms of stability, all films are stable at lower applied currents (up to -40 mA), and a slight decrease in overpotential is observed over each 500-s step. Furthermore, MoS_2 films electrodeposited from the solution with hypophosphite possess worse catalytic activity at lower currents than in the absence of it, as they reach the same current density at higher overpotentials. However, at cathodic currents higher than -50 mA, the curves overlap, and the films electrodeposited with hypophosphite exhibit improved catalytic activity. These results are in line with the Tafel analysis discussed above, because these films were found to have lower Tafel slopes values, and, as a result, their catalytic activity reaches its full ability only at high applied currents or overpotentials. However, at higher cathodic currents (over -50 mA), a rapid drop in measured overpotential is observed, which indicates a loss in catalytic activity. This is likely due to the cathodic corrosion, i.e., shortening of the polymeric S-Mo-S chains by cleavage of Mo-S bonds, as described in [20]. Experimental observations support this theory, because the colourless sulphuric acid solution attained a faint yellow hue, likely due to sulphide ions dissolving into the solution.
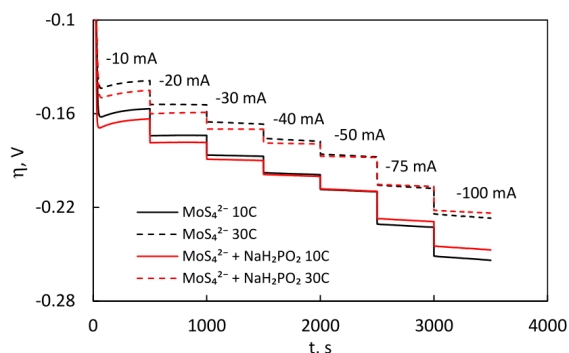

Figure 5. Galvanostatic stability curves of MoS_2 films, electrodeposited with and without NaH_2PO_2.

2.5. HER Study by EIS

EIS can be an informative and non-destructive method to characterise a heterogeneous catalyst-solution interface. This method is especially useful to characterise electrodes that have an uncertain geometric surface area (such as metallic foams) based on the parameters of double-layer (C_{dl}) and polarisation (C_p) capacitance that are directly proportional to the electrochemically and electrocatalytically active surface area. The spectra were registered at increasingly cathodic overpotentials (0, −0.1, −0.15, −0.175, −0.2, −0.25 and −0.3 V) to obtain more data (in addition to Tafel analysis) on the kinetics of HER catalysis. Based on the results of Kramers–Kronig procedure, the system was found to be linear and stable, and spectra obtained even at high overpotentials were of good quality. The impedance of the system decreases dramatically with the increase of the overpotential (Figure 6), owing to the intensity of HER. Two semicircles become especially pronounced from −0.15 V, when hydrogen evolution begins to occur at an increasing rate (Figure 6a). At higher overpotentials, the semicircles become similar in magnitude (Figure 6b). If the spectra were to be registered at even higher overpotentials, only the high-frequency semicircle could be distinguished. The Bode plots (Figure 6c) also show two distinguishable peaks, with the low-frequency peak shrinking in magnitude when the overpotential is increased. Such behaviour of the system can be described by equivalent electric circuit (EEC) containing two time constants in the system: τ_{HF} and τ_{LF} shown in Figure 7. This EEC is commonly used to interpret EIS data for electrode processes containing adsorbed intermediate compounds, and it is often applied to model HER in both acidic and alkaline media [46]. Here, the double layer capacitance C_{dl} and polarisation capacitance C_a are represented by constant phase elements that account the inhomogeneity of the surface. In agreement with the previously discussed spectra, this model contains two time constants: $\tau_{HF} = C_{dl}R_{ct}$ and $\tau_{LF} = C_aR_a$. Values of CPE were recalculated into capacitance by Brug et al.'s Equation [47]:

$$C_{dl} = T_{dl}^{\frac{1}{n}}\left(\frac{1}{R_s} + \frac{1}{R_{ct}}\right)^{1-\frac{1}{n}} \tag{1}$$

$$C_a = T_a^{\frac{1}{n}}\left(\frac{1}{R_s + R_{ct}} + \frac{1}{R_a}\right)^{1-\frac{1}{n}} \tag{2}$$

Here, T_{dl} and T_a are values of the CPE_{dl} and CPE_a elements, respectively.

Although at lower overpotentials the system behaves in a moderately blocking manner (Figure 6d), the rate of HER increases rapidly, reactive resistance decreases and the system becomes almost conductive.

EIS spectra vary with amount of charge used for MoS_2 film electrodeposition from the solutions with and without hypophosphite ions (Figure 8). At the same overpotential, the shape of the spectra remains identical, and two semicircles can be distinguished for all films. It means that the mechanism of HER does not change. The magnitude of the impedance spectra, however, decreases with increasing charge used for electrodeposition of MoS_2. The most significant difference is obtained for the low-frequency semicircle, which, as discussed below, is correlated to the polarisation resistance and capacitance. The spectra also show that the MoS_2 films which were electrodeposited with hypophosphite have lower impedance magnitudes and are thus more catalytically active.

All of the parameters of the EEC are correlated to the material's electrocatalytic activity towards HER, and therefore their relation to the applied overpotential reveals important information about kinetics. The inverse of charge transfer resistance ($1/R_{ct}$) is directly proportional to the reaction rate, assuming a simplified Volmer–Heyrovsky mechanism. The $1/R_{ct}-\eta$ plots for all studied MoS_2 films (Figure 9) show that the rate of HER is generally higher when the films were electrodeposited at more charges passed for MoS_2 deposition. Furthermore, addition of hypophosphite to the electrodeposition solution increases the catalytic activity of the films. The tendencies in terms of HER activity as a function of deposition charge correspond to the polarisation curves seen in Figure 4.
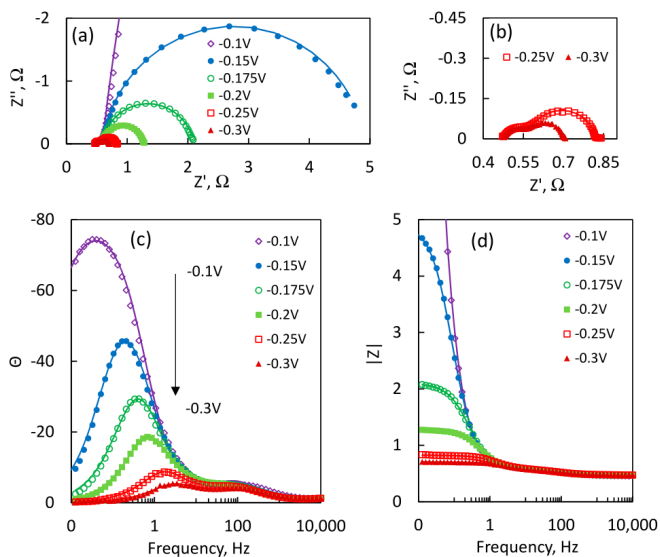
Figure 6. EIS spectra of HER from 0.5 M H_2SO_4 on the electrodeposited MoS_2 film (Q = 10 C): (**a**) Nyquist plots obtained at various overpotentials; (**b**) spectra, obtained at higher overpotentials; and (**c,d**) Bode plots of respective overpotentials. Points are experimental data, while lines represent fitting to EEC shown in Figure 7.
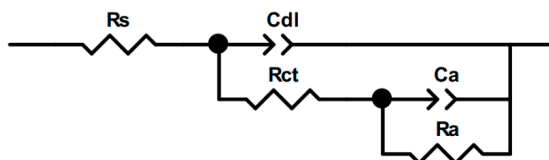

Figure 7. Equivalent electrical circuit, used to model impedance data. R_s, solution resistance; C_{dl}, constant phase element related to double layer capacitance; R_{ct}, charge transfer resistance; C_a, polarisation capacitance; R_a, polarisation resistance.
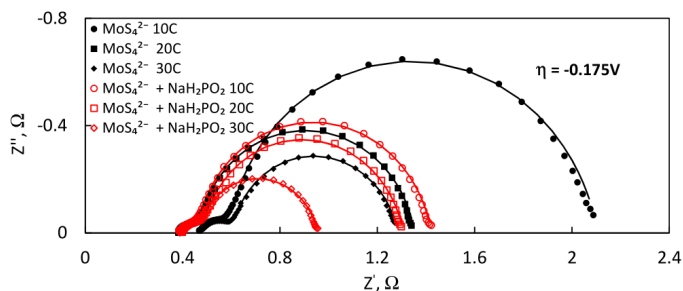

Figure 8. Nyguist plot of EIS for films, electrodeposited with and without NaH_2PO_2, for a different amount of charge. Points are experimental data, while lines represent fitting to EEC shown in Figure 7.
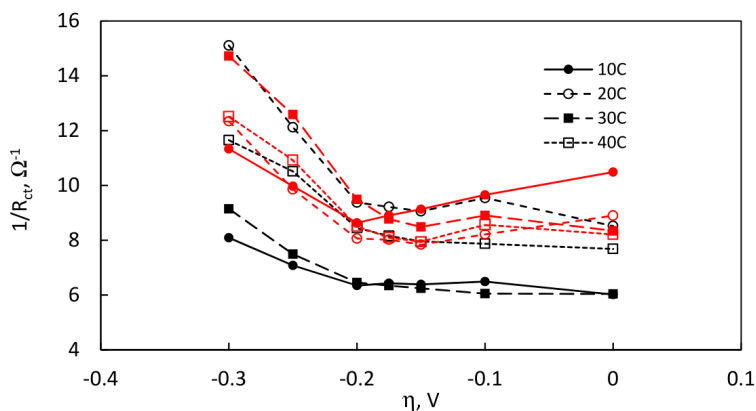
Figure 9. The dependence of $1/R_{ct}$ on overpotential. (Red lines correspond to samples, deposited with NaH_2PO_2).

The measured double layer capacitance C_{dl} is directly proportional to the electrochemically active surface area of the electrode, and it is especially important to approximate when the geometrical surface area is uncertain. The values of C_{dl} also vary as a function of overpotential (Figure 10) and reach a peak at ~-0.2 V. Overall, the C_{dl} values of the MoS_2 films, electrodeposited with hypophosphite, are larger throughout the entire overpotential range, meaning that the observed smoother surface morphology in fact results in a larger electrochemically active surface area in contact with the electrolyte. The apparent values of C_{dl} are on the order of 10–100 mF, which is a conceivably large value, given the vast surface area of the Cu-foam electrode and the affinity of MoS_2 to adsorb H^+ under these experimental conditions.
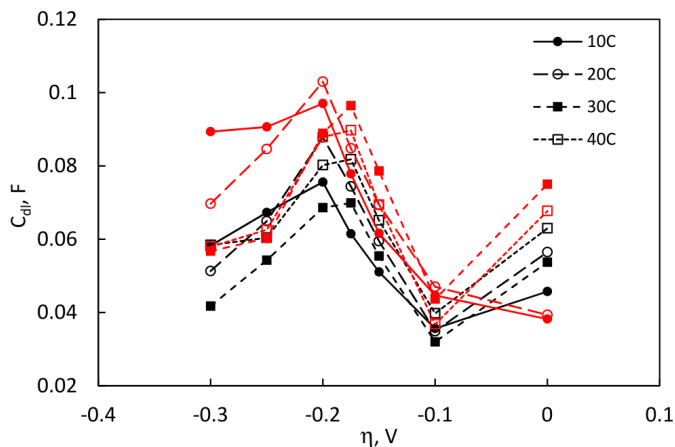

Figure 10. The dependence of double layer capacitance on overpotential. (Red lines correspond to samples, deposited with NaH_2PO_2).

As discussed above, the low-frequency RC-element in the equivalent circuit used to fit the impedance data causes the formation of a large depressed semicircle that is strongly correlated to

the applied overpotential (Figures 6 and 8). It is therefore expected that the values of C_a and R_a should also change significantly. C_a, which can also be imagined as a pseudocapacitance that arises from the modulating surface coverage by adsorbed hydrogen H_{ads}, is relatively constant until −0.2 V, after which it increases linearly with applied overpotential (Figure 11a). As it is generally assumed that with increasingly negative overpotential the surface coverage Θ_H approaches to 1 [6], C_a could be expected to plateau at even larger overpotentials, but that was not observed in this experimental series. When considering the effect of hypophosphite on the electrodeposited MoS_2 films, it can be seen that the values of C_a are lower than for the respective films from the base solution. This suggests that there is a change in the surface coverage by H_{ads} when the films act electrocatalytically, but the precise kinetic reason is difficult to establish from these data alone. In addition, as the difference seems to exist only in the intermediate overpotential range and at −0.3 V, the C_a values for the respective compared MoS_2 films overlap. The other component in the low-frequency RC-element—an adsorption resistance, R_a—decreases exponentially with applied overpotential, and it is the most significantly affected parameter of the system (Figure 11b). Note that here the data from 0 V are not presented, but R_a can be imagined to trend towards infinity. R_a values decrease by several magnitudes over the measured overpotential range (for example, for a MoS_2 film, deposited for 30 C, a decrease from 26.1 Ω at −0.1 V to 0.09 Ω at −0.3 V is seen). R_a as a function of η begins to plateau at overpotentials larger than −0.2 V and could conceivably reach a constant value. Here, it can also be seen that the MoS_2 films, electrodeposited with NaH_2PO_2, exhibit lower R_a values than those electrodeposited in the base solution.
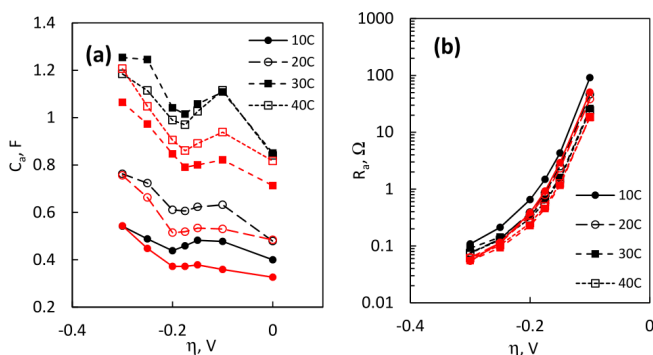

Figure 11. Values of the low-frequency RC circuit as a function of overpotential (red lines correspond to samples, deposited with NaH_2PO_2): (**a**) capacitance, related to hydrogen adsorption and desorption, and (**b**) hydrogen adsorption resistance.

All the data from the EIS fitting and calculations can be summed up in terms of time constants and their dependence on the HER overpotential. Because the time constant is a measure of the system response rate to an applied overpotential perturbation, the τ_{HF} and τ_{LF} values will be correlated to HER kinetics. The high frequency time constant $\tau_{HF} = R_{ct} \cdot C_{dl}$ rises until it reaches a peak value, after which it begins to decrease (Figure 12a). This tendency was also seen for the double layer capacitance (Figure 10) and is likely related to the surface coverage by H_{ads}. At a certain overpotential, the two capacitances diverge: C_a increases, while C_{dl} begins to drop, and this point corresponds to the highest value of τ_{HF}. It is interesting to note that the high frequency response at low and high overpotentials is similar; the peak only occurs at ~−0.2 V, at which point hydrogen evolution is already intense with a current of up to −100 mA, as seen from polarisation experiments. The low-frequency time constant is a product of C_a and R_a, and, because of the small changes of C_a, it is completely determined by the R_a component. Like R_a, τ_{LF} decreases exponentially with overpotential by several

magnitudes over the measured range (Figure 12b). At high overpotentials of −0.3 V, both τ_{HF} and τ_{LF} become comparable for all samples. For example, for the MoS_2 film, electrodeposited for 10 C with NaH_2PO_2, τ_{LF} is 0.029 s^{-1}, τ_{HF} is 0.0078 s^{-1} and $\tau_{LF}/\tau_{HF} = 3.7$. It is also apparent that films with less catalyst loading (i.e., less electrodeposition charge used for MoS_2 deposition) have a faster response to perturbation (lower τ_{LF} values). In fact, these results correlate directly to the Tafel slopes presented in Table 2: the film with the lowest Tafel slope also has the lowest τ_{LF} values at the entire overpotential range. The results provide an insightful observation: although higher catalyst loading does result in increased total electrode activity, the intrinsic activity is degraded.
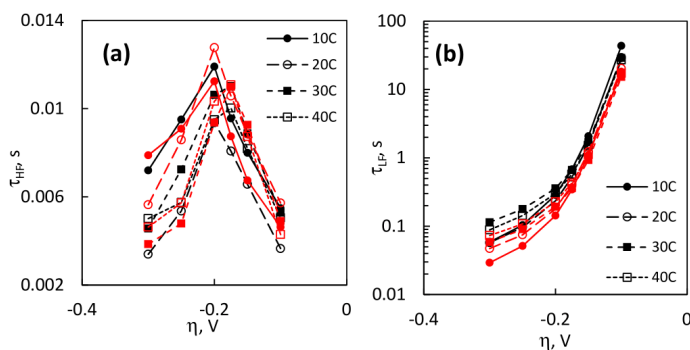

Figure 12. The dependence of (**a**) the high frequency time constant and (**b**) the low frequency time constant on overpotential. (Red lines correspond to samples, deposited with NaH_2PO_2).

2.6. Turnover Frequency and Active Site Calculations

In a previous attempt to apply EIS for the approximation of the number of active sites on a MoS_2 electrocatalyst, it has been shown that with certain assumptions the values of C_a obtained from impedance fitting could be used in calculations [28]. However, there the number was likely underestimated due to the low applied overpotential (−0.1 V). In theory, the surface coverage by adsorbed hydrogen approaches $\Theta_H = 1$ at highly negative overpotentials [6]. Therefore, the same analysis was done in this study in order to approximate the number of active sites on the MoS_2 deposited on the Cu-foam electrodes, and to calculate the turnover frequencies.

It must be noted that both physically and mathematically the number of active sites will depend on the applied overpotential, so the following calculations were performed using the most cathodic overpotential for which experimental data were obtained in this study: −0.3 V. The following assumptions were made: hydrogen adsorption is a one-electron process, one active site adsorbs one H^+ and $\Theta_H \sim\approx 1$. Then, the charge needed to attain a monolayer of H_{ads} is:

$$Q_a = C_a\eta \tag{3}$$

where C_a is the adsorption capacitance, η is the applied overpotential (−0.3 V).

The number of active sites is calculated from Equation (4):

$$N_a = \frac{Q_a N_A}{nF} \tag{4}$$

It may then be inferred, from the results in Figure 11a, that at sufficiently negative overpotentials the compared MoS_2 films that were electrodeposited with and without hypophosphite will have the same number of active sites. Indeed, no significant difference is seen in the values, as presented in Table 3. N_a increases with electrodeposition charge as more material is deposited. The values in total

for the whole electrode are on the order of 10^{18}, which, accounting for the large geometrical surface area of the substrate, are within range of commonly reported values. In comparison, the previous application of this method resulted in N_a of up to 2.8×10^{16} sites cm^{-2} for MoS$_2$, electrodeposited on a Cu rod electrode [28].

Table 3. Calculated numbers of active sites and turnover frequencies (at −0.2 V) for the electrodeposited MoS$_4{}^{2-}$ films from electrolytes containing MoS$_4{}^{2-}$ and MoS$_4{}^{2-}$ + NaH$_2$PO$_2$ (denoted with *).

Q, C	$N_a \times 10^{18}$, Total Sites	$N_a \times 10^{18}$, Total Sites *	TOF$_{\eta\,=\,-0.19\,V} \times 10^{-2}$, s^{-1}	TOF$_{\eta\,=\,-0.19\,V} \times 10^{-2}$, s^{-1} *
10	1.01	1.02	7.81	12.5
20	1.43	1.42	10.8	11.0
30	2.35	1.99	9.7	14.7
40	2.22	2.26	10.7	12.4

The turnover frequencies (number of hydrogen molecules evolved per site per second) were then calculated using the obtained number of active sites (Table 3). For comparison, TOFs at overpotential of −0.19 V (where experimental data were available for all measurements) are also given. Even though hydrogen evolution is vigorous and large cathodic currents are observed at this overpotential (see Figure 4a), the actual TOFs are fairly small owing to the large number of active sites. However, the turnover frequencies of MoS$_2$ films electrodeposited with NaH$_2$PO$_2$ are marginally higher than those of MoS$_2$ electrodeposited from the base solution. This again suggests that incorporation of hypophosphite into the electrodeposition solution results in catalytic MoS$_2$ films that exhibit higher per-site activity, as the enhanced HER performance can no longer be attributed to changes in surface morphology alone.

It has been suggested that the ideal way to compare catalysts regardless of geometrical surface area is plotting the turnover frequency as a function of overpotential [48]. Therefore, Figure 13 presents these dependencies for all catalytic films examined in this study. It can be seen that the MoS$_2$ films, electrodeposited with NaH$_2$PO$_2$, exhibit distinctly better electrocatalytic activity. They reach higher TOF values at lower overpotentials, which signals a more rapid hydrogen evolution performance of their active sites. The TOF values may be susceptible to error due to the method used in approximation of the number of active sites. However, regardless of possible errors in calculations, the general tendency is that using hypophosphite in the electrodeposition bath did result in enhanced catalytic performances of the deposited MoS$_2$ films.
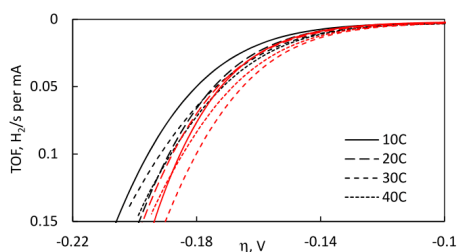

Figure 13. TOF values plotted as a function of overpotential for MoS$_2$ films, electrodeposited without and with NaH$_2$PO$_2$. (Red lines correspond to samples, deposited with NaH$_2$PO$_2$).

3. Materials and Methods

3.1. Electrolyte Preparation

Molybdenum disulphide films were electrodeposited from a tetrathiomolybdate (MoS$_4{}^{2-}$/TTM) solution, containing 25 mM MoS$_4{}^{2-}$ and 0.1 M Na$_2$SO$_4$. This base solution was prepared via a chemical

four-step sulphidation of molybdate reaction, as described in our previous work [34], but without additional surfactants. The pH of the solution was kept neutral at ~pH 7, to prevent precipitation of insoluble MoS_3 and suppress hydrogen evolution during electrodeposition. To study the effect of a chemical reducer, 0.1 M of sodium hypophosphite (NaH_2PO_2) was added to the base solution. The pH was again adjusted to pH 7 prior to an electrodeposition.

3.2. MoS₂ Electrodeposition

All electrochemical measurements (galvanostatic electrodeposition, linear sweep voltammetry (LSV), electrochemical impedance spectroscopy (EIS), cyclic voltammetry (CV)) were performed in a standard three-electrode cell set-up using a potentiostat/galvanostat Autolab 302N (Metrohm, Utrecht, The Netherlads). Unless specified otherwise, the potentials are in reference to an Ag/AgCl electrode. Commercial open-cell copper foam was used as the deposition substrate. The foam had a density of 1.02 g cm^{-3}, a porosity of 87.6% and an approximate ligament diameter of 150–200 μm. Electrodes for deposition were prepared from a 2 cm × 2 cm × 0.13 cm cut-out of the copper foam sheet, shaped into a cylinder to promote equal current density distribution across the entire geometrical surface area. The substrates were degreased in acetone in an ultrasonic bath for 5 min. Before electrodeposition, they were immersed into a 2 M H_2SO_4 solution to remove surface oxides, and then rinsed well with distilled water. Cyclic voltammetry measurements were used to assess the working potential range for MoS_2 electrodeposition in both solutions. The electrodeposition was carried out for four values of passed charge, namely 10, 20, 30 and 40 C (at a galvanostatic current of −10 mA), to evaluate the effect of catalyst loading on HER activity. The electrodes were weighed before electrodeposition and after characterisation. Current efficiencies were calculated from the obtained data, assuming that MoS_2 electrodeposition is a two electron reaction (Equation (5)) [24].

$$MoS_4{}^{2-} + 2e^- + 2H_2O \rightarrow MoS_2 + 2SH^- + 2OH^- \tag{5}$$

The surface morphology and chemical composition of the electrodeposited MoS_2 films were evaluated using a scanning electron microscope (SEM, Hitachi TM 3000, Tokyo, Japan) with an integrated energy-dispersive X-ray module (EDS, Oxford Instruments, Buckinghamshire, UK).

The XPS analyses were carried out with a Kratos Axis Supra spectrometer (Kratos Analytical Limited, Manchester, UK) using a monochromatic Al K(alpha) source (25 mA, 15 kV). The Kratos charge neutraliser system was used on all specimens. Survey scan analyses were carried out with an analysis area of 300 μm × 700 μm and a pass energy of 160 eV. High resolution analyses were carried out with an analysis area of 300 μm × 700 μm and a pass energy of 20 eV. The XPS signal due to adventitious carbon located at 284.8 eV was used as a binding energy (BE) reference.

3.3. Electrocatalytic Activity Measurements

The deposited films were rinsed with distilled water, and immediately transferred into a 0.5 M H_2SO_4 electrolyte for HER electrocatalysis experiments. A typical characterisation procedure consisted of the following steps: (1) settling of open circuit potential (OCP) for 120 s; (2) LSV at a rate of 2 mV s^{-1} from 0 V vs. RHE to a cut off condition of −100 mA, for 3 curves; and (3) EIS measurements at increasingly cathodic overpotentials (0, −0.1, −0.15, −0.175, −0.2, −0.25 and −0.3 V). The EIS spectra were measured in the frequency range from 10 kHz to 10 MHz, with an amplitude of 20 mV. The system had satisfactory linearity, causality and stability, and therefore this amplitude provided excellent electrochemical impedance spectra. The EIS data were interpreted in the frame of equivalent electric circuit (EEC). The determined solution resistance (Rs) was used to correct the iR drop in the recorded voltammetric data. The values of the pseudocapacitance, attributed to the adsorption time constant process, were used for an approximation of the number of active sites.

4. Conclusions

In this study electrodes for efficient HER catalysis were prepared by electrodepositing thin MoS_2 films onto 3D copper-foam substrates. MoS_2 was deposited cathodically from a solution with or without the reducing agent NaH_2PO_2. It was found that sodium hypophosphite had no influence on the mechanism of MoS_2 formation, but a decrease in the micro-level roughness of the deposited films was observed. XPS study showed that, when electrodeposition is carried out with hypophosphite, a much stronger Mo^{4+}-S bond signal is observed. Thus, the effect of NaH_2PO_2 on the electrochemical deposition of MoS_2 is mainly targeting the suppression of Mo-O bond formation or, conversely, the assistance of Mo-S bond formation. The catalytic effect for HER from 0.5 M H_2SO_4 was determined, and total electrode activity increased with higher catalyst loading. MoS_2 films, electrodeposited with hypophosphite, exhibited greater catalytic activity and had slightly lower Tafel slopes. The lowest slope (42.5 mV dec^{-1}) was observed for a MoS_2 film, electrodeposited with NaH_2PO_2, with low loading (equivalent to 10 C charge passed for electrodeposition of MoS_2). The films were stable at low overpotentials, but lost activity rapidly when operating at high currents. The results of the polarisation experiments, Tafel and EIS analyses of HER show that addition of sodium hypophosphite into the electrodeposition solution results in MoS_2 films with better intrinsic per-site activity. Films, electrodeposited with NaH_2PO_2, had lower R_{ct}, larger C_{dl} values and smaller R_a values, indicating faster charge transfer, a larger electrochemically active surface area and more rapid hydrogen adsorption/desorption. A method for the approximation of the number of active sites based on the calculated pseudocapacitance is proposed. The calculations resulted in values of about 10^{18}, which is comparable to those found in our previous research on thin plane MoS_2 films. The number of active sites was identical for films, electrodeposited from both solutions, which meant that, in terms of turnover frequency, the films, deposited with hypophosphite, were conclusively more catalytically active.

Author Contributions: Methodology, R.L.; investigation, R.L.; writing—original draft preparation, R.L.; writing—review and editing, R.L., N.T. and H.C.; visualisation, R.L.; and supervision, N.T. and H.C. All authors have read and agreed to the published version of the manuscript.

Conflicts of Interest: The authors declare no conflict of interest.

References

1. Holade, Y.; Servat, K.; Tingry, S.; Napporn, T.W.; Remita, H.; Cornu, D.; Kokoh, K.B. Advances in Electrocatalysis for Energy Conversion and Synthesis of Organic Molecules. *ChemPhysChem* **2017**, *18*, 2573–2605. [CrossRef] [PubMed]
2. Rostrup-Nielsen, J.R. Fuels and energy for the future: The role of catalysis. *Catal. Rev. Sci. Eng.* **2004**, *46*, 247–270. [CrossRef]
3. Salem, R.R. Theory of the electrolysis of water. *Prot. Met.* **2008**, *44*, 120–125. [CrossRef]
4. Trasatti, S. Water electrolysis: Who first? *J. Electroanal. Chem.* **1999**, *476*, 90–91. [CrossRef]
5. Krstajic, N. Hydrogen Evolution Reaction. *Encycl. Appl. Electrochem.* **2014**, 1039–1044. [CrossRef]
6. Lasia, A. Mechanism and kinetics of the hydrogen evolution reaction. *Int. J. Hydrogen Energy* **2019**, *44*, 19484–19518. [CrossRef]
7. Trasatti, S. Work function, electronegativity, and electrochemical behaviour of metals. III. Electrolytic hydrogen evolution in acid solutions. *J. Electroanal. Chem.* **1972**, *39*, 163–184. [CrossRef]
8. Petrii, O.A.; Tsirlina, G.A. Electrocatalytic activity prediction for hydrogen electrode reaction: Intuition, art, science. *Electrochim. Acta* **1994**, *39*, 1739–1747. [CrossRef]
9. Conway, B.E.; Jerkiewicz, G. Relation of energies and coverages of underpotential and overpotential deposited H at Pt and other metals to the 'volcano curve' for cathodic H_2 evolution kinetics. *Electrochim. Acta* **2000**, *45*, 4075–4083. [CrossRef]

10. Nørskov, J.K.; Bligaard, T.; Logadottir, A.; Kitchin, J.R.; Chen, J.G.; Pandelov, S.; Stimming, U. Trends in the Exchange Current for Hydrogen Evolution. *J. Electrochem. Soc.* **2005**, *152*, J23. [CrossRef]

11. Quaino, P.; Juarez, F.; Santos, E.; Schmickler, W. Volcano plots in hydrogen electrocatalysis-uses and abuses. *Beilstein J. Nanotechnol.* **2014**, *5*, 846–854. [CrossRef] [PubMed]

12. Yan, Y.; Xia, B.Y.; Zhao, B.; Wang, X. A review on noble-metal-free bifunctional heterogeneous catalysts for overall electrochemical water splitting. *J. Mater. Chem. A* **2016**, *4*, 17587–17603. [CrossRef]

13. Wang, J.; Yue, X.; Yang, Y.; Sirisomboonchai, S.; Wang, P.; Ma, X.; Abudula, A.; Guan, G. Earth-abundant transition-metal-based bifunctional catalysts for overall electrochemical water splitting: A review. *J. Alloys Compd.* **2020**, *819*, 153346. [CrossRef]

14. Wang, T.; Xie, H.; Chen, M.; D'Aloia, A.; Cho, J.; Wu, G.; Li, Q. Precious metal-free approach to hydrogen electrocatalysis for energy conversion: From mechanism understanding to catalyst design. *Nano Energy* **2017**, *42*, 69–89. [CrossRef]

15. Zou, X.; Zhang, Y. Noble metal-free hydrogen evolution catalysts for water splitting. *Chem. Soc. Rev.* **2015**, *44*, 5148–5180. [CrossRef] [PubMed]

16. Hinnemann, B.; Moses, P.G.; Bonde, J.; Jørgensen, K.P.; Nielsen, J.H.; Horch, S.; Chorkendorff, I.; Nørskov, J.K. Biomimetic hydrogen evolution: MoS_2 nanoparticles as catalyst for hydrogen evolution. *J. Am. Chem. Soc.* **2005**, *127*, 5308–5309. [CrossRef] [PubMed]

17. Jaramillo, T.F.; Jørgensen, K.P.; Bonde, J.; Nielsen, J.H.; Horch, S.; Chorkendorff, I. Identification of active edge sites for electrochemical H_2 evolution from MoS_2 nanocatalysts. *Science* **2007**, *317*, 100–102. [CrossRef]

18. Li, G.; Zhang, D.; Qiao, Q.; Yu, Y.; Peterson, D.; Zafar, A.; Kumar, R.; Curtarolo, S.; Hunte, F.; Shannon, S.; et al. All the Catalytic Active Sites of MoS_2 for Hydrogen Evolution. *J. Am. Chem. Soc.* **2016**, *138*, 16632–16638. [CrossRef]

19. Kibsgaard, J.; Jaramillo, T.F.; Besenbacher, F. Building an appropriate active-site motif into a hydrogen-evolution catalyst with thiomolybdate $[Mo_3S_{13}]^{-2}$ clusters. *Nat. Chem.* **2014**, *6*, 248–253. [CrossRef]

20. Tran, P.D.; Tran, T.V.; Orio, M.; Torelli, S.; Truong, Q.D.; Nayuki, K.; Sasaki, Y.; Chiam, S.Y.; Yi, R.; Honma, I.; et al. Coordination polymer structure and revisited hydrogen evolution catalytic mechanism for amorphous molybdenum sulfide. *Nat. Mater.* **2016**, *15*, 640–646. [CrossRef]

21. Huo, J.; Ge, R.; Liu, Y.; Guo, J.; Lu, L.; Chen, W.; Liu, C.; Gao, H.; Liu, H. Recent advances of two-dimensional molybdenum disulfide based materials: Synthesis, modification and applications in energy conversion and storage. *Sustain. Mater. Technol.* **2020**, *24*. [CrossRef]

22. Merki, D.; Hu, X. Recent developments of molybdenum and tungsten sulfides as hydrogen evolution catalysts. *Energy Environ. Sci.* **2011**, *4*, 3878–3888. [CrossRef]

23. Zhang, L.; Wu, L.; Li, J.; Lei, J. Electrodeposition of amorphous molybdenum sulfide thin film for electrochemical hydrogen evolution reaction. *BMC Chem.* **2019**, *13*, 1–9. [CrossRef]

24. Ponomarev, E.A.; Neumann-Spallart, M.; Hodes, G.; Lévy-Clément, C. Electrochemical deposition of MoS_2 thin films by reduction of tetrathiomolybdate. *Thin Solid Films* **1996**, *280*, 86–89. [CrossRef]

25. Benck, J.D.; Hellstern, T.R.; Kibsgaard, J.; Chakthranont, P.; Jaramillo, T.F. Catalyzing the hydrogen evolution reaction (HER) with molybdenum sulfide nanomaterials. *ACS Catal.* **2014**, *4*, 3957–3971. [CrossRef]

26. Benck, J.D.; Chen, Z.; Kuritzky, L.Y.; Forman, A.J.; Jaramillo, T.F. Amorphous molybdenum sulfide catalysts for electrochemical hydrogen production: Insights into the origin of their catalytic activity. *ACS Catal.* **2012**, *2*, 1916–1923. [CrossRef]

27. Merki, D.; Vrubel, H.; Rovelli, L.; Fierro, S.; Hu, X. Fe, Co, and Ni ions promote the catalytic activity of amorphous molybdenum sulfide films for hydrogen evolution. *Chem. Sci.* **2012**, *3*, 2515–2525. [CrossRef]

28. Wu, L.; Dzade, N.Y.; Yu, M.; Mezari, B.; van Hoof, A.J.F.; Friedrich, H.; de Leeuw, N.H.; Hensen, E.J.M.; Hofmann, J.P. Unraveling the Role of Lithium in Enhancing the Hydrogen Evolution Activity of MoS_2: Intercalation versus Adsorption. *ACS Energy Lett.* **2019**, *4*, 1733–1740. [CrossRef]

29. Tedstone, A.A.; Lewis, D.J.; O'Brien, P. Synthesis, Properties, and Applications of Transition Metal-Doped Layered Transition Metal Dichalcogenides. *Chem. Mater.* **2016**, *28*, 1965–1974. [CrossRef]

30. Mosconi, D.; Till, P.; Calvillo, L.; Kosmala, T.; Garoli, D.; Debellis, D.; Martucci, A.; Agnoli, S.; Granozzi, G. Effect of Ni Doping on the MoS2 Structure and Its Hydrogen Evolution Activity in Acid and Alkaline Electrolytes. *Surfaces* **2019**, *2*, 531–545. [CrossRef]

31. Liu, Q.; Liu, Q.; Kong, X. Anion Engineering on Free-Standing Two-Dimensional MoS_2 Nanosheets toward Hydrogen Evolution. *Inorg. Chem.* **2017**, *56*, 11462–11465. [CrossRef] [PubMed]

32. Huang, H.; Chen, L.; Liu, C.; Liu, X.; Fang, S.; Liu, W.; Liu, Y. Hierarchically nanostructured MoS_2 with rich in-plane edges as a high-performance electrocatalyst for the hydrogen evolution reaction. *J. Mater. Chem. A* **2016**, *4*, 14577–14585. [CrossRef]

33. Kosmala, T.; Mosconi, D.; Giallongo, G.; Rizzi, G.A.; Granozzi, G. Highly Efficient MoS_2/Ag_2S/Ag Photoelectrocatalyst Obtained from a Recycled DVD Surface. *ACS Sustain. Chem. Eng.* **2018**, *6*, 7818–7825. [CrossRef]

34. Levinas, R.; Tsyntsaru, N.; Cesiulis, H. Insights into electrodeposition and catalytic activity of MoS_2 for hydrogen evolution reaction electrocatalysis. *Electrochim. Acta* **2019**, *317*, 427–436. [CrossRef]

35. Vrubel, H.; Moehl, T.; Grätzel, M.; Hu, X. Revealing and accelerating slow electron transport in amorphous molybdenum sulphide particles for hydrogen evolution reaction. *Chem. Commun.* **2013**, *49*, 8985–8987. [CrossRef]

36. Tremblay, M.L.; Martin, M.H.; Lebouin, C.; Lasia, A.; Guay, D. Determination of the real surface area of powdered materials in cavity microelectrodes by electrochemical impedance spectroscopy. *Electrochim. Acta* **2010**, *55*, 6283–6291. [CrossRef]

37. Reid, O.; Saleh, F.S.; Easton, E.B. Determining electrochemically active surface area in PEM fuel cell electrodes with electrochemical impedance spectroscopy and its application to catalyst durability. *Electrochim. Acta* **2013**, *114*, 278–284. [CrossRef]

38. Thangaraj, N.; Tamilarasan, K.; Sasikumar, D. Effect of current density on electrodeposited ferrous tungsten thin films. *Indian J. Pure Appl. Phys.* **2014**, *52*, 395–398.

39. Park, D.Y.; Myung, N.V.; Schwartz, M.; Nobe, K. Nanostructured magnetic CoNiP electrodeposits: Structure-property relationships. *Electrochim. Acta* **2002**, *47*, 2893–2900. [CrossRef]

40. Li, L.; Qin, Z.; Ries, L.; Hong, S.; Michel, T.; Yang, J.; Salameh, C.; Bechelany, M.; Miele, P.; Kaplan, D.; et al. Role of sulfur vacancies and undercoordinated Mo regions in MoS_2 nanosheets toward the evolution of hydrogen. *ACS Nano* **2019**, *13*, 6824–6834. [CrossRef]

41. Choi, J.G.; Thompson, L.T. XPS study of as-prepared and reduced molybdenum oxides. *Appl. Surf. Sci.* **1996**, *93*, 143–149. [CrossRef]

42. Baltrusaitis, J.; Mendoza-Sanchez, B.; Fernandez, V.; Veenstra, R.; Dukstiene, N.; Roberts, A.; Fairley, N. Generalized molybdenum oxide surface chemical state XPS determination via informed amorphous sample model. *Appl. Surf. Sci.* **2015**, *326*, 151–161. [CrossRef]

43. Vernickaite, E.; Lelis, M.; Tsyntsaru, N.; Pakštas, V.; Cesiulis, H. XPS studies on the Mo-oxide based coatings electrodeposited from highly saturated acetate bath. *Chemija* **2020**, *31*, 203–209.

44. Eda, G.; Yamaguchi, H.; Voiry, D.; Fujita, T.; Chen, M.; Chhowalla, M. Photoluminescence from chemically exfoliated MoS_2. *Nano Lett.* **2011**, *11*, 5111–5116. [CrossRef]

45. Syari'Ati, A.; Kumar, S.; Zahid, A.; el Yumin, A.A.; Ye, J.; Rudolf, P. Photoemission spectroscopy study of structural defects in molybdenum disulfide (MoS_2) grown by chemical vapor deposition (CVD). *Chem. Commun.* **2019**, *55*, 10384–10387. [CrossRef]

46. Lasia, A. *Electrochemical Impedance Spectroscopy and Its Applications*, 1st ed.; Springer: New York, NY, USA, 2014; ISBN 9781461489337.

47. Brug, G.J.; van den Eeden, A.L.G.; Sluyters-Rehbach, M.; Sluyters, J.H. The analysis of electrode impedances complicated by the presence of a constant phase element. *J. Electroanal. Chem.* **1984**, *176*, 275–295. [CrossRef]

48. Voiry, D.; Chhowalla, M.; Gogotsi, Y.; Kotov, N.A.; Li, Y.; Penner, R.M.; Schaak, R.E.; Weiss, P.S. Best Practices for Reporting Electrocatalytic Performance of Nanomaterials. *ACS Nano* **2018**, *12*, 9635–9638. [CrossRef]

NOTES

NOTES